Thermomechanical Characterization and Modeling of Superelastic Shape Memory Alloy Beams and Frames

by

Ryan Watkins

A dissertation submitted in partial fulfillment
of the requirements for the degree of
Doctor of Philosophy
(Aerospace Engineering)
in the University of Michigan
2015

Doctoral Committee:

Professor John A. Shaw, Chair
Associate Professor Samantha H. Daly
Professor David S. Grummon, Michigan State University
Emeritus Professor Nicolas Triantafyllidis
Professor Anthony M. Waas

Acknowledgments

This work was made possible by the support and encouragement of many people and organizations:

- my mentors, Dr. John Shaw, Dr. Nicolas Triantafyllidis, and Dr. Ryan Elliott, who helped guide me through the world of shape memory alloys, Bloch wave stability analysis, and the wider world of academia and research;
- my labmates Benjamin Reedlunn, Kannan Dasharathi, Daniel Biggs, Will LePage, and Corin Bowen, who not only helped guide my research and debug the many issues that arose during my experimental work, but also supported me through the general day–to–day ups and downs of research;
- the Aerospace Engineering support staff, including Terry Larrow, Tom Griffin, Dave McLean, and Aaron Borgman, who provided much needed technical assistance in my experimental work;
- the National Science Foundation Graduate Research Student Fellowship Program (Award CMS0409084), the National Defense Science and Engineering Graduate (NDSEG) Fellowship (32 CFR 168a), and the Air Force Office of Scientific Research (Award FA9550-08-1-0313), who financially supported my research and me, allowing me to focus all my attention on my studies; and
- my friends and family, including my fiancé Corinne, my parents, my brother, my sister, my grandparents, David Olson, Mark Huizenga, Sayuri Yapa, Matt Parno, and Brent Pomeroy, who provided emotional support throughout the six years of my graduate studies.

Table of Contents

List of Figures

Figure

List of Tables

Table

Abstract

Of existing applications, the majority of shape memory alloy (SMA) devices consist of beam (orthodontic wire, eye glasses frames, catheter guide wires) and framed structures (cardiovascular stents, vena cava filters). Although uniaxial tension data is often sufficient to model basic beam behavior (which has been the main focus of the research community), the tension-compression asymmetry and complex phase transformation behavior of SMAs suggests more information is necessary to properly model higher complexity states of loading. In this work, SMA beams are experimentally characterized under general loading conditions (including tension, compression, pure bending, and buckling); furthermore, a model is developed with respect to general beam deformation based on the relevant phenomena observed in the experimental characterization.

Stress induced phase transformation within superelastic SMA beams is shown to depend on not only the loading mode, but also kinematic constraints imposed by beam geometry (such as beam cross-section and length). In the cases of tension and pure bending, the structural behavior is unstable and corresponds to phase transformation localization and propagation. This unstable behavior is the result of a local level up–down–up stress/strain response in tension, which is measured here using a novel composite–based experimental technique. In addition to unstable phase transformation, intriguing post-buckling straightening is observed in short SMA columns during monotonic loading (termed unbuckling here). Based on this phenomenological understanding of SMA beam behavior, a trilinear based material law is developed in the context of a Shanley column model and is found to capture many of the relevant features of column buckling, including the experimentally observed unbuckling behavior. Due to the success of this model, it is generalized within the context of beam theory and, in conjunction with Bloch wave stability analysis, is used to model and design SMA honeycombs.

Chapter 1

Introduction

Over the past few decades, the demand for higher efficiency structures has grown as engineers continually look to improve performance while decreasing operational costs. To address these demands, the field of Smart Structures has begun to incorporate additional functionality (such as actuation and sensing) into traditional passive load bearing structures. Some of the most prominent focuses within the Smart Structures field are integrated structural health monitoring systems, morphing structures (such as control surfaces on aircraft), adaptively tuned structures (such as variable stiffness car shocks), and energy harvesters.

Multi-functionality is often enabled within Smart Structures through the use of Adaptive Materials (also referred to as Smart Materials) which are a class of materials that mechanically interact with external stimuli (such as electric, thermal, and/or magnetic fields). Due to their mechanical interaction with the environment, Adaptive Materials are primarily used as actuators (an external stimulus is used to activate the material mechanically); although, some also have the capability to function as sensors (a mechanical input generates an external field which can be measured). Some of the most common Adaptive Material classes are shape memory alloys, shape memory polymers, piezoelectrics, and magnetostrictives. The performance capabilities of these active material classes (such as the actuation work output, response rate and magnitude of deformation) vary considerably as outlined in Table 1.1, lending each to their own niche applications. Of interest in this dissertation are shape memory alloys, which are most suitable for high work output actuation at moderately large strokes and low actuation frequencies. For an in-depth overview of shape memory alloy applications and properties, see Shaw et al. [2010]; however, for completeness, a brief overview is provided here.

Table 1.1: Shape memory alloys provide the greatest actuation work output of common Adaptive Materials, although at relatively slow actuation frequencies.

Material class	Most popular materials	Actuation field	Work output	Response rate	Deformation magnitude
Shape memory alloy	NiTi, CuZnAl	Temperature	High	Slow	Moderate
Shape memory polymer	styrene acrylate, epoxy	Temperature	Very low	Very slow	High
Piezoelectric	PZT, PVDF	Electric	Low	Fast	Low
Magnetostrictive	Terfenol-D, Galfenol	Magnetic	Low	Moderate	Low

1.1 Shape Memory Alloys Background

Shape memory alloys (SMAs) are a class of metals which exhibit two unique properties: the shape memory effect and superelasticity. The more well known (one-way) shape memory effect describes the material's ability to recover apparent permanent deformation when heated above a threshold temperature (see ①–②–③–① in Figure 1.1); additionally, if processed correctly, a preferred high and low temperature state can be established, resulting in a two-way shape memory effect. The temperature induced deformation of the shape memory effect is often used in actuator-based applications and is the property that classifies SMAs as Adaptive Materials. Superelasticity describes the material's enhanced flexibility when operating at temperatures above the threshold temperature for the shape memory effect (see ①–④–① in Figure 1.1). Unlike typical metals which begin to permanently deform when strained to the order of $0.1\,\%$, superelastic materials can recover deformations on the order of $10\,\%$ strain. Superelastic SMAs are therefore often used in applications where the strength of a metal is needed, but high flexibility is also required.

1.1.1 Applications

A number of SMAs have been discovered over the past century (Figure 1.2); however, as many of them consist of precious metals, only a few have been shown to be commercially viable. The most commonly used SMA is near equiatomic NiTi (often referred to as Nitinol), which arguably possesses the best shape memory and superelastic behavior of all known SMAs; additionally, NiTi is biocompatible, enabling its use in biomedical applications.

In application, the shape memory effect is primarily used for actuation. Functioning under the one-way shape memory effect, an SMA can only actuate in one direction; however, two-way

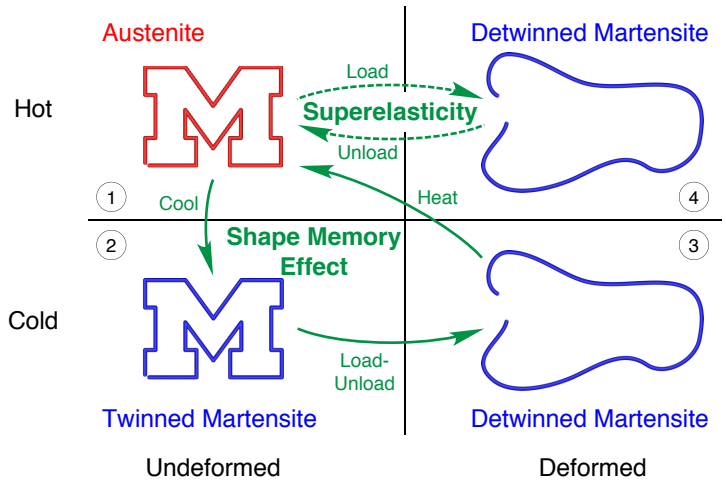

Figure 1.1: Starting in the austenite phase (①), a shape memory cycle consists of cooling the material below the martensite transformation temperature (①–②), loading-unloading the material such that residual deformation is present (②–③), followed by heating the material to recover the original shape (③–①); whereas, superelasticity corresponds to the recovery of large deformations when loaded-unloaded at temperatures above the austenite transformation temperature (①–④–①).

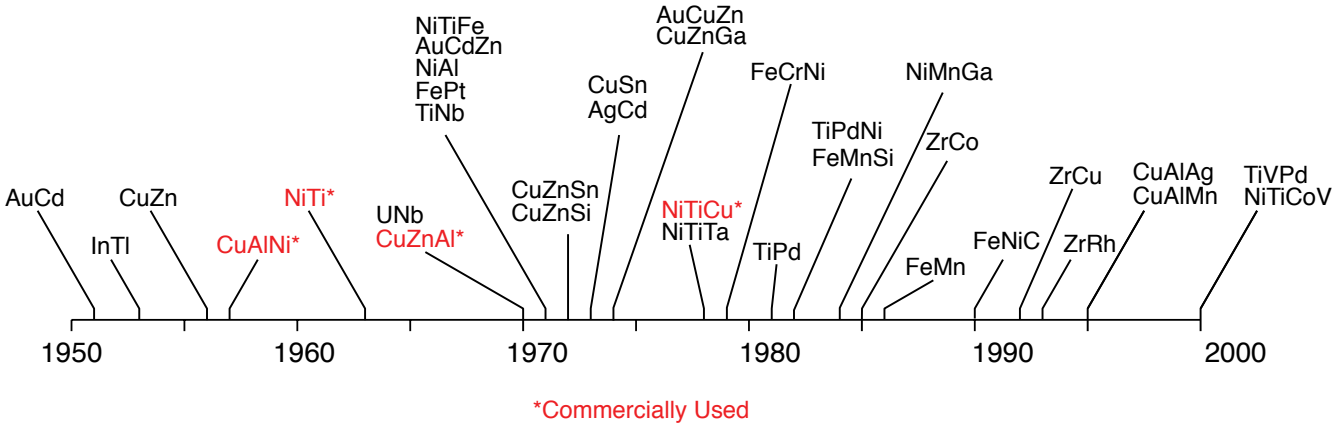

Figure 1.2: A number of SMAs have been discovered since the early 1950s; however, only a few of them are commercially viable (reproduction of Figure 2a from Shaw et al. [2010]).

SMAs or one-way SMAs coupled with a biased spring can achieve two-way actuation. The first commercially successful application of the one-way shape memory effect was the Cryofit™ shrink fit pipe coupler developed by Raychem Corporation in 1969, which was most notably used on fuel lines in the F-14 fighter [Kauffman and Mayo, 1997]. Following suit, other forms of SMA couplers were developed, such as Cryocon, Cryolive®, Betaflex™, Crotact™, Tinel® -lock and Unilok® [Humbeeck, 1999]. In 1992, the Flangibolt® was developed by TiNi Aerospace to shear off bolt heads using the one-way shape memory effect [Johnson, 1992], providing an alternative to explosive release mechanisms on spacecraft. More recently, actuator SMAs have been integrated in

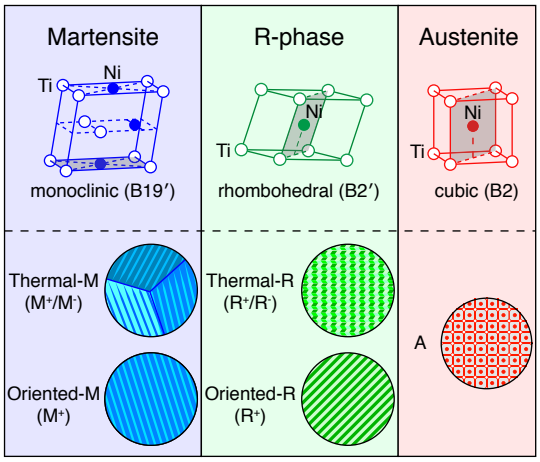

Figure 1.3: There are three primary crystallographic phases in NiTi: cubic B2 austenite, monoclinic B19′ martensite and the rhombohedral B2′ R-phase (reproduction of Figure 6a from Shaw et al. [2010]).

mainstream applications, such as the hatch vent of the 2014 Chevrolet Corvette [Alexander et al., 2014], thermal cutoff valves [Tucholski and Pedicini, 1990], automatic transmission cold-start valves [Xie et al., 2013], and optical image stabilization systems [Topliss and Leedham, 2014]. In the future, the shape memory effect is planned to be integrated into more advanced applications, such as morphing control surfaces (control surfaces of aircraft and the chevrons of jet turbines) and deployable structures in space.

Although less well known, superelastic SMA devices make up the vast majority of SMA applications to date. The first successful commercial application of superelastic SMAs was as orthodontic bridge wires in the 1970s, being both more flexible and less stiff than traditionally used stainless steel wires [Kauffman and Mayo, 1997]. In the subsequent years, superelastic SMAs found their way into eye glasses frames, cell phone antennas, and flexible support in clothing [Humbeeck, 1999]; however, the most notable application of superelastic SMAs has been as biomedical tools and implants (such as cardiovascular stents, root canal files, embolic filters, vena cava filters, and catheter guide wires [Lecce and Concilio, 2014]), which was quoted to have a market value of $130 billion in 2002 [Yoneyama and Miyazaki, 2008] and has continued to grow since then.

1.1.2 Origins of the Shape Memory Effect and Superelasticity

The shape memory and superelastic phenomena found in SMAs originate from a solid-to-solid state martensitic transformation between a high temperature parent austenite phase and a low temperature martensite phase. This diffusionless process corresponds to a shearing of the lattice that

results in an abrupt change in the crystallographic structure. In the case of NiTi, two crystallographic systems of martensite can form within the operational range of the material, resulting in three relevant phases (see Figure 1.3):

- a high symmetry B2 cubic crystal structure which corresponds to the austenite phase (A),
- a moderate symmetry B2′ rhombohedral crystal structure which corresponds to one possible martensitic phase (R), and
- a low symmetry B19′ monoclinic crystal structure which corresponds to another possible martensitic phase (M).

The martensitic B2′ rhombohedral phase (often referred to as the R-phase) is only observed for a subset of NiTi alloys and exhibits small amplitude shape memory and superelastic behavior (usually less than $1\,\%$ strain); whereas, the martensitic B19′ monoclinic phase (often simply referred to as martensite) is usually the primary focus of NiTi behavior due to its high amplitude shape memory and superelastic behavior (usually on the order of $6\,\%$ to $8\,\%$ strain).

Although martensitic transformations are found in many metallic systems, the shape memory effect and superelasticity only occur for a subset of martensitic transformations which adhere to a strict set of conditions [Bhattacharya, 2003, Elliott et al., 2002b]:

- the austenite phase must have a higher symmetry than the martensite phase, allowing for the formation of multiple symmetry related variants of martensite which can develop complex twinned microstructures;
- the martensitic transformation must be "proper" (which defines a group-subgroup relationship between the high and low symmetry phases that results in infinitesimal displacements of atoms) instead of "reconstructive" (which involves finite displacements of atoms and often the breaking and reforming of atomic bonds);
- the transformation from austenite to martensite must be self–accommodating, allowing for thermally induced transformation between the two phases with no macroscopic deformation; and
- the phase transformation must be reversible (thermoelastic).

In addition to these restrictions, the appropriate grain size and precipitate structure (usually achieved through heat treatment and cold work) are necessary to prevent early onset plasticity within the material.

Due to the higher symmetry of the austenite phase, the martensite microstructure can reside in either a twinned or detwinned state: in a twinned state, multiple variants of the base crystal co-

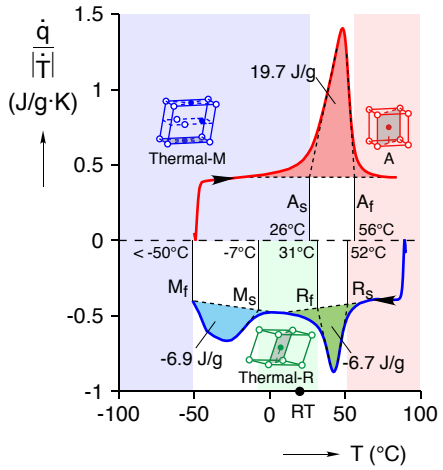

(a) Example DSC response of a NiTi alloy (reproduction of Figure 6b from Shaw et al. [2010])

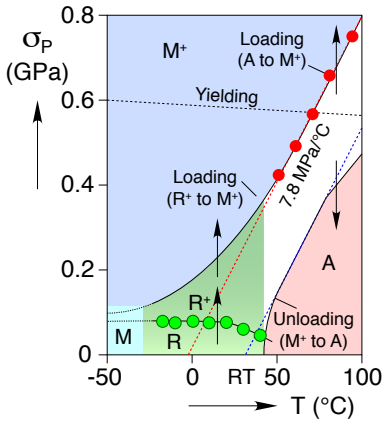

(b) Example Clausius-Clapeyron relationship of a NiTi alloy (reproduction of Figure 7b from Shaw et al. [2010])

Figure 1.4: Phase transformation in SMAs is dependent on both temperature and the loading state. The stress free temperature behavior is measured using DSC (a) while the stress dependent behavior is characterized by the Clausius-Clapeyron slope (b).

exist within the microstructure; whereas, in a detwinned state, only a single variant of the crystal exists within the microstructure. When an SMA is cooled from austenite to martensite, the resulting crystal structure forms into a twinned microstructure which is often referred to as thermal martensite. This formation of the twinned phase is self–accommodating, resulting in no macroscopic deformation of the material. When sufficiently stressed, twinned martensite reorients into detwinned martensite (often referred to as oriented martensite) which does not reverse back to twinned martensite when unloaded, resulting in residual macroscopic deformation.

Table 1.2: The temperature ranges associated with phase transformation within SMAs are referred to by their start and finish temperatures, as shown here for a generic NiTi alloy.

Transformation	Label	Start temperature	Finish temperature
Austenite to R-phase	$A \rightarrow R$	R_s	R_f
R-phase to martensite	$R \rightarrow M$	M_s	M_f
Martensite to austenite	$M \rightarrow A$	A_s	A_f

Under stress-free conditions, austenite is thermodynamically stable at high temperatures while martensite is thermodynamically stable at low temperatures. As phase transformation does not occur at a single temperature, but rather over a small temperature range, a start and finish temperature

are used to characterize the transformation behavior (an example of which are parameterized for NiTi in Table 1.2). In general, the temperatures at which phase transformation begins and ends are hysteretic with respect to the direction of phase transformation (as is the case for $A \leftrightarrow M$ transformations in NiTi); however, some cases exist in which the transformation temperatures are almost nonhysteretic (such as the $A \leftrightarrow R$ transformations in NiTi which usually only has a hysteresis of $2\,^{\circ}\text{C}$ to $5\,^{\circ}\text{C}$). Furthermore, some phase transformations occur concurrently (such as the transformation from martensite in NiTi where R-phase and austenite nucleate concurrently). These transformation temperatures (along with the latent heats of transformation and the material specific heat) are usually measured using differential scanning calorimetry (DSC), an example of which is shown in Figure 1.4a for a NiTi alloy. In the case of NiTi alloys, M_{f} usually ranges from $-150\,^{\circ}\text{C}$ to $60\,^{\circ}\text{C}$ and A_{f} from $-30\,^{\circ}\text{C}$ to $90\,^{\circ}\text{C}$ depending on stoichiometric composition and material processing.

In addition to temperature change, phase transformation can be induced by external loading. Starting load free in the austenite phase, stress induced phase transformation results in twinned martensite which transforms back into the austenite phase upon unloading. Similar to thermally induced phase transformation, the stress at which phase transformation is induced (σ_p) is hysteretic with respect to the direction of phase transformation; furthermore, σ_p varies nearly linearly with respect to temperature according to the Clausius-Clapeyron slope, an example of which is shown in Figure 1.4b for a NiTi alloy. In the case of NiTi alloys, the Clausius-Clapeyron slope usually ranges between $5\,\text{MPa}/^{\circ}\text{C}$ to $8\,\text{MPa}/^{\circ}\text{C}$.

The shape memory effect and superelasticity correspond to differing aspects of these complex martensitic behaviors:

- The shape memory effect is the result of twinning/detwinning behavior and the reversibility of thermally induced phase transformations. To help illustrate the behavior, a depiction of the shape memory effect is shown in ①–②–③–① of Figure 1.1. Starting at a high temperature in the austenite phase (①), the material is cooled below M_{f}, resulting in thermal (twinned) martensite (②). Due to the self–accommodating nature of the phase transformation between austenite and thermal martensite, there is no macroscopic deformation associated with this process (except for basic thermal contraction due to the temperature change). At these low temperatures, loading the material detwins the microstructure, resulting in residual deformation upon unloading (③). If the material is then heated above the austenite finish temperature, the crystal structure transforms into the high symmetry austenite phase, recovering the residual strain incurred by detwinning of the microstructure (①).
- Superelasticity is the result of reversible stress-induced phase transformation between austen-

ite and detwinned martensite. To help illustrate the behavior, a depiction of superelasticity is shown in ①–④–① of Figure 1.1. Operating at temperatures above the A_f, stress induced phase transformation from austenite results in detwinned martensite (④). The transformation into the twinned phase results in large macroscopic strains, which are recovered when the loading is released and the material transforms back into the austenite phase (①).

1.2 Motivations

Due to their complex thermomechanical behavior, constitutive modeling of SMAs has been an elusive problem. Most current SMA devices are therefore developed based on empirical rules or trial and error design. Although these design techniques have sufficed for relatively simple design requirements (such as highly flexible devices or linear wire actuation), a robust material model is required to fully utilize the beneficial properties of SMAs for more advanced applications.

One of the many issues associated with the development of a robust SMA constitutive model is the limited availability of experimental data for phenomenological understanding and calibration and validation purposes. Due to the large recoverable deformations observed in SMAs, non-standard procedures are required to sufficiently probe and measure the full range of material behavior; furthermore, both mechanical and thermal conditions must be tightly controlled to account for their coupled thermomechanical behavior. The majority of experimental data on SMAs have therefore been with respect to tension of wire and strip, with only a few cases focusing on more complex forms of loading [Berg, 1995, 1997, Bundara et al., 2000, Rahman et al., 2001, Sun and Li, 2002, Rejzner et al., 2002, Urushiyama et al., 2003, Grabe and Bruhns, 2008, Reedlunn et al., 2013, Bechle and Kyriakides, 2013]. From these data, SMAs have been found to exhibit thermomechanical coupling [Shaw and Kyriakides, 1995], hysteresis with respect to mechanical and thermal loading, local mechanical phenomena such as phase transformation localization [Shaw and Kyriakides, 1997], history dependent mechanical and thermal shakedown, tension/compression asymmetry [Gall and Sehitoglu, 1999], and loading rate sensitivity [Shaw and Kyriakides, 1995]; however, this phenomenological understanding is limited to a relatively small set of loading cases of an anisotropic material. Although sufficient to develop and validate tensile models (see for example Chang et al. [2006]), this information has been insufficient to validate models representing general SMA behavior.

1.3 Objectives and Contributions

The primary objective of this dissertation is to facilitate the development of SMA material models. Due to the prevalence of thin-walled superelastic SMA structures in existing SMA applications, this objective is approached in the context of superelastic beams and frames.

- To begin, the general thermomechanical behaviors of superelastic NiTi beams are examined experimentally in Chapter 2, probing the primary deformation modes of beams (tension, compression, pure bending, and column buckling).
- Due to the presence of deformation localization in the tensile experiments of Chapter 2, a novel composite–based experimental technique is used in Chapter 3 to measure the homogeneous tensile deformation of NiTi, providing a better understanding of the underlying material behavior.
- Based on this phenomenological understanding, a simple two degree of freedom model is developed and implemented in Chapter 4 to investigated and explain an interesting unbuckling phenomenon discovered during some of the column buckling experiments of Chapter 2.
- Motivated by the success of this simple model, it is generalized within the context of beam theory and implemented within the finite element framework in Chapter 5.
- Shifting to the examination of framed SMA structures with an underlying periodicity (in particular, honeycombs), *Bloch wave* stability analysis is outlined in Chapter 6.
- Finally, the performance capabilities of SMA honeycombs are experimentally quantified and the model developed in Chapter 5 and the stability analysis discussed in Chapter 6 are used to investigate the energy absorption properties of superelastic SMA honeycombs in Chapter 7.

Chapter 2

Experimental Study of Superelastic SMA Beams

In many existing applications, SMA devices consist of slender beams and frames, such as catheter guide wires, cardiovascular stents, isolation bars for highway bridges, wire re-centering devices for civil buildings, flexible eye glasses frames, and flexible support in clothing (such as shoes and brassieres) [Duerig et al., 1999, Song et al., 2006, Humbeeck, 1999]. The prevalence of thin-walled structures in SMA applications is likely due to two factors: (1) the bending dominated kinematics of beams and frames amplifies recoverable displacements, resulting in highly deformable devices, and (2) excellent shape memory and superelastic properties are predominately available in high aspect ratio forms (wires, thin strips and tubes) where drawing and controlled heat treatment can be advantageously employed in their fabrication/processing. Understanding the mechanical behavior of SMA beams and their potential structural/material instabilities is therefore important to not only improve the fidelity of existing constitutive models, but also to enable the design and analysis of new and more complex thin-walled devices.

The kinetics of phase transformation in SMA beams are still not fully understood, especially for loading modes other than uniaxial tension. It is expected that many of the common features found in the uniaxial behavior, such as

- a non-monotonic nonlinear mechanical response,
- strong temperature sensitivity,
- loading-rate sensitivity due to thermo-mechanical coupling,
- mechanical and thermal hysteresis,
- texture and anisotropy,
- significant tension-compression asymmetry, and
- unstable stress-induced transformation (which often results in localization of the strain field and propagation of macroscopic phase transformation boundaries),

will be present under general loading conditions; however, it is unclear how these phenomena will interact and what other unknown behaviors will be present.

To date, a small body of experimental data exists in the literature addressing combined modes of deformation, mostly focusing on pure bending, tension-torsion, and buckling behavior [Berg, 1995, 1997, Bundara et al., 2000, Rahman et al., 2001, Sun and Li, 2002, Rejzner et al., 2002, Urushiyama et al., 2003, Grabe and Bruhns, 2008, Reedlunn et al., 2013, Bechle and Kyriakides, 2013]. Within this literature, often only the tensile response and one additional mode of loading are examined on a single specimen geometry (and occasionally the compressive behavior as in Reedlunn et al. [2013], Bechle and Kyriakides [2013]). To gain a more comprehensive understanding of general SMA beam behavior, I examine the mechanical response and phase transformation kinetics of two different SMA beam geometries under four different modes of loading.

This chapter presents isothermal experiments on commercially-available superelastic NiTi cylindrical rods and tubes of the same nominal outer diameter and with similar superelastic responses. Beginning with the underlying uniaxial and bending deformations found in beam kinematics, pure tension, pure compression and pure bending experiments are examined. Column buckling experiments are then presented, studying SMA beam behavior under combined uniaxial and bending deformation; additionally, the buckling experiments investigate the interaction between material and structural instability. In all experiments, stereo digital image correlation (DIC) is used to examine full field surface displacements and strains through the course of a loading procedure, allowing for the observation of strain field localization when present and the measurement of averaged field quantities. The general properties of the rod and tube are briefly discussed in Section 2.1, followed by the experimental setups and procedures for each experiment type in Section 2.2. In Section 2.3, the experimental results for both cross-sectional geometries are compared and contrasted for each loading mode, focusing on the macroscopic mechanical responses and the evolution and morphology of phase transformation. The major contributions of this chapter are

- the observation of multiple phase transformation localization morphologies which depend on the loading mode and specimen cross-sectional geometry,
- that, even in the presence of phase transformation localization, plane sections remain plane in rods (solid cross-sections), but only on average in tubes (hollow cross-sections),
- the discovery of unbuckling behavior in short SMA columns (that is, the post-buckling straightening of a column under continued monotonic compression), and
- a survey of superelastic SMA beam behavior under four modes of loading on two specimen cross-sectional geometries, providing a database of high quality experimental data (including full field surface displacements and strains) which can be used for both model calibration and

validation.

2.1 Materials

Experiments were performed on specimens cut from commercially available, straight, superelastic NiTi rod (NDC SE508, Lot # 2006303) and tube (Memry BB, Lot # 957152). Due to the extreme sensitivity of SMA material behavior to the manufacturing process (such as stoichiometric composition, heat treatment, and cold work), it was difficult to obtain different geometric forms with the same material properties; therefore, these materials were selected to be as similar as possible, but were not quite identical. The NiTi rod had a measured outer diameter $D = 3.150\,\text{mm}$; whereas, the NiTi tube had a measured outer diameter $D = 3.176\,\text{mm}$ and wall thickness $H = 0.318\,\text{mm}$ (resulting in an approximate diameter to thickness ratio $D/H \approx 10$). All experiments presented were performed on new specimens in the as-received condition.

Differential scanning calorimetry (DSC) was conducted on both materials to characterized their stress-free phase transformation behavior. Each geometric form was cut at a slow speed with a water cooled diamond cutoff wheel to minimize specimen heating and stress-induced phase transformation; the resulting rod and tube specimens were $21.4\,\text{mg}$ and $35.4\,\text{mg}$, respectively. As is common practice when conducting DSC on SMAs, the DSC experiments started at a temperature sufficiently high to ensure the material was in the parent austenite phase, cooled at a constant rate of $-10\,^{\circ}\text{C/min}$ to a sufficiently cold temperature to ensure the material was fully in the martensite phase, allowed to equilibrate for a short time, and then heated to the start temperature at a constant temperature rate of $10\,^{\circ}\text{C/min}$. The DSC results are shown in Figure 2.1, demonstrating distinct transformations from austenite to R-phase and R-phase to martensite on cooling (two distinct latent heat valleys), but overlapping reverse transformations on heating (overlapping latent heat peaks). The sub-room temperature austenite finish temperatures (A_f) of $10\,^{\circ}\text{C}$ and $19\,^{\circ}\text{C}$ for the rod and tube, respectively, indicate both forms were superelastic at room temperature.

2.2 Experimental Setups

All experiments were performed in a general purpose uniaxial load frame under global elongation (δ) control. Each specimen was gripped within the experimental fixture[1], loaded at a constant loading rate $|\dot{\delta}| = |\text{d}\delta/\text{d}t|$ to a peak elongation, and then unloaded to a state of zero load. Ex-

[1] Steel pins were inserted within the gripped sections of the tube specimens.

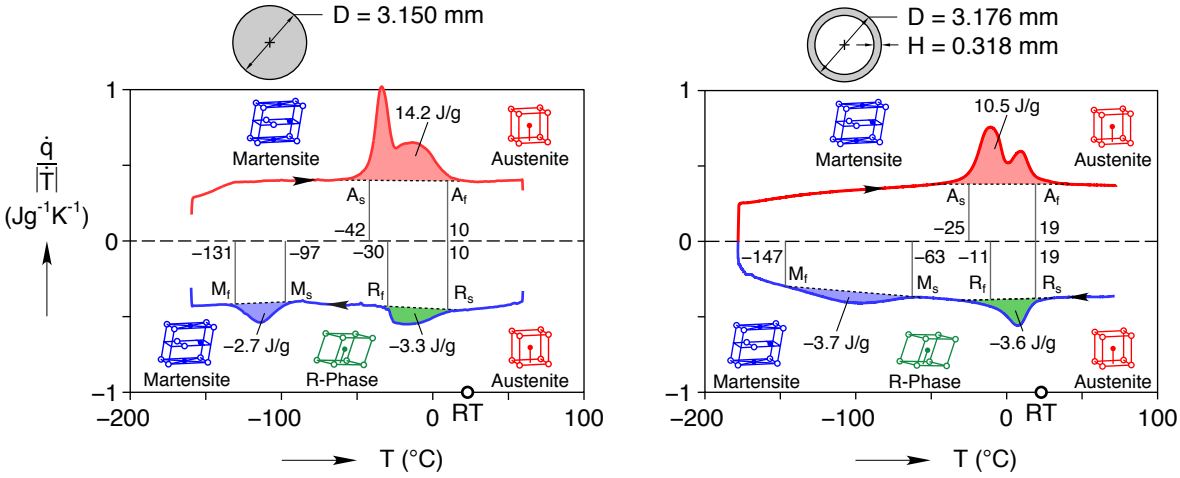

(a) Rod (b) Tube

Figure 2.1: Cross-section geometries and differential scanning calorimetry (DSC) thermograms (specific heat flow $\dot{q}/\dot{T}$ vs. temperature T) for the rod and tube specimens. Both materials had similar outer diameters and were superelastic at room temperature (RT).

periments were performed in stagnant room temperature air at sufficiently slow loading/unloading rates to achieve near isothermal loading conditions (less than $1\,°\text{C}$ temperature change). During each experiment, the axial load P and cross-head displacement δ were measured, along with imaging of the specimen; additionally, at the end of each experiment, the following post-processing procedures were conducted:

- Stereo digital image correlation (DIC) was used in all experiments to measure surface displacements and strains, allowing for the investigation of localized deformations. To enable these measurements, the gauge section of each specimen was painted with a base coat of white paint, followed by black speckles. This gauge section was then imaged through the course of the experiment by two cameras positioned with a relative stereo angle between them. Each camera consisted of a Pt. Grey Research Grasshopper (GRAS-50S5M-C) charge-coupled device (CCD), Fujinon HF75SA $75\,\text{mm}$ lens and appropriate lens extension tubes (between $20\,\text{mm}$ to $60\,\text{mm}$) to ensure the full specimen was in the field of view of the cameras while maximizing the number of pixels across the specimen width (atleast 100 pixels). At the end of the experiment, the stereo image pairs were post-processed using the commercially available software Vic-3D 2010 [Solutions, 2012] to calculated surface displacements and strains. For a more in-depth discussion of the DIC measurement technique, see Reedlunn et al. [2011], Sutton et al. [2009]. Due to its suitability for modeling beam kinematics (for example, see Humer [2011]), all DIC strain fields are reported using the Biot

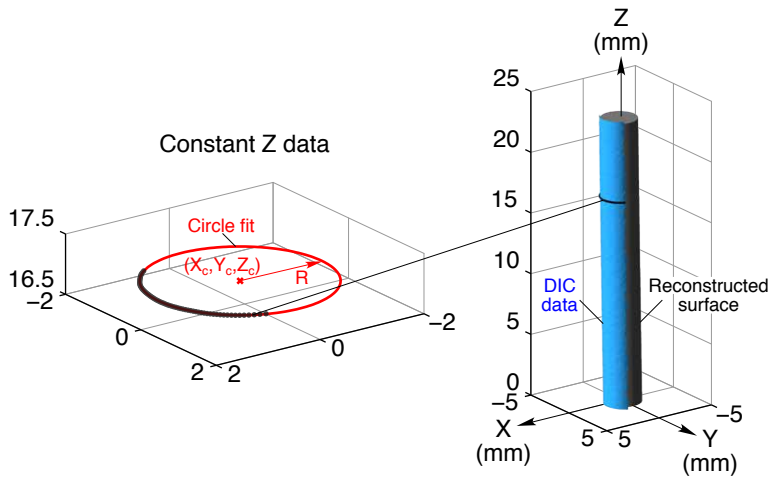

(a) Reference configuration

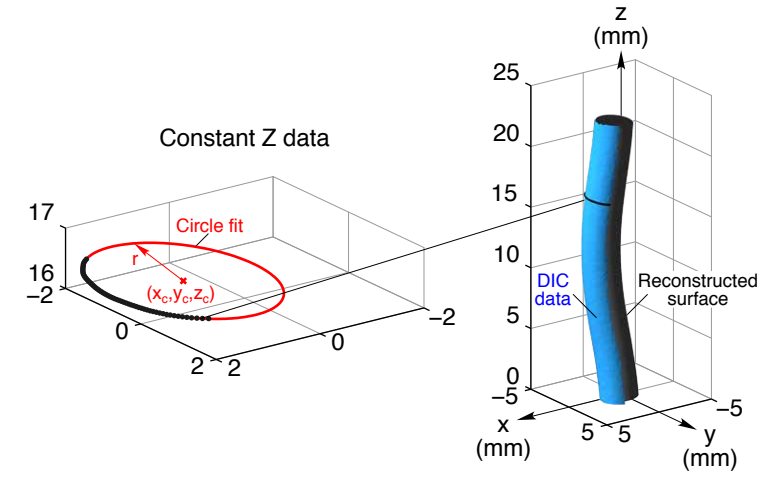

(b) Deformed configuration

Figure 2.2: To extrapolate the specimen centerline from the DIC data, circles were fit to material points with similar Z values in the reference configuration and accumulated to define the specimen geometry.

strain measure[2], $\boldsymbol{\varepsilon}^{\mathrm{B}} = \boldsymbol{U} - \boldsymbol{I}$, where $\boldsymbol{U}$ is the right stretch tensor and $\boldsymbol{I}$ is the identity tensor.

- The specimen centerlines during the course of an experiment were extrapolated based on the 3D surface data from the DIC analysis, quantifying the cross-sectionally averaged axial and bending deformation. An illustration of the centerline extrapolation is shown in Figure 2.2. From the DIC analysis, a discrete number of material points on the surface of the beam with coordinates (X, Y, Z) were established in the reference configuration of the structure (the first stereo image pair), where the Z axis corresponds to the beam axis. These material points were then tracked during the experiment, measuring the (x, y, z) coordinates for every

[2]For a more detailed discussion on why the Biot strain measure was chosen over the Green-Lagrange strain measure, see Section 3.3 and Appendix B of Reedlunn et al. [2013]

material point at each time step (each successive stereo image pair). This corresponds to a Lagrangian type measurement where all displacements and strains are with respect to the reference configuration. To reconstruct the column centerline, all of the material points were first grouped together according to their Z location along the column length, resulting in bins of material points with the same Z coordinate in the reference configuration. For a given instant in time, a circle was fit to each bin of material points, determining the column center point (x_c, y_c, z_c) and radius r at each location along the length of the column. This procedure was conducted for each frame of the DIC data, resulting in a reconstruction of the column centerline through the course of an experiment. There are two assumptions in this procedure which affect its accuracy: plane section remain plane during the deformation and cross-sections remain circular. In reality, plane sections do not necessarily remain plane (as will be discussed in Section 2.3.3) nor do the cross-sections remain perfectly circular due to ovalization in bending; however, the errors associated with these effects are expected to be small due to the averaging associated with the circle fitting procedure.

- In evaluating the mechanical response of an experiment, a "virtual" extensometer was used to average the deformation along the gauge length of the specimen while avoiding unwanted end-effects near loading fixtures. The gauge section length L_e of the "virtual" extensometer was established within the central section of the extrapolated specimen centerline in the reference configuration and its relative deformation was measured through the course of the experiment. This "virtual" measurement was particularly useful for the experiments where mechanical or laser extensometers could not be used, as was the case for the pure bending and buckling experiments.

- Depending on the experiment, select measurements were differentiated (such as the tangent modulus of the uniaxial behavior or the time rate of change of a quantity). Of the many possible differentiation methods, some of the most popular consist of fitting the data with a smoothing interpolant (such as a polynomial or spline), of which the derivative is then analytically evaluated [Berghaus and Cannon, 1973]; smoothing splines were used here. These methods allow for easy tuning of the derivative smoothness while maintaining sufficient accuracy; furthermore, the data can be piecewise fit to accommodate kinks or discrete changes in the data.

As shown schematically in Figure 2.3, four experimental setups were used in this study to characterize the respective tension, compression, pure bending and column buckling behaviors of the NiTi specimens. The tension, compression and pure bending setups were identical to those found in Section 3 of Reedlunn et al. [2013], the details of which are only highlighted here; however, the buckling setup was new and is discussed in more detail.

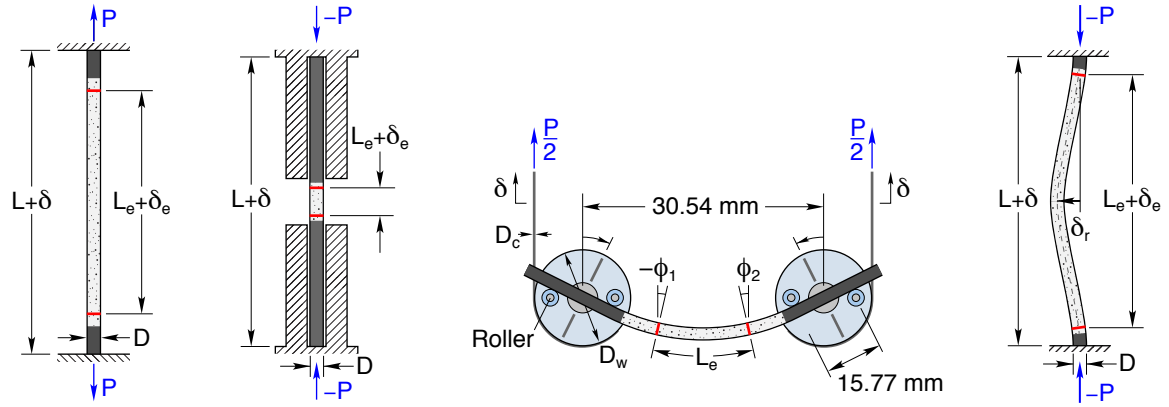

Figure 2.3: Schematics of respective setups for the tension, compression, pure bending, and buckling experiments, highlighting the deformation modes and experimental measurements.

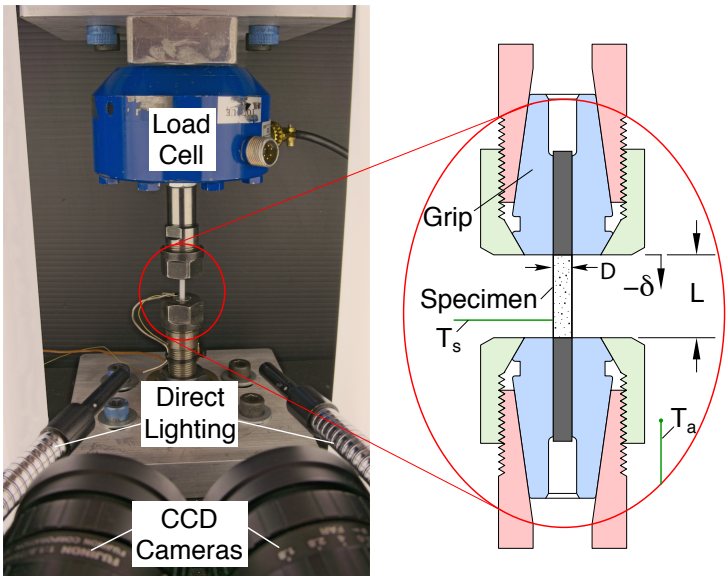

Figure 2.4: The buckling setup consisted of a uniaxial load cell in–line with ER collet grips, resulting in a short and stiff stackup resistant to buckling; additionally, two CCD cameras were used to image the specimen during the loading procedure.

- **Tension**: The tensile experimental setup applied a uniform tensile load along the gauge section of the specimen as shown schematically in Figure 2.3a. The specimen was gripped within a uniaxial load frame using ER collets, exposing a free length of L. The mechanical response was characterized according to the engineering stress $P/A_0 > 0$ and engineering strain $\delta_e/L_e > 0$, where A_0 is the reference cross-sectional area of the specimen.

- **Compression**: The compressive experimental setup applied a uniform compressive load

along the gauge length of the specimen as shown schematically in Figure 2.3b. The specimen was gripped within a uniaxial load frame using custom compression grips. The compression grips were designed to reduce the structure's propensity to buckle (while using a sufficient specimen length to minimize unwanted end-effects) by laterally supporting the specimen over most of its length, leaving only a small unsupported length for imaging; additionally, the stack-up was designed to be short and stiff to minimize its propensity to buckle. The mechanical response was characterized according to the engineering stress $P/A_0 < 0$ and engineering strain $\delta_e/L_e < 0$.

- **Bending**: The pure bending experimental setup applied a constant moment along the gauge length of the specimen as shown schematically in Figure 2.3c. The specimen was gripped in a custom 4-point bending fixture designed to load the specimen under pure bending to large rotations. As the linear motion of the uniaxial load frame was converted into rotation through two loading wheels, the applied moment was calculated according to the relationship $M = P(D_w + D_c)/4$ where $D_w = 23.86\,\text{mm}$ and $D_c = 1.19\,\text{mm}$. After the experiment, the mean offset of the neutral strain plane from the beam centerline $\overline{Y}_0$ was determined from the DIC data according to the relationship $\int_0^{L_e} \varepsilon_{ZZ}^{B}(\overline{Y}_0, Z)\mathrm{d}Z = 0$. The mechanical response was characterized according to the normalized bending moment MC/I, the normalized neutral axis offset $\overline{Y}_0/C$ and normalized average curvature $C\overline{\kappa}$, where $C \equiv D/2$ is the outer radius of the specimen, I is the reference cross-sectional area moment of inertia of the specimen in bending, and $\overline{\kappa} \equiv (\phi_2 - \phi_1)/L_e$ is the average curvature of the beam along the DIC extensometer gauge length.

- **Buckling**: The column buckling experimental setup compressed the specimen under clamped-clamped boundary conditions as shown in the photograph of Figure 2.4 and schematically in Figure 2.3d. The experimental stack-up was designed to be short and stiff to encourage buckling of the specimen, but not of the stack-up. To simulate clamped-clamped boundary conditions, the specimen was gripped within a uniaxial load frame using ER collets, exposing a free length of L. Since geometric imperfections and loading eccentricities can drastically affect the buckling response of a structure, the position of the grips were not disturbed between experiments. A fine K-type thermocouple was attached to the base of the specimen (T_s) using OmegaTherm thermal paste to verify isothermal loading while another thermocouple was positioned in the air near the bottom grip (T_a) to measure the ambient temperature. After the experiment, the magnitude of the lateral displacement at the beam midpoint (δ_r) was measured by averaging the DIC lateral displacement data over a small

area around the beam midpoint. The macroscopic stress $P/A_0 < 0$, normalized radial (lateral) midpoint displacement δ_r/L and DIC extensometer strain[3] $\delta_e/L_e < 0$ were used to characterize the buckling response. To examine the effects of geometry on buckling behavior, columns with approximate aspect ratios L/D of 5, 7.5, 10, 15 and 20 were buckled. Due to the differing cross-sectional geometries of the rod and tube, it is also useful to define the column slenderness ratio, $\ell \equiv L/\sqrt{I/A_0}$, where $\sqrt{I/A_0}$ is the radius of gyration of the cross-section. As a final note, due to the axisymmetric specimens used, there was no preferred buckling direction; therefore, buckling displacements often did not occur in the imaging plane, so one should be aware that strain images shown later may be at oblique angles to the plane of buckling.

The relevant parameters for the uniaxial, pure bending and buckling experiments are shown in Tables 2.1 to 2.3, respectively. For clarity, each experiment is referred to by a formatted label of the form X-Y(-Z), where X refers to the experiment type (T for tension, C for compression, M for bending, and B for buckling), Y refers to the cross-sectional geometry (R for rod and T for tube) and, in the case of the buckling experiments, Z refers to the approximate length/diameter aspect ratio (either 5, 7.5, 10, 15, or 20). Also, it should be noted that the results for experiments T-T, C-T and M-T are the same as for experiments T1, C1 and B1, respectively, from Reedlunn et al. [2013].

Table 2.1: Uniaxial experimental parameters.

	Tension		Compression	
Parameter	Rod	Tube	Rod	Tube
Label	T-R	T-T	C-R	C-T
L (mm)	15.35	14.13	37.91	41.59
L_e (mm)	12.38	9.57	2.18	5.33
$\dot{\delta}/L$ (s^{-1})	$\pm 5 \times 10^{-5}$	$\pm 2.18 \times 10^{-5}$	$\mp 2 \times 10^{-5}$	$\mp 2.18 \times 10^{-5}$

2.3 Results and Discussion

In general, beam behavior consists of both uniaxial and bending deformation. These two deformation modes are first investigated individually, looking at the tension (Section 2.3.1), compression

[3]During buckling, bending of the specimen results in rotation of the extensometer cross-sections which is not accounted for in the extensometer strain measurement. To mitigate these effects, the extensometer ends are positioned close to the grips where the cross-sectional rotations are nearly zero.

Table 2.2: Pure bending experimental parameters.

Parameter	Rod	Tube
Label	M-R	M-T
L_e (mm)	8.04	9.58
$\dot{\delta}$ (mm/s)	± 0.0025	± 0.0025

Table 2.3: Buckling experimental parameters.

	Rod approximate L/D					Tube approximate L/D				
Parameter	5	7.5	10	15	20	5	7.5	10	15	20
Label	B-R-5	B-R-7.5	B-R-10	B-R-15	B-R-20	B-T-5	B-T-7.5	B-T-10	B-T-15	B-T-20
L (mm)	15.38	22.80	30.12	47.12	62.50	16.11	23.27	31.50	47.01	63.10
L_e (mm)	14.55	22.75	29.90	46.36	61.65	15.19	22.09	30.26	45.15	61.56
L/D	4.9	7.2	9.4	15.0	20.2	5.1	7.3	9.9	14.8	19.9
ℓ	19.5	28.9	37.6	59.9	80.6	15.8	22.9	31.0	46.3	62.1
$\dot{\delta}/L$ (s^{-1})	$\mp 1 \times 10^{-4}$					$\mp 1 \times 10^{-4}$				

(Section 2.3.2) and pure bending (Section 2.3.3) behaviors. Subsequently, the buckling behavior of columns with differing length/diameter aspect ratios are discussed (Section 2.3.4), examining various cases of combined uniaxial and bending deformation.

2.3.1 Tension

The tensile mechanical behavior of the rod and tube (engineering stress P/A_0 vs extensometer strain δ_e/L_e as shown in the the upper right quadrant of Figure 2.5a) aligns with the characteristic isothermal flag-shaped response of superelastic NiTi. In general, the rod and tube behaved similarly, with the rod exhibiting a 7 % higher and 15 % longer loading stress plateau than the tube. The only significant qualitative difference between the rod and tube responses was in the initial pre-plateau behavior, where the rod behaved nearly linearly, while the tube behaved nonlinearly (this is most easily seen in the tangent modulus (E_t) data presented in Figure 2.5b). The nonlinearity in the tube behavior is associated with a homogeneous transformation from austenite to the rhombohedral phase (R-phase) commonly found in NiTi materials operating at temperatures slightly above A_f as was the case here (the tube A_f was 19 °C, while the room temperature experiment was conducted around 21 °C).

For each tensile specimen, the pronounced stress plateau in the mechanical response was due

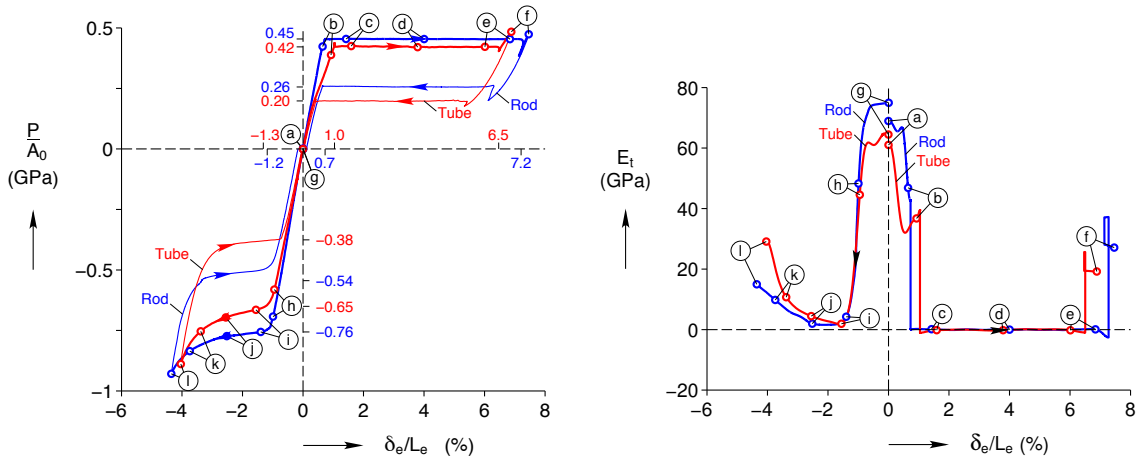

(a) Mechanical response (b) Loading tangent modulus

Figure 2.5: The uniaxial responses of the rod (T-R and C-R) and tube (T-T and C-T) exhibited tension-compression asymmetry, hysteretic behavior and flat stress plateaus in tension.

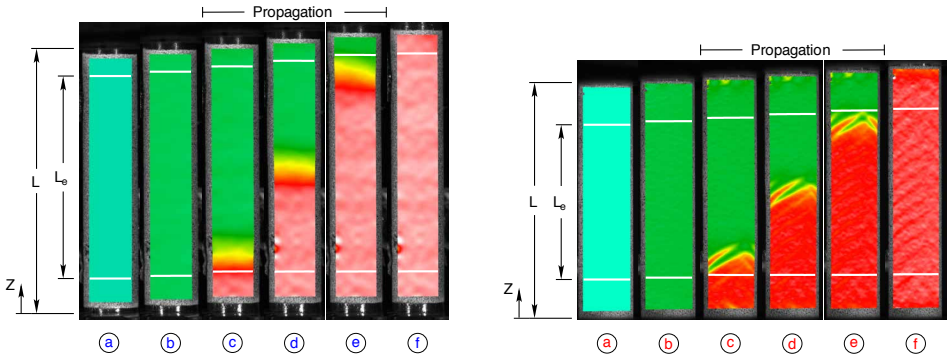

(a) Rod in tension (b) Tube in tension

Figure 2.6: Phase transformation localized and propagated along the length of the specimens under tensile loading, forming a diffuse high strain phase boundary in the rod and a criss-crossing high strain finger–like boundary in the tube.

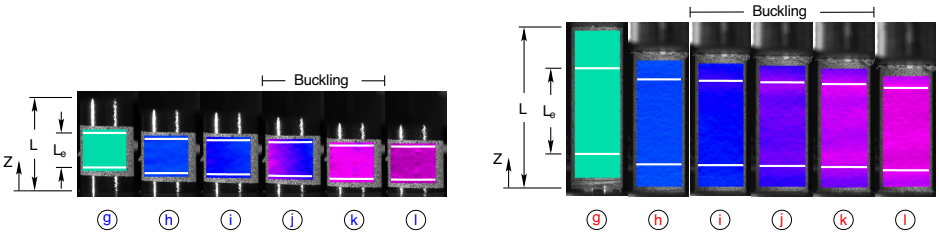

(a) Rod in compression (b) Tube in compression

Figure 2.7: Phase transformation was a nearly homogeneous process during compression of the rod and tube specimens, with small inhomogeneities occurring in the axial strain field (ε^{B}_{ZZ}) due to minor buckling of the specimens.

to the localization of a high strain front which propagated along the specimen length (see the axial strain fields $\varepsilon^{\mathrm{B}}_{\mathrm{ZZ}}$ in ⓒ – ⓔ of Figure 2.6). This formation of a high strain localization corresponded to the nucleation of stress-induced phase transformation which unstably progressed along the specimen. Due to the mixed strain state during localized propagation, it is important to note that this portion of the loading corresponds to an *averaged* structural response rather than the homogeneous deformation often associated with the local constitutive behavior of the material. As will be discussed further in Chapter 3, the suppression of phase transformation localization in tension results in a nonmonotonic up–down–up mechanical response which is likely more suitable for the purposes of material modeling.

Although phase transformation localized in both the rod and tube, the morphology of the phase transformation front differed (see the surface axial strain data $\varepsilon^{\mathrm{B}}_{\mathrm{ZZ}}$ in Figure 2.6). In the case of the rod, the localized phase boundary was diffuse (for example, ⓓ of Figure 2.6a); whereas the tube phase boundary consisted of distinct criss–crossing "fingers" (for example, ⓓ of Figure 2.6b). This difference in the phase transformation features is attributed to the differing cross-sectional geometries of the rod and tube. Kinematically, the formation of a distinct phase boundary requires strain compatibility tangential to the phase boundary plane (see Shaw and Kyriakides [1998] for a more in-depth discussion on this topic). Although this compatibility condition cannot be met exactly for either the rod or tube, the *thin* wall of the tube better accommodates it than the solid cross-section of the rod. The tube can therefore localize with sharp phase boundaries, while the rod can only accommodate a diffuse neck-like phase boundary.

2.3.2 Compression

Similar to the tensile responses, the compression responses of the rod and tube were characterized by hysteretic trilinear-like behavior, although with smoother corners, as shown in the lower left quadrant of Figure 2.5a. Of the differences between the tensile and compressive behaviors, one of the most notable is the absence of flat plateaus in compression due to stable homogenous transformation. Quantitatively, the magnitudes of the compressive transformation stresses were about 1.5 times larger than the corresponding tensile transformation stresses, while the magnitudes of the compressive transformation strains were about $2/5$ times smaller than the corresponding tensile transformation strains. This tension-compression asymmetry is now a well-known and prevalent feature of common commercial NiTi materials and is likely due to the strong crystallographic texture induced during the processing of wire, rod, and tube [Gall and Sehitoglu, 1999]. Comparing between the rod and tube behaviors, the magnitude of the compressive transformation stress for the rod was nearly $15\,\%$ higher than the tube, while the transformation strain was only marginally

higher (although it is somewhat difficult to quantify the end of transformation due to the smooth mechanical response). In a similar fashion to the tensile response, the tube exhibited a slight nonlinearity prior to transformation to martensite, which I believe corresponds to a phase change from the austenite to the R-phase; whereas, the rod response was again nearly linear up to the initiation of phase transformation to the martensite phase (see the tangent modulus response shown in Figure 2.5b).

Although the compression fixture was designed to suppress buckling, the soft material response at the start of phase transformation resulted in minor buckling of both materials as seen in the axial strain data of Figure 2.7. In the case of the rod, the deformation remained uniform through ⓗ, after which a column buckling mode of deformation was observed, as seen in ⓘ–ⓙ; whereas, in the case of the tube, the deformation remained uniform through ⓘ, after which a faint axisymmetric shell-type buckling mode of deformation was detected, as seen in ⓙ–ⓚ. Interestingly, upon further loading, both the rod and tube "unbuckled" by ⓛ, returning to a straight configuration and again deforming uniformly (this behavior is discussed further in Section 2.3.4 and Chapter 4). Due to the nonuniform strain fields associated with buckling of both the rod and tube during the compression experiments, the reported responses are not necessarily the "pure" compressive responses corresponding to uniform deformation; however, results from other compression experiments (not shown here), which buckled with varying amplitudes, suggest that the reported data have nearly converged on the homogeneous compressive responses. As a final note, phase transformation localization was not observed in either of the compression experiments, corresponding to the absence of stress plateaus in the mechanical responses (Figure 2.5a).

2.3.3 Pure Bending

The pure bending mechanical behaviors (normalized moment MC/I vs normalize curvature $C\overline{\kappa}$) were characterized by hysteretic stiff–soft–stiff responses (Figure 2.8). Initially exhibiting the same (elastic) bending stiffnesses, the tube mechanical response began to deviate from the linear rod response at a normalized curvature of 0.5 % as the outer fibers of the tube began to transform to the R-phase. At a normalized curvature of approximately 1.3 %, the moment curvature responses of both materials began to soften as the outer fibers of the specimens began to transform to martensite; due to the solid cross-section of the rod, this softening behavior occurred more gradually in the rod than for the tube. Upon further loading, the effects of phase transformation dominated, resulting in nearly flat moment plateaus, which ultimately stiffened as the majority of phase transformation completed. Similar to the stress plateaus found in the tensile responses, the moment plateaus of the pure bending responses corresponded to localization of phase transformation (Figure 2.9). Finally,

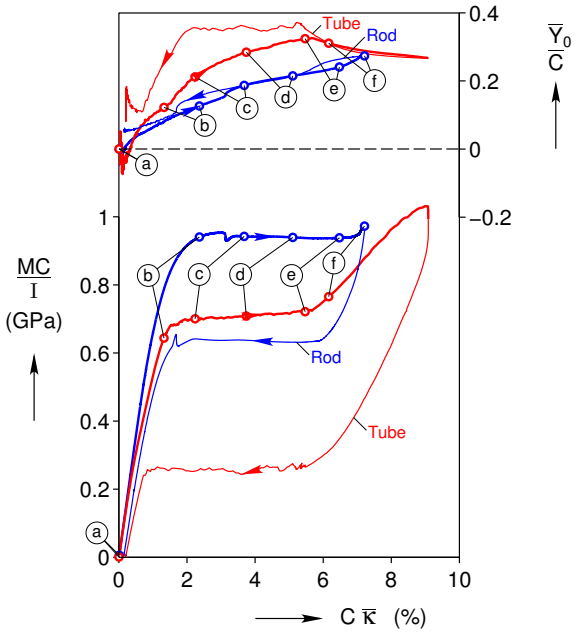

Figure 2.8: The normalized moment (MC/I) of the pure bending experiments plateaued with respect to the normalized curvature ($C\overline{\kappa}$) due to localized stress induced phase transformation, while the tension-compression asymmetry of the rod and tube uniaxial responses caused the normalized neutral plane location ($\overline{Y}_0/C$) to shift from the beam centerline towards the compressive side of the beams.

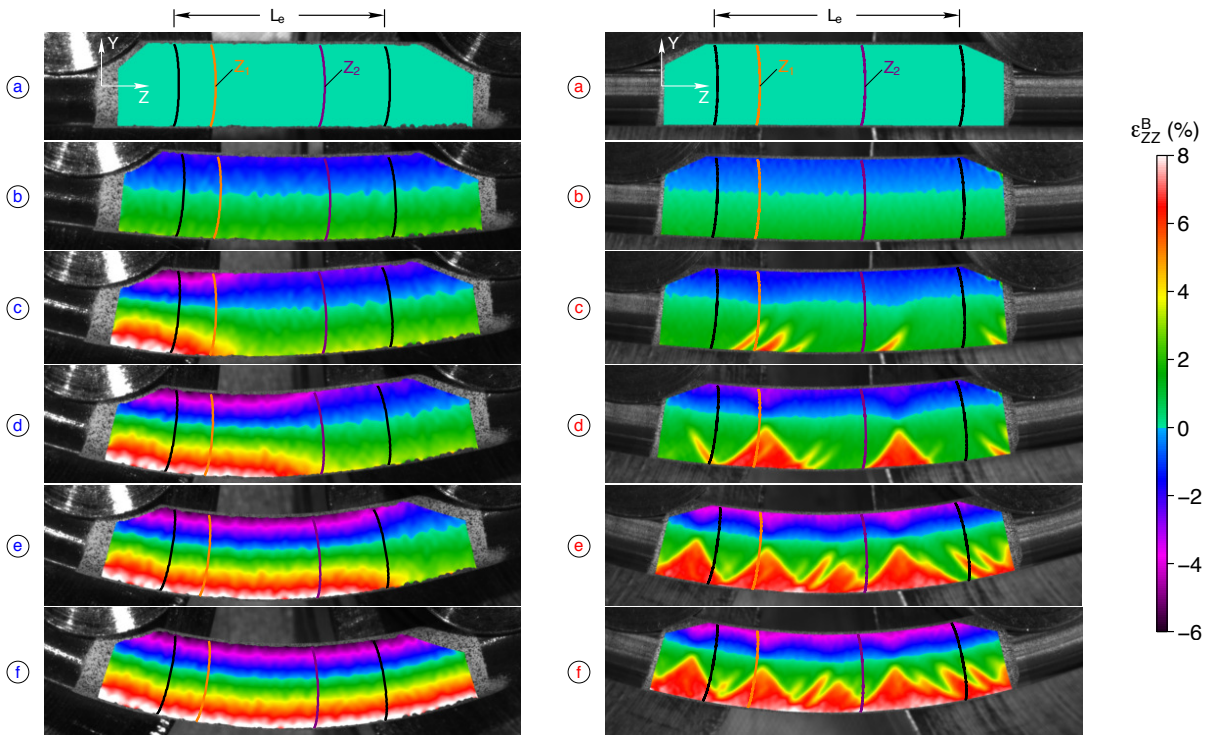

(a) Rod (b) Tube

Figure 2.9: In pure bending, the axial strain field (ε^B_{ZZ}) of the rod localized into a diffuse high curvature region which propagated along the length of the beam, while the axial strain field of the tube localized into finger/wedge-like regions at discrete locations along the tensile side of the beam.

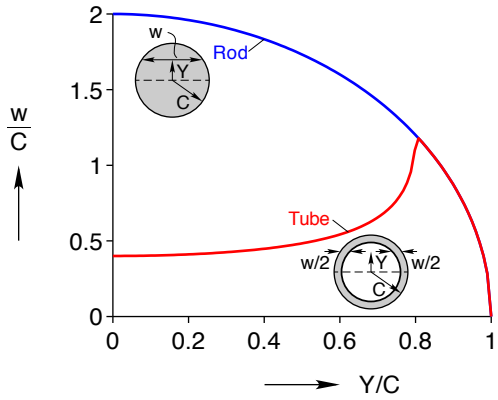

Figure 2.10: Quantified by the cross-sectional width distribution w through the thickness of the specimen, the material is concentrated at the inner portion of the rod and outer portion of the tube.

it should be recognized that the moment hysteresis between the two pure bending responses are not directly comparable, since the tube was taken well past the moment plateau, which is known to suppress reverse transformation.

Due to the nonlinear uniaxial behavior of NiTi, it was not possible to normalize the bending mechanical behavior to be independent of the cross-sectional geometry of the specimen. This is best exemplified by the definition of the moment in a beam:

$$M = -\int_A \sigma(Y) Y \, \mathrm{d}A, \tag{2.1}$$

where σ is the axial stress, Y is the thickness-wise position, and the integration is conducted over the cross-section of the beam. In the case of a linear elastic beam, Eq. (2.1) reduces to

$$M = EI\overline{\kappa}, \tag{2.2}$$

which defines a constitutive relationship between MC/I and $C\overline{\kappa}$, parameterized by the elastic modulus of the material (E); however, for the nonlinear constitutive behavior of NiTi, the moment definition Eq. (2.1) cannot be manipulated to decouple material and structural effects. Therefore, the presented results of Figure 2.8 do not represent purely constitutive behavior and should not be compared directly (except for during the initial linear elastic behavior of the materials).

Unlike the elasto-plastic behavior of most metals, the average location of the neutral strain plane ($\overline{Y}_0$) shifted from the centerline of both the rod and tube as shown in the upper portion of Figure 2.8. This shift in the neutral plane is best exemplified through the axial equilibrium equation

for a beam during pure bending:

$$\begin{aligned} N &= \int_A \sigma(Y)\,\mathrm{d}A \\ &= \underbrace{\int_{-D/2}^{\overline{Y}_0} w(Y)\sigma_{\mathrm{T}}(Y)\,\mathrm{d}Y}_{\text{Tensile contribution}} + \underbrace{\int_{\overline{Y}_0}^{D/2} w(Y)\sigma_{\mathrm{C}}(Y)\,\mathrm{d}Y}_{\text{Compressive contribution}} = 0, \end{aligned} \tag{2.3}$$

where N is the axial force in the beam, Y is the thickness-wise position, $w(Y)$ is the cross-sectional width (as shown in Figure 2.10), and $\sigma_{\mathrm{T}}(Y) > 0$ and $\sigma_{\mathrm{C}}(Y) < 0$ are tensile and compressive stress, respectively. Since the magnitude of the transformation stress is greater in compression than in tension for NiTi, the neutral plane is shifted towards the compressive side ($\overline{Y}_0 > 0$) for both the rod and tube. Due to the differing cross-sectional width distributions (Figure 2.10), the tube required the neutral axis to shift farther from the beam centerline than the rod to maintain axial equilibrium.

Although the strain fields localized in the bending of both the rod and tube, the morphology and evolution of the localized behaviors were fundamentally different (Figure 2.9). In the case of the rod, propagating high curvature traversed the beam length from left to right as shown in Figure 2.9a, initiating at the moment drop just prior to ⓒ and culminating just after ⓔ. In contrast, the strain field localized on the tensile side of the tube according to the crisscrossing finger-like structures as seen in ⓒ–ⓕ of Figure 2.9b, eventually developing into wedge-shaped high strain regions towards the end of loading. The slightly negative tangent modulus of the rod moment plateau suggests that the propagation phenomenon within the specimen corresponds to an unstable structural response; whereas the slightly positive tangent modulus of the tube moment plateau suggests the finger-like growth of phase transformation corresponds to a structurally stable response.

It is tempting to attribute the differing modes of localization evolution in the rod and tube to their differing cross-sections; however, the propagating high curvature observed in the NiTi *tube* tested by Bechle and Kyriakides [2013] suggests more factors are involved. In examining the behavior of Bechle and Kyriakides's tubes, similar high strain "fingers" and wedges seen in my tubes were observed in the high curvature sections of their specimens. In both cases, these discrete wedge regions had an approximate width on the order of the tube's diameter and suggests that the length scale of a high curvature localization in a tube must be on the order of the tube diameter. I therefore postulate that a localized high curvature region could more easily "fit" in the long free length of Bechle and Kyriakides's bending setup (which was on the order of 14 tube diameters), but not within the relatively short free length of my bending setup (which was on the order of 4.5 tube diameters). In the case of the rod, the kinematic restraints on phase transformation localization

due to it's solid cross-section resulted in a relatively small transition region between the high and low curvature regions (on the order of 0.5 rod diameters) of the beam during propagation. Unlike the tube, the high curvature localization could therefore "fit" within the short free length of my bending setup. This reasoning suggests that both the beam cross-section and free length affect the localization morphology. Another contributing factor is likely the stiffness of the material response during phase transformation (both in tension and compression); for example, the initial stiffness in compression of my rod and Bechle and Kyriakides's tube were much shallower than my tube, suggesting the softer initial behavior contributes to the presence of propagating curvature. In all likelihood, structural stability of superelastic SMAs in pure bending is a function of both specimen geometry (length and cross-section) and the stiffness of the material response.

Due to the localized deformations of both the rod and tube in bending, the mechanical responses correspond to averaged responses of the structures; however, unlike the uniaxial behavior, these averaged responses correspond to differing structural events. In the case of the rod, the unstable propagation (slightly negative tangent modulus) of the high curvature front had similar behavior to the propagation of the high strain front in tension: the low curvature section of the beam corresponds to the curvature at the start of the moment plateau, the high curvature section corresponds to the curvature at the end of the moment plateau, and the structural response corresponds to the weighted average of the high and low curvatures according to the degree of propagation. The material behavior of the rod is therefore expected to have an up-down-up moment-curvature relationship. In contrast, the stable transformation in the tube (positive tangent modulus) could potentially be used as an averaged constitutive relationship (although it is dependent on the cross-sectional geometry as discussed previously); however, it is difficult to determine if this stable behavior was the result of the material behavior or the kinematic restrictions of the experimental setup.

The localization of the rod and tube strain fields during pure bending brings into question the validity of the classical beam theory assumption that cross-sectional planes remain planar through the course of loading for SMA beams. To investigate the applicability of this assumption for SMA beams, the axial strain profiles ($\varepsilon^{\mathrm{B}}_{\mathrm{ZZ}}$) through the thickness of the rod and tube are shown in Figure 2.11 for two locations along the beam axes (Z_1 and Z_2); additionally, the averaged axial strain profile along the Z direction,

$$\bar{\varepsilon}^{\mathrm{B}}_{\mathrm{ZZ}}(Y) = \frac{1}{L_{\mathrm{e}}} \int_0^{L_{\mathrm{e}}} \varepsilon^{\mathrm{B}}_{\mathrm{ZZ}}(Y, Z)\mathrm{d}Z \tag{2.4}$$

and the strain profile predicted by Euler-Bernoulli beam theory (which assumes that cross-sectional

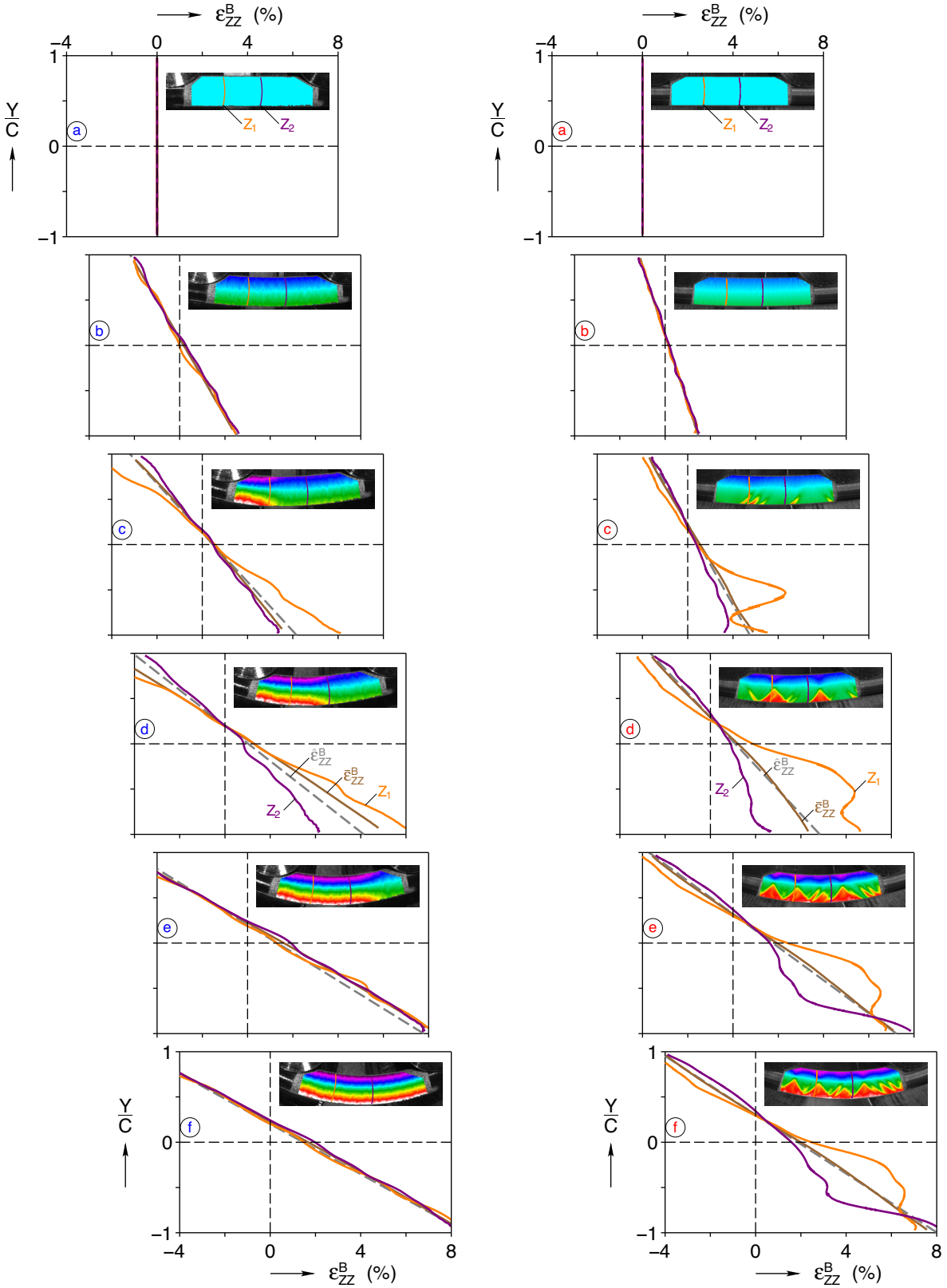

(a) Rod (b) Tube

Figure 2.11: Axial strain profiles through the thickness of the rod and tube during pure bending at the points of interest labeled in Figure 2.8, showing that plane sections remain plane for the rod, but only on average for the tube.

planes not only remain planar, but also normal to the deformed centerline of the beam),

$$\hat{\varepsilon}^{\mathrm{B}}_{\mathrm{ZZ}}(Y) = \overline{\kappa}(\overline{Y}_0 - Y), \tag{2.5}$$

where $\overline{\kappa}$ and $\overline{Y}_0$ are the values measured in M-R and M-T (and taken from Figure 2.8). In the case of the rod (Figure 2.11a), the axial strain profiles remained nearly linear through the course of loading, only differing in slope along the beam axis (Z_1 vs. Z_2) due to the propagation of the high curvature front. In contrast, the tube strain profiles (Figure 2.11b) became nonlinear in the presence of phase transformation localization as seen in the strain distributions of ⓒ–ⓕ. Consequently, cross-sectional planes only remained planar in the case of the rod geometry. With that said, the averaged axial strain profile $\overline{\varepsilon}^B_{ZZ}$ (Eq. (2.4)) was nearly planar for both the rod and tube, even in the presence of phase transformation localization. Furthermore, $\overline{\varepsilon}^B_{ZZ}$ aligned with the prediction by Euler-Bernoulli beam theory (Eq. (2.5)), suggesting that the classical assumption of beam theory is valid on average along the length of the beam. Therefore, classical beam theory appears to be a viable approach to model SMA beam kinematics on average, even in the presence of localization phenomena (such that the exact morphology of phase transformation is not of interest).

2.3.4 Column Buckling

The column buckling experiments spanned a wide range of loading conditions, investigating the interaction between kinematic and material nonlinearity. The general characteristics of superelastic SMA buckling are examined first, followed by a comparison between the measured and predicted onset of buckling (critical buckling load). Lastly, the observation of post-buckling straightening is the short SMA columns is discussed.

General Buckling Behavior

In the column buckling experiments, the mechanical response characteristics varied significantly with respect to the column aspect ratio (Figure 2.12). Until the onset of buckling, all of the columns loaded according to the compressive response of the material (C-R or C-T). Upon buckling, the mechanical responses of the

- low aspect ratio columns (B-R-5, B-T-5, B-T-7.5) monotonically increased, initially softening (although with a positive tangent modulus), but ultimately stiffening and rejoined the compressive response;

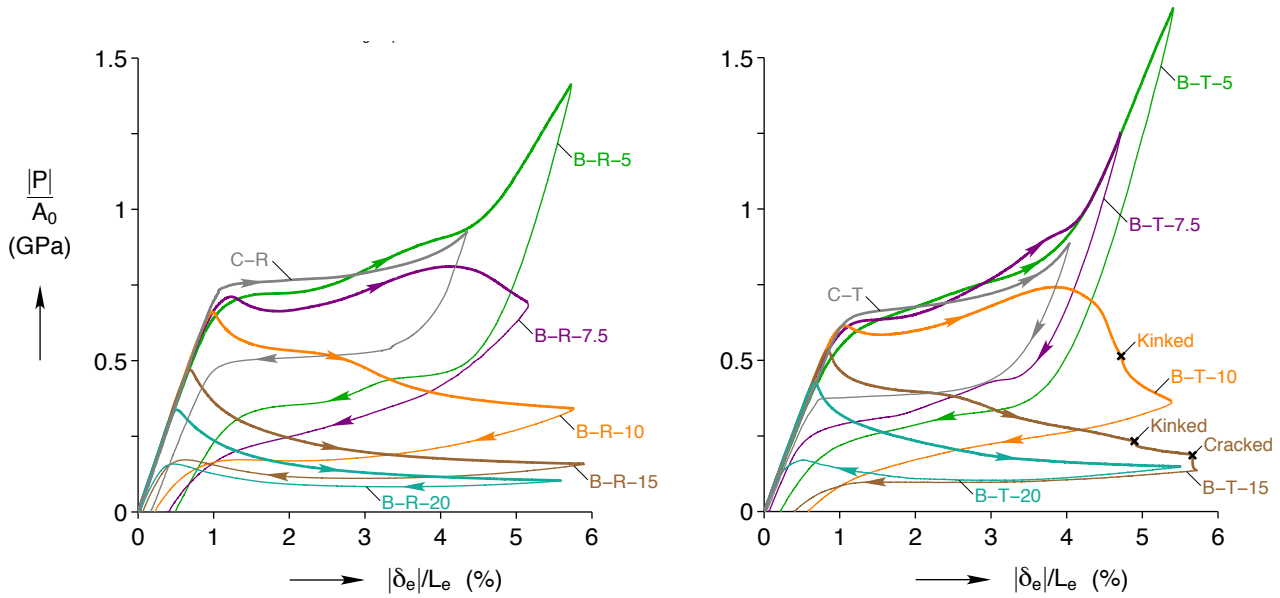

(a) Rod (b) Tube

Figure 2.12: The post buckling mechanical responses (normalized load P/A_0 vs normalized displacement δ_e/L_e) of the column buckling experiments varied significantly with column aspect ratio, exhibiting monotonically increasing behavior for low aspect ratio columns, nonmonotonic down–up–down behavior for mid aspect ratio columns, and monotonically decreasing behavior for high aspect ratio columns.

- mid aspect ratio columns (B-R-7.5, B-T-10) exhibited nonmonotonic down–up–down behavior;
- high aspect ratio columns (B-R-10, B-R-15, B-R-20, B-T-15, B-T-20) monotonically decreased, softening quickly, but ultimately asymptoting to a neutral tangent modulus.

During unloading, the mechanical responses were characterized by smoother paths with only the high aspect ratio columns exhibiting nonmonotonic behavior. At the end of unloading, the majority of the buckling deformation was recovered in the columns, demonstrating the robustness of superelastic SMAs to even the extreme loading conditions of buckling.

In general, the rod and tube specimens with similar aspect ratios showed different characteristic behaviors, as is evident by a direct comparison between the mechanical responses of Figures 2.12a and 2.12b. A better metric for comparison is the slenderness ratio of the column ($\ell \equiv L/\sqrt{I/A_0}$), which accounts for both the column aspect ratio and the cross-sectional geometry. Of the columns examined in this study, there were two rod/tube pairs which had similar slenderness ratios: B-R-7.5/B-T-10 and B-R-15/B-T-20 (see Table 2.3). As shown in Figure 2.13, the mechanical responses

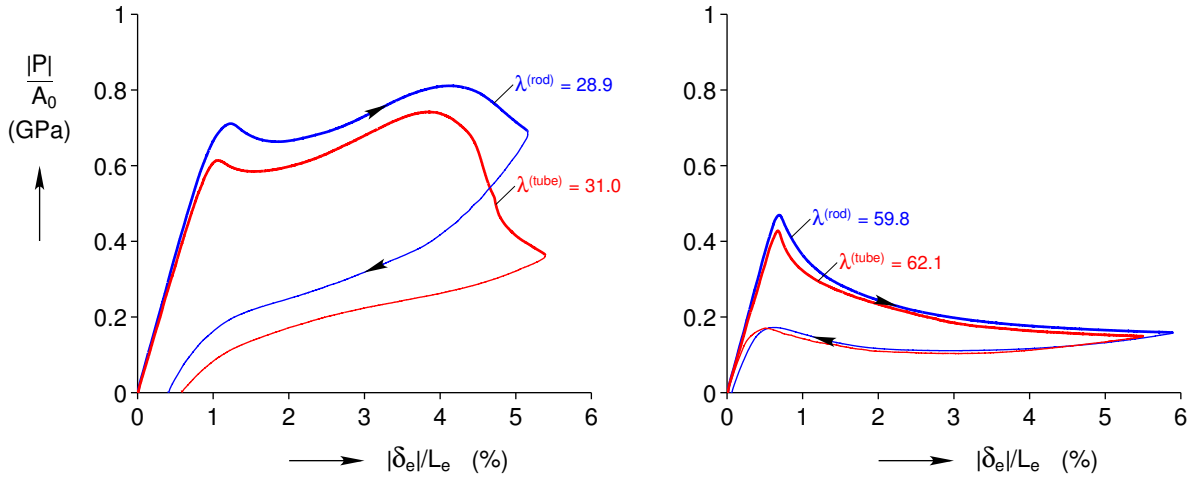

(a) B-R-7.5 and B-T-10

(b) B-R-15 and B-T-20

Figure 2.13: Columns with similar slenderness ratios (ℓ) had qualitatively similar mechanical responses (normalized load P/A_0 vs normalized displacement δ_e/L_e).

of these rod/tube pairs had comparable qualitative characteristics, although the magnitudes differed due to the differing uniaxial behaviors of the two materials (Figure 2.5a).

In the tube buckling experiments B-T-10 and B-T-15, the columns kinked at their midlength late in loading, resulting in significant stress drops in the mechanical responses as marked in Figure 2.12b; additionally, the tube with an aspect ratio of 15 cracked along the beam axis on the compressive side of the tube when loaded beyond kinking, corresponding to the second stress drop in the B-T-15 response. In both cases, the residual strain at the end of unloading was higher than the other tube buckling experiments; however, the majority of post-buckling deformation was still recovered, further highlighting the robustness of superelastic SMAs to even extreme localized deformation. A more in-depth look into the kinking behavior is shown in Figure 2.14, comparing the the mechanical responses (Figure 2.14a) and select axial strain fields of B-R-10 and B-T-10 (Figures 2.14b and 2.14c, respectively). In the case of B-R-10, the rod deformed with no signs of kinking as indicated by the smooth axial strain fields of Figure 2.14b; whereas, in the case of B-T-10, the initial signs of kinking are evident in ⓔ of Figure 2.14c and more distinct by ⓕ. As kinking results from the ovalization of the column cross-section during loading, it is not surprising that kinking was not observed in the buckling of the rods due to their solid cross-sections, which ovalize less than the hollow cross-sections of the tubes. Interestingly, the tube with an aspect ratio of 20 did not kink in the loading range of the experiment, although I postulate that the tube would have kinked if it had been loaded further.

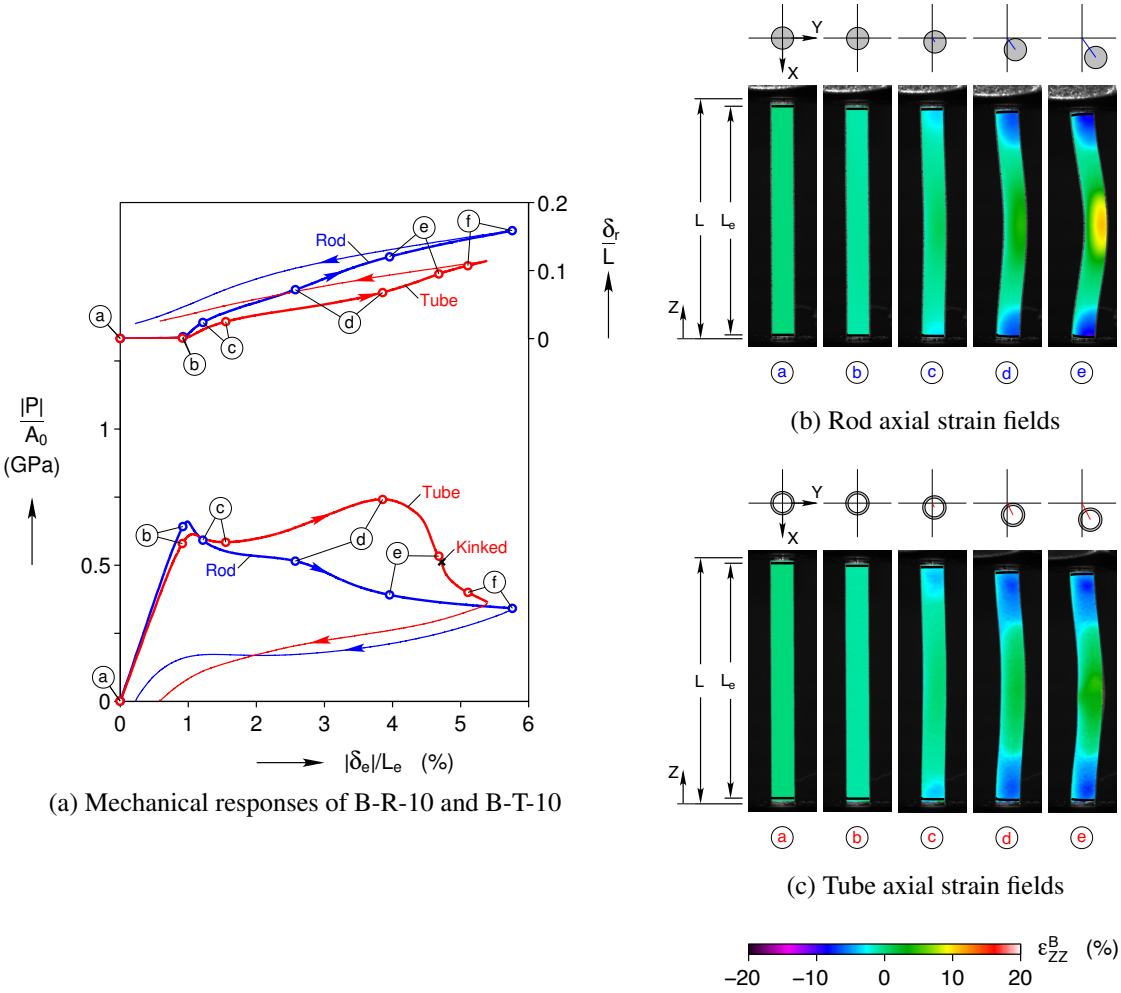

(a) Mechanical responses of B-R-10 and B-T-10

(b) Rod axial strain fields

(c) Tube axial strain fields

Figure 2.14: The load drop in B-T-10 was the result of kinking at the tube midlength, a phenomenon that was not observed in any of the rod specimens due to the rod's greater resistance to ovalization.

Unlike the uniaxial and pure bending experiments, transformation localization was less prominent in the buckling experiments. In the case of the rods and the low aspect ratio tubes, transformation localization did not occur, although high strain regions developed consistent with the usual expectations for inelastic post-buckling behavior. Only the high aspect ratio tubes of B-T-15 and B-T-20 showed signs of sharp localizations, an example of which is shown in ⓓ of Figure 2.15c at the beam half length. Even so, the presence of localized phase transformation had little effect on the qualitative characteristics of the structural response (for example, see the mechanical response comparison of columns with similar ℓ's of Figure 2.13b, where the tube response corresponds to the one shown in Figure 2.15a).

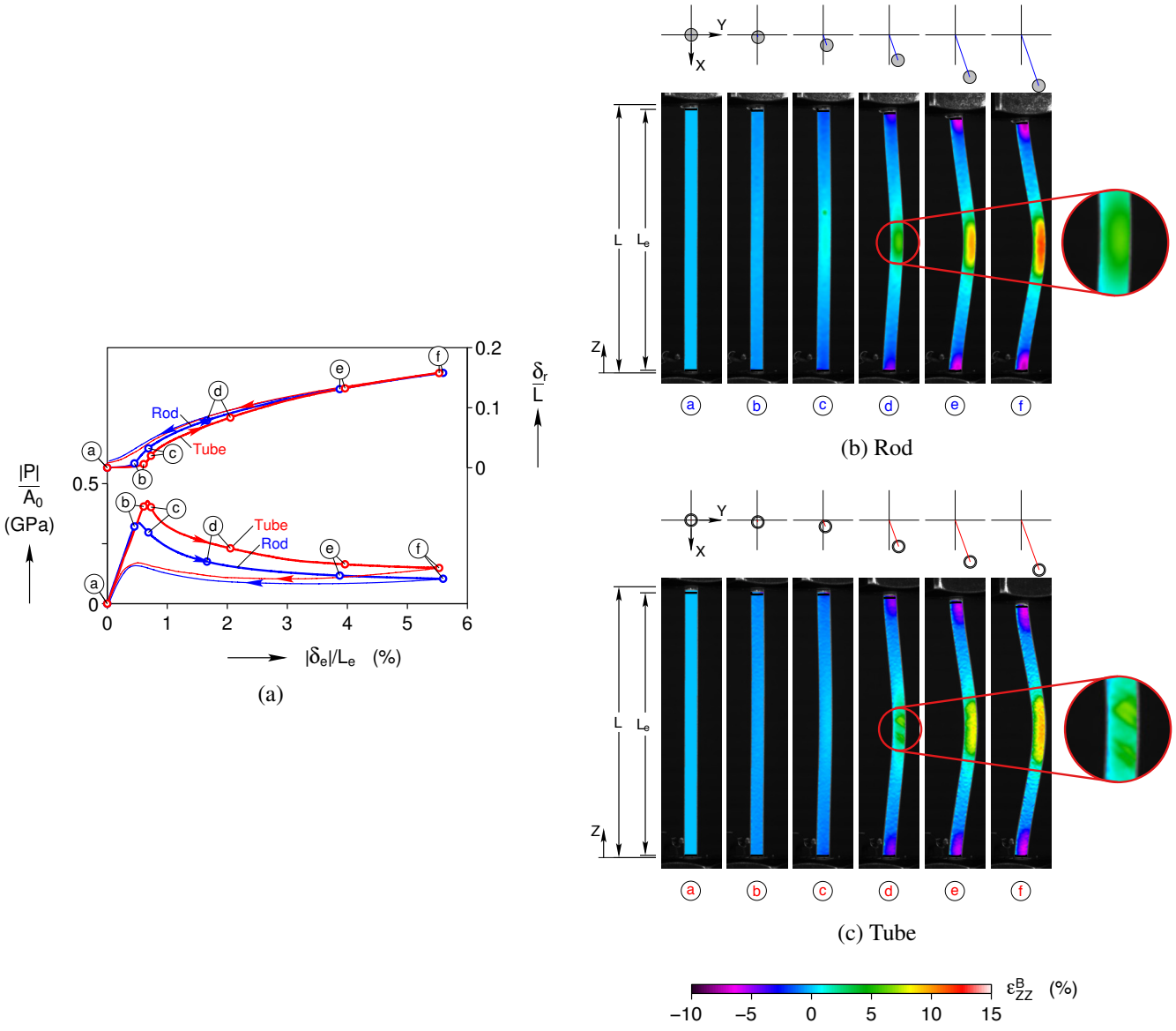

Figure 2.15: In the case of the highest aspect ratio columns (B-R-20 and B-T-20), the axial strain field localized at the midlength of the tube, but remained smooth in the rod; however, unlike the tensile and bending responses, localization had no apparent effect on the mechanical response of the tube.

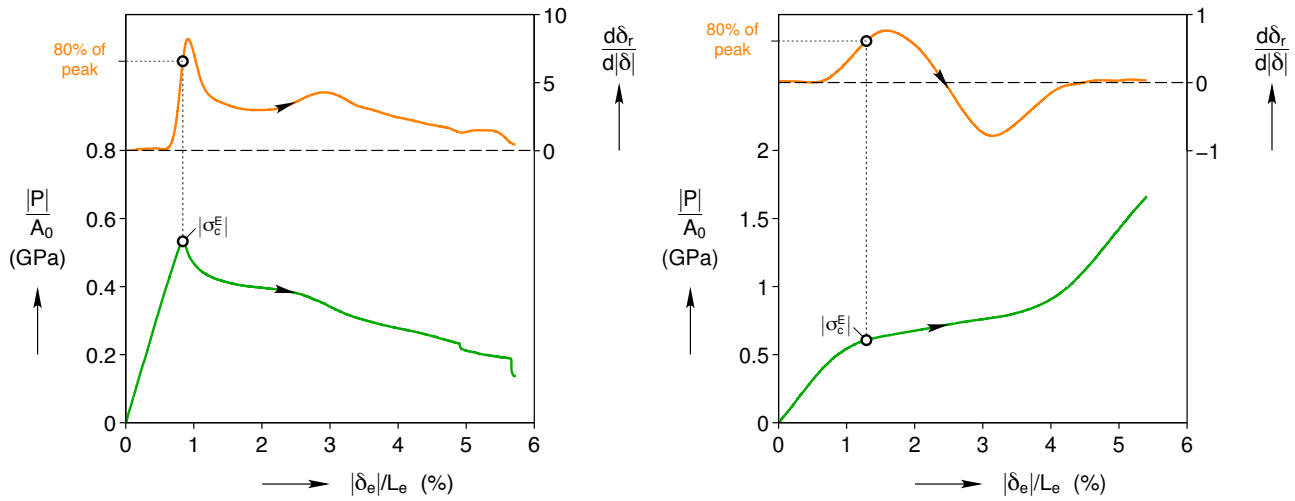

(a) Elastic (B-T-15) (b) Inelastic (B-T-5)

Figure 2.16: The critical buckling stress (σ_c^E) is defined here as the point in which $d\delta_r/d\delta$ reaches $80\,\%$ of its peak, as is show for two example cases: (a) elastic and (b) inelastic buckling.

For each buckling experiment, the critical buckling stress (σ_c^E) was determined using the measured lateral deflection of the column midlength. Since buckling is defined as the bifurcation from the principal deformation path (a straight column) to a secondary deformation path (a bent column), a theoretical step should exist in the derivative of the lateral displacement ($d\delta_r/d\delta$) at the point of bifurcation. In reality, the change is smooth, so the point corresponding to $80\,\%$ of the $d\delta_r/d\delta$ peak value was used[4]. Two examples of the measurement method of σ_c^E are shown in Figure 2.16: Figure 2.16a corresponds to the elastic buckling of experiment B-T-20 and Figure 2.16b corresponds to the inelastic buckling of experiment B-T-5. The measured critical buckling stresses for all of the buckling experiments are shown in Figure 2.17.

In addition to measuring the experimental critical buckling stress, the theoretical critical buckling stress (σ_c^T) for a perfect column was calculated for each buckling experiment. According to the tangent modulus theory for inelastic column buckling, the critical buckling stress of a clamped-clamped column is

$$\sigma_c^T = -4\pi^2 E_t^* \ell^{-2}, \tag{2.6}$$

where E_t^* is the compressive tangent modulus of the material *at the critical buckling stress*. A

[4]The value of $80\,\%$ of the $d\delta_r/d\delta$ peak was calibrated by the experiments in which the column buckled elastically with a pronounced stress peak in the response.

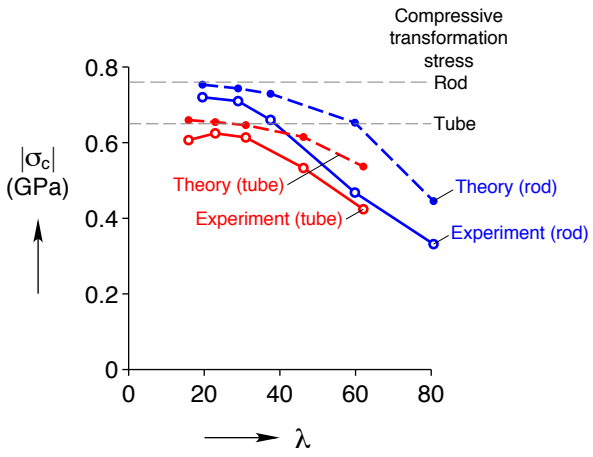

Figure 2.17: The buckling theory predictions for critical buckling stress over predict the measured critical buckling stresses which is likely due to imperfections in the experimental setup that are not accounted for in the theoretical predictions.

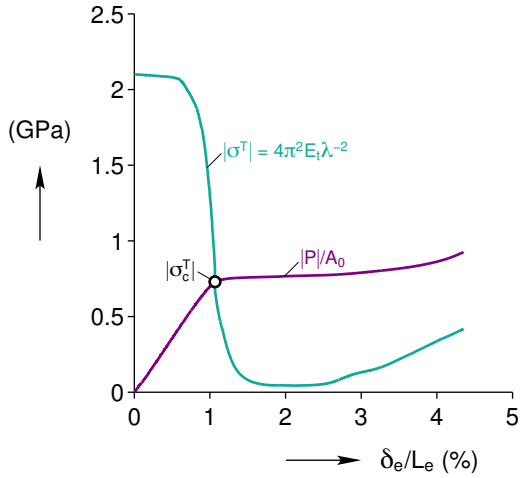

Figure 2.18: The theoretical critical buckling stress σ_c^T of each column was determined by the intersection of the compressive material response (Figure 2.5a) with the function $\sigma^T(E_t) = -4\pi^2 E_t \ell^{-2}$ (see Figure 2.5b for the E_t behavior), an example of which is shown here for experiment B-R-10.

column's resistance to buckling is therefore a function of two factors: the material stiffness (E_t) and the column slenderness ratio (ℓ). Due to the functional dependence of E_t on the applied load, Eq. (2.6) is an implicit equation in terms of σ_c^T. To aid in the determination of σ_c^T, the function

$$\sigma^T \equiv -4\pi^2 E_t \ell^{-2} \tag{2.7}$$

is defined, where E_t is the loading tangent modulus of the material for a given loading state δ_e/L_e (see Figure 2.5b). The theoretical critical buckling stress σ_c^T then corresponds to the intersection of the specimen's compressive P/A_0 vs δ_e/L_e response (Figure 2.5a) with σ^T vs δ_e/L_e; for example,

see the calculation of σ_c^T for B-R-10 in Figure 2.18. The calculated critical buckling stresses for all of the buckling experiments are shown in Figure 2.17.

As is commonly found in the comparison between experimental and theoretical buckling stresses, the magnitude of the experimentally measured critical buckling stresses were lower than the theoretical predictions as shown in Figure 2.17. The over-prediction of the buckling theory is likely due to subtle geometric imperfections and/or loading eccentricities in the experimental setup which are not accounted for in the theory. I also postulate that superelastic SMA columns are more sensitive to imperfections/eccentricities than conventional elasto-plastic materials due to the rapid softening of the compressive response of supereleastic SMAs at the initiation of phase transformation (Figure 2.5b).

Buckling–Unbuckling of Short Columns

In the buckling experiments B-R-5, B-T-5 and B-T-7.5, and the compression experiments C-R and C-T, an intriguing buckling–unbuckling behavior was observed during the loading and unloading portions of each experiment. As buckling defines the deformation of a straight column to a bent column under axial compression, *unbuckling* is defined here as the return of a buckled column to its original straight form under continued axial compression. To better illustrate unbuckling, a comparison of the mechanical responses and select axial strain fields of experiments B-R-7.5 and B-T-7.5 are shown in Figure 2.19. In the case of experiment B-R-7.5, the rod midlength lateral displacement (δ_r) increased monotonically with increasing compressive loading (δ_e/L_e) as shown in Figures 2.19a and 2.19b, corresponding to the conventional notion of buckling; whereas, in the case of B-T-7.5, the tube midlength lateral displacement initially increased after buckling at ⓑ, but subsequently decreased to a near zero value by ⓕ (unbuckled) as shown in Figures 2.19a and 2.19c. In addition to its observation during loading, buckling-unbuckling was also observed in the unloading portions of C-R, C-T, B-R-5, B-T-5 and B-T-7.5 (for example, see the unloading portion of the δ_r response in Figure 2.19a).

The absence of buckling–unbuckling behavior in conventional materials suggests that the stiff–soft–stiff uniaxial material behavior of superelastic SMAs plays an important role in unbuckling behavior; furthermore, the restriction of unbuckling to the low aspect ratio column experiments implies a coupling between the specimen geometry and material behavior. For a more in–depth discussion on the factors that influence unbuckling, see Chapter 4.

Other manifestations of unbuckling have been observed in the literature, such as balloon inflation [Alexander, 1971, Haughton, 1980, Chen and Healey, 1991], SMA columns in the martensite phase [Urushiyama et al., 2003, Richter et al., 2011], and tension of thin sheets [Healey et al.,

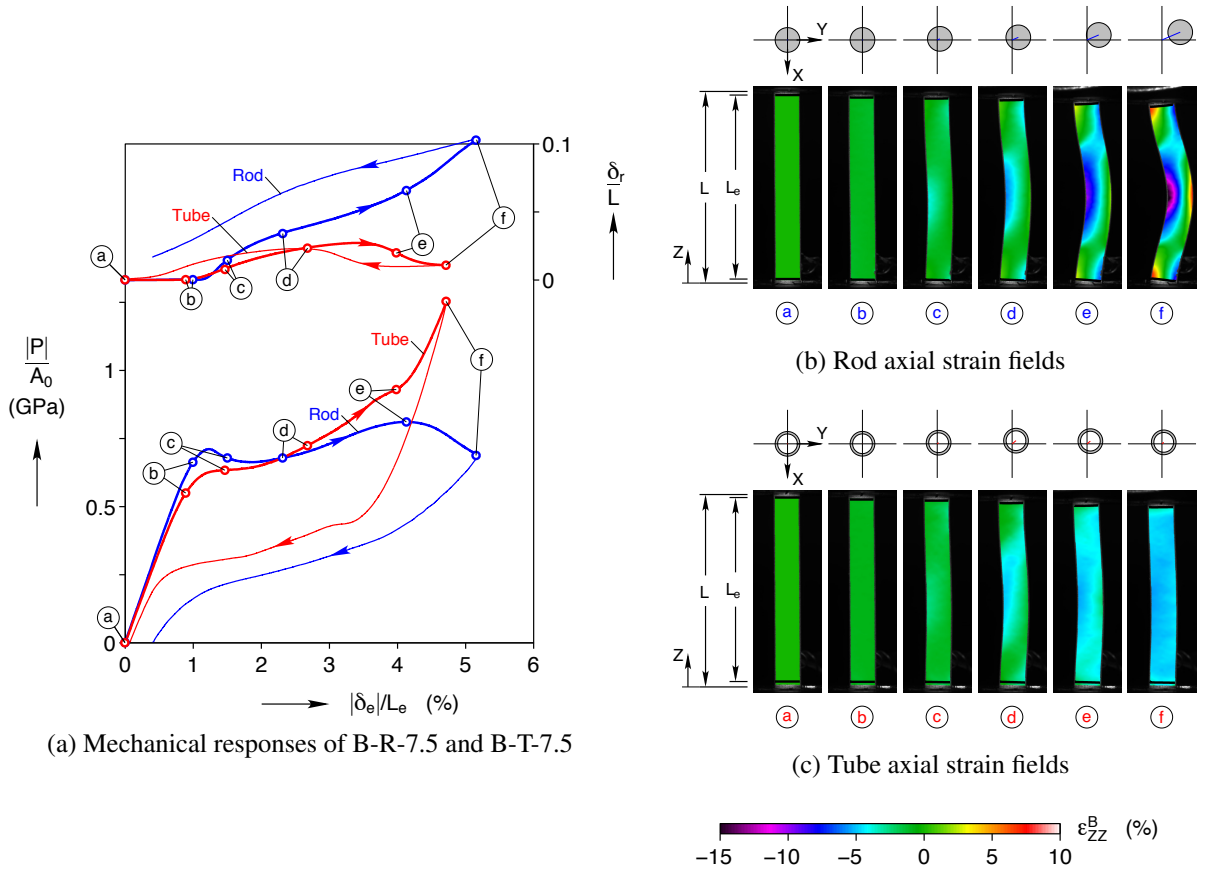

(a) Mechanical responses of B-R-7.5 and B-T-7.5

(b) Rod axial strain fields

(c) Tube axial strain fields

Figure 2.19: For the columns with an approximate aspect ratio of 7.5, the rod specimen exhibited monotonically increasing buckling deformation; whereas the tube specimen exhibited post-buckling straightening (unbuckling).

2013, Nayyar et al., 2014]; however, to the best of our knowledge, this is the first observation of column unbuckling under monotonic loading. Of these, the unbuckling-like behavior observed by Urushiyama et al. [2003] is the most similar to the behavior observed here. In their experiments, they used a three part loading procedure: (1) a column was axially compressed in a load frame until the microstructure of the SMA material began to detwin and was then unloaded; (2) the column was removed from the load frame and mechanically deformed into a "cosine" shape; (3) the column was again installed into a load frame and axially compressed, resulting in straightening of the column. While this disjoint loading procedure does not strictly satisfy my definition for unbuckling (since their columns were never buckled), steps (1) and (2) result in a configuration similar to a buckled column. It should also be noted that mechanical behavior of SMAs in the *martensite* phase differs from that of superelastic SMAs (which were examined here), although both exhibit the seemingly necessary stiffening at large strains for unbuckling to occur.

2.4 Conclusions

To better understand the combined uniaxial and bending behavior found in SMA beams, along with the effects of beam cross-sectional geometry, tension, compression, pure bending and column buckling experiments were performed on superelastic NiTi rods and tubes. In each experiment, stereo digital image correlation (DIC) was performed to measure surface strains, allowing for the observation of phase transformation localization when present. The mechanical responses and phase transformation morphologies were evaluated, identifying the unique phenomena associated with superelastic SMA beam deformation.

The tensile behavior of the rod and tube both exhibited usual hysteretic flag-shaped behavior with flat stress plateaus corresponding to unstable propagation of localized phase transformation. Although exhibiting similar mechanical behaviors, a diffuse phase transformation boundary developed in the rod upon localization; whereas, distinct finger-like phase boundaries developed in the tube. The difference in strain localization between the rod and tube is attributed to the differing restrictions on kinematic compatibility across phase boundaries where the solid cross-section of the rod is less accommodating to thickness-wise compatibility than the thin-walled tube.

In compression, the rod and tube again exhibited hysteretic behavior, but with smaller transformation strains, greater transformation stresses and smoother transitions than their tensile counterparts. Unlike the localized phase transformation in tension, phase transformation in compression was a stable process that was nearly homogeneous throughout the length of the specimen. Even while using grips designed specially to suppress buckling, minor buckling was observed in both the rod and tube due to the softening of the material response at the initiation of stress-induced phase transformation.

When subjected to pure bending, the mechanical responses of the rod and tube exhibited hysteretic flag-shaped behavior, but with distinctive quantitative and qualitative differences. Similar to the tensile response, phase transformation localization was observed in both specimen geometries. In the case of the rod, phase transformation localized in the form of a propagating high curvature front; whereas, phase transformation localized at disparate locations along the tensile side of the tube with similar finger-like phase boundaries as those observed in the tube tension experiment. Due to the differing localization behaviors, it was found that the rod specimen abided by the classical beam theory assumption that plane sections remain plane, which was only true on average for the tube.

In the column buckling experiments, the rods and tubes with similar slenderness ratios (L/r) had similar mechanical responses. Especially for the high aspect ratio columns (length/diameter),

the majority of the post-buckling deformation was recovered upon unloading, suggesting that buckling of SMAs need not indicate failure as is commonly concluded for elasto-plastic materials. Short columns were found to buckle inelastically due to the onset of phase transformation induced softening; whereas, long columns buckled elastically. Sharp phase transformation localization was only observed in the buckling of high aspect ratio tubes; however, unlike the tensile and pure bending responses, phase transformation localization in buckling did not propagate nor did it appreciably affect the mechanical response. Interestingly, in the case of low L/r columns, unbuckling behavior was observed, corresponding to the post-buckling straightening of the columns under increasing compressive loading. To the authors' knowledge, this is the first documentation of unbuckling behavior in superelastic SMA columns.

This chapter presented some of the effects of loading and structural geometry on the phase transformation and mechanical behavior of SMA materials. It was shown that phase transformation localization occurs in loading modes other than tension and that its morphology and evolution is dependent on the geometry of the structure. In general, the morphology of localization is governed by strain compatibility at phase boundaries which is most influenced by the the cross-sectional geometry of beam specimens: thin-walled structures allow for sharp localizations, while solid cross-sections can only localize according to diffuse 'necks'. The evolution of localization (such as propagation phenomena) is then dependent on the the overall geometry of the beam and the mode of deformation. Therefore, proper representation of these interactions between loading and structural kinematics are of the many challenges that must be faced when developing high fidelity SMA constitutive laws and structural simulations.

Chapter 3

Material Response in Tension

At the foundation of most constitutive model calibrations is the uniaxial tension experiment. Applying a state of constant stress throughout the gauge section of the specimen, tension experiments typically result in uniform deformation, giving a direct relationship for the material's tensile stress–strain response. Unfortunately, in the case of superelastic SMAs, unstable stress induced phase transformation between the austenite and martensite phases results in localization and propagation of a high strain field (Figure 3.1). The resulting mechanical response corresponds to an averaged structural behavior (Figure 3.1a), providing limited information with respect to the homogeneous material behavior; in particular, the local stress–strain behavior during phase transformation is un-

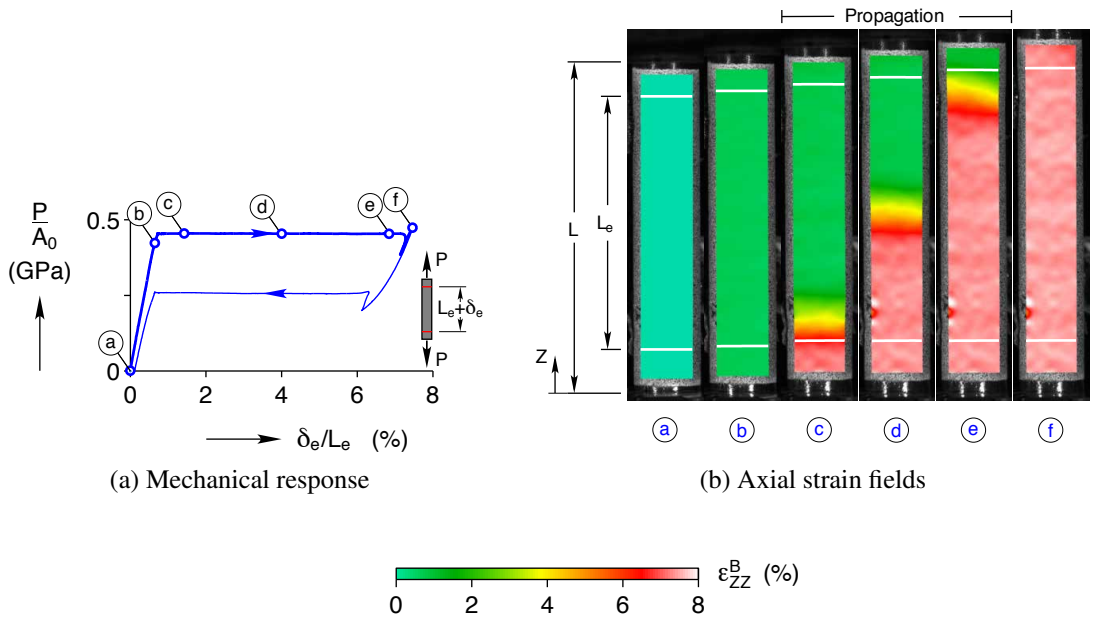

(a) Mechanical response

(b) Axial strain fields

Figure 3.1: Pulled in uniaxial tension, the deformation field of the superelastic NiTi rod from Chapter 2 localizes during phase transformation (ⓒ–ⓔ), deviating from the desired homogeneous behavior.

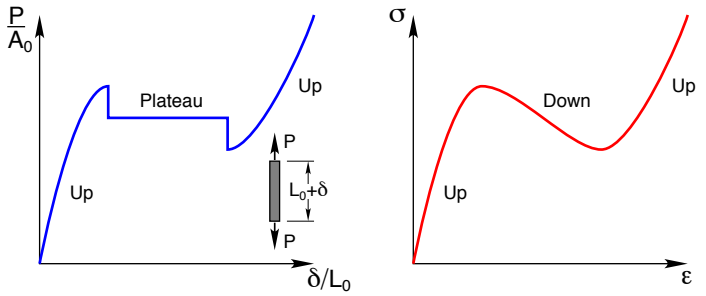

(a) Structural (b) Material

Figure 3.2: In his work on the tensile behavior of bars, Ericksen [1975] proposed that the stress plateau of the structural response (P/A_0 vs δ/L_0) is due to up–down–up material behavior (σ vs ε).

known (i.e. during the stress plateau). Ideally, an experiment could be designed to suppress phase transformation localization within the material while measuring the tensile response; however, this is difficult to achieve in practice.

In the seminal work of Ericksen [1975] on the equilibrium of bars, he hypothesized that general localization and propagation behavior (which is found in a wide range of physical systems, such as Lüders banding during tension of mild steel [Hallai and Kyriakides, 2013] or bulging of a thin membrane during inflation [Kyriakides and Chang, 1991] with the characteristic stress plateau shown in Figure 3.2a) derives from up–down–up material behavior (Figure 3.2b). Upon observation of localization and propagation in superelastic SMAs, the SMA community therefore adopted this hypothesis regarding the local material behavior; however, it wasn't until the recent work by Hallai and Kyriakides [2013] that this hypothesis was experimentally confirmed.

To measure the local material behavior of NiTi, Hallai and Kyriakides conducted two tension experiments: in the first, a composite structure consisting of a thin superelastic NiTi strip sandwiched between and joined to two stainless steel strips was pulled in tension; whereas, in the second experiment, a stainless steel strip (of the same material used in the composite experiment) was pulled in tension. After conducting both experiments, the mechanical response of the stainless steel strip was subtracted from the mechanical response of the composite structure. Since the NiTi and stainless steel were loaded in parallel during the composite experiment, the subtraction of the stainless steel behavior from the composite response resulted in the effective response of the NiTi; furthermore, the stiff response of the stainless steel in the composite prevented localization in the NiTi, resulting in the measurement of the homogeneous NiTi behavior during phase transformation.

The composite experimental setup of Hallai and Kyriakides [2013] is adapted here to measure

the local tensile material behavior of the superelastic NiTi rod examined in Chapter 2. The experimental procedure is first discussed in detail, outlining the composite manufacturing process (Section 3.1) and the loading procedure (Section 3.2). The experimental results are then discussed, examining validation results on aluminum rod (Section 3.3) and the measured NiTi local material response (Section 3.4). The major contributions of this chapter are

- the validation of the composite based experimental setup of Hallai and Kyriakides [2013],
- a more thorough constitutive understanding of superelastic SMA tensile behavior, and
- the measurement of the local material behavior of the rod specimen from Chapter 2, which can be used in conjunction with the experimental results from Chapter 2 for both model calibration and validation purposes.

3.1 Materials and Composite Preparation

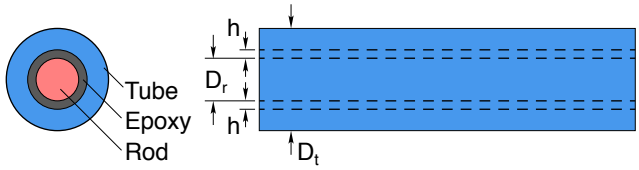

Figure 3.3: The composite specimens used in the measurement of the local material response of an unstable material consist of an inner rod (with outer diameter D_r), an outer tube (with outer diameter D_t), and an interfacial epoxy layer (with thickness h).

To measure the local material behavior of rod specimens, composite specimens were manufactured by joining the rod with a stiffer outer tube (Figure 3.3). Special care was taken in choosing the geometry of the outer tube, ensuring that the wall thickness was sufficiently large to suppress localization within the inner rod, while remaining small enough so as not to overwhelm the measured rod signal; furthermore, the inner diameter of the tube was chosen such that the gap between the rod and tube was large enough to allow for good bonding, but small enough so as not to affect the compliance of the structure. Two composites were manufactured for this study: NiTi rod + steel tube and Al rod + steel tube. The NiTi-based composites consisted of $3.15\,$mm (~$1/8$") diameter superelastic NiTi rod (the same as examined in Chapter 2) and $8.01\,$mm (~$5/16$") outer diameter and $3.25\,$mm (0.128") inner diameter 4130 steel tube; whereas, the Al-based composites (used for validation purposes) consisted of $3.165\,$mm (~$1/8$") diameter 2024 aluminum rod and $6.40\,$mm (~$1/4$") outer diameter and $3.80\,$mm (1.50") inner diameter 4130 steel tube.

The rod and tube materials in the composite specimens were joined together using an epoxy adhesive (JB Weld™). To ensure good bonding, the composites were manufactured according to the following process:

1. the exterior of the rod was roughened using coarse grained sandpaper;
2. the surface of the rod and the inner surface of the tube were thoroughly cleaned with acetone;
3. the surface of the rod and the inner surface of the tube were coated with epoxy and the rod was inserted into the tube;
4. the composite was cured in an oven at $100\,^{\circ}\mathrm{C}$ ($212\,^{\circ}\mathrm{F}$) for 30 min and then cooled in room temperature air.

The resulting bonds were found to be sufficiently strong for the composite experiments examined here[1].

3.2 Setup and Procedure

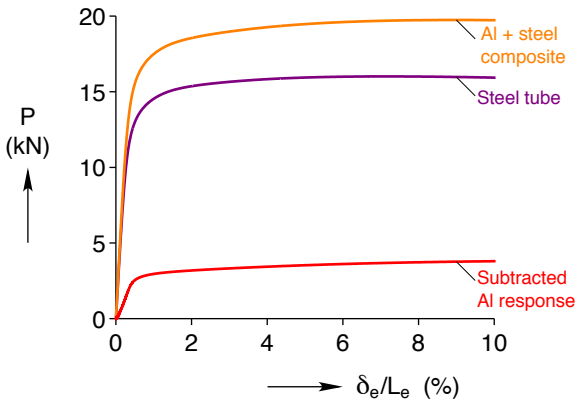

Figure 3.4: In the processing of the composite experimental results, the mechanical response (axial load P vs the extensometer strain $\delta_{\mathrm{e}}/L_{\mathrm{e}}$) of the steel tube was subtracted from the mechanical response of the composite, resulting in the response of the inner rod. Here, the process is demonstrated for the Al–based composite.

Two experiments were performed to measure the local material behavior of either the NiTi or Al rod: a tension experiment on the composite material and an equivalent tension experiment on the tube. All experiments were performed in a general purpose uniaxial load frame under global elongation (δ) control. Each specimen was gripped using mechanical wedge grips with roughened

[1] On a few occasions, debonding occurred and corresponded to sharp drops in the load response of the composite. In these cases, the results were disregarded and another composite experiment was conducted.

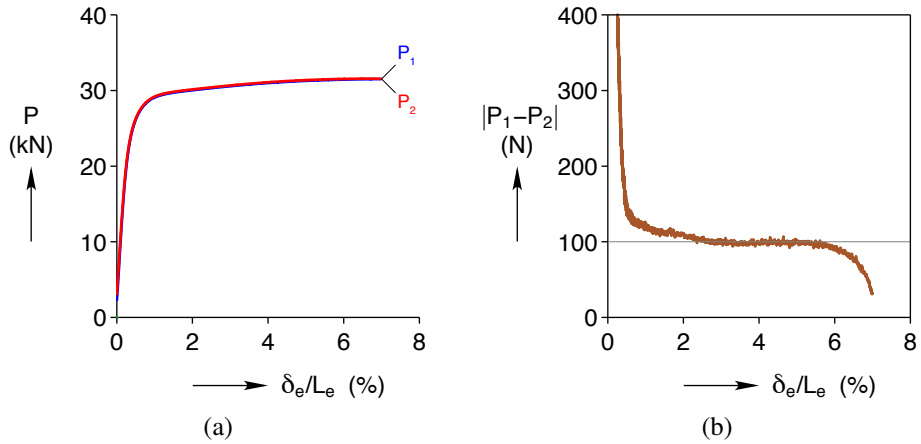

Figure 3.5: The scatter in the mechanical response between the steel tube experiments (as shown for two experiments indicated by P_1 and P_2) was on the order of $100\,\text{N}$, resulting in scatter on the order of $2.5\,\%$ of the full scale baseline subtracted results.

V–grooved platens[2], exposing a free length $L = 51\,\text{mm}$ (2'') between the grips. The specimen was then loaded at a constant loading rate $|\dot{\delta}| = |\text{d}\delta/\text{d}t|$ to a peak elongation. Experiments were performed in stagnant room temperature air at the slow loading rate of $\dot{\delta}/L = 5 \times 10^{-5}\,\text{s}^{-1}$ to achieve near isothermal loading conditions (less than $1\,^{\circ}\text{C}$ temperature change as measured by a thermocouple on the composite surface). During the experiment, the axial load P and cross-head displacement δ were measured, along with mechanical extensometer displacement δ_e. After completing an experimental pair, the P vs. δ_e/L_e response of the tube material was subtracted from the P vs. δ_e/L_e response of the composite to determine the mechanical response of the rod, an example of which is shown in Figure 3.4 for the Al-based composite.

Due to inaccuracies in the measurement of physical signals, their tends to be scatter in the baseline subtraction process. To help illustrate the effects of these inaccuracies, the mechanical response of the $8.01\,\text{mm}$ outer diameter steel tube was measured on two separate specimens (Figure 3.5a). In theory, the two measured responses should be identical; however, direct subtraction of the second response from the first (Figure 3.5b) results in a difference on the order of $100\,\text{N}$. In the context of the steel behavior, the $100\,\text{N}$ difference is of relatively little consequence since it is only $0.33\,\%$ of the $30\,\text{kN}$ full scale load experienced by the material; however, in the context of the baseline subtraction of the composite experiment, this $100\,\text{N}$ scatter propagates to the measured response of the inner rod, which is on the order of $4\,\text{kN}$, resulting in a more significant difference of $2.5\,\%$.

[2]Steel pins were inserted within the gripped sections of the secondary specimens when tested on their own.

3.3 Validation Results

The baseline subtraction technique attempts to measure the pure tension response of the NiTi rod in the absence of phase transformation localization and propagation; however, the mismatching Poisson–type contractions of the two joined materials in the composite (be that due to elasticity, plasticity or phase transformation) results in a combined state of axial and radial stress that differs slightly from the desired state of pure axial stress. The measured local material behavior of the NiTi rod therefore deviates from the true pure tension behavior, the severity of which is unknown.

To examine the effects of combined loading on the measured local material response in a composite experiment, a set of validation experiments were conducted on aluminum rod. Since the tensile response of aluminum is stable under moderate deformations, the local material response can be measured using typical tensile experimental procedures. The deviation between the pure tension and composite tension measurements can therefore be evaluated, providing a sense of the validity of the composite experimental procedure.

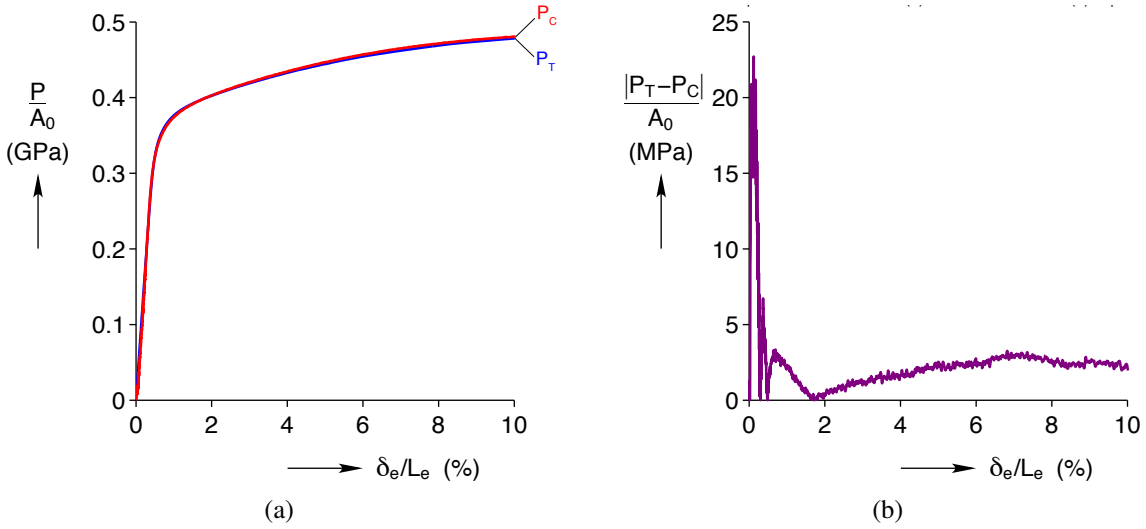

Figure 3.6: In the comparison between the true aluminum tensile response (denoted by subscript T) and the baseline subtracted tensile response from the composite experiment (denoted by a subscript C), the error between the two was on the order of $5\,\text{MPa}$ (about $1\,\%$ of full scale), validating the use of the composite experimental procedure.

The mechanical response of the Al rod measured with the composite experimental procedure was found to correspond well with the pure tensile behavior (Figure 3.6). With the naked eye, the deviations between the two mechanical responses are almost imperceptible (Figure 3.6a). Subtracting the response measured by the composite experiment (P_C) from the pure tension response (P_T) (Figure 3.6b), the maximum deviation was on the order of $25\,\text{MPa}$, with the majority of the

deviation being less than $5\,\text{MPa}$. Since $5\,\text{MPa}$ is only $1\,\%$ of the full scale mechanical behavior, the affect of the material response due to the combined loading state in the composite structure is therefore minimal. As the linear elastic behavior of NiTi and Al are similar (both having elastic moduli near $70\,\text{GPa}$) and the fact that both plasticity and phase transformation are nearly volume preserving (i.e., similar Poisson–type behavior), it is expected that the composite experimental procedure is also valid for NiTi.

3.4 Experimental Results

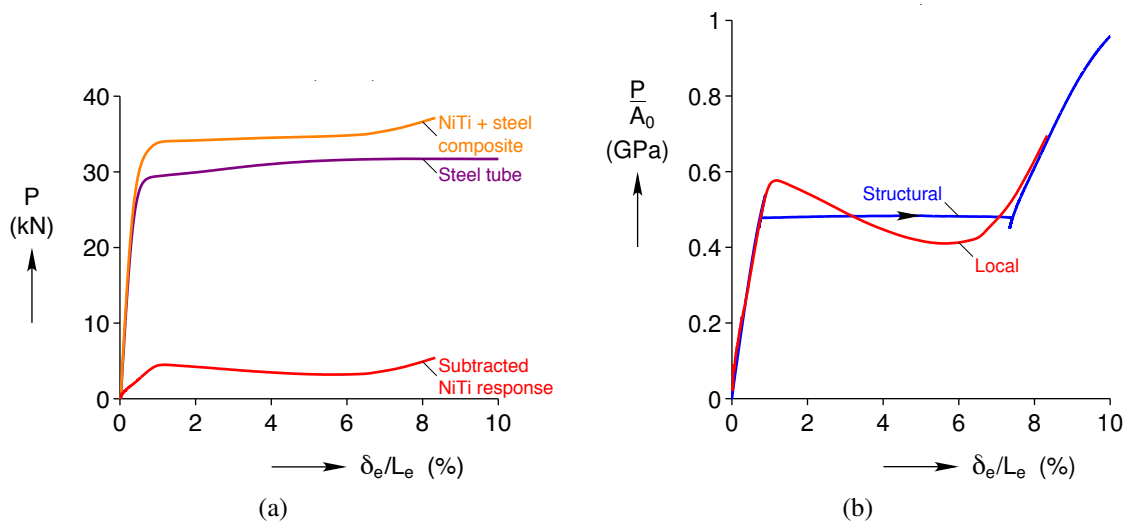

Figure 3.7: The measured local material response (engineering stress P/A_0 vs engineering strain δ_e/L_e) corresponds to the expected up–down–up behavior.

The measured local material response of the NiTi rod corresponds to the expected up–down–up behavior as shown in Figure 3.7. Unlike the structural response (which is also shown in Figure 3.7 for reference), the local response exhibited smooth behavior with a sharper "up" to "down" transition than "down" to "up" transition. Interestingly, the second "up" portion of the local response began before the end of the stress plateau in the structural response. It is difficult to determine whether this corresponds to the actual material behavior, or if it is an artifact of the baseline subtraction process; although, the flat and slightly peaked steel tube response (Figure 3.7a) starting at around $6\,\%$ axial strain, which is often associated with the onset of necking in the specimen (i.e., inhomogeneous deformation), suggests the stiffer than expected behavior in the measured local response is an artifact of the baseline subtraction process.

To verify the suppression of localized deformation in the composite, a supplementary composite

experiment was conducted using stereo digital image correlation (DIC) to measure full field strains. Unfortunately, due to the makeup of the composite, DIC could only measure strains on the surface of the composite's outer steel tube, providing only an indirect understanding of the inner tube deformation. The axial strain fields (ε^B_{ZZ}) at select points during the loading (Figure 3.8a) are shown in Figure 3.8c; additionally, the averaged axial strain profiles through the thickness (D) along the axis of the composite as defined by

$$\bar{\varepsilon}^B_{ZZ}(Z) = \frac{1}{D}\int_{-D/2}^{D/2} \varepsilon^B_{ZZ}(Y,Z)\,\mathrm{d}Y \tag{3.1}$$

are shown in Eq. (3.1), providing a more quantitative sense of inhomogeneities in the deformation. Up through ⓒ, the composite deformed homogeneously; however, during phase transformation (ⓒ–ⓕ), two high strain regions developed, exhibiting a maximum strain variation of $1.4\,\%$ along the length of the specimen. Since the strain field localized, the measured mechanical response corresponds to an averaged response; however, the suppression of unstable propagation still allowed for the measurement of the up–down–up material behavior during phase transformation. It should be noted that, due to the lower accuracy of the DIC virtual extensometer measurements used in these experiments in comparison to the mechanical extensometer used in the previous experiments, the baseline subtraction results were noisier (Figure 3.8a); in particular, the initial linear elastic behavior.

3.5 Conclusions

A novel experimental technique was used to measure the unstable local material response of superelastic NiTi rod. Through the use of a composite structure, phase transformation localization was suppressed within the NiTi material. The NiTi component of the composite behavior was then determined by subtracting off the material response of the outer steel tube and consisted of a non-monotonic up–down–up response. This local behavior provides a better constitutive representation of the material than the structural tensile response (which is contaminated by inhomogeneous deformation) that is measured using a conventional tensile experiment.

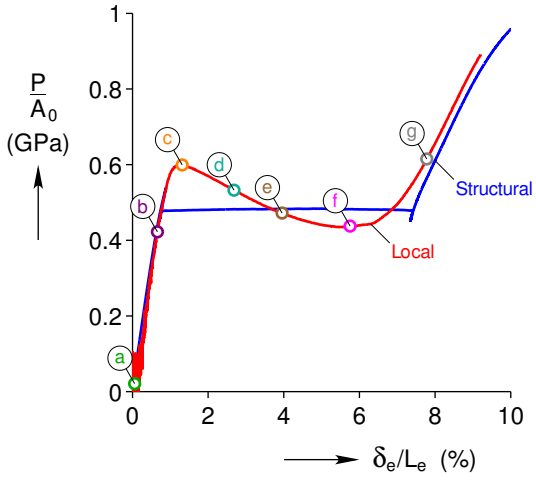

(a)

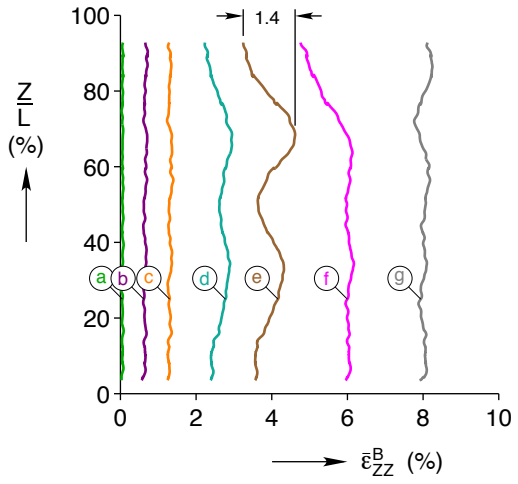

(b)

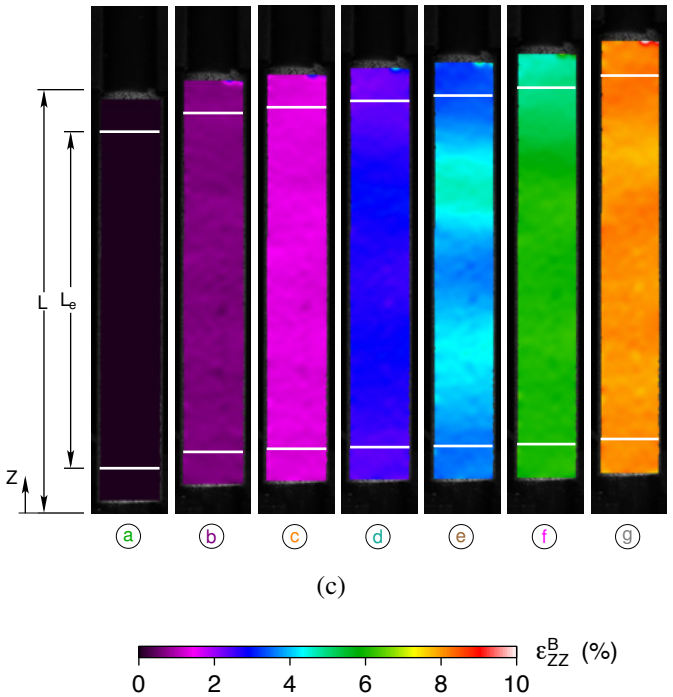

(c)

Figure 3.8: As shown for select points of interest in the mechanical response (a), the axial strain fields ε^B_{ZZ} (c) localized slightly as highlighted by the $1.4\,\%$ maximum deviation in the averaged axial strain profiles $\bar{\varepsilon}^B_{ZZ}$ (b).

Chapter 4

Superelastic Column Unbuckling

For conventional structural materials (such as metals, ceramics and composites), classical compressive buckling of columns is a monotonic process where the degree of buckling (bending) increases under increased axial loading; however, as shown in Chapter 2, nonlinear material behavior and large recoverable kinematics can lead to more complex nonintuitive buckling phenomena. One such phenomenon was observed in the low aspect ratio column buckling experiments of Chapter 2 where short columns buckled (bent), but then later straightened, all during monotonic compressive loading. Since buckling is characterized by the departure from the principal equilibrium path to a bifurcated path, this return of a buckled structure (on a bifurcated equilibrium path) to its pre-buckled configuration (principal path) under continued monotonic loading is therefore defined here as *unbuckling*.

Other related cases of unbuckling have been reported in the literature, although researchers have used various names (such as *detwinning effect*, *anti-buckling* and *isola bifurcation*) to describe the phenomenon. The following are a few notable examples that share some common traits:

- An early observation of unbuckling behavior was by Alexander [1971] where he experimentally examined the inflation of a spherical neoprene balloon. At a critical inflation pressure the balloon buckled into an asymmetric mode yet, under further inflation, regained its spherical shape (see Figure 4.1a). As an extension to Alexander's work, Haughton [1980], and later Chen and Healey [1991], analytically modeled the unbuckling behavior of balloon inflation using an Ogden material model, reproducing the observed behavior of Alexander. A similar phenomenon was observed by Kyriakides and Chang [1991] during the inflation of cylindrical latex-rubber balloons, where at a critical pressure a bulge formed, propagated along its length, and eventually regained its nominally cylindrical shape (once the bulge has consumed the entire length) at sufficiently high pressure. Both of these are a consequence of the inherent non-monotonic (up-down-up) pressure-volume relationship of the balloons, arising from nonlinearities in the material behavior and large-deformation kinematics.

- More recently, Urushiyama et al. [2003] experimentally examined the unbuckling-like behavior of SMA columns in the *martensite* phase. In their experiments, they used a three part loading procedure to demonstrate unbuckling-like behavior: (1) a column was axially compressed in a load frame until the microstructure of the SMA material began to detwin and was then unloaded; (2) the column was removed from the load frame and mechanically deformed into a "cosine" shape; (3) the column was again installed into a load frame and axially compressed, resulting in straightening of the column (see Figure 4.1b). While this disjoint loading procedure does not strictly satisfy my definition for unbuckling, since their columns were never buckled, steps (1) and (2) result in a configuration similar to a buckled column. It should also be noted that mechanical behavior of SMAs in the *martensite* phase differs from that of superelastic SMAs (which are examined here), although both exhibit the seemingly necessary stiffening at large strains for unbuckling to occur. As a followup to this work, Richter et al. [2011] used a finite element model to capture the behavior of SMA columns in the martensite phase, successfully simulating the straightening during compression.

- Another recent example of unbuckling behavior was found in the wrinkling of thin sheets pulled in tension (see Figure 4.1c). Although the wrinkling problem has been studied for a number of years, Healey et al. [2013] were the first to discover the unbuckling behavior of thin sheets analytically, which was later experimentally verified in polyethylene thin sheets by Nayyar et al. [2014].

This work looks to provide a deeper understanding of the mechanisms behind unbuckling, examining the buckling of superelastic SMA columns as a lens into more general post-buckling behavior. The remainder of this chapter is outlined as follows:

- Section 4.1 reviews two relevant column buckling experiments of superelastic SMAs from Chapter 2, reiterating the phenomenon of unbuckling;

- Section 4.2 develops a simple two degree-of-freedom superelastic Shanley column model that exhibits buckling–unbuckling behavior;

- Section 4.3 investigates the model behavior, presenting the general characteristics of unbuckling (Section 4.3.1), comparing the model against experimentally observed unbuckling (Section 4.3.2), and identifying the necessary geometric and material parameters for unbuckling to occur, thereby providing an analytical tool for the design of columns that unbuckle (Section 4.4);

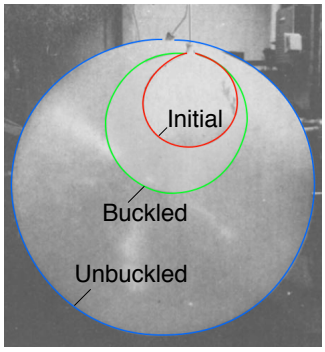

(a) balloon inflation (reproduction from [Alexander, 1971])

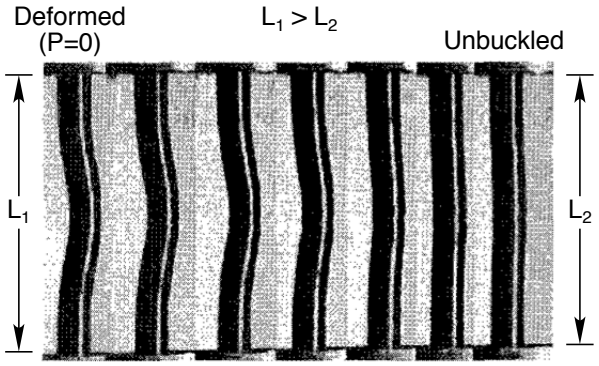

(b) martensitic SMA column straightening (reproduction from [Urushiyama et al., 2003])

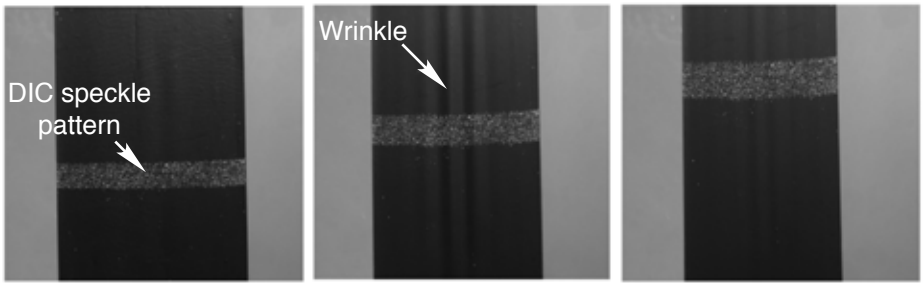

(c) sheet wrinkling in tension (reproduction from [Nayyar et al., 2014])

Figure 4.1: Other unbuckling phenomena have been observed experimentally.

4.1 Superelastic Buckling Experiments

Two relevant experiments from Chapter 2, involving buckling and unbuckling of superelastic SMA columns, are reviewed here. Experiments were performed on initially straight *superelastic* as-received NiTi rods (NDC SE508) and tubes (Memry BB) with a nominal outer diameter (D) of $3.175\,\text{mm}$ ($1/8\,\text{in}$). The NiTi rod had a measured outer diameter $D = 3.150\,\text{mm}$ and austenite finish temperature $A_\text{f} = 10\,^\circ\text{C}$; whereas, the NiTi tube had a measured outer diameter $D = 3.176\,\text{mm}$, wall thickness $H = 0.318\,\text{mm}$, and $A_\text{f} = 19\,^\circ\text{C}$.

In all experiments, stereo digital image correlation (DIC) was used to measure surface displacements and strains. Prior to each experiment, the gauge section of the specimen was painted with a base coat of white paint, followed by black speckles. Stereo images were then captured during each experiment and post-processed using Vic-3D (Solutions [2012]) to calculate the surface displacements and strains. For the purpose of characterizing global mechanical responses, a "virtual" extensometer of length L_e was established within the DIC gauge section and its elongation δ_e was

used to measure the average axial strain δ_e/L_e in the gauge section (Figure 4.3a). This avoided difficulties with the use of conventional mechanical extensometers in the presence of bending deformation during column buckling.

For reference, uniaxial mechanical responses of the two SMA specimens (rod and tube) are shown in Figure 4.2, depicting superelastic responses typical of commercially-available NiTi. These are plotted in terms of nominal engineering stress F/A_0 (axial tensile force F, reference cross-section area A_0) versus average axial strain δ_e/L_e in the DIC extensometer gage section. The responses are similar (but not identical), both exhibiting loading-unloading hysteresis, an intermediate softening due to phase transformation between austenite (low strain) and stress-induced martensite (high strain) phases, and significant asymmetry in tension versus compression.

For the buckling experiments, specimens were compressed axially in a load frame (Instron 5585) under clamped-clamped boundary conditions (see Figure 4.3a schematic). Experiments were performed in room temperature air under slow, end-displacement control to achieve near isothermal loading conditions, since superelastic SMAs are exceptionally strain-rate sensitive [Shaw and Kyriakides, 1995]. The specimen was gripped by ER-16 collets, exposing a free length L, and was loaded-unloaded in axial compression at a constant rate of shortening $\dot{\Delta}/L = \pm 1 \times 10^{-4}\,\mathrm{s}^{-1}$. During each experiment, continuous measurements were made of the axial load P (by a 12.5 kN load cell), grip displacement Δ (by the load frame actuator), and specimen temperature T_s (by a thermocouple affixed with thermally-conductive paste). The maximum temperature deviation

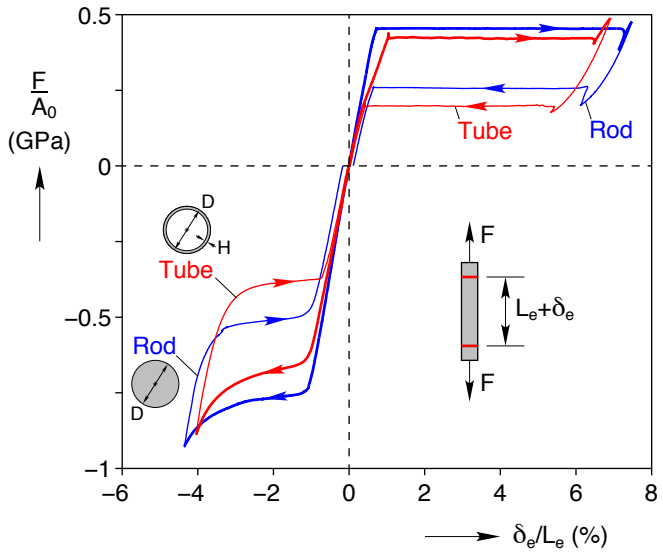

Figure 4.2: Uniaxial isothermal mechanical responses (engineering stress F/A_0 vs. engineering strain δ_e/L_e) of superelastic NiTi rod and tube in tension and compression, demonstrating hysteretic non-monotonic structural responses.

of the specimen was less than $1\,^{\circ}\mathrm{C}$ in all buckling experiments. The buckling response of the specimen was characterized by the macroscopic compressive stress (P/A_0), compressive DIC extensometer strain (Δ_e/L_e), normalized radial (lateral) midspan displacement (δ_r/L) and outer fiber strains (ε_1 and ε_2).

To better illustrate buckling–unbuckling behavior, the buckling responses of the NiTi rod and NiTi tube with aspect ratios $L/D = 7.24$ and 7.33, respectively, are compared in Figure 4.3. Mechanical responses during loading (only) are shown in Figure 4.3b in terms of normalized axial force (P/A_0, lefthand vertical axis) and lateral displacement of the column's midspan (δ_r/L, righthand vertical axis) versus normalized axial shortening in the gage section (Δ_e/L_e), and selected DIC axial strain field images are shown in Figure 4.3c and Figure 4.3d for the respective rod and tube specimens. Consistent with the experiments of [Reedlunn et al., 2013], DIC strain fields are reported here using the Biot strain measure, $\boldsymbol{\varepsilon}^{\mathrm{B}} = \boldsymbol{U} - \boldsymbol{I}$ where $\boldsymbol{U}$ is the right stretch tensor and $\boldsymbol{I}$ is the identity tensor, to give engineering-like bending strains that are invariant to cross-section rotations. As seen in Figure 4.3b, the rod specimen begins to buckle at ⓑ, reaches a limit load between ⓑ and ⓒ, stiffens somewhat just before ⓓ, and reaches a collapse load at ⓔ after which the load drops steeply. While this is not quite the traditional elasto-plastic post-buckling response of conventional materials, the degree of bending (δ_r) continues to grow past point ⓑ, so no unbuckling occurs in this case. I term this behavior 'monotonic' buckling in the sense that the lateral deflection continues to grow, while recognizing that the axial load response may still be non-monotonic (as in the rod response of Figure 4.3b). By contrast, after early buckling near ⓑ, the tube specimen's force-shortening response significantly stiffens and the degree of bending decreases past point ⓓ as shown by the decrease in δ_r (Figure 4.3b upper pane) and the return to a relatively uniform strain field in $\varepsilon^{\mathrm{B}}_{ZZ}$ (Figure 4.3d) at ⓕ. This post-buckling straightening is the unbuckling phenomenon of interest in this chapter.

4.2 Superelastic Shanley Column Model

A modified Shanley column model is developed here to investigate the origins of unbuckling behavior observed in superelastic SMA columns. The objectives are to (1) examine the mechanisms of unbuckling within a simple framework, (2) identify the conditions under which it occurs, and (3) develop simple guidelines for the design of columns that functionally buckle-unbuckle.

Developed by Shanley in the 1940s to characterize the onset of elasto-plastic buckling, the original Shanley column was a reduced-order model of simply supported column buckling [Shanley, 1947]. Noting that the majority of post-buckling deformation is localized in a hinge at the column

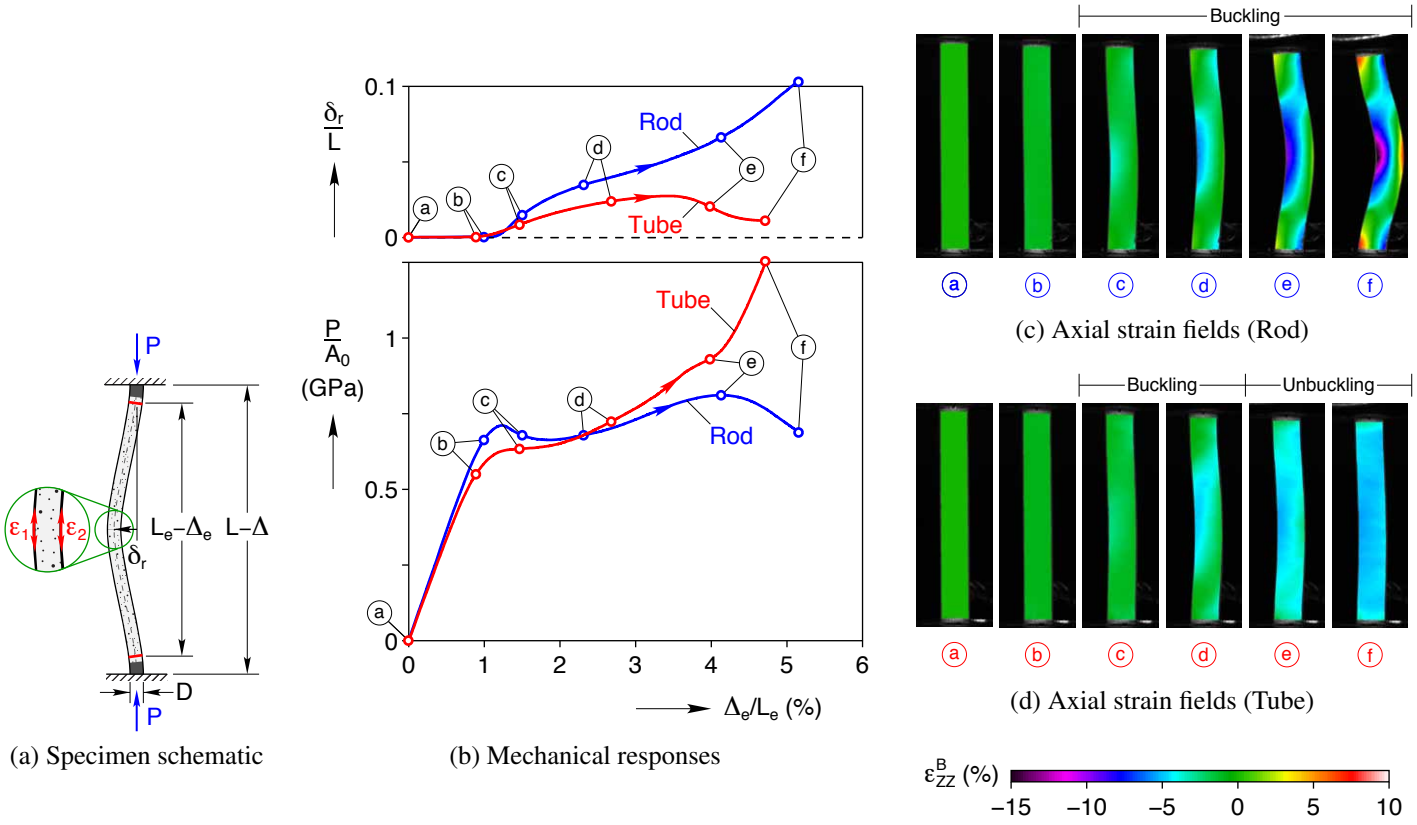

(a) Specimen schematic

(b) Mechanical responses

(c) Axial strain fields (Rod)

(d) Axial strain fields (Tube)

Figure 4.3: Comparison of the column buckling responses of the NiTi rod and tube specimens (aspect ratios $L/D = 7.24$ and 7.33, respectively). The rod exhibits buckling with increasing bending and eventual collapse, yet the tube exhibits buckling then unbuckling as it straightens under increasing load.

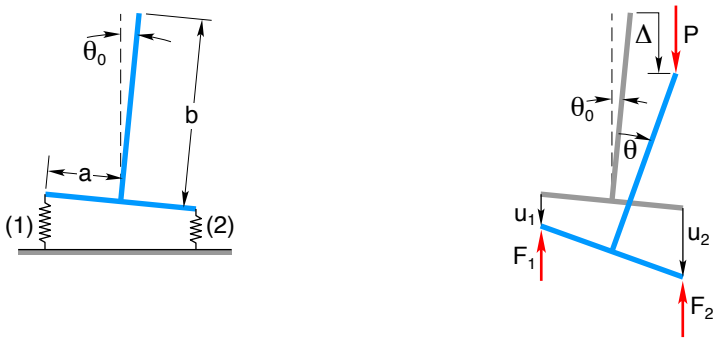

(a)
Reference configuration

(b)
Current configuration

Figure 4.4: The Shanley Column consists of a axially loaded (by a force P) rigid inverted 'T' resting on two nonlinear spring, deforming with a tip displacement Δ and rotation θ.

midspan, the Shanley column models the symmetric half-length of the column by a rigid inverted 'T' supported by two springs at its base (see Figure 4.4a). The length of the Shanley column is b and the halfwidth is a. A small angle θ_0 defines a possible initial misalignment of the column to include the effects of geometric imperfection. When subjected to a compressive vertical load P, the degrees-of-freedom (DOFs) are the axial tip translation Δ and rotation θ, as shown in Figure 4.4b. I selected the upper tip displacement instead of the commonly-chosen translation of the base center point, since the tip displacement is what is typically measured in a column buckling experiment. Although this choice of the translational DOF is immaterial in the case of linear kinematics, it does affect the stability results.

My modification to the Shanley column is in the constitutive law for the support springs, now modeled as nonlinear elastic springs to mimic superelastic behavior (in contrast to the elaso-plastic behavior originally used by Shanley). The mechanical behavior is idealized by assuming each quadrant[1] of force-deflection behavior is trilinear with a softer intermediate segment (Figure 4.5a). In the interest of simplicity, I neglect the loading-unloading hysteresis, tension-compression asymmetry, any differences in elastic moduli between austenite (low strain magnitude) and martensite (high strain magnitude), and the rounded corners in the actual SMA behavior (Figure 4.2). These likely affect the quantitative results, but not the essential origins of unbuckling.

[1]Here, compressive behavior is the upper right quadrant, while tensile behavior is the lower left quadrant.

The idealized force displacement response of the spring behavior is defined by

$$F(u) = \begin{cases} -\left[k_{\mathrm{e}}u_{\mathrm{s}} + k_{\mathrm{t}}(u_{\mathrm{f}} - u_{\mathrm{s}}) + k_{\mathrm{e}}(-u - u_{\mathrm{f}})\right] & : u < -u_{\mathrm{f}} \\ -\left[k_{\mathrm{e}}u_{\mathrm{s}} + k_{\mathrm{t}}(-u - u_{\mathrm{s}})\right] & : -u_{\mathrm{f}} \le u < -u_{\mathrm{s}} \\ k_{\mathrm{e}}u & : |u| \le u_{\mathrm{s}} \\ k_{\mathrm{e}}u_{\mathrm{s}} + k_{\mathrm{t}}(u - u_{\mathrm{s}}) & : u_{\mathrm{s}} < u \le u_{\mathrm{f}} \\ k_{\mathrm{e}}u_{\mathrm{s}} + k_{\mathrm{t}}(u_{\mathrm{f}} - u_{\mathrm{s}}) + k_{\mathrm{e}}(u - u_{\mathrm{f}}) & : u > u_{\mathrm{f}} \end{cases}, \tag{4.1}$$

where F is the compressive spring force and u is the spring shortening. Focussing on just the positive quadrant, the constitutive law is trilinear with the following parameter constants: u_{s} and u_{f} are the respective start and finish displacements of the second linear segment, k_{e} is the tangent stiffness of the first and third segments, and k_{t} is the tangent stiffness of the second segment. Note that u_{s}, u_{f}, k_{e}, and k_{t} are all positive parameters with $0 < k_{\mathrm{t}} < k_{\mathrm{e}}$ and $0 < u_{\mathrm{s}} < u_{\mathrm{f}}$.

To generalize the analysis, dimensionless variables for spring force f and spring displacement ε, along with dimensionless spring parameters α, β and η, are defined as

$$f \equiv \frac{F}{k_{\mathrm{e}}b}, \quad \varepsilon \equiv \frac{u}{b}, \quad \alpha \equiv \frac{u_{\mathrm{s}}}{b}, \quad \beta \equiv \frac{u_{\mathrm{f}} - u_{\mathrm{s}}}{b}, \quad \eta \equiv \frac{k_{\mathrm{t}}}{k_{\mathrm{e}}} \in (0, 1). \tag{4.2}$$

The dimensionless form of the constitutive law (as shown in Figure 4.5b) is therefore

$$f(\varepsilon) = \begin{cases} \varepsilon + (1-\eta)\beta & : \varepsilon < -\alpha - \beta & (A) \\ \eta\varepsilon - (1-\eta)\alpha & : -\alpha - \beta \le \varepsilon < -\alpha & (B) \\ \varepsilon & : -\alpha \le \varepsilon < 0 & (C) \\ \varepsilon & : 0 \le \varepsilon < \alpha & (D) \\ \eta\varepsilon + (1-\eta)\alpha & : \alpha \le \varepsilon < \alpha + \beta & (E) \\ \varepsilon - (1-\eta)\beta & : \varepsilon \ge \alpha + \beta & (F) \end{cases}. \tag{4.3}$$

For later reference, each piecewise segment of the constitutive response is referenced by the capital letters in Eq. (4.3) and Figure 4.5b.

The kinematics of the Shanley column are defined by the rigid body motion of the inverted 'T'. For a downward displacement (Δ) and clockwise rotation (θ), the respective displacements in

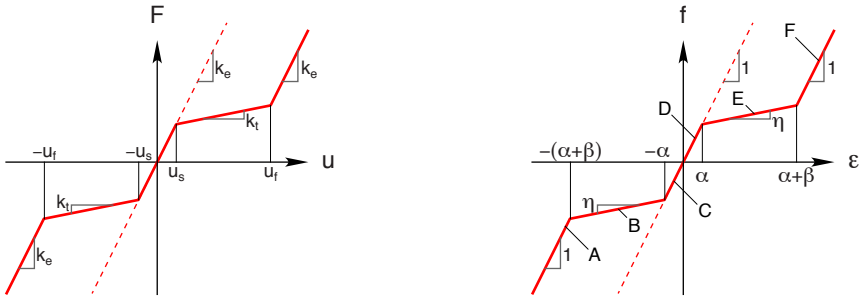

(a) Dimensional (b) Dimensionless

Figure 4.5: To imitate superelastic-like material behavior, the foundation springs of the Shanley column are modeled by a trilinear constitutive law.

Springs 1 and 2 (assuming they remain vertical) are

$$u_1 = \Delta + b\left[\cos(\theta+\theta_0) - \cos\theta_0\right] - a\left[\sin(\theta+\theta_0) - \sin\theta_0\right], \tag{4.4a}$$

$$u_2 = \Delta + b\left[\cos(\theta+\theta_0) - \cos\theta_0\right] + a\left[\sin(\theta+\theta_0) - \sin\theta_0\right]. \tag{4.4b}$$

Defining the dimensionless aspect (slenderness) ratio ℓ and dimensionless tip displacement as

$$\ell \equiv \frac{b}{a}, \quad \delta \equiv \frac{\Delta}{b}, \tag{4.5}$$

the dimensionless spring displacements of Eq. (4.2) are

$$\varepsilon_1 = \delta + \cos(\theta+\theta_0) - \cos\theta_0 - \frac{\sin(\theta+\theta_0) - \sin\theta_0}{\ell}, \tag{4.6a}$$

$$\varepsilon_2 = \delta + \cos(\theta+\theta_0) - \cos\theta_0 + \frac{\sin(\theta+\theta_0) - \sin\theta_0}{\ell}. \tag{4.6b}$$

For small rotations, the kinematics can be linearized by $\sin\theta \to \theta$ and $\cos\theta \to 1$, giving

$$\varepsilon_1 \approx \delta - \frac{\theta}{\ell}, \tag{4.7a}$$

$$\varepsilon_2 \approx \delta + \frac{\theta}{\ell}. \tag{4.7b}$$

Due to the dead loading and elastic (yet nonlinear) spring behavior, this model represents a conservative system (contrary to the original elasto-plastic Shanley column model) which can be

represented by the total potential energy $\widetilde{\Pi} = \widetilde{U} + \widetilde{\Omega}$ of the system, where

$$\widetilde{U} = \int_0^{u_1} F_1(u)\,\mathrm{d}u + \int_0^{u_2} F_2(u)\,\mathrm{d}u, \tag{4.8a}$$

$$\widetilde{\Omega} = -P\Delta, \tag{4.8b}$$

are the internal and external potential energies, respectively. Using Eqs. (4.2) and (4.5), and defining the dimensionless applied load

$$p \equiv \frac{P}{k_e b}, \tag{4.9}$$

the dimensionless potential energy is

$$\Pi \equiv \frac{\widetilde{\Pi}}{k_e b^2} = U + \Omega = \int_0^{\varepsilon_1} f_1(\varepsilon)\,\mathrm{d}\varepsilon + \int_0^{\varepsilon_2} f_2(\varepsilon)\,\mathrm{d}\varepsilon - p\delta. \tag{4.10}$$

Equilibrium states are found from stationary points of the potential energy $\Pi(\delta, \theta)$ according to

$$\frac{\partial \Pi}{\partial \delta} = 0 = f_1 + f_2 - p, \tag{4.11a}$$

$$\frac{\partial \Pi}{\partial \theta} = 0 = \frac{f_2 - f_1}{\ell}\cos(\theta + \theta_0) - (f_1 + f_2)\sin(\theta + \theta_0), \tag{4.11b}$$

which also could have been found from a simple force and moment balance using the free body diagram (Figure 4.4b). In the case of linear kinematics, force equilibrium (Eq. (4.11a)) remains the same while moment equilibrium (Eq. (4.11b)) reduces to

$$(f_2 - f_1) - \ell\,(f_1 + f_2)\,(\theta + \theta_0) = 0. \tag{4.12}$$

Explicit analytical solutions of the equilibrium paths exist for both the kinematically nonlinear and linear models. Due to the piecewise linear behavior of the springs, however, it was necessary to perform an extensive search of all possible equilibrium paths. Without any loss in generality, I assumed that $\theta > 0$, $\theta_0 > 0$ and $\delta > 0$. All relevant permutations of the springs' constitutive behaviors (a total of nine as listed in Table 4.1) were substituted into the equilibrium equations and solved with respect to either δ or θ, depending on which was more convenient. The equilibrium paths were then constructed piecewise according to the relevant regimes of the constitutive behavior. An example solution procedure is as follows (assuming $\theta_0 = 0$ and linear kinematics for simplicity):

Table 4.1: Nine relevant pairs of the springs' constitutive regimes exist during compression of the Shanley column.

Loading state	Constitutive behavior
Pure compression	*D/D*, *D/E*, *D/F*, *E/E*, *E/F*, *F/F*
Mixed tension and compression	*A/F*, *B/F*, *C/F*

- Choose a permutation of the springs' constitutive behavior: suppose Springs 1 and 2 both lie along branch D of the response (denoted *D/D*), which corresponds to $f_i = \varepsilon_i$ for i = 1,2;
- Substitute the constitutive behavior into the kinematically linear equilibrium equation, Eq. (4.12):

$$(\varepsilon_2 - \varepsilon_1) - (\varepsilon_1 + \varepsilon_2)\ell\theta = 0;$$

- Substitute the linear kinematic relations of Eq. (4.7) and simplify:

$$\left(1 - \delta\ell^2\right)\theta = 0;$$

- Solve the resulting equation in terms of the DOFs, and use Eq. (4.11a) to find the resulting external load $p = f_1 + f_2$:
  1. $\theta = 0$, which corresponds to the principal branch with $p = 2\delta$;
  2. $\delta = \ell^{-2}$, which corresponds to a bifurcation point at $\theta = 0$ and a secondary branch at $p = 2\ell^{-2}$;
- Create piecewise constructions of each equilibrium branch based on the assumed regime of constitutive behavior ($0 \leq \varepsilon_i < \alpha$):
  1. For $\theta = 0$, $\varepsilon_1 = \varepsilon_2 = \delta$, which implies solution 1 is valid for $0 \leq \delta < \alpha$;
  2. For $\delta = \ell^{-2}$, $\varepsilon_1 = (\ell^{-1} - \theta)\ell^{-1}$ and $\varepsilon_2 = (\ell^{-1} + \theta)\ell^{-1}$. Since by assumption $\theta > 0$, $0 \leq \varepsilon_1 < \varepsilon_2 < \alpha$, which implies solution 2 is valid for $0 \leq \theta < \alpha\ell - \ell^{-1}$.

The Shanley column is stable when the potential energy is positive definite with respect to small admissible perturbations away from an equilibrium state. Stability with respect to displacement δ control is therefore determined by

$$\frac{\partial^2 U}{\partial \theta^2} > 0; \tag{4.13}$$

whereas, stability with respect to load control is determined by

$$\frac{\partial^2 \Pi}{\partial \delta^2} > 0, \tag{4.14a}$$

$$\text{and} \quad \frac{\partial^2 \Pi}{\partial \theta^2}\frac{\partial^2 \Pi}{\partial \delta^2} - \left(\frac{\partial^2 \Pi}{\partial \delta\, \partial \theta}\right)^2 > 0, \tag{4.14b}$$

each evaluated at a particular equilibrium solution (δ, θ). Note that Eq. (4.14a) evaluates to

$$f_1' + f_2' > 0, \tag{4.15}$$

where $f_1' = f'(\varepsilon_1)$ and $f_2' = f'(\varepsilon_2)$ are the tangent stiffnesses of the springs, so the condition is always true for $\eta > 0$ (stable spring response) as assumed here. The two remaining criteria Eqs. (4.13) and (4.14b) correspond to

$$K_\delta = f_1' + f_2' - l^2(f_1 + f_2) > 0, \quad \text{for } \delta\text{-control}, \tag{4.16a}$$

$$\text{or} \quad K_p = 4 - l^2 p\left[\frac{1}{f_1'} + \frac{1}{f_2'}\right] > 0, \quad \text{for } p\text{-control}. \tag{4.16b}$$

Consistent with how the experiments in Section 4.1 were performed, subsequent stability results will be evaluated with respect to displacement control (Eq. (4.16a)) unless otherwise specified.

To get an initial sense of the expected buckling behavior, it is useful to map the stability regimes along the principal branch for the perfect column ($\theta_0 = 0$). Along the principal branch ($\theta = 0 \implies \delta = \varepsilon_1 = \varepsilon_2$), a straightforward stability analysis (with respect to δ-control) using Eqs. (4.3)

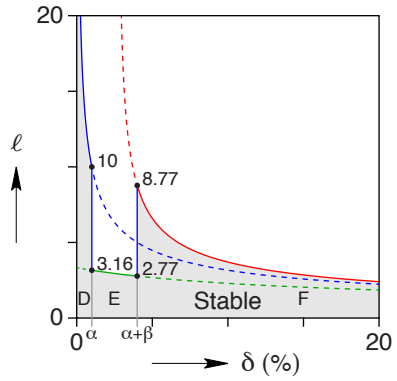

Figure 4.6: The stability of the principal path (denoted by the gray region) depends on the aspect ratio of the column ($\ell \equiv b/a$) as determined by Eq. (4.17).

and (4.16a), and accounting for the regimes of spring behaviors, show that bifurcations exist at

$$\delta_{\mathrm{B}} = \begin{cases} \ell^{-2} & \text{in } \textit{D/D} \text{ if } \ell > \dfrac{1}{\sqrt{\alpha}}, \\ \ell^{-2} - \alpha\left(\eta^{-1} - 1\right) & \text{in } \textit{E/E} \text{ if } \sqrt{\dfrac{\eta}{\alpha+\beta\eta}} < \ell < \sqrt{\dfrac{\eta}{\alpha}}, \\ \ell^{-2} + \beta\left(1-\eta\right) & \text{in } \textit{F/F} \text{ if } \ell < \dfrac{1}{\sqrt{\alpha+\beta\eta}}. \end{cases} \tag{4.17}$$

To provide a better sense of the principal branch behavior, the stability regime according to $K_\delta > 0$ is plotted in Figure 4.6 as a function of the aspect ratio ℓ, where the material parameters of the springs are $\alpha = 1\,\%$, $\beta = 3\,\%$, and $\eta = 10\,\%$ (which approximate the uniaxial compressive response of superelastic NiTi (Figure 4.2)).

4.3 Results

To examine buckling-unbuckling behavior, simulation results using the modified Shanley column model are presented (Section 4.3.1) and then compared to experimental results on superelastic SMA columns (Section 4.3.2). This is followed by an analysis of the necessary conditions for buckling-unbuckling to occur, thereby defining a design space of columns that unbuckle (Section 4.4).

4.3.1 Simulation Results

Simulations of the superelastic Shanley column are shown here to establish the different types of possible post-buckling behaviors and to describe why buckling-unbuckling can occur. The model is simple, having only two DOFs, yet as will be shown, its structural response exhibits a surprisingly rich set of post-buckling equilibrium paths, arising from the interplay between the trilinear constitutive response of the springs and the column's aspect ratio ℓ. For now, the model has no initial geometric imperfection ($\theta_0 = 0$) and nonlinear kinematics are used; furthermore, the material properties are chosen to represent generic superelastic compressive behavior (Figure 4.2) and correspond to $\alpha = 1\,\%$, $\beta = 3\,\%$, and $\eta = 10\,\%$. The equilibrium paths shown in subsequent figures are denoted by solid (stable) or dotted (unstable) lines, and stability is determined with respect to displacement (δ) control (although not necessarily a monotonic rate so as to better see all possible equilibria); additionally, open circles indicate bifurcation points, and solid circles indicate either a change in stability or a transition in constitutive behavior of the springs.

For fixed material properties, the structural responses of the superelastic Shanley column can be classified into four types based on the aspect ratio ℓ: long, midlength, short, and very short (Figures 4.7 to 4.10, respectively).

1. When loading starts from zero load, the structural response of "long" columns aligns with the usual notion of monotonic buckling. The response has three equilibrium branches, as shown in Figure 4.7 for an aspect ratio $\ell = 4.8$. Branch 0 is the principal branch with $\theta = 0$, which is stable until the first bifurcation point at $\delta = \alpha = 1\ \%$ that is triggered by the softening of the spring responses. Branch 1 emanates from the first bifurcation point and diverges from the principal branch with monotonically increasing θ. Branch 2 emanates from the second bifurcation point at $\delta = \alpha + \beta = 4\ \%$ on the principal branch (where one spring has transitioned from soft segment E to stiff segment F), that interestingly loops back to return to the principal branch at a third bifurcation point at $\delta = \ell^{-2} + \beta(1-\eta) \approx 7\ \%$. While Branch 2 has a portion that is stable, these states would not be realized by continuous loading from zero load. Note, however, that segment *E/F* in Figure 4.7a initially hooks toward Branch 1 ($\dot{\delta} < 0$) but turns around before reaching it.

2. The response of "midlength" columns correspond to unbuckling behavior (shown for $\ell = 4.4$ in Figure 4.8), since Branch 1 emanates from the first bifurcation point but eventually loops back along segment *E/F* to reattach to the principal branch at the second bifurcation point. In this case Branch 2 starts at the third bifurcation point at $\delta = \ell^{-2} + \beta(1-\eta) \approx 7.9\,\%$ and diverges without returning to the principal branch. Note that, unlike the long column, equilibria associated with spring behaviors *E/F* are now split between Branch 2 (stable) and Branch 3 (unstable). Thus, upon loading from zero load, the column would buckle, unbuckle, then buckle again if loading persists.

3. The response of "short" columns (shown for $\ell = 3.0$ in Figure 4.9, noting the change in δ and p scales) is similar to that of "midlength" columns, except that the first bifurcation occurs at $\delta = \ell^{-2} + \alpha(1 - 1/\eta) \approx 2.1\,\%$ after both springs have already softened (*E/E*). A third bifurcation point exists at a larger value $\delta = \ell^{-2} + \beta(1-\eta) \approx 13.8\,\%$, where buckling again occurs, but without returning to the principal branch.

4. The response of "very short" columns (shown for $\ell = 2.7$ in Figure 4.10) is simpler, with only two equilibrium branches and no unbuckling. The structure remains on the principal branch to large spring strains *F/F* before encountering a single bifurcation point at $\delta = \ell^{-2} + \beta(1-\eta) \approx 16.4\,\%$ and then buckling away from the principal branch.

Unbuckling behavior therefore occurs only in short to midlength columns, within a bounded range of column aspect ratios $\ell_{\text{min}} < \ell < \ell_{\text{max}}$. Further analysis to define this range will be provided in

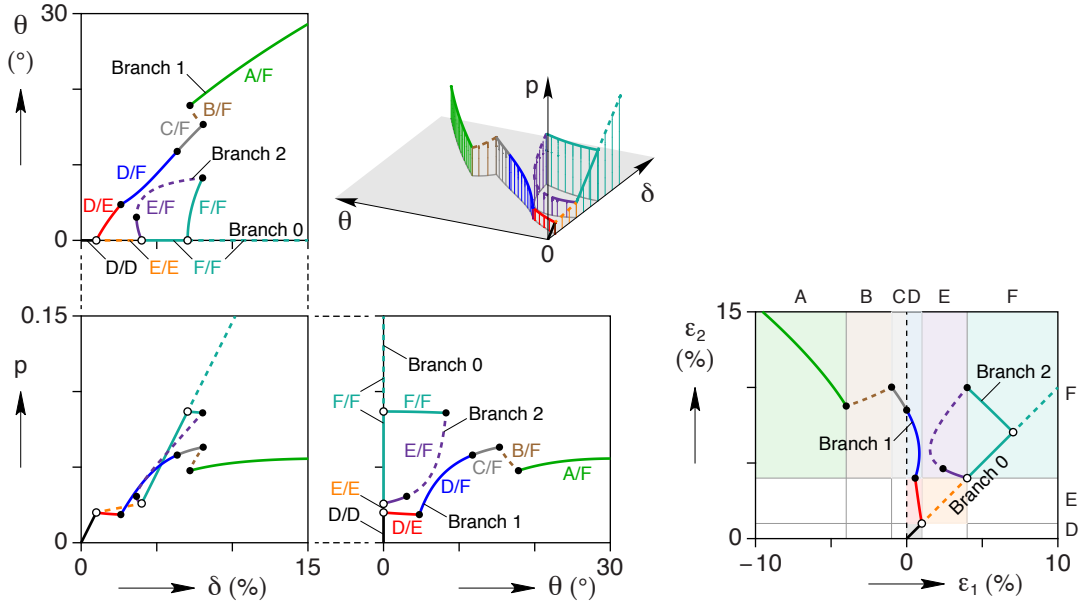

(a) Three projections and isometric view of equilibrium paths (b) Spring responses

Figure 4.7: "Long" Shanley columns ($\ell = 4.8$ shown) buckle along Branch 1 after the first bifurcation with no return to the principal path.

Section 4.4.

The reasons for unbuckling can be deduced by comparing the ε_1-ε_2 spring responses of the long and midlength columns, Figures 4.7b and 4.8b, respectively. In both cases, buckling initiates due to the softening of the tangent moduli in the spring responses at the end of the *D/D* segment ($\varepsilon_1 = \varepsilon_2 = \alpha$). Upon buckling, Spring 1 unloads along segment D, while Spring 2 loads along softer segment E. This mismatch in spring tangent stiffnesses enhances the clockwise moment to produce the rotated (buckled) configuration. Upon continued loading, Spring 2 eventually stiffens as it reaches the onset of segment F; initially, this also causes Spring 1 to load somewhat. After this point, however, the behaviors of the long and midlength columns differ. For the long column, Spring 1 reaches a maximum strain and then begins to unload again, while Spring 2 continues to load monotonically. For the midlength column, by contrast, Spring 1 is able to reach the onset of segment E where its tangent modulus softens. The stiffness mismatch with Spring 2 creates an incremental restoring (counter-clockwise) moment that arrests the rotation and reverses it. Thus, while buckling is caused by the softening in Spring 2 (while Spring 1 remains stiff), unbuckling is caused by the softening in Spring 1 (while Spring 2 remains stiff). The reason Spring 1 in the shorter midlength column was able to load into segment E was due to the lesser incremental applied moment coming from the reaction at the top end.

Without this analysis, it would have been natural to conclude that unbuckling occurs simply

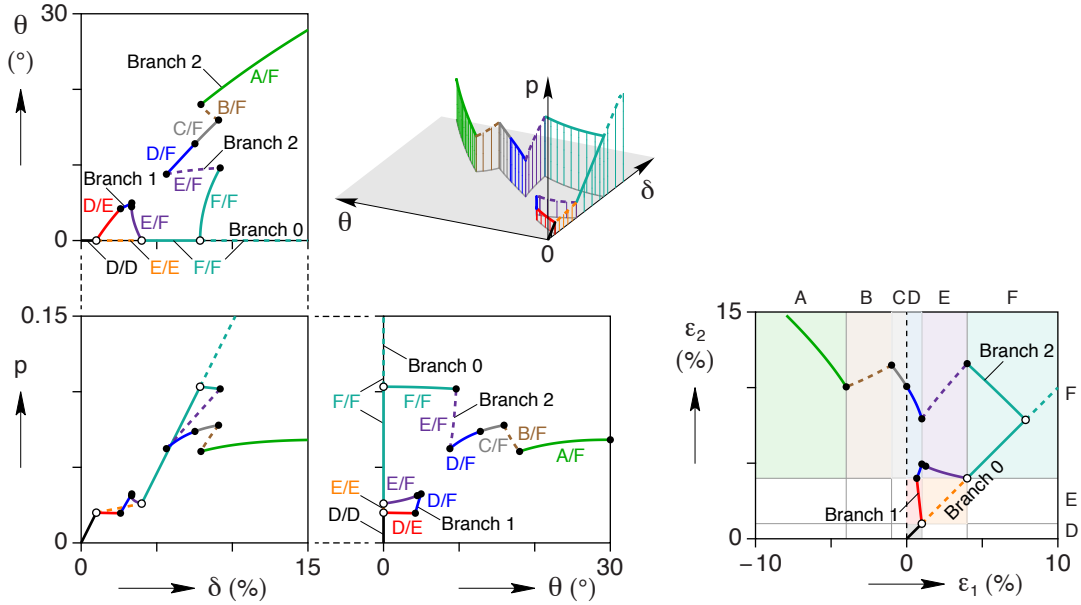

(a) Three projections and isometric view of equilibrium paths (b) Spring responses

Figure 4.8: "Midlength" Shanley columns ($\ell = 4.4$ shown) buckle-unbuckle stably along Branch 1, followed by buckling along Branch 2 at large strains.

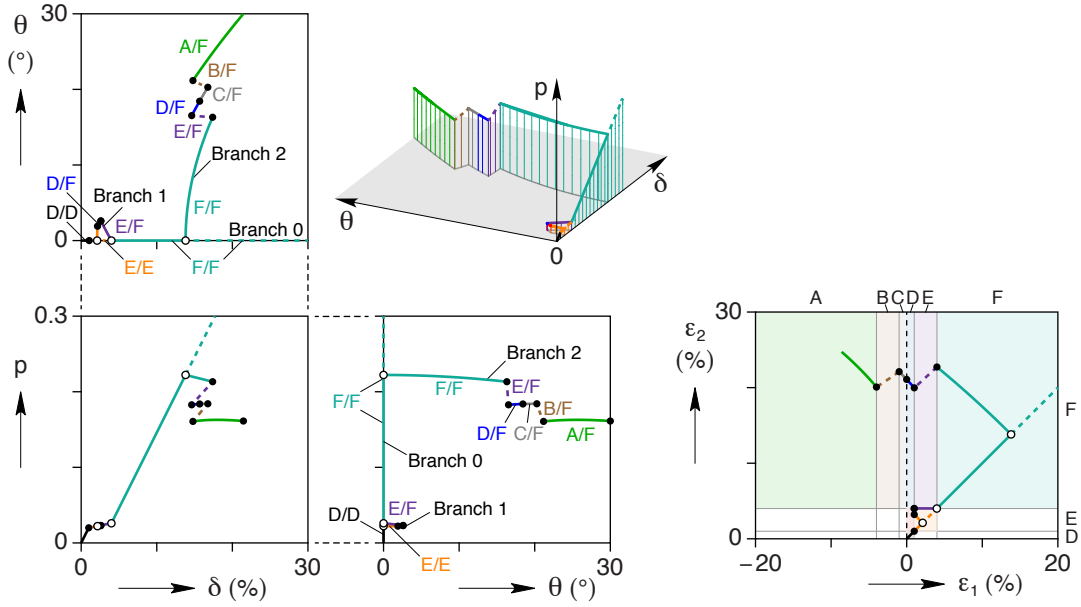

(a) Three projections and isometric view of equilibrium paths (b) Spring responses

Figure 4.9: "Short" Shanley columns ($\ell = 3.0$ shown) buckle to Branch 1 within the soft spring regime (*E/E*), unbuckle back to the principal path, and subsequently buckle a second time along Branch 2 at large strains.

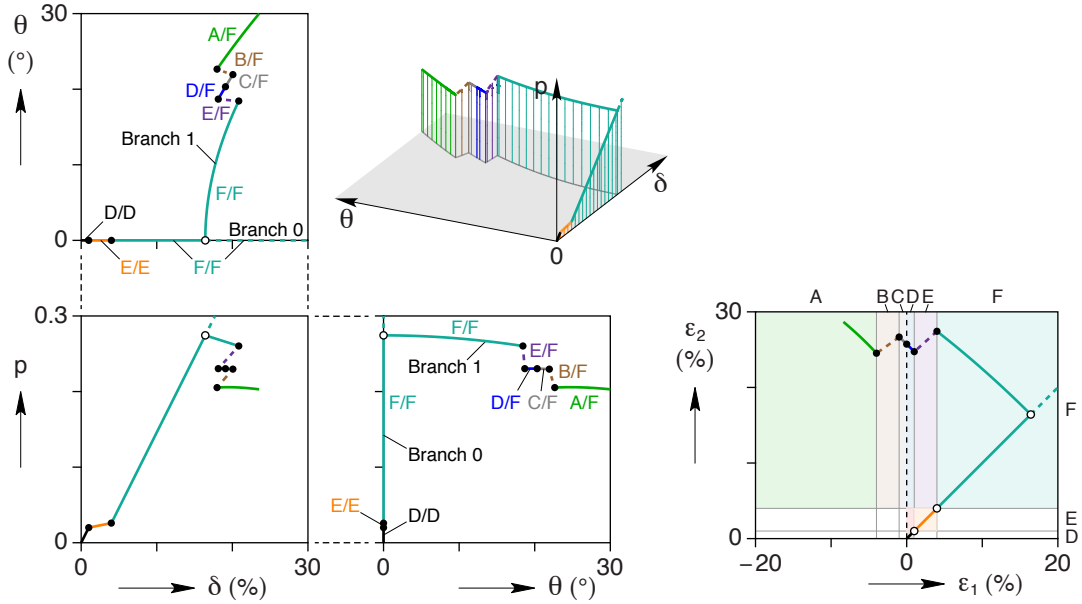

(a) Three projections and isometric view of equilibrium paths (b) Spring responses

Figure 4.10: "Very short" Shanley columns ($\ell = 2.7$ shown) buckle at large spring strains from the first (and only) bifurcation with no return to the principal path.

due to the late stiffening in the constitutive law (segment F), but this is inaccurate. Late stiffening in the constitutive law is not a sufficient condition for unbuckling. A special combination of both geometry and nonlinear material behavior is necessary to induce softening of one spring (transition from segment D to E) while having a stiff response in the other spring. It would be more correct to say that the existence of buckling-unbuckling requires just the right sequencing of softening in the two springs, along with the late stiffening.

As noted previously, the long column in fact has two secondary equilibrium branches, one that corresponds to the post-buckling path (Branch 1) and another that is never reached (Branch 2), albeit attached at two bifurcation points to the principal branch at large strains (Figure 4.7b). Although both secondary branches are attached to Branch 0, they are disjoint to one another. Repeating the simulation (not shown) at a slightly reduced aspect ratio (length) results in the two branches moving towards eachother. Eventually, the two segments touch each other at a tangency point as the length of the column is reduced further. This special case, which occurs for $\ell_{\max} \approx 4.61$ for the material parameters chosen here, is shown in Figure 4.11. This represents the highest aspect ratio $\ell_{\max}$, or upper bound, for columns that can unbuckle. As the aspect ratio is reduced further yet, one can imagine the branches would overlap, but instead the equilibrium segments annihilate one another wherever they would overlap. This effectively splits Branches 1 and 2 for the long column into two segments for the midlength column, creating two new secondary branches consisting of pieces of each of the original ones. The new Branch 1 (as in Figure 4.8b) is now attached

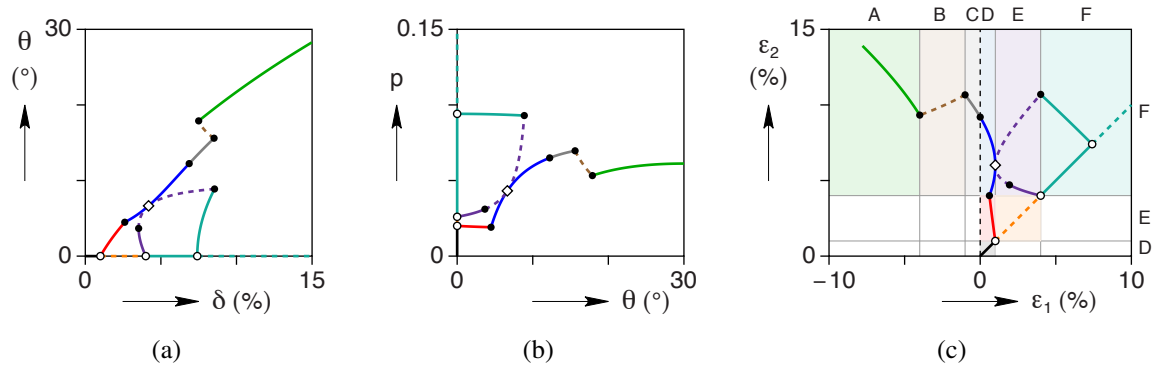

Figure 4.11: At a critical length ($\ell_{\text{max}} = 4.610$ shown), the secondary branches in the response of the Shanley column share a common tangent point (open diamond).

at two bifurcation points to the principal branch, thereby creating a looping path for buckling then unbuckling.

As the length of the column is reduced further (see Figure 4.9), the first bifurcation occurs later, within *E/E*. Although buckling-unbuckling still exists, the size of the loop and maximum rotation attained are less than that of somewhat longer columns. Eventually, the size of the loop collapses entirely in sufficiently (very) short columns (Figure 4.10) and no buckling-unbuckling occurs. Somewhere between these two cases, a lower bound ℓ_{min} exists, below which unbuckling is not possible.

As can be seen in Figures 4.7 to 4.10, each equilibrium branch consists of various stable and unstable segments. Most of the changes in stability are associated with the transitions (kinks) in the spring constitutive behaviors, but not all. The two exceptions are (1) segment *F/F* of the principal branch, which eventually loses stability at sufficiently large strains in all columns (Euler-like buckling), and (2) loss of stability midway in segment *E/F* of Branch 2 in long columns, although this is not a realizable path from zero load. All stability results shown so far assumed δ-control (Eq. (4.16a)), i.e., stability with respect to a 'hard' loading device; however calculations for stability with respect to p–control (Eq. (4.16b)) were also conducted, i.e. stability with respect to a 'soft' loading device. Although explicit results are not shown here, the stability of several paths under load control are found to differ from displacement control: segment *F/F* becomes unstable when present, segment *E/E* becomes unstable for the short column ($\ell = 3$), and segments *D/E* and *E/F* becomes unstable for midlength ($\ell = 4.4$) and long ($\ell = 4.8$) columns (since *E/F* is the segment involved in unbuckling, it is unlikely unbuckling would ever be observed in load-control).

The introduction of a geometric imperfection ($\theta_0 \neq 0$) can significantly alter the response of the column, including elimination of the possibility for unbuckling. As an example, responses of

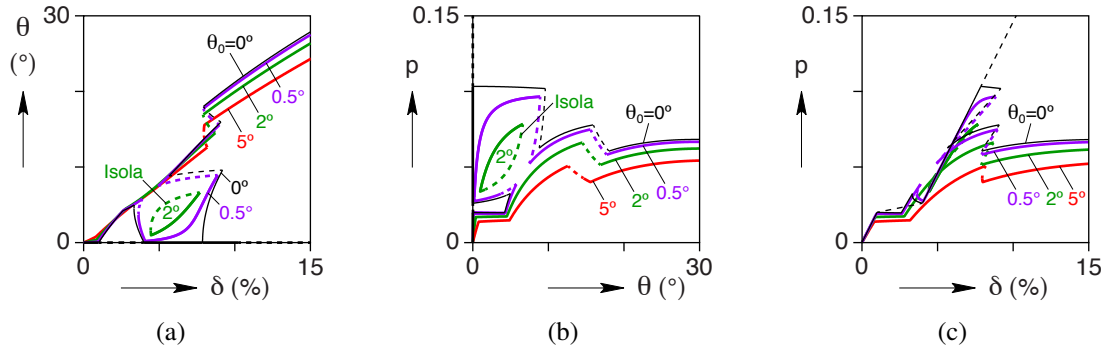

Figure 4.12: Increasing the geometric imperfection (θ_0) in "midlength" Shanley columns ($\ell = 4.4$ shown) causes the column structural response to transition from buckling-unbuckling to monotonic buckling.

the midlength column ($\ell = 4.4$) for several imperfections are shown in Figure 4.12. For small imperfections (see the case $\theta_0 = 0.5^{\circ}$), the column buckles-unbuckles similar to the perfect column; however, with a large imperfection ($\theta_0 = 5^{\circ}$), the response resembles that of a long column without unbuckling. For intermediate imperfections (see $\theta_0 = 2^{\circ}$), interestingly, an isolated equilibrium loop, or *isola*[2], appears, although the unbuckling path never traverses it (see Dellwo et al. [1982] for more information on *isola bifurcations*).

4.3.2 Comparison to Experimental Results

Two column buckling experiments on the NiTi rod were chosen to evaluate the performance of the Shanley column: $\overline{L} \equiv L/D$ of 6.3 and 5. These aspect ratios were selected to mimic the behavior of the long and midlength Shanley columns discussed in Section 4.3.1. The axial compressive strain (Δ_e/L), normalized midspan lateral displacement (δ_r/L), compressive engineering stress (P/A_0), and midspan outer-fiber strains (ε_1 and ε_2) roughly correspond to the respective end-displacement (δ), rotation (θ), axial load (p) and spring displacements (ε_1 and ε_2) of the Shanley column, respectively, and were therefore chosen as metrics for comparison. To enable a more realistic comparison with the experimental results, the Shanley model was given a small geometric imperfection $\theta_0 = 0.5°$.

The qualitative agreement of the model and experiments is quite good (Figures 4.13 and 4.14), with the simulations exhibiting all the relevant features of the experimental behavior. For long columns, the experiment and model both show a relatively monotonic post-buckling response in the lateral deflection (δ_r/L) and rotation (θ), although the model also predicts the existence of an

[2]Italian for *island*.

isola that would never be reached (Figures 4.13a and 4.13b). The axial load responses, whether plotted against lateral deflection–rotation (Figures 4.13c and 4.13d) or axial strain (Figures 4.13e and 4.13f), show up-down-up-down behaviors, which are predicted reasonably well by the model (albeit with sharper corners); likewise, the general shapes of bending/spring strain response curves correspond nicely (Figures 4.13g and 4.13h). For midlength columns, the SMA rod and model buckle, unbuckle, and then buckle again at higher loading (Figure 4.14). The good comparison between the model simulations and the experiments provides convincing evidence that the model captures the underlying mechanisms responsible for unbuckling (and superelastic column buckling in general).

The critical (upper bound) aspect ratio $\overline{L}_{\text{max}}$ for unbuckling was experimentally determined for SMA columns by bracketing the value between two experiments, where one exhibited unbuckling but the other did not. For the tube, a limited amount of material was available, so only a few column aspect ratios were examined. It was found that a $\overline{L} = 7.33$ tube unbuckled, while a $\overline{L} = 9.92$ tube did not; thus, the critical value for the SMA tube lies somewhere in between, with an estimated value of $\overline{L}_{\text{max}}^{\text{tube}} = 8.6 \pm 1.3$. More material was available for SMA rod specimens, so a larger number of experiments were performed to better refine the bracket for the critical aspect ratio. In the performed experiments, an experiment on a $\overline{L} = 5.49$ rod unbuckled, while another experiment on a $\overline{L} = 5.52$ rod did not, thereby giving a reasonably tight estimate for the SMA rod of $\overline{L}_{\text{max}}^{\text{rod}} = 5.50 \pm 0.02$. Although the rod and tube had slightly different material properties, the disparate results by over 50 % suggests that unbuckling depends on the cross-sectional geometry as well as the aspect ratio. It should be emphasized that these results were for clamped-clamped boundary conditions, which would be different if other boundary conditions were used.

To compare the experiment and simulation results somewhat more quantitatively, I sought to determine a correspondence between the aspect ratio of the Shanley column and the geometry of the SMA specimens used in the experiments. The SMA column experiments were performed using clamped-clamped boundary conditions, rather than the simply supported conditions as originally envisioned by Shanley, so 'plastic' hinges tended to form at the midspan and at both ends, as was seen in Figure 4.3c. This suggests a simple equivalence, in which the Shanley column represents 1/4 of the experimental specimen based on symmetry about the midspan and the expected inflection points of the buckling mode at $z = L/4, 3L/4$ (see Figure 4.15). Thus, the length of the Shanley column corresponds to $b = L/4$.

Unfortunately, in the simplification from a beam-column to the Shanley column, the cross-sectional information is lost; however, an understanding of beam deformation can be used to guide the choice of the Shanley column halfwidth a to appropriately represent beam–columns. The following are three possibilities:

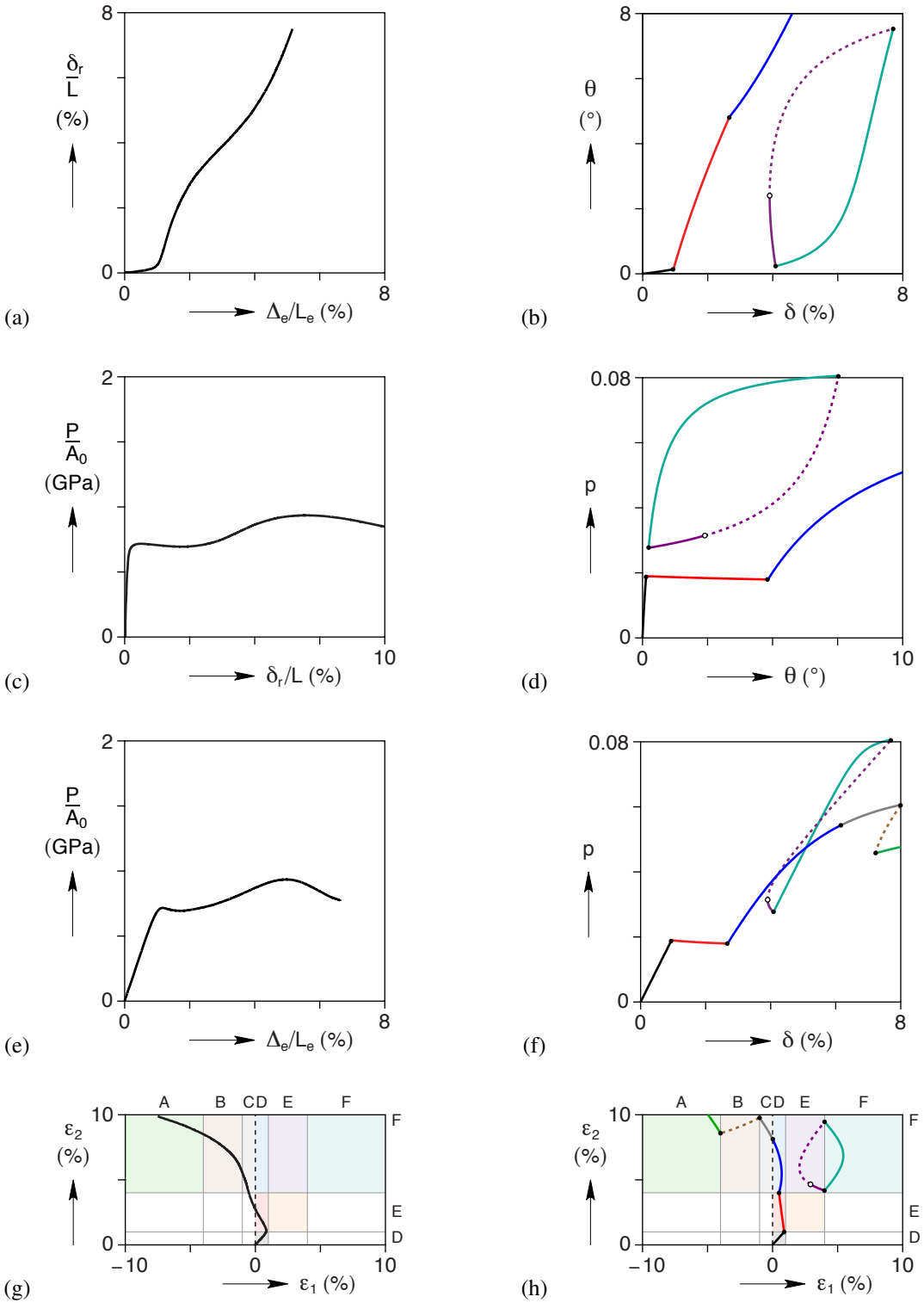

Figure 4.13: A comparison of experimental measurements [(a), (c), (e), and (g)] and model simulations [(b), (d), (f), and (h)] for "long" columns (SMA rod $L/D = 6.3$; Shanley model $\ell = 4.8$, $\theta_0 = 0.5^{\circ}$) shows good qualitative agreement with monotonic post-buckling deflections.

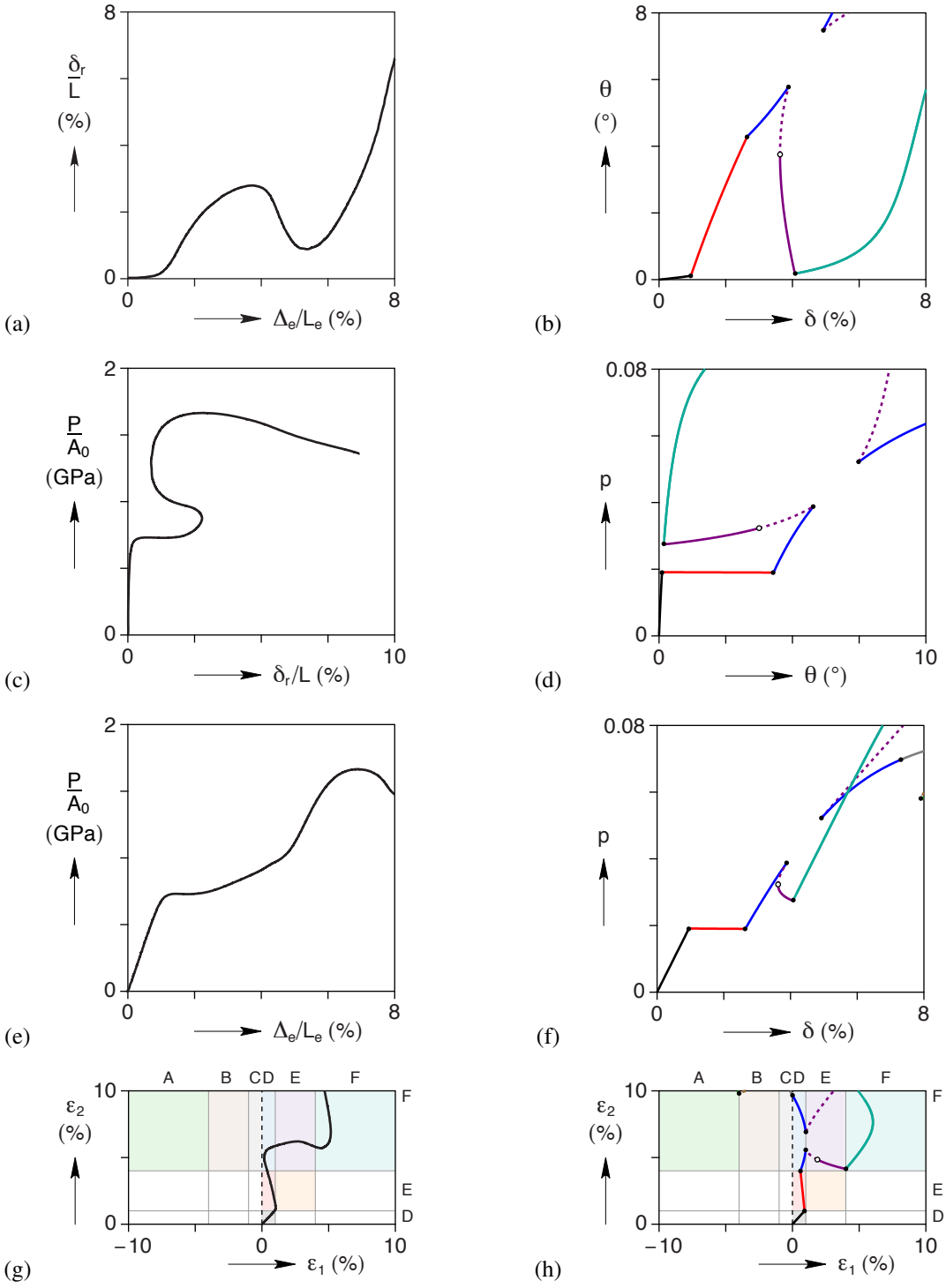

Figure 4.14: A comparison of experimental measurements [(a), (c), (e), and (g)] and model simulations [(b), (d), (f), and (h)] for "midlength" columns (SMA rod $L/D = 5.0$; Shanley model $\ell = 4.4$, $\theta_0 = 0.5^{\circ}$) shows good qualitative agreement with buckling-unbuckling.

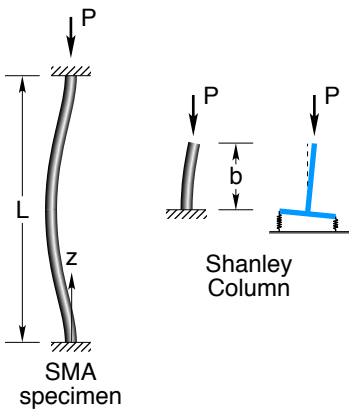

Figure 4.15: The Shanley column of length b (clamped-free boundary conditions) is roughly equivalent to $1/4$ the length of the experimental SMA specimens (clamped-clamped boundary conditions).

1. One could simply imagine the Shanley springs at the outer radius of the beam column, or

$$a = \frac{D}{2}, \tag{4.18}$$

since this is where the magnitudes of the bending strains are greatest. This might be reasonable for the SMA tube, but less so for the SMA rod since a larger fraction of the axial load is supported by stress near the central axis.

2. One could use the radius of gyration of the cross-section as a characteristic width. The radius of gyration is defined as $r = \sqrt{I_0/A_0}$, where I_0 and A_0 are the reference bending moment of inertia and reference area of the cross-section, respectively. In this view $a = r$, giving

$$a = \begin{cases} \dfrac{D}{4} & : \text{rod}, \\ \dfrac{D}{4}\sqrt{2 - 2h + h^2} & : \text{tube}, \end{cases} \tag{4.19}$$

where $h = 2H/D$ is the normalized tube wall thickness based on the outer radius. This approach is consistent with buckling in the linear elastic range of material behavior, so one expects it would give a reasonable estimate for linear elastic (Euler) buckling but not for buckling of nonlinear materials.

3. Alternatively, one could define a characteristic half-width dimension $a = M/(F_1 - F_2)$, where M is the bending moment and F_1 and F_2 are resultant forces acting on each half area of the cross-section (A_1 and A_2, respectively). The actual stress distribution in the cross-section is unknown due to the complex material behavior of SMAs, but Figures 4.13g and 4.14g

both show that at the onset of buckling one side of the column unloads elastically (in D) while the other loads along the soft segment (in E). At this point the nominal compressive strain is $\varepsilon = \alpha + y\kappa$ as bending begins, where y is the lateral buckling direction and κ is the bending curvature. Incrementally, this creates a piecewise linear stress distribution: $\Delta\sigma_1 = Ey\Delta\kappa$ on the unloading side (in A_1), and $\Delta\sigma_2 = \eta Ey\Delta\kappa$ on the loading side (in A_2). The incremental moment is $\Delta M = \int_A y\Delta\sigma \, \mathrm{d}A$ and the incremental force difference is $\Delta F_1 - \Delta F_2 = \int_{A_1} \Delta\sigma_1 \, \mathrm{d}A - \int_{A_2} \Delta\sigma_2 \, \mathrm{d}A$. Taking the ratio and simplifying leads to the characteristic half-width $a = I_1/Q_1$, where $Q_1 = \int_{A_1} y \, \mathrm{d}A$ and $I_1 = \int_{A_1} y^2 \, \mathrm{d}A$ are the first and second area moments, respectively, of half of the cross-section. This definition gives

$$a = \begin{cases} \dfrac{3D}{32\pi} & : \text{rod}, \\ \dfrac{3D}{32\pi}\left[\dfrac{4 - 6h + 4h^2 - h^3}{3 - 3h + h^2}\right] & : \text{tube}. \end{cases} \tag{4.20}$$

For a clamped-clamped column with length L and outer diameter D, the aspect ratio of the real column ($\overline{L}$) is related to the Shanley column model through the relationship

$$\overline{L} = \frac{L}{D} = \frac{4b}{D} = 4\bar{a}\ell, \tag{4.21}$$

where $\bar{a} = a/D$ relates the half width of the Shanley column (a) to the outer diameter of the real column (D) through one of the options listed above, (Eqs. (4.18) to (4.20)). Using our baseline material parameters $\alpha = 1\,\%$, $\beta = 3\,\%$, and $\eta = 10\,\%$, $h = 1/5$ for the tube, and $\ell_{\text{max}} = 4.610$, the predicted critical aspect ratios from the Shanley model are provided in Table 4.2. In general, the concentrated-forces method (Eq. (4.20)) gives a good estimate for the rod, while concentrated-forces and the outer radius methods (Eqs. (4.18) and (4.20)) reasonably bracket the range for the tube.

Table 4.2: The concentrated forces representation of the rod (using Eq. (4.21)) nearly predicts the experimentally measured upper bound on column aspect ratio for unbuckling ($\overline{L}_{\text{max}}$); whereas, the outer radius and concentrated forces representations of the tube bracket $\overline{L}_{\text{max}}$.

		Calculated from the Shanley model		
	Measured $\overline{L}_{\text{max}}$	Outer Radius	Radius of Gyration	Concentrated Forces
Rod	5.5	9.2	4.6	5.4
Tube	between (7.3, 9.9)	9.2	5.9	6.6

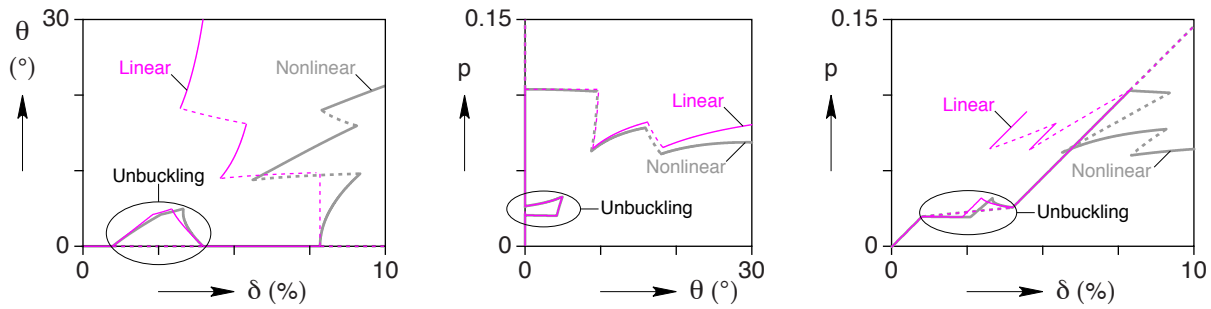

Figure 4.16: Comparison of linear and nonlinear kinematics for a "midlength" Shanley column ($\ell = 4.4$), showing similar results in the unbuckling region ($\theta < 5°$, $\delta < 4\,\%$).

4.4 Design of Columns that Unbuckle

Finally, a parametric study is performed to map the 'design space' of columns, in terms of the geometry (ℓ and θ_0) and material parameters (α, β, η), for which buckling-unbuckling occurs. Figure 4.16 shows a comparison of calculated equilibrium paths from the superelastic Shanley model using both linear and nonlinear kinematics. Clearly, the secondary branches at large rotations and strains are significantly different, but this regime of loading is of little concern to unbuckling behavior. In the case of the moderate rotations and strains ($\theta < 5°$, $\delta < 4\,\%$) associated with unbuckling, there is little difference between the linear and nonlinear kinematics and no essential features are lost (as might generally be the case for nonlinear problems). Thus, the following analysis will be done using linear kinematics, from which closed-form relations can be more conveniently found.

As was mentioned, the transition from unbuckling behavior in a midlength column (Figure 4.8) to monotonic buckling in a long column (Figure 4.7) indicates the existence of an upper-bound on column aspect ratio for unbuckling to occur. The limiting case between these two was shown in Figure 4.11, for which the two secondary branches just touch at a common point. This occurs when $\delta_{D/F} = \delta_{E/F}$ at a single θ, where,

$$\delta_{D/F} = \frac{1}{\ell^2} + \frac{\beta(1-\eta)(\ell\theta - 1)}{2\ell\theta}, \tag{4.22a}$$

$$\delta_{E/F} = \frac{\ell^2(\beta-\alpha)(1-\eta)\theta + (1+\eta)\theta - \ell(1-\eta)\left(\alpha+\beta+\theta^2\right)}{\ell\left[\eta - 1 + \ell(1+\eta)\theta\right]}, \tag{4.22b}$$

using linear kinematics. This corresponds to a cubic equation with three roots. The first root is

$\theta = -1/\ell$, which does not apply since $\ell > 0$ and $\theta \geq 0$ was assumed. The remaining roots are

$$\theta = \frac{1 + \ell^2\left(\bar{\beta} - \alpha\right)}{2\ell} \pm \sqrt{\left[\frac{1 + \ell^2\left(\bar{\beta} - \alpha\right)}{2\ell}\right]^2 - \bar{\beta}}, \tag{4.23}$$

where $\bar{\beta} = (1 - \eta)\beta/2$ has been defined for convenience. When the quantity inside the radical is less than zero, the solutions are imaginary, indicating that no unbuckling is possible. When the radical quantity is greater than zero, two unique positive solutions for θ exist, which correspond to points on the overlapping (in δ) secondary branches seen in Figures 4.8 and 4.9, and unbuckling occurs. When the radical is exactly zero, the two solutions collapse to the same θ, which is the limiting case for unbuckling. Solving the resulting bi-quadratic equation for ℓ^2 and, taking the positive root, gives the following relation for the upper-bound on column aspect ratio:

$$\ell_{\text{max}} = \frac{1}{\sqrt{\alpha} + \sqrt{\bar{\beta}}}. \tag{4.24}$$

Using our baseline material parameters, this calculates to $\ell_{\text{max}} = 4.626$ (based on linear kinematics), which is quite close to 4.610 that was (numerically) found using nonlinear kinematics.

If the system has a geometric imperfection ($\theta_0 > 0$), the critical aspect ratio generalizes to

$$\hat{\ell}_{\text{max}} = \frac{1}{\sqrt{\alpha} + \theta_0/2 + \sqrt{\left(\theta_0/2\right)^2 + \theta_0\sqrt{\alpha} + \bar{\beta}}}. \tag{4.25}$$

This upper bound for the imperfect geometry (as denoted by the caret in $\hat{\ell}_{\text{max}}$) is always less than for the perfect geometry (Eq. (4.24)) and Eq. (4.25) is a monotonically decreasing function with increasing imperfection as shown in Figure 4.17. To gain a sense of the imperfection sensitivity, an imperfection angle of $2°$ results in a decrease in ℓ_{max} by $13\,\%$ and an imperfection of $4°$ results in a decrease of $23\,\%$.

A lower bound also exists on the column aspect ratio for unbuckling to occur, since the short column (Figure 4.9) buckled-unbuckled but the very short column (Figure 4.10) did not. The case delimiting these two behaviors is when the principal branch first remains stable in *E/E* as the aspect ratio is decreased. Stability of the principal branch was established previously in Figure 4.6, where the largest aspect ratio for *E/E* to be completely stable was 2.77 for our material parameters, which according to Eq. (4.17) was

$$\ell_{\text{min}} = \sqrt{\frac{\eta}{\alpha + \beta\eta}}. \tag{4.26}$$

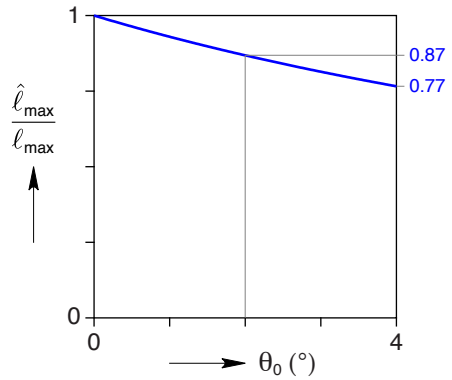

Figure 4.17: The upper bound on the Shanley column aspect ratio $\hat{\ell}_{max}$ for unbuckling to exist is a monotonically decreasing function of increasing geometric imperfection θ_0.

This defines the lower-bound on the column aspect ratio for unbuckling in perfect columns. In the case of an imperfect system, however, the lower-bound is zero ($\hat{\ell}_{min} = 0$) as a small degree of unbuckling is always present in short columns.

Since $\hat{\ell}_{min}$ is zero for an imperfect column, ℓ_{max} is the only parameter of practical importance when designing a column to unbuckle. Based on the relationship for ℓ_{max} (Eq. (4.24)), the feasible design space for perfect columns is shown in Figure 4.18. For a column aspect ratio $\ell = 4$, for example, all materials that lie within the shaded region (sufficiently small α and $\bar{\beta}$) exhibit unbuckling behavior; for real columns that are imperfect, the design space is slightly smaller, since $\hat{\ell}_{max} \leq \ell_{max}$. As ℓ_{max} increases, the feasible region shrinks significantly as shown in Figure 4.18. In the case of superelastic NiTi materials, the Shanley column aspect ratio must be less than about 4.5 to exhibit unbuckling behavior. Since other nonlinear materials have stiff-soft-stiff behavior (like elastomeric materials), or even just soft-stiff (bilinear) behavior where $\alpha \approx 0$ (like biological tissue), it seems possible that column unbuckling might also manifest in other materials; however, due to the strong material parameter restrictions on unbuckling, it seems unlikely, since most of these materials tend to stiffen only at very large strains (i.e., large β), thereby requiring an aspect ratio that would be too small to be of practical use in a column.

Although all imperfect columns with aspect ratios less than $\hat{\ell}_{max}$ unbuckle, the amplitude of unbuckling (that is, the peak rotation along the unbuckling path) decreases with decreasing aspect ratio. For a given aspect ratio, the maximum rotation (θ_{max}) occurs at the start of the return path to the principal solution, which always occurs at the start of path *E/F*. This point depends on the

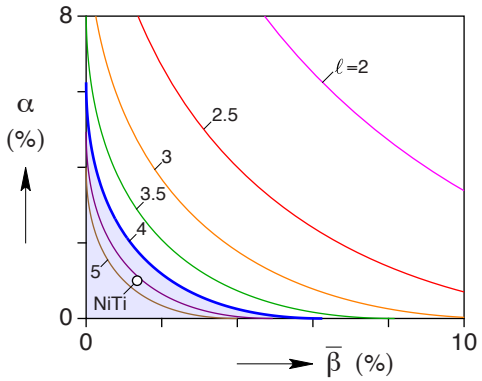

Figure 4.18: For a selected column aspect ratio ℓ, the design space of material parameters for unbuckling is below the applicable curve according to Eq. (4.24). The feasible space for $\ell = 4$ is shaded, and the design space shrinks as the aspect ratio of the column increases.

aspect ratio of the column, leading to the two relations

$$2\theta_{\max} = \begin{cases} \frac{\ell}{\ell_{\min}^2} - \frac{1}{\ell} - \theta_0 + \sqrt{\left(\frac{1}{\ell} + \frac{\ell}{\ell_{\min}^2} + \frac{2}{\ell_{\min}} + \theta_0\right)\left(\frac{1}{\ell} + \frac{\ell}{\ell_{\min}^2} - \frac{2}{\ell_{\min}} + \theta_0\right)} & : \hat{\ell}_{\min} \le \ell < \ell^* \\ \dfrac{1 + \ell^2\left(\bar{\beta} - \alpha\right)}{\ell} - \theta_0 - \sqrt{\left(\dfrac{1 + \ell^2\left(\bar{\beta} - \alpha\right)}{\ell} + \theta_0\right)^2 - 4\left(\bar{\beta} + \dfrac{\theta_0}{\ell}\right)} & : \ell^* \le \ell \le \hat{\ell}_{\max} \end{cases} \tag{4.27}$$

where

$$\ell^* = \sqrt{\left(\frac{2\eta}{2\alpha + \beta\eta}\right)^2 + \left(\frac{\theta_0}{\beta}\right)^2} - \frac{\theta_0}{\beta}. \tag{4.28}$$

The best case $\theta_{\max} = \sqrt{\bar{\beta}}$ occurs at $\ell_{\max}$ when $\theta_0 = 0$ and decreases monotonically to zero at $\ell_{\min}$ (Figure 4.19). Thus, to maximize the "stroke" of unbuckling columns should be as close to $\ell_{\max}$ as possible. Furthermore, since $\bar{\beta} = (1 - \eta)\beta/2$, the plateau length ($\beta$) and relative stiffness (η) are the dominant parameters affecting $\theta_{\max}$, with the optimum stroke corresponding to maximum β and minimum η.

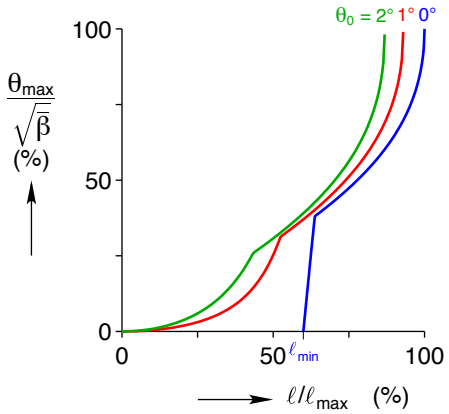

Figure 4.19: The peak rotation of unbuckling, $\theta_{\max}$, is maximum at an aspect ratio of $\ell = \hat{\ell}_{\max}$ and decreases monotonically to zero at an aspect ratio of $\ell = \hat{\ell}_{\min}$.

4.5 Summary & Conclusions

Defined as the return of a buckled structure to the principal path under monotonic loading, unbuckling has been found in the literature to occur in the inflation of balloons, column buckling and the wrinkling of thin sheets. Column buckling of superelastic shape memory alloy columns was used here as a lens into the underlying mechanisms of unbuckling behavior. A modified Shanley column was developed to model unbuckling behavior, using a trilinear material response to represent the superelastic response of shape memory alloys. The explicit solutions of the proposed model exhibited unbuckling behavior and agreed well with experimental results on NiTi columns. It was also found that stiffening late in the material response is a sufficient condition for unbuckling to occur given the appropriate kinematic conditions. Applying the model, a relationship was developed for the design of columns which unbuckle, relating the necessary geometry of the column to material behavior. Materials such as shape memory alloys can therefore be used in the development and design of novel structures which functionally unbuckle.

Chapter 5

Superelastic Beam Modeling

In Chapter 4, a Shanley column model with trilinear spring behavior successfully captured the unbuckling behavior of superelastic SMA columns; furthermore, the model replicated many of the general qualitative characteristics of superelastic column buckling behavior (Figures 4.13 and 4.14). Unfortunately, the simplicity of the two degree of freedom model did not accurately capture the quantitative behavior of the column. The trilinear spring material law is therefore generalized here from the two degree of freedom system to the continuum level to more accurately model quantitative behavior.

Continuum level material models are usually developed in the context of thin-walled (beams, frames and shells), two dimensional (plane stress or strain) or fully three dimensional structures. In the context of SMAs, the majority of current applications consist of thin–walled structures, motivating the extension of the Shanley column model of Chapter 4 to a thin-walled framework; furthermore, due to the focus on beam and framed structures here, a model based on beam theory is developed.

In this chapter, a simple SMA beam model is presented. The model framework is discussed in Section 5.1, outlining the kinematics of deformation (Section 5.1.1), equilibrium (Section 5.1.2), and the generalization of the trilinear material model (Section 5.1.3). The implementation details in the context of the finite element method are then discussed in Section 5.2, focusing on the beam element formulation (Sections 5.2.1 and 5.2.2), issues with numerical integration (Section 5.2.3), and loss of ellipticity of the model when using an up–down–up tensile response (Section 5.2.4).

5.1 Beam Model

A model is developed to capture the large rotation bending and the superelastic properties of SMA beams. Within the development of the model, a balance is struck between accuracy and efficiency:

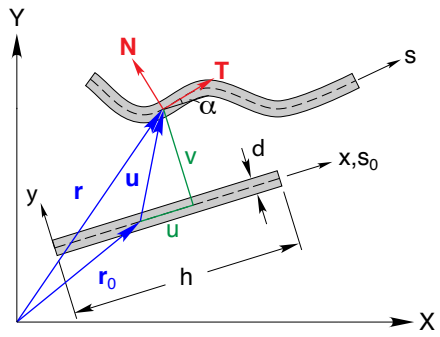

Figure 5.1: Fully nonlinear kinematics of an SMA beam defined in two coordinate frames: the local frame of the beam (x-y) and the global coordinate system (X-Y).

kinematically exact deformations fully capture the general large deformations of SMAs and their structural stability characteristics, while a phenomenological SMA material model efficiently captures the stress-induced phase transformation behavior of superelastic SMAs.

5.1.1 Kinematics

In defining the kinematics for the model, it is important to capture both the large rotation bending of SMA beams and the overall stability characteristics of the structure. As the linearized kinematics of traditional beam theory are insufficient for these purposes, the kinematically exact extensible elastica model (comparable to Reissner [1972], Magnusson et al. [2001], Humer [2011]) is adopted. Within this framework, cross-sectional planes are assumed to remain plane and normal to the deformed centerline of the beam (i.e., the Euler Bernoulli assumption), restricting the model application to slender beams.

The deformation kinematics are developed within the context of an initially flat beam with length h and thickness d (Figure 5.1). The position vector of the beam centerline in the reference configuration is

$$\mathbf{r}_0(s_0) = X(s_0)\,\mathbf{e}_I + Y(s_0)\,\mathbf{e}_J, \tag{5.1}$$

where s_0 is the arc length parameter of the beam with respect to the reference configuration, and $\mathbf{e}_I$ and $\mathbf{e}_J$ are orthonormal vectors corresponding to the global X-Y frame[1]. For a given displacement, $\mathbf{u} = u\,\mathbf{e}_i + u\,\mathbf{e}_j$, where $\mathbf{e}_i$ and $\mathbf{e}_j$ are orthonormal vectors corresponding to the local x-y frame, the

[1] All variables with the subscript 0 refer to the reference configuration.

position vector of the current configuration centerline is

$$\mathbf{r} = \mathbf{r}_0 + \mathbf{u}. \tag{5.2}$$

Of primary importance to the beam deformation are the centerline stretch ratio

$$\lambda \equiv \frac{\mathrm{d}s}{\mathrm{d}s_0} = \left\|\mathbf{r}'\right\| \tag{5.3}$$

and centerline curvature

$$\kappa \equiv \frac{\mathrm{d}\alpha}{\mathrm{d}s} = \frac{\mathrm{d}\mathbf{T}}{\mathrm{d}s} \cdot \mathbf{N}, \tag{5.4}$$

where

$$\mathbf{T}(s_0) = \frac{\mathbf{r}'(s_0)}{\left\|\mathbf{r}'(s_0)\right\|} \text{ and } \mathbf{N}(s_0) = \frac{\mathbf{T}'(s_0)}{\left\|\mathbf{T}'(s_0)\right\|} \tag{5.5}$$

are respectively the the unit tangent and normal vectors of the beam centerline in the current configuration. As κ is defined with respect to the current configuration, the relative centerline curvature

$$\hat{\kappa} \equiv \alpha'(s_0) = \mathbf{T}' \cdot \mathbf{N} \tag{5.6}$$

is defined to relate the curvature to the reference configuration. Since $\mathbf{T}$ and $\mathbf{N}$ are orthonormal vectors ($\|\mathbf{T} \times \mathbf{N}\| = 1$) and

$$\mathbf{T} \times \mathbf{N} = \frac{1}{\hat{\kappa}\lambda^2}\left(\mathbf{r}' \times \mathbf{r}''\right), \tag{5.7}$$

$\hat{\kappa}$ can be related to the position vector by

$$\hat{\kappa} = \frac{\left\|\mathbf{r}' \times \mathbf{r}''\right\|}{\lambda^2}. \tag{5.8}$$

Combining the definition of the position vector (Eq. (5.2)) with the stretch ratio and relative curvature definitions (Eqs. (5.3) and (5.8)),

$$\lambda = \sqrt{\left(1+u'\right)^2 + \left(v'\right)^2} \tag{5.9a}$$

$$\hat{\kappa} = \frac{\left(1+u'\right)v'' - v'u''}{\left(1+u'\right)^2 + \left(v'\right)^2}. \tag{5.9b}$$

The model is developed within the context of traditional beam theory assumptions, limiting its

scope to slender beams. This deformation and geometry type leads to a small strain, large rotation approximation of the kinematics of SMA beams where plane sections remain plane and normal to the deformed centerline. It should be noted that, although strain localization occurs under certain loading conditions in SMAs (such as tension and pure bending as discussed in Sections 2.3.1 and 2.3.3), the assumption that plane sections remain plane was found to be valid on average along the beam length as discussed in Section 2.3.3. Under these assumptions, and the geometry defined in Figure 5.1, the x and y displacement fields are respectively

$$\bar{u}(s_0, y) = u(s_0) - y \sin \alpha(s_0), \tag{5.10a}$$

$$\bar{v}(s_0, y) = v(s_0) - y(1 - \cos \alpha(s_0)) \tag{5.10b}$$

where $\bar{(.)}$ denotes a noncenterline quantity. From basic vector calculus, the trigonometric quantities $\sin \alpha$ and $\cos \alpha$ can be related to the centerline displacement fields through the relationships

$$\cos \alpha = \mathbf{T} \cdot \mathbf{e}_i = \frac{1 + u'}{\lambda} \tag{5.11a}$$

$$\sin \alpha = \|\mathbf{T} \times \mathbf{e}_i\| = \frac{v'}{\lambda}. \tag{5.11b}$$

Although the Lagrangian strain is commonly used in solid mechanics, the Biot strain is more convenient for the given kinematics. The Biot strain tensor is defined as

$$\mathbf{E}^B = \mathbf{U} - \mathbf{I}, \tag{5.12}$$

where $\mathbf{I}$ is the second order identity tensor, $\mathbf{U}$ is the right stretch tensor defined by

$$\mathbf{U} = \left(\mathbf{F}^T \mathbf{F}\right)^{1/2}, \tag{5.13}$$

and $\mathbf{F}$ is the deformation gradient tensor defined by

$$\mathbf{F} = \frac{\partial \bar{\mathbf{u}}}{\partial \mathbf{r}_0} + \mathbf{I}. \tag{5.14}$$

Combining Eqs. (5.10a), (5.10b), (5.11a) and (5.11b) with Eq. (5.12) results in the only nonzero strain

$$\varepsilon^{\mathrm{B}}_{\mathrm{ZZ}}(s_0, y) = e(s_0) - y\hat{\kappa}(s_0), \tag{5.15}$$

which corresponds to the axial strain, where $e \equiv \lambda - 1$ is the midline strain and y is the normal distance from the beam centerline.

5.1.2 Equilibrium

Due to the later implementation of the model within the context of a finite element formulation, equilibrium is defined in its weak form. From the principal of virtual work,

$$\delta W^I = \delta W^E, \tag{5.16}$$

where $\delta(.)$ defines a "virtual" quantity and δW^I and δW^E denote the internal and external virtual work on the system, respectively. For the chosen Biot strain measure, the internal virtual work is

$$\delta W^I = \int_0^h \int_A \mathbf{\Pi}^B : \delta \mathbf{E}^B \mathrm{d}A \, \mathrm{d}s_0, \tag{5.17}$$

where $\mathbf{\Pi}^B$ is the Biot Stress tensor and A corresponds to integration across the cross-sectional. The Biot stress is the work conjugate pair to the Biot strain measure and is defined by

$$\mathbf{\Pi}^B = \det(\mathbf{F})\mathbf{F}^{-1} \cdot \boldsymbol{\sigma} \cdot \mathbf{R}, \tag{5.18}$$

where $(.)^{-1}$ denotes a tensor inverse, $\boldsymbol{\sigma}$ is the Cauchy stress tensor, and $\mathbf{R}$ is the rotation tensor associated with the deformation gradient $\mathbf{F}$ such that, from the polar decomposition theorem,

$$\mathbf{R} = \mathbf{F} \cdot \mathbf{U}^{-1}. \tag{5.19}$$

Applying Eqs. (5.13), (5.14) and (5.19) to the definition of the Biot stress (Eq. (5.18)) results in a single nonzero stress component which corresponds to the axial engineering stress ($\sigma^{\mathrm{B}}_{\mathrm{ZZ}}$). The internal virtual work (Eq. (5.17)) therefore reduces to

$$\delta W^I = \int_0^h \int_A \sigma^{\mathrm{B}}_{\mathrm{ZZ}} \delta \varepsilon^{\mathrm{B}}_{\mathrm{ZZ}} \mathrm{d}A \, \mathrm{d}s_0, \tag{5.20}$$

Defining the axial force and bending moment as

$$N = \int_{-d/2}^{d/2} \sigma^{\mathrm{B}}_{\mathrm{ZZ}} w \, \mathrm{d}y \tag{5.21a}$$

$$M = \int_{-d/2}^{d/2} -\sigma^{\mathrm{B}}_{\mathrm{ZZ}} w y \, \mathrm{d}y, \tag{5.21b}$$

respectively, where w is the width of the cross-section at a location y through the thickness, Eq. (5.20) becomes

$$\delta W^I = \int_0^h \int_A (N\,\delta e + M\,\delta\hat{\kappa})\,\mathrm{d}A\,\mathrm{d}s_0. \tag{5.22}$$

Equilibrium is therefore defined by

$$\int_0^h \int_A (N\,\delta e + M\,\delta\hat{\kappa})\,\mathrm{d}A\,\mathrm{d}s_0 = \delta W^E, \tag{5.23}$$

where δW^E is dependent on the external loading of the beam. The resulting formulation corresponds to the exact definition of equilibrium, which is not always the case in nonlinear mechanics.

5.1.3 Constitutive Model

A phenomenological constitutive definition similar to that used in Chapter 4 is used to model the superelastic behavior of the SMA material. Figure 5.2a reports typical isothermal mechanical behavior for superelastic NiTi, highlighting the defining characteristics of superelastic SMA: large reversible deformation, hysteretic loading/unloading behavior, nonlinear stiffness, tension/compression asymmetry, and up–down–up tensile behavior (see Chapter 3). An asymmetric, hysteretic, trilinear material model is presented here with the focus of capturing these characteristics (see Figure 5.2b).

Superelasticity in SMAs is the result of a reversible stress induced phase transformation between the austenite and martensite phases, which is represented here with an internal variable formulation. The phase fraction (ξ) is defined such that $\xi \in [-1, 1]$, where $\xi = 0$ denotes the austenite phase, $\xi = 1$ denotes the tensile martensite phase, $\xi = -1$ denotes the compressive martensite phase, and $\xi \in (-1, 0) \cup (0, 1)$ denotes a mixture of phases[2]. The trilinear material model used here is broken into three parts (see Figure 5.2b): at low strains, the material is in the austenite phase and behaves according to the first linear branch ($\xi = 0$); at intermediate strains, a mixed phase material governs the behavior according to the second (hysteretic) linear branch ($\xi \in (-1, 0) \cup (0, 1)$); and, at high absolute strains, the material is in the martensite phase and behaves according to the last linear branch ($\xi = \pm 1$). When completely in the austenite or martensite phase (first or third branch), the material behavior is defined by Hooke's Law:

$$\sigma_A(\varepsilon) = E_A\varepsilon \tag{5.24}$$

[2]It is assumed here that the temperature is sufficiently high such that tensile and compressive martensite cannot coexist.

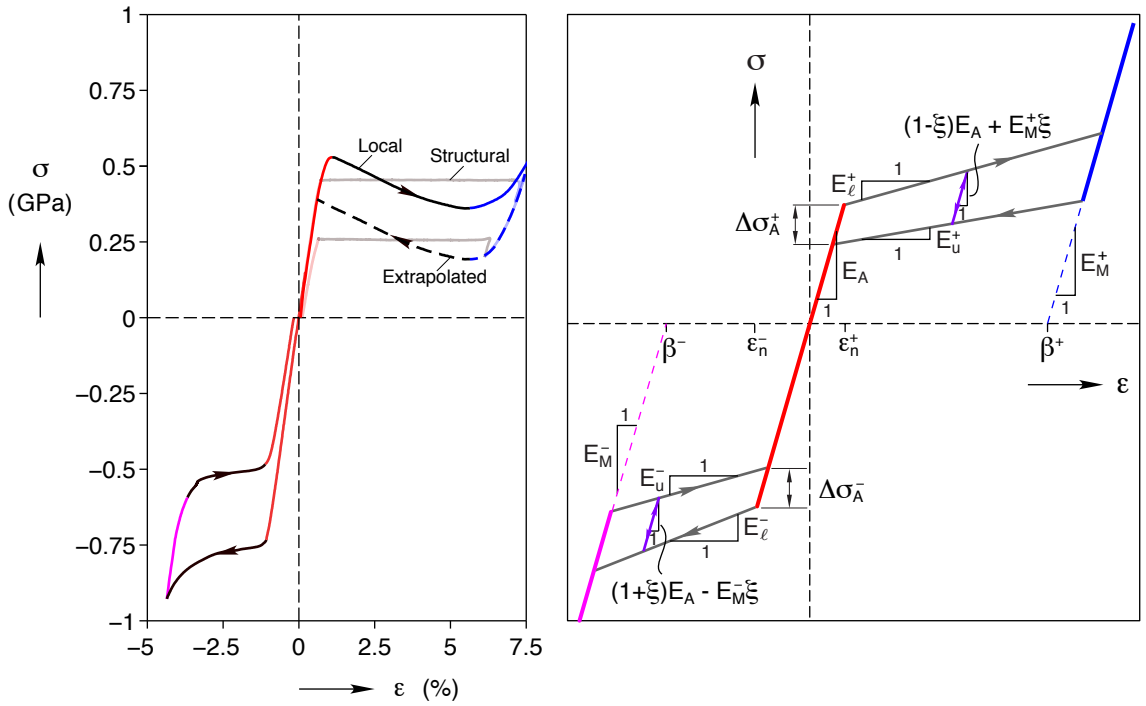

Figure 5.2: Comparison of experimental behavior of NiTi (a) with the material model (b), highlighting the trilinear, asymmetric and hysteretic characteristics.

or

$$\sigma_M^{\pm}(\varepsilon) = E_M^{\pm}(\varepsilon - \beta^{\pm}), \tag{5.25}$$

respectively, where E_A is the modulus of elasticity of austenite, $E_M^{\pm}$ is the modulus of elasticity of martensite, $\beta^{\pm}$ is the transformation strain, and $(.)^{\pm}$ denotes a material parameter in the tensile $(+)$ or compressive $(-)$ region of the response. When in the mixed phase region (second branch), the response can be further classified by three sub-branches: loading ($A \rightarrow M^{\pm}$), unloading ($M^{\pm} \rightarrow A$), and intermediate (within the hysteresis loop). The material behavior for the loading, unloading and intermediate sub-branches are defined by

$$\sigma_{\ell}^{\pm}(\varepsilon) = E_A\varepsilon_n^{\pm} + E_{\ell}^{\pm}(\varepsilon - \varepsilon_n^{\pm}), \tag{5.26a}$$

$$\sigma_u^{\pm}(\varepsilon) = E_A\varepsilon_n^{\pm} + E_u^{\pm}(\varepsilon - \varepsilon_n^{\pm}) \pm \left(\frac{E_u^{\pm}}{E_A} - 1\right), \tag{5.26b}$$

and

$$\sigma_h^{\pm}(\varepsilon,\xi) = \eta(\varepsilon,\xi)^{\pm}\sigma_u^{\pm}(\varepsilon_u(\xi)) + \left[1-\eta^{\pm}(\varepsilon,\xi)\right]\sigma_\ell^{\pm}(\varepsilon_\ell(\xi)), \tag{5.26c}$$

respectively, where $\varepsilon_n^{\pm}$ is the nucleation strain, $E_\ell^{\pm}$ is the modulus of elasticity during $A \to M^{\pm}$ transformation, $E_u^{\pm}$ is the modulus of elasticity during $M^{\pm} \to A$ transformation, and

$$\eta^{\pm}(\varepsilon,\xi) = \frac{\varepsilon - \varepsilon_u^{\pm}(\xi)}{\varepsilon_\ell^{\pm}(\xi) - \varepsilon_u^{\pm}(\xi)}, \tag{5.27}$$

such that

$$\varepsilon_\ell^{\pm}(\xi) = \varepsilon_n^{\pm} \mp \frac{E_M\left(\beta^{\pm} - \varepsilon_n^{\pm}\right) + E_A\varepsilon_n^{\pm}}{E_\ell^{\pm} - E_M^{\pm}}\xi \tag{5.28a}$$

and

$$\varepsilon_u^{\pm}(\xi) = \varepsilon_n^{\pm} \mp \frac{\Delta\sigma_A^{\pm}}{E_A} + \left[\frac{\Delta\sigma_A^{\pm}}{E_A} \mp \varepsilon_n^{\pm} \pm \frac{E_M^{\pm}\beta^{\pm} + \left(E_A - E_u^{\pm}\right)\left(\varepsilon_n^{\pm} \mp \frac{\Delta\sigma_A^{\pm}}{E_A}\right)}{E_M^{\pm} - E_u^{\pm}}\right]\xi. \tag{5.28b}$$

The corresponding phase transformation behavior is governed by the kinetic relations

$$\dot{\xi}(\varepsilon,\dot{\varepsilon},\xi) = \begin{cases} \dot{\xi_\ell^{+}}(\dot{\varepsilon}) & \text{if} \quad \eta(\varepsilon,\xi) = 1 \text{ and } \dot{\varepsilon} > 0 \text{ and } \xi < 1 \\ \dot{\xi_\ell^{-}}(\dot{\varepsilon}) & \text{if} \quad \eta(\varepsilon,\xi) = 1 \text{ and } \dot{\varepsilon} < 0 \text{ and } \xi > -1 \\ \dot{\xi_u^{+}}(\dot{\varepsilon}) & \text{if} \quad \eta(\varepsilon,\xi) = -1 \text{ and } \dot{\varepsilon} < 0 \text{ and } \xi > 0 \\ \dot{\xi_u^{-}}(\dot{\varepsilon}) & \text{if} \quad \eta(\varepsilon,\xi) = -1 \text{ and } \dot{\varepsilon} > 0 \text{ and } \xi < 0 \\ 0 & \text{otherwise} \end{cases} \tag{5.29}$$

where

$$\dot{\xi_\ell}^{\pm}(\dot{\varepsilon}) = \frac{\pm\left(E_M^{\pm} - E_\ell^{\pm}\right)}{E_M\left(\beta^{\pm} - \varepsilon_n^{\pm}\right) + E_A\varepsilon_n^{\pm}}\dot{\varepsilon} \tag{5.30a}$$

and

$$\dot{\xi_u^{\pm}}(\dot{\varepsilon}) = \frac{E_A\left(E_M^{\pm} - E_u^{\pm}\right)}{E_A^2\varepsilon_n^{\pm} \pm E_M^{\pm}\Delta\sigma_A^{\pm} \mp E_A\left[\Delta\sigma_A^{\pm} \mp E_M^{\pm}\left(\beta^{\pm} - \varepsilon_n^{\pm}\right)\right]}\dot{\varepsilon}. \tag{5.30b}$$

In summary, the constitutive relationship is defined by

$$\sigma(\varepsilon,\dot{\varepsilon},\xi) = \begin{cases} \sigma_A(\varepsilon) & \text{if} \quad \xi = 0 \\ \sigma_\ell^+(\varepsilon) & \text{if} \quad 0 < \xi < 1 \ \text{ and } \ \dot{\xi}(\varepsilon,\dot{\varepsilon},\xi) > 0 \\ \sigma_\ell^-(\varepsilon) & \text{if} \quad -1 < \xi < 0 \ \text{ and } \ \dot{\xi}(\varepsilon,\dot{\varepsilon},\xi) < 0 \\ \sigma_u^+(\varepsilon) & \text{if} \quad 0 < \xi < 1 \ \text{ and } \ \dot{\xi}(\varepsilon,\dot{\varepsilon},\xi) < 0 \\ \sigma_u^-(\varepsilon) & \text{if} \quad -1 < \xi < 0 \ \text{ and } \ \dot{\xi}(\varepsilon,\dot{\varepsilon},\xi) > 0 \\ \sigma_h^+(\varepsilon,\xi) & \text{if} \quad 0 < \xi < 1 \ \text{ and } \ \dot{\xi}(\varepsilon,\dot{\varepsilon},\xi) = 0 \\ \sigma_h^-(\varepsilon,\xi) & \text{if} \quad -1 < \xi < 0 \ \text{ and } \ \dot{\xi}(\varepsilon,\dot{\varepsilon},\xi) = 0 \\ \sigma_M^+(\varepsilon) & \text{if} \quad \xi = 1 \\ \sigma_M^-(\varepsilon) & \text{if} \quad \xi = -1 \end{cases} . \tag{5.31}$$

The asymmetric, hysteretic, trilinear material model is a balance between accuracy and computational efficiency. Many of the main characteristics of superelasticity are captured, while ignoring some of the more complex mechanisms, such as latent heat effects (which often manifests as loading rate sensitivity) and shakedown (also known as functional fatigue). This model is therefore best suited for the quasistatic loading of a precycled material.

5.2 Numerical Implementation

The nonlinear behavior of the SMA kinematics and constitutive behavior results in a system which is difficult to examine analytically, motivating a numerical finite element implementation. Due to the nonstandard kinematics and material behavior, a number of material element implementations are possible. Two element definitions are discussed in Sections 5.2.1 and 5.2.2, highlighting their advantages and disadvantages; additionally, there are also important numerical issues that must be considered in thickness-wise integrals (Section 5.2.3) and the potential loss of ellipticity of the governing equations due to the up–down–up tensile behavior of SMAs (Section 5.2.4).

5.2.1 Three nodal degrees of freedom

In traditional beam elements, three nodal degrees of freedom – two translational (u and v) and one rotational (α) – are used in the discretization of the system. As these three field quantities are related by

$$\tan\alpha = \frac{v'}{1+u'}, \tag{5.32}$$

which derives from the kinematic relationship of Eq. (5.11), the finite element shape function definitions for these three field variables must be coupled. For the small rotations assumed for linear beam elements, the coupling equation Eq. (5.32) simplifies to

$$v' \approx \lambda\alpha, \tag{5.33}$$

which linearly relates v' with α. Standard polynomial shape functions (the order of which depend on the number of nodes used in the beam element) can therefore be used for each degree of freedom, with the α polynomial being one degree lower than the v polynomial. Unfortunately, in the case of the nonlinear kinematic model used here, it is not possible to define polynomial shape functions for the three field variables without violating the coupling equation Eq. (5.32). The resulting element is more computationally costly than standard polynomial implementations.

For a two node beam element, one possible choice for shape functions is linear u, cubic v, and direct enforcement of Eq. (5.32) for α:

$$u(s_0) = a_0 + a_1 s_0 \tag{5.34a}$$

$$v(s_0) = b_0 + b_1 s_0 + b_2 s_0^2 + b_3 s_0^3 \tag{5.34b}$$

$$\alpha(s_0) = \arctan\left(\frac{b_1 + 2b_2 s_0 + 3b_3 s_0^2}{a_1}\right). \tag{5.34c}$$

Relating the shape function definitions to the nodal degrees of freedom,

$$u_1 \equiv u(0); \quad u_2 \equiv u(h); \quad v_1 \equiv v(0); \quad v_2 \equiv v(h); \quad \alpha_1 \equiv \alpha(0); \quad \alpha_2 \equiv \alpha(h); \tag{5.35}$$

the shape functions coefficients are

$$a_0 = u_1 \tag{5.36a}$$

$$a_1 = \frac{u_2 - u_1}{h} \tag{5.36b}$$

$$b_0 = \frac{[\tan(\alpha_1) + \tan(\alpha_2)](h - u_1 + u_2) + 2(v_1 - v_2)}{h^2} \tag{5.36c}$$

$$b_1 = v_1 \tag{5.36d}$$

$$b_2 = \frac{\tan(\alpha_1)(h - u_1 + u_2)}{h} \tag{5.36e}$$

$$b_3 = -\frac{(h - u_1 + u_2)[2\tan(\alpha_1) + \tan(\alpha_2)] + 3(v_2 - v_1)}{h^2}. \tag{5.36f}$$

In addition to the computational costs of evaluating Eq. (5.34c), this element definition has computation issues associated with nodal rotations near $90°$ as the $\tan(\alpha_i)$ terms found in the shape function coefficients begin to approach infinity. This therefore limits this element implementation to rotations of less than $90°$.

5.2.2 Four nodal degrees of freedom

To address some of the issues associated with the three nodal degree of freedom element definition, an element can be defined which uses two translational (u and v) and two rotation–like (u' and v') nodal degrees of freedom. As the rotation–like degrees of freedom are derivatives of the translational degrees of freedom, traditional polynomial shape functions can be used; furthermore, there are no restrictions on the beam rotation as there are no ill posed functions in the shape function definition.

Unfortunately, the trigonometric relationship between the rotation–like degrees of freedom and the beam centerline rotation (Eq. (5.32)) make it difficult to prescribe rotation-based (α) continuity and boundary conditions. For proper compatibility between elements, continuity of u, v, and α are required. A sufficient condition for continuity of α between elements is to enforce continuity of both u' and v'[3]. It should be noted that this implementation of the rotational continuity condition additionally results in continuity of the centerline stretch ratio λ (see Eq. (5.9a)). For the case in which elements are connected along a smooth beam (see Figure 5.3a), λ continuity implies axial strain continuity between elements, suppressing the possibility of strain localization. For the

[3]Alternatively, an optimization procedure (such as a Lagrange Multiplier formulation) could be used to minimize the difference in α between connecting elements, thus enforcing α continuity. Unlike enforcing $\bar{u}'$ and $\bar{v}'$ continuity, there are no assumptions with respect to λ at the element connections; however, this comes at the cost of being more computationally complex and expensive.

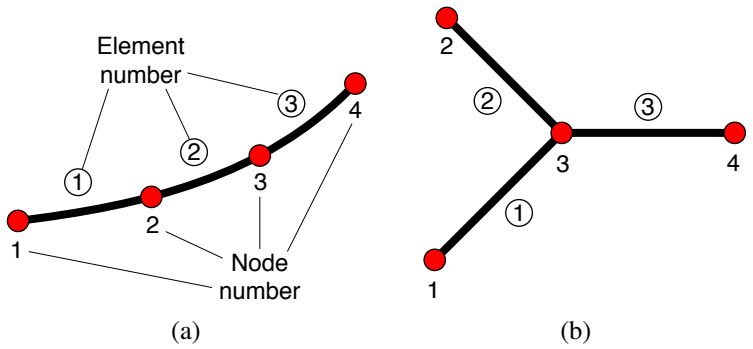

Figure 5.3: Schematics of element connection conditions: (a) demonstrates element connections within a single beam, while (b) demonstrates element connections at a juncture in which multiple beams meet.

case in which elements connect at the juncture of multiple beams (see Figure 5.3b), continuity of λ results in aphysical behavior; for example, if nodes 1 and 2 in Figure 5.3b were vertically compressed, strain would develop in elements ① and ② ($\lambda \neq 1$ at node 3), but element ③ would remain unloaded ($\lambda = 1$ at node 3), which is contradictory to the continuity of λ at node 3. Fortunately, in the special case of the thin beams investigated here, in which bending dominates over axial deformation, $\lambda \approx 1$ at the joints. There are therefore only minor effects from the extra constraint of λ continuity. It should also be noted that specifying α as a boundary condition, through specification of $\bar{u}'$ and $\bar{v}'$, can have unforeseen consequences; in particular, there are a number of $\bar{u}'$ and $\bar{v}'$ pairs which result in the same α, but different boundary conditions.

For a two node element, a natural choice for the shape functions are cubic polynomials for the translational degrees of freedom and quadratic polynomials for the rotation–like degrees of freedom:

$$u(s_0) = a_0 + a_1 s_0 + a_2 s_0^2 + a_3 s_0^3 \tag{5.37a}$$

$$v(s_0) = b_0 + b_1 s_0 + b_2 s_0^2 + b_3 s_0^3 \tag{5.37b}$$

$$u'(s_0) = a_1 + 2a_2 s_0 + 3a_3 s_0^2 \tag{5.37c}$$

$$v'(s_0) = b_1 + 2b_2 s_0 + 3b_3 s_0^2. \tag{5.37d}$$

Relating the shape function definitions to the nodal degrees of freedom,

$$u_1 \equiv u(0); \quad u_2 \equiv u(h); \quad v_1 \equiv v(0); \quad v_2 \equiv v(h); \tag{5.38}$$

$$u_1' \equiv u'(0); \quad u_2' \equiv u'(h); \quad v_1' \equiv v'(0); \quad v_2' \equiv v'(h) \tag{5.39}$$

the shape function coefficients are

$$a_0 = u_1 \qquad b_0 = v_1 \tag{5.40a}$$

$$a_1 = u_1' \qquad b_1 = v_1' \tag{5.40b}$$

$$a_2 = -\frac{3(u_1 - u_2) + h(2u_1' + u_2')}{h^2} \qquad b_2 = -\frac{3(v_1 - v_2) + h(2v_1' + v_2')}{h^2} \tag{5.40c}$$

$$a_3 = \frac{2(u_1 - u_2) + h(u_1' + u_2')}{h^3} \qquad b_3 = \frac{2(v_1 - v_2) + h(v_1' + v_2')}{h^3}. \tag{5.40d}$$

5.2.3 Integration Considerations

The heterogeneous mixture of phases in SMAs can result in large stress and strain gradients, requiring special considerations when numerically integrating these quantities. In the case of uniaxial deformation, the loading is uniform along the length, exhibiting small gradients in stress and strain (except for the case of phase localization) and suggesting the need for only a small number of integration points. Even in the case of localization, mesh refinement allows for accurate capture of the associated high gradients. For these reasons, Gauss quadrature based integration with four integration points is used in all implementations of the model for the length-wise integrals. In the case of bending, the model assumes a linear strain profile through the thickness of the beam. Due to the nonlinear relationship between stress and strain, the resulting thickness-wise stress profile is nonlinear, containing kinks in the profile at phase boundaries. Integration of the thickness-wise stress, as in the evaluation of the axial load (Eq. (5.21a)) and bending moment (Eq. (5.21b)), therefore requires a relatively large number of integration points for accurate evaluation. Although Gauss quadrature can be used (which is one of the most common integration schemes used in the finite element method), it tends to be inefficient due to the necessity to either calculate the quadrature weights or tabulate the weights for a wide range of integration points. This inefficiency can be somewhat alleviated by sectioning the beam cross-section and using a smaller number of integration points over each section; however, this adds in unnecessary complication. Instead, trapezoidal integration is used due to its greater flexibility and efficient implementation. In convergence studies run using the presented model, between 51 and 201 integration points[4] were found to be sufficient to accurately evaluate the thickness-wise integrals.

[4] An odd number of trapezoidal integration points are always used so that the end points align with the edges of the beam.

5.2.4 Loss of Ellipticity: Localization and Propagation

Due to the negative tangent modulus of the "down" portion of the up–down–up tensile response of superelastic SMAs (see Chapter 3), the strain field within the material can localize into high strain regions (as seen in the tensile and pure bending experiments of Sections 2.3.1 and 2.3.3, respectively). From a modeling perspective, localization is associated with the loss of ellipticity of the governing partial differential equations and causes issues with solving boundary value problems. In the context of the finite element method, which is developed to solve elliptic partial differential equations, loss of ellipticity results in mesh dependent results and numerical instability. For an illustrative example of these issues, see Section 2 of Jirsek [2002].

There are several modeling techniques which can be used to regularize the localization problem, incorporating a characteristic length scale to essentially penalize high strain gradients. These techniques range from the addition of strain gradients, to nonlocal parameters, to rate dependence, each of which have their benefits and drawbacks. In all cases, these techniques require a non-standard finite element implementation, which is beyond the scope of this work. Instead, the structural response of the material is used to avoid the issues associated with loss of ellipticity (as in Section 7.2), with the understanding that this simplification omits important information about the material behavior (the effects of which are also left for future work).

5.3 Summary

A basic phenomenological model was presented for superelastic SMAs in the context of beam theory. An extensible elastica framework was implemented to capture the large rotation kinematics of SMA beams while a phenomenologically inspired trilinear material law was used to model the constitutive behavior of the material. Implementation of the model within the finite element framework was then discussed, providing three node and four node element definitions, along with potential implementation issues regarding numerical integration and loss of ellipticity of the model when using an up–down–up tensile response.

Chapter 6

Bloch Wave Stability Analysis

Many biological and engineered systems function at multiple length scales, ranging from muscle tissue and bones, to composites and corrugations. Unfortunately, it is often mathematically intractable to explicitly model all of the relevant length scales in the entire system. In the case of systems with an underlying periodic length scale, analysis is often simplified using homogenization techniques to represent the system by a homogeneous continua (although not necessarily isotropic) with effective properties derived from the averaged behavior of the mesostructure. Unfortunately, homogenization loses some of the physical aspects of the original structure, such as the stability characteristics at the mesoscopic scale; for example, micro-buckling of fibers in a fiber reenforced composite. Alternatively, a periodic structure can be represented by the minimum repeating unit of the structure (the unit cell) subjected to periodic boundary conditions. Unlike the homogenization technique, some of the mesoscopic behavior can be preserved, but at the cost of suppressing other behaviors, such as instabilities with a wavelength greater than the unit cell. To avoid the short comings of the aforementioned analyses, a third method founded on Bloch's theorem can be used to tractably represent the meso- and macroscopic characteristics of structures with underlying periodicity.

Developed by Felix Bloch in 1928 to describe the conduction of electrons within crystalline materials [Bloch, 1928], Bloch's theorem defines the general solution to the linear Schrödinger's equation in three dimensions. Although independently developed by Bloch, Bloch's theorem was actually a rediscovery of a concept discovered by a number of researchers in the late 1800s, the most notable of which was Gaston Floquet who developed an equivalent theory (Floquet theory) in the context of linear ordinary differential equations with periodic coefficients [Floquet, 1883]. The rediscovery of this theory within different fields emphasizes its generality and applicability to a range of problems in which there is a fundamental periodicity to the problem.

Extension of Bloch's theorem from solid state physics to continuum mechanics is relatively straight forward due to the similarities in their governing equations. Mead was of the early re-

searchers to apply Bloch's theorem to mechanics, examining the vibrational characteristics of periodic structures such as stiffened plates [Mead, 1970, 1973, 1975a,b], along with Anderson who looked into buckling and natural vibrations of periodic lattice structures [Anderson, 1981, Anderson and WIlliams, 1986]. Since then, the general framework for Bloch wave analysis was formally established by Triantafyllidis and coworkers, rigorously proving the mathematical framework [Geymonat et al., 1993] and applying the theory to the analysis of laminated composites [Triantafyllidis and Bardenhagen, 1996], fiber reinforced composites [Triantafyllidis and Maker, 1985, Michel et al., 2010], metallic honeycombs [Triantafyllidis and Schraad, 1998, Michailidis et al., 2009, López Jiménez and Triantafyllidis, 2013], and phase transformation in SMAs [Elliott et al., 2002a, 2006a,b]. Since then, the theory has been used to examine wave propagation in two dimensional lattices [Phani et al., 2006] and elasto-plastic buckling of rigid joint lattices [Hutchinson and Fleck, 2006].

Bloch's theorem in the context of stability analysis of infinite structures with underlying periodicity is of primary interest here. Although there is a broad literature on the subject matter, there are relatively few cases which provide a thorough discussion of the theory in the context of simple problems and applications; this work looks to address these concerns. To set the stage, infinite structures with underlying periodicity are briefly discussed in Section 6.1. Bloch's theorem is then presented (Section 6.2), along with some of its many intricacies (Section 6.3), its implementation in the context of structural stability analysis (Section 6.4), and some simple illustrative examples of its implementation (Section 6.5).

6.1 Infinite Structures with Underlying Periodicity

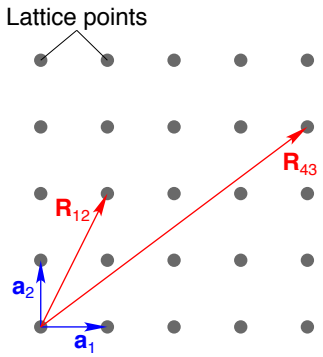

Figure 6.1: The periodicity of a two–dimensional lattice is defined by its lattice vector $\mathbf{R}_{uv} = u\mathbf{a}_1 + v\mathbf{a}_2$.

The periodicity of a structure is defined by its Bravais lattice. In three dimensions, there are a

total of 14 possible Bravais lattices which range from a low symmetry triclinic unit cell[1] to a high symmetric cubic unit cell. Mathematically, the Bravais lattice is described by a lattice vector and corresponding reciprocal lattice vector. If the corners of a unit cell are defined as lattice points, then the lattice vector defines the vector from one lattice point to all other lattice points within the structure:

$$\mathbf{R}_{uvw} = u\mathbf{a}_1 + v\mathbf{a}_2 + w\mathbf{a}_3, \tag{6.1}$$

where (u, v, w) are integers parameterizing the lattice points and $\mathbf{a}_i$ are the vectors defining the directions and magnitudes of translational symmetry; an example two–dimensional lattice is shown in Figure 6.1, along with its corresponding lattice vector. Transforming the lattice vector into the Fourier domain (which corresponds to the spatial frequency of planes of lattice points), there exists a reciprocal lattice vector

$$\mathbf{G}_{\ell mn} = \ell\mathbf{b}_1 + m\mathbf{b}_2 + n\mathbf{b}_3, \tag{6.2}$$

where (ℓ, m, n) are integers parameterizing the reciprocal lattice points and $\mathbf{b}_i$ are vectors defined such that $\mathbf{a}_i \cdot \mathbf{b}_j = \delta_{ij}$ and δ_{ij} is the Kronecker delta. For a more detailed discussion on lattice structures, refer to most any text on crystallography; for example, see Chapter 2 of Rohrer [2001].

6.2 Bloch's Theorem

Bloch's theorem states that the general solution to a system of *linear* differential equations with periodic coefficients is

$$\boldsymbol{\psi}(\mathbf{r}; \mathbf{k}) = \mathrm{e}^{i\mathbf{k}\cdot\mathbf{r}}\mathbf{p}(\mathbf{r}; \mathbf{k}), \tag{6.3}$$

where $i = \sqrt{-1}$, $\boldsymbol{\psi} : \mathbb{R}^N \times \mathbb{R}^N \mapsto \mathbb{C}^N$ is the general solution vector (where the dimensionality of the problem is defined by N), $\mathbf{r}$ is the vector of independent variables (which resides in the physical domain), $\mathbf{k}$ is the Bloch wavevector (which resides in the reciprocal domain), and $\mathbf{p} : \mathbb{R}^N \times \mathbb{R}^N \mapsto \mathbb{C}^N$ is a function periodic with respect to the periodicity of the coefficients in the governing differential equations. Eq. (6.3) consists of a plane wave modified by a periodic function and is often referred to as a *Bloch wave*. In the context of mechanics, $\mathbf{r}$ defines a position vector and the periodicity of the governing differential equations is due to the underlying periodicity of

[1] The unit cell is defined as the fundamental repeating unit of the structure with respect to translational symmetry.

the lattice structure ($\mathbf{R}_{uvw}$). The resulting periodicity of $\mathbf{p}$ is therefore

$$\mathbf{p}(\mathbf{r} + \mathbf{R}_{uvw}) = \mathbf{p}(\mathbf{r}) \tag{6.4}$$

for all integers (u, v, w). To interpret the physical characteristics of the complex valued $\boldsymbol{\psi}$, either the real or imaginary part of $\boldsymbol{\psi}$ can be taken at the end of the analysis. It should be noted that $\boldsymbol{\psi}$ could be equivalently defined in the real domain; however, the mathematical convenience of the complex representation out weighs the resulting obscuration of the physical interpretation.

6.3 Properties of Bloch Waves

The building block of Bloch's theorem, *Bloch waves* are almost-periodic functions containing no fundamental period in the exact sense. A classic example of an almost-periodic function is

$$f(x) = \sin(\pi x) + \sin(\pi\sqrt{2}x), \tag{6.5}$$

which appears to be a periodic function due to the superposition of two periodic functions, but in reality has no true fundamental frequency. Formally, a complex valued function $f(x)$ defined for $-\infty < x < \infty$ is called almost-periodic if for any $\epsilon > 0$ there exists a trigonometric polynomial $T_\epsilon(x)$, such that

$$|f(x) - T_\epsilon(x)| < \epsilon \quad \text{for} \quad -\infty < x < \infty, \tag{6.6}$$

where a trigonometric polynomial is defined by

$$T(x) = \sum_{j=1}^{n} c_j e^{i\lambda_j x}, \tag{6.7}$$

c_j are complex numbers and λ_j are real numbers [Corduneanu et al., 1989]; as a corollary, all trigonometric polynomials are almost-periodic functions. Given the one-dimensional *Bloch wave*

$$\psi(x) = e^{ikx} p(x), \tag{6.8}$$

where $p(x+nL) = p(x)$ for any integer n, the unit periodic function p can be expanded according to its equivalent Fourier Series:

$$\psi(x) = e^{ikx} \sum_{m=-\infty}^{\infty} c_m e^{i\frac{2\pi m}{L}x} = \sum_{m=-\infty}^{\infty} c_m e^{i(\frac{2\pi m}{L}+k)x}, \tag{6.9}$$

where the c_m are Fourier coefficients. Eq. (6.9) is a trigonometric polynomial and, therefore, all Bloch waves are almost-periodic functions. Note that, although this discussion was conducted in the context of a one-dimensional *Bloch wave* for clarity, the ideas generalize to the three-dimensional case in a straightforward manner.

Due to the almost-periodic properties of *Bloch waves*, care must be taken when interpreting their spatial characteristics. Although *Bloch waves* have no fundamental wavelength in general, Eq. (6.9) reduces to a Fourier Series (upon redefinition of the index integer m) when $k = 2\pi a/(Lb)$ and a/b is an irreducible fraction, implying that a subset of *Bloch waves* are periodic functions. For this subset of *Bloch waves*, the fundamental wavelength is bL, which has several ramifications:

- The term "Bloch wavenumber" for k is deceiving as it does not align with the classical notion of a wavenumber; that is, the Bloch wavenumber does *not* correspond to the wavelength (λ) of a Bloch wave through the typical relation $\lambda = 2\pi/k$, even in the case that the *Bloch wave* is periodic.
- Numerically, only periodic *Bloch waves* can be represented due to the truncation of irrational numbers to rational numbers in computers.
- The denseness of rational and irrational numbers on the number line results in a highly discontinuous mapping between the k and wavelength space of periodic *Bloch waves*. Numerically, the selected precision of k therefore drastically affects the interpreted wavelength of a *Bloch wave* (as will be shown in Section 6.5.2).
- There are b periodic *Bloch waves* with same wavelength bL.

By definition, *Bloch waves* are not uniquely specified by the wavevector $\mathbf{k}$ due to the periodicity of $\mathbf{p}$. For example, let $\hat{\boldsymbol{\psi}}$ be a *Bloch wave* with wavevector $\hat{\mathbf{k}} = \mathbf{k} + \mathbf{G}_{\ell mn}$:

$$\hat{\boldsymbol{\psi}}(\mathbf{r};\hat{\mathbf{k}}) = e^{i\hat{\mathbf{k}}\cdot\mathbf{r}}\hat{\mathbf{p}}\left(\mathbf{r};\hat{\mathbf{k}}\right) = e^{i\mathbf{k}\cdot\mathbf{r}}\left[e^{i\mathbf{r}\cdot\mathbf{G}_{\ell mn}}\hat{\mathbf{p}}\left(\mathbf{r};\hat{\mathbf{k}}\right)\right]. \tag{6.10}$$

As $\mathbf{p} \equiv e^{i\mathbf{r}\cdot\mathbf{G}_{\ell mn}}\hat{\mathbf{p}}\left(\mathbf{r};\hat{\mathbf{k}}\right)$ has the same unit periodicity as $\hat{\mathbf{p}}$, the righthand side of Eq. (6.10) defines

another *Bloch wave* $\boldsymbol{\psi} \equiv e^{i\mathbf{k}\cdot\mathbf{r}}\mathbf{p}(\mathbf{r};\mathbf{k})$ such that

$$\hat{\boldsymbol{\psi}}(\mathbf{r};\mathbf{k}+\mathbf{G}_{\ell mn}) = \boldsymbol{\psi}(\mathbf{r};\mathbf{k}). \tag{6.11}$$

Eq. (6.11) implies that $\boldsymbol{\psi}$ and $\hat{\boldsymbol{\psi}}$ represent identical *Bloch waves*, although they are parameterized by different wavevectors. To simplify the representation, $\mathbf{k}$ is often restricted to the smallest set centered around the origin which completely represents all *Bloch waves* (referred to here as the set $\mathcal{B}$). This set is referred to as the First Brillouin Zone in the solid state physics literature and is defined by the Wigner-Seitz cell (which is analogous to a Vorinoi cell) of the reciprocal lattice. For the remaining discussion, the parameterization of $\boldsymbol{\psi}$ with respect to $\mathbf{k}$ will be suppressed with the assumption that $\mathbf{k} \in \mathcal{B}$.

6.4 Stability Analysis

Intuitively, stability defines a system's ability to maintain a given state when subjected to small perturbations (be they mechanical, thermal, etc). An overview of stability theory is discussed here to provide a general mathematical framework (Section 6.4.1); however, the interested reader is referred to Iooss and Joseph [1990] for a more in depth discussion of the subject matter. The specialization of this theory in the context of infinite media with underlying periodic structure is then detailed within this framework (Section 6.4.2).

6.4.1 General Stability Analysis

Stability analysis of a mechanical system can be broken into two fundamental components: determination of the system's equilibrium paths and the stability assessment of each equilibrium path. The equilibrium paths of the system provide a map of all possible states of the system for the given loading conditions; whereas the stability assessment determines which of these states are stable, and hence physically relevant. In most practical cases, stability of the principal solution path (equilibrium path emanating from the initially unloaded state of the system) is of primary interest as deformation along secondary equilibrium paths often result in permanent deformation and failure of the structure; furthermore, in the case of nonconservative systems, the behavior of the system is path dependent, so the analysis requires the system to be examined starting from the initial load free condition.

For the sake of clarity in simplicity, stability analysis is discussed here for the relatively simple

case of conservative systems (both with respect to material behavior and external loading conditions), noting that the implementation details with respect to Bloch's theorem discussed in Section 6.4.2 are the same regardless of conservative or nonconservative systems. A conservative system can be modeled according to its total potential energy Π, which consists of a combination of the internal potential energy of the system U and the potential energy of the external loads Ω: $\Pi = U + \Omega$. At a given loading state λ, stability of the conservative system is governed by the convexity of $\Pi(\mathbf{u};\lambda)$ with respect to the deformation field $\mathbf{u}$ (which is kinematically admissible with the boundary conditions of the system), where stable equilibria correspond to minima of $\Pi(\mathbf{u};\lambda)$.

Mathematically, the vector $\mathbf{u}_0$ is a (local) minimum of Π ($\mathbf{u}$;λ) such that

$$\Delta\Pi(\mathbf{u}_0;\lambda) \equiv \Pi(\mathbf{u};\lambda) - \Pi(\mathbf{u}_0;\lambda) > 0 \quad \forall \quad 0 < ||\mathbf{u} - \mathbf{u}_0|| < \varepsilon \tag{6.12}$$

and ε is small. The solution to this optimization problem is often considered with respect to the Taylor series expansion about the point $\mathbf{u}_0$:

$$\Delta\Pi(\mathbf{u}_0;\lambda) = \Pi_{,\mathbf{u}}(\mathbf{u}_0;\lambda)\cdot\Delta\mathbf{u} + \left(\Pi_{,\mathbf{uu}}(\mathbf{u}_0;\lambda)\cdot\Delta\mathbf{u}\right)\cdot\Delta\mathbf{u} + ..., \tag{6.13}$$

where $\Delta\mathbf{u} \equiv \mathbf{u} - \mathbf{u}_0$ is a small perturbation about the equilibrium point. In the case of discrete systems, the $\Pi_{,\mathbf{u}}(\mathbf{u}_0;\lambda)$ and $\Pi_{,\mathbf{uu}}(\mathbf{u}_0;\lambda)$ terms of Eq. (6.13) corresponds to the Jacobian vector and Hessian matrix of Π evaluated at the point $\mathbf{u}_0$, respectively; whereas, in the case of continuous systems, the $\Pi_{,\mathbf{u}}(\mathbf{u}_0;\lambda)\cdot\Delta\mathbf{u}$ and $\left(\Pi_{,\mathbf{uu}}(\mathbf{u}_0;\lambda)\cdot\Delta\mathbf{u}\right)\cdot\Delta\mathbf{u}$ terms of Eq. (6.13) are the first and second variational derivatives (i.e. Gâteaux derivatives) of Π evaluated at $\mathbf{u}_0$ such that

$$\Pi_{,\mathbf{u}}(\mathbf{u}_0;\lambda)\cdot\mathbf{w} = \left.\frac{\partial\Pi(\mathbf{u}_0+\varepsilon\mathbf{w};\lambda)}{\partial\varepsilon}\right|_{\varepsilon=0} \tag{6.14a}$$

$$\left(\Pi_{,\mathbf{uu}}(\mathbf{u}_0;\lambda)\cdot\mathbf{w}\right)\cdot\mathbf{v} = \left.\frac{\partial^2\Pi(\mathbf{u}_0+\varepsilon\mathbf{w}+\eta\mathbf{v};\lambda)}{\partial\varepsilon\partial\eta}\right|_{\varepsilon=\eta=0}, \tag{6.14b}$$

respectively. If the point $\mathbf{u}_0$ is a stationary point (i.e. minimum, maximum, or saddle point) of Π, then

$$\Pi_{,\mathbf{u}}(\mathbf{u}_0;\lambda)\cdot\Delta\mathbf{u} = 0 \quad \forall \quad \Delta\mathbf{u} \neq 0, \tag{6.15}$$

which is the weak form of equilibrium. Since $\Delta\mathbf{u} \neq 0$, equilibrium can be reformulated into the equivalent strong form

$$\Pi_{,\mathbf{u}}(\mathbf{u}_0;\lambda) = \mathbf{0}. \tag{6.16}$$

To then ensure that $\mathbf{u}_0$ is a minima and, hence, a stable equilibrium point,

$$\left(\Pi_{,\mathbf{uu}}(\mathbf{u}_0;\lambda)\cdot\Delta\mathbf{u}\right)\cdot\Delta\mathbf{u}>0\quad\forall\quad\Delta\mathbf{u}\neq\mathbf{0}. \tag{6.17}$$

Of interest is the critical loading parameter λ_c along the principal solution $\overset{0}{\mathbf{u}}$ in which the system first loses stability; that is,

$$\underbrace{\left(\Pi_{,\mathbf{uu}}(\lambda_c;\overset{0}{\mathbf{u}}_c)\cdot\Delta\overset{1}{\mathbf{u}}_c\right)}_{I}\cdot\underbrace{\Delta\overset{1}{\mathbf{u}}_c}_{II}=0, \tag{6.18}$$

where $\overset{0}{\mathbf{u}}_c$ is the equilibrium solution on the principal path at λ_c and $\Delta\overset{1}{\mathbf{u}}_c$ is the direction about $\overset{0}{\mathbf{u}}_c$ corresponding to zero curvature in $\Pi(\lambda_c,\overset{0}{\mathbf{u}}_c)$ (and correspondings to the direction of the intersecting secondary solution path $\overset{1}{\mathbf{u}}$)[2]. Since the trivial solution $\Delta\overset{0}{\mathbf{u}}_c=0$ is not of interest, $II\neq0$ and, hence, $I=0$. Eq. (6.18) therefore corresponds to the eigenvalue problem

$$\Pi_{,\mathbf{uu}}(\lambda_c;\overset{0}{\mathbf{u}}_c)\cdot\Delta\overset{1}{\mathbf{u}}_c=\mathbf{0}. \tag{6.19}$$

Eq. (6.19) is the strong form for the critical loading state which can be reformulated to its corresponding weak form,

$$\left(\Pi_{,\mathbf{uu}}(\lambda_c;\overset{0}{\mathbf{u}}_c)\cdot\Delta\overset{1}{\mathbf{u}}_c\right)\cdot\delta\mathbf{u}=0\quad\forall\quad\delta\mathbf{u}\neq\mathbf{0}, \tag{6.20}$$

where $\delta\mathbf{u}$ is an arbitrary weighting function (which is kinematically admissible with the boundary conditions of the system). Since the convexity of Π is only probed within a small distance from the equilibrium point, Eq. (6.20) is typically linearized about $\overset{0}{\mathbf{u}}_c$ to simplify the analysis (and later to allow for the use of Bloch's theorem).

To recapitulate, the critical loading parameter λ_c in which a system first loses stability is determine as follows:

1. the principal equilibrium path $\overset{0}{\mathbf{u}}$ is determined according to the equilibrium equation Eq. (6.16);
2. the critical point along $\overset{0}{\mathbf{u}}$ is then determined from Eq. (6.20).

As a final note, often the second step in the stability analysis (i.e., evaluating the stability of the equilibrium paths) is neglected. Instead, the uniqueness of the principal equilibrium path $\overset{0}{\mathbf{u}}$ is investigated, noting that loss of uniqueness corresponds to a bifurcation point. As most "real"

[2]In general, a system can lose stability with respect to multiple directions at a single critical load; however, these cases are not discussed here for the sake of simplicity.

physical systems lose stability at the first bifurcation point, this analysis method allows for the quantification of the first load in which the system likely becomes unstable and deviates from the principal path; however, it should be cautioned that there are no guarantees when using this method as stability is never explicitly verified.

6.4.2 Stability Analysis with Bloch's Theorem

For an infinite structure with underlying periodicity, the governing equations (Eqs. (6.16) and (6.20)) derived from the potential energy of a *continuous* structure correspond to differential equations with periodic coefficients. In the case of equilibrium, the governing differential equations are in general *nonlinear*; whereas, in the case of stability, the governing differential equations have been linearized and are, hence, *linear*. Due to the infinite size of the structure, the solutions of these governing equations are intractable; however, the underlying periodicity of the governing equations can be utilized to reduce the problem to a specialized analysis of the structure's unit cell.

The first step in the stability analysis is the determination of the principal path ($\overset{0}{\mathbf{u}}$). Since the governing equations for equilibrium (Eq. (6.16)) are in general *nonlinear*, Bloch's theorem is not applicable; however, it can be shown that a solution periodic with the same periodicity as the coefficients of the governing equations always exists, even in the case of nonlinear systems. Assuming that the behavior of the structure is unique on an interval near the start of loading (i.e., the principal path is unique near $\lambda = 0$), then it follows that the principal solution corresponds to the solution having the same periodicity as the governing equations' coefficients (and, hence, the structure). Therefore, the governing equations for the principal path can be reduced from the infinite domain to the unit cell with periodic boundary conditions.

The second step is then to determine when the principal path first loses stability (λ_c). Since the governing equations for stability are *linear* (Eq. (6.20)), Bloch's theorem is applicable and solutions take the form of *Bloch waves*. From the periodicity of the function $\mathbf{p}$ in the definition of a *Bloch wave* (Eq. (6.4)),

$$\boldsymbol{\psi}(\mathbf{r} + \mathbf{R}_{uvw}) = e^{i\mathbf{k}\cdot(\mathbf{r}+\mathbf{R}_{uvw})}\mathbf{p}\left(\mathbf{r} + \mathbf{R}_{uvw}\right) = e^{i\mathbf{k}\cdot\mathbf{R}_{uvw}}\boldsymbol{\psi}(\mathbf{r}) \tag{6.21}$$

defines the relationship for the values of a *Bloch wave* between unit cells. For $\mathbf{r}$ on a boundary face of the unit cell and $\mathbf{R}_{uvw}$ in the set $\mathcal{S} = \{\mathbf{R}_{u,v,w} \mid u \in \{0,1\}, v \in \{0,1\}, w \in \{0,1\}\}$, Eq. (6.21) can be used to relate $\boldsymbol{\psi}$ between the boundary faces of the unit cell. These relationships are similar to periodic boundary conditions, but with the addition of the $e^{i\mathbf{k}\cdot\mathbf{R}_{uvw}}$ modifier. The stability problem can therefore be reduced to the analysis of the unit cell subjected to periodic–like

boundary conditions defined according to Eq. (6.21) (which are referred to here as Bloch boundary conditions).

Due to the complex variable definition of *Bloch waves*, the governing stability equation Eq. (6.20) defined in the context of real variables is somewhat ambiguous and needs to be modified. The main modification stems from the synonymous definition of the dot (inner) product with matrix multiplication for real variables, which doesn't hold for complex variables; that is, for the column vectors $\mathbf{a}, \mathbf{b} \in \mathbb{C}$,

$$\mathbf{a}^T\mathbf{b} \equiv \sum_i a_i b_i \neq \langle \mathbf{a}, \mathbf{b} \rangle \equiv \sum_i a_i \bar{b}_i, \tag{6.22}$$

where $\bar{(\cdot)}$ denotes the complex conjugate of a quantity and $\langle ., . \rangle$ defines a generalized dot product. In the original derivation of the strong form of stability (Eq. (6.19)), the $\cdot$ operator defines a matrix multiplication type operation; however, the conversion to the weak form, which looks to produce a sesquilinear form (which is the generalization of a bilinear form for complex numbers) with an arbitrary weighting function, defines a generalized dot product. The critical stability equation Eq. (6.19) therefore needs to be redefined as

$$\left\langle \left(\Pi_{,\mathbf{uu}}(\lambda_c; \overset{0}{\mathbf{u}}_c) \cdot \Delta \overset{1}{\mathbf{u}}_c(\mathbf{k}) \right), \delta\mathbf{u}(\mathbf{k}) \right\rangle = 0 \quad \forall \quad \delta\mathbf{u}(\mathbf{k}) \neq \mathbf{0}, \tag{6.23}$$

noting the dependence of $\overset{1}{\mathbf{u}}_c$ and $\delta\mathbf{u}$ on the Bloch wavevector $\mathbf{k}$ due to the imposition of the Bloch boundary conditions. The parameterization of the critical stability condition with respect to $\mathbf{k}$ implies that λ_c is dependent on $\mathbf{k}$; therefore, the *first* loss of stability is defined by

$$\lambda_c^* = \inf_{\mathbf{k} \in \mathcal{B}} \lambda_c(\mathbf{k}). \tag{6.24}$$

In the case of discrete systems, the governing equations derived from Eqs. (6.16) and (6.23) are not systems of differential equations; rather, they are systems of algebraic equations. The differential equation–based arguments used to reduce infinite continuous systems to the analysis of the unit cell with specialized boundary conditions therefore do not directly apply; however, similar arguments can be formulated to result in the same conclusions. The evaluation of the principal path therefore corresponds to the examination of the unit cell loading under periodic boundary conditions; whereas, the determination of the critical point in which the principal solution loses stability corresponds to the perturbation analysis of the unit cell under Bloch boundary conditions.

6.5 Examples

There are many intricacies associated with *Bloch wave* stability analysis that are not initially obvious from the theoretical framework. To better provide insight into the application and interpretation of *Bloch wave* stability analysis, a series of examples are presented. These examples range from analysis of a simple rigid link system (Section 6.5.1), to a continuous beam (Section 6.5.2), to a two dimensional honeycomb (Section 6.5.3).

6.5.1 1D Rigid Link System

A rigid link system is first examined to introduce the implementation of *Bloch wave* stability analysis. The simplicity of the system helps to prevent distracting computational complexities from overshadowing the analysis technique.

Problem Statement

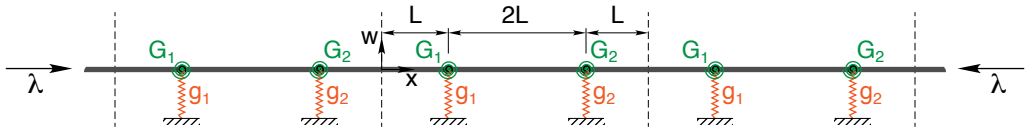

(a) Geometry and loading

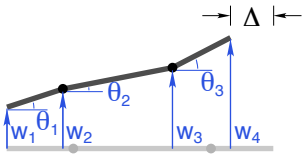

(b) Deformed configuration of unit cell

Figure 6.2: An infinite rigid link system, with a unit cell consisting of three rigid links, two rotational springs, and two translational springs, is axially compressed by a load p until it buckles.

The first example explores the infinite one-dimensional rigid link system schematically represented in Figure 6.2a. The unit cell of the link system consists of three initially flat links connected in series by pins and having lengths L, $2L$ and L, respectively. At the first link juncture, there is a rotational spring with spring stiffness G_1 and a translational spring oriented perpendicular to the links with spring stiffness g_1; there is similarly a rotational spring and a translational spring at the second link juncture, but with spring stiffnesses G_2 and g_2, respectively. In the context of the gen-

eral outline of the *Bloch wave* analysis in Section 6.4.2, the unit cell lattice vector is $\mathbf{R}_u = 4Lu\mathbf{e}_1$ and the First Brillouin zone is $\mathcal{B} = \{k \mid 4Lk \in (-\pi, \pi]\}$.

The system is axially compressed by a load p and, upon buckling, the unit cell deforms according to the translational displacements w_i for $i = 1, .., 4$ and the rotationals θ_i for $i = 1, .., 3$ as shown in Figure 6.2b. Due to the rigid nature of the system, three of the seven generalized displacements are dependent on the others, resulting in only four independent degrees of freedom. For convenience in the later application of the Bloch boundary conditions, the generalized displacement vector $\mathbf{q} = [w_1, \theta_1, w_4, \theta_3]$ is defined here to contain the degrees of freedom on the boundary of the unit cell. The remaining generalized displacements are defined from the geometry of the system by

$$w_2(\mathbf{q}) = w_1 + L\sin\theta_1 \tag{6.25a}$$

$$w_3(\mathbf{q}) = w_4 - L\sin\theta_3 \tag{6.25b}$$

$$\sin\theta_2(\mathbf{q}) = \frac{w_3 - w_2}{2L} = \frac{(w_4 - L\sin\theta_3) - (w_1 + L\sin\theta_1)}{2L} \tag{6.25c}$$

Of interest is the critical load p_c in which the system first loses stability.

Model

The defined system is conservative with respect to both material behavior and external loading, allowing for a representation of the unit cell according to its total potential energy ($\tilde{\Pi} = \tilde{U} + \tilde{\Omega}$). Based on the spring configuration, the internal potential energy of the unit cell is

$$\tilde{U} = \frac{1}{2}\left[G_1\left(\theta_2(\mathbf{q}) - \theta_1\right)^2 + G_2\left(\theta_3 - \theta_2(\mathbf{q})\right)^2 + g_1 w_2^2(\mathbf{q}) + g_2 w_3^2(\mathbf{q})\right]; \tag{6.26}$$

whereas, based on the rigid geometry and the external loading, the external potential energy of the unit cell is

$$\tilde{\Omega} = -p\Delta = -pL\left(4 - \cos\theta_1 - 2\cos\theta_2(\mathbf{q}) - \cos\theta_3\right). \tag{6.27}$$

Nondimensionalizing according to

$$W_i \equiv \frac{w_i}{L}, \quad P \equiv \frac{p}{g_1 L}, \quad \eta \equiv \frac{G_1}{g_1 L^2}, \quad \xi \equiv \frac{G_2}{G_1}, \quad \text{and} \quad \zeta \equiv \frac{g_2}{g_1}, \tag{6.28}$$

the nondimensional potential energy of the system is

$$\widetilde{\Pi}(\mathbf{Q},P)=\frac{1}{2}g_1L^2\left(W_2^2(\mathbf{Q})+\zeta W_3^2(\mathbf{Q})+\eta[\theta_1-\theta_2(\mathbf{Q})]^2+\eta\xi[\theta_2(\mathbf{Q})-\theta_3]^2 \right. \\ \left. -2P\left[4-\cos\theta_1-2\cos\theta_2(\mathbf{Q})-\cos\theta_3\right]\right), \tag{6.29}$$

where $\mathbf{Q}=[W_1,\theta_1,W_4,\theta_3]$ and

$$W_2(\mathbf{Q})=(W_1+\sin\theta_1) \tag{6.30a}$$

$$W_3(\mathbf{Q})=(W_4-\sin\theta_3) \tag{6.30b}$$

$$\sin\theta_2(\mathbf{q})=\frac{(W_4-\sin\theta_3)-(W_1+\sin\theta_1)}{2}. \tag{6.30c}$$

Solution

From Eq. (6.15), the general weak form of equilibrium for the unit cell is

$$\widetilde{\Pi}_{,\mathbf{Q}}(\mathbf{Q}_0;P)\cdot\Delta\mathbf{Q}=0 \quad \forall \quad \Delta\mathbf{Q}\neq 0, \tag{6.31}$$

where

$$\widetilde{\Pi}_{,\mathbf{Q}}(\mathbf{Q};P)=\left[\widetilde{\Pi}_{,W_1}(\mathbf{Q};P),\widetilde{\Pi}_{,\theta_1}(\mathbf{Q};P),\widetilde{\Pi}_{,W_4}(\mathbf{Q};P),\widetilde{\Pi}_{,\theta_3}(\mathbf{Q};P)\right]^T \tag{6.32}$$

is the Jacobian vector for the system. Interested in the principal solution $\overset{0}{\mathbf{Q}}$ which corresponds to deformation of the unit cell under periodic boundary conditions, the generalized displacements are related according to

$$W_4=W_1 \tag{6.33a}$$

$$\theta_3=\theta_1 \tag{6.33b}$$

$$\Delta W_4=\Delta W_1 \tag{6.33c}$$

$$\Delta\theta_3=\Delta\theta_1. \tag{6.33d}$$

Substituting the periodic boundary conditions of Eq. (6.33) into the general weak form of equilibrium Eq. (6.31),

$$\left[\widetilde{\Pi}_{,W_1}(\overset{0}{\mathbf{Q}};P)+\widetilde{\Pi}_{,W_4}(\overset{0}{\mathbf{Q}};P),\widetilde{\Pi}_{,\theta_1}(\overset{0}{\mathbf{Q}};P)+\widetilde{\Pi}_{,\theta_3}(\overset{0}{\mathbf{Q}};P)\right]\cdot\Delta\mathbf{Q}_\alpha=0\quad\forall\quad\Delta\mathbf{Q}_\alpha\neq\mathbf{0},\tag{6.34}$$

where $\mathbf{Q}_\alpha=[W_1,\theta_1]$ and $\overset{0}{\mathbf{Q}}=[\overset{0}{W}_1,\overset{0}{\theta}_1,\overset{0}{W}_1,\overset{0}{\theta}_1]$. The resulting strong form for equilibrium of the principal path is

$$\widetilde{\Pi}_{,W_1}(\overset{0}{\mathbf{Q}};P)+\widetilde{\Pi}_{,W_4}(\overset{0}{\mathbf{Q}};P)=0\tag{6.35a}$$

$$\widetilde{\Pi}_{,\theta_1}(\overset{0}{\mathbf{Q}};P)+\widetilde{\Pi}_{,\theta_3}(\overset{0}{\mathbf{Q}};P)=0,\tag{6.35b}$$

where

$$\widetilde{\Pi}_{,W_1}(\overset{0}{\mathbf{Q}};P)=g_1L^2(\overset{0}{W}_1+\eta\overset{0}{\theta}_1(1+\xi)\sec\overset{0}{\theta}_1+\sin\overset{0}{\theta}_1-P\tan\overset{0}{\theta}_1)\tag{6.36a}$$

$$\widetilde{\Pi}_{,\theta_1}(\overset{0}{\mathbf{Q}};P)=g_1L^2(\eta\overset{0}{\theta}_1(3+\xi)-2P\sin\overset{0}{\theta}_1+\cos\overset{0}{\theta}_1(W_1+\sin\overset{0}{\theta}_1))\tag{6.36b}$$

$$\widetilde{\Pi}_{,W_4}(\overset{0}{\mathbf{Q}};P)=-g_1L^2\sec\overset{0}{\theta}_1(\eta\overset{0}{\theta}_1(1+\xi)-P\sin\overset{0}{\theta}_1+\zeta\cos\overset{0}{\theta}_1(-\overset{0}{W}_1+\sin\overset{0}{\theta}_1))\tag{6.36c}$$

$$\widetilde{\Pi}_{,\theta_3}(\overset{0}{\mathbf{Q}};P)=g_1L^2(\eta\overset{0}{\theta}_1(1+3\xi)-2P\sin\overset{0}{\theta}_1+\zeta\cos\overset{0}{\theta}_1(-\overset{0}{W}_1+\sin\overset{0}{\theta}_1)).\tag{6.36d}$$

By inspection, $\overset{0}{W}_1=\overset{0}{\theta}_1=0$ satisfies Eq. (6.35), hence the principal solution is $\overset{0}{\mathbf{Q}}=[0,0,0,0]$ (which is independent of the applied load). This conclusion seems obvious given the rigid system and the loading conditions; however, the procedure was conducted so as to show the general procedure within the framework discussed in Section 6.4.

Stability of the principal path $\overset{0}{\mathbf{Q}}=[0,0,0,0]$ then derives from Eq. (6.23) for the unit cell:

$$\left\langle\left(\widetilde{\Pi}_{,\mathbf{QQ}}(\overset{0}{\mathbf{Q}};P_c)\cdot\Delta\overset{1}{\mathbf{Q}}\right),\delta\mathbf{Q}\right\rangle=0\quad\forall\quad\delta\mathbf{Q}\neq\mathbf{0}.\tag{6.37}$$

To apply Bloch's theorem, Eq. (6.37) must first be linearized about $\overset{0}{\mathbf{Q}}$, which is most easily accomplished by applying the small angle assumptions $\sin\theta\approx\theta$ and $\cos\theta\approx1$ (which are applied after evaluating the derivatives of $\widetilde{\Pi}$). Due to the discrete nature of the system, the only term of Eq. (6.37) affected by the the linearization is $\widetilde{\Pi}_{,\mathbf{QQ}}(\overset{0}{\mathbf{Q}};P)$, resulting in

$$\left\langle\left(\mathbf{K}(P_c)\cdot\Delta\overset{1}{\mathbf{Q}}\right),\delta\mathbf{Q}\right\rangle=0\quad\forall\quad\delta\mathbf{Q}\neq\mathbf{0},\tag{6.38}$$

where

$$\mathbf{K}(P) = \frac{1}{4} g_1 L^2 \begin{bmatrix} -(2P-\eta(\xi+1)-4) & -(2P-\eta(\xi+3)-4) & (2P-\eta(\xi+1)) & -(2P-\eta(3\xi+1)) \\ -(2P-\eta(\xi+3)-4) & -(6P-\eta(\xi+9)-4) & (2P-\eta(\xi+3)) & -(2P-3\eta(\xi+1)) \\ (2P-\eta(\xi+1)) & (2P-\eta(\xi+3)) & -(2P-4\zeta-\eta(\xi+1)) & (2P-4\zeta-\eta(3\xi+1)) \\ -(2P-\eta(3\xi+1)) & -(2P-3\eta(\xi+1)) & (2P-4\zeta-\eta(3\xi+1)) & -(6P-4\zeta-\eta(9\xi+1)) \end{bmatrix} \tag{6.39}$$

is the linearized version of $\widetilde{\Pi}_{,\mathbf{QQ}}(\overset{0}{\mathbf{Q}}; P)$ and corresponds to the tangent stiffness matrix of the unit cell. Based on the geometry of the unit cell (Figure 6.2b), the Bloch boundary conditions are defined by

$$\underbrace{\begin{bmatrix} \Delta\overset{1}{W}_4 \\ \Delta\overset{1}{\theta}_3 \end{bmatrix}}_{\Delta\overset{1}{\mathbf{Q}}_\beta} = \underbrace{\begin{bmatrix} \mathrm{e}^{i2\pi\kappa} & 0 \\ 0 & \mathrm{e}^{i2\pi\kappa} \end{bmatrix}}_{\mathbf{A}(\kappa)} \underbrace{\begin{bmatrix} \Delta\overset{1}{W}_1 \\ \Delta\overset{1}{\theta}_1 \end{bmatrix}}_{\Delta\overset{1}{\mathbf{Q}}_\alpha} \tag{6.40a}$$

$$\delta\mathbf{Q}_\beta = \mathbf{A}(\kappa) \cdot \delta\mathbf{Q}_\alpha, \tag{6.40b}$$

where $\kappa = 4Lk/(2\pi)$ is the dimensionless Bloch wavenumber such that $\mathcal{B} = \{\kappa \mid \kappa \in (-1/2, 1/2]\}$ is the corresponding First Brillouin Zone[3]. Applying the Bloch boundary conditions (Eq. (6.40)) to the linear critical stability condition (Eq. (6.38)),

$$\delta\mathbf{Q}_\alpha^H(\kappa)\tilde{\mathbf{K}}(P_c;\kappa^*)\Delta\overset{1}{\mathbf{Q}}_\alpha(\kappa) = 0 \quad \forall \quad \delta\mathbf{Q}_\alpha(\kappa) \neq \mathbf{0}, \tag{6.41}$$

where

$$\tilde{\mathbf{K}}(P_c;\kappa) = \mathbf{K}_{\alpha\alpha}(P_c) + \mathbf{A}^H(\kappa)\mathbf{K}_{\beta\alpha}(P_c) + \mathbf{K}_{\alpha\beta}(P_c)\mathbf{A}(\kappa) + \mathbf{A}^H(\kappa)\mathbf{K}_{\beta\beta}(P_c)\mathbf{A}(\kappa) \tag{6.42}$$

and $(.)^H$ denotes the conjugate transpose of a matrix (or vector). Due to the form of Eq. (6.42), $\tilde{\mathbf{K}}$ is a Hermitian matrix (i.e. $\tilde{\mathbf{K}}^H = \tilde{\mathbf{K}}$) and, hence, has real eigenvalues. Eq. (6.41) corresponds to the eigenvalue problem

$$\tilde{\mathbf{K}}(P_c;\kappa)\Delta\overset{1}{\mathbf{Q}}_\alpha = \mathbf{0} \tag{6.43}$$

which has a nontrivial solution (i.e., $\Delta\overset{1}{\mathbf{Q}}_\alpha \neq 0$) when

$$\det\tilde{\mathbf{K}}(P_c;\kappa) = 0. \tag{6.44}$$

[3]Note that the subscripts α and β are labels, not indices.

Applying Eq. (6.39) and Eq. (6.40) to determine $\tilde{\mathbf{K}}$, Eq. (6.44) is defined by

$$\begin{aligned} 8\sin^2(\kappa\pi)P^2 + 4\left[\eta(1+\xi)\cos(2\pi\kappa) - 2(1+\zeta) - \eta(1+\xi)\right]P \\ + 4\eta + 8\zeta(1+\eta) + \eta\xi(8+4\zeta+3\eta) \\ + 4\eta(1+\zeta\xi-\eta\xi)\cos(2\pi\kappa) + \eta^2\xi\cos(4\pi\kappa) = 0, \end{aligned} \tag{6.45}$$

which is a quadratic equation with the solutions

$$P_c^{(1)}(\kappa) = \frac{1}{4}\left[2\eta(1+\xi) + 2(1+\zeta)\csc^2(\kappa\pi) - \chi(\kappa)\right] \tag{6.46a}$$

$$P_c^{(2)}(\kappa) = \frac{1}{4}\left[2\eta(1+\xi) + 2(1+\zeta)\csc^2(\kappa\pi) + \chi(\kappa)\right] \tag{6.46b}$$

where

$$\begin{aligned} \chi(\kappa) = \csc^2(\kappa\pi)\Big[(2+2\zeta+\eta+\eta\xi-\eta(1+\xi)\cos^2(2\pi\kappa) \\ -2\sin^2(\kappa\pi)\left(4\eta + 8\zeta(1+\eta) + \eta(8+4\zeta+3\eta)\xi\right. \\ \left. +4\eta(1+\zeta\xi-\eta\xi)\cos(2\pi\kappa) + \eta^2\xi\cos(4\pi\kappa)\right)\Big]^{1/2}. \end{aligned} \tag{6.47}$$

Noting that $\chi(\kappa) > 0$ for all $\kappa \in \mathcal{B}$, $P_c^{(1)}(\kappa) \leq P_c^{(2)}(\kappa)$. Since we are interested in the first loss of stability of the principal solution path, $P_c^{(1)}(\kappa)$ is therefore the only relevant solution; additionally, due to the dependence of $P_c^{(1)}$ on κ, the solution must be further refined to be

$$P_c^* = \inf_{\kappa\in\mathcal{B}} P_c^{(1)}(\kappa) \tag{6.48}$$

and κ^* is defined such that $P_c^* = P_c^{(1)}(\kappa^*)$. In general, P_c^* cannot be solved for analytically and must therefore be solved numerically using a root finding algorithm (such as a Newton–Raphson solver).

The mode shape $\Delta\overset{1}{\mathbf{Q}}_\alpha = [\Delta\overset{1}{W}_1, \Delta\overset{1}{\theta}_1]$ corresponding to the load P_c (be that $P_c^{(1)}$, $P_c^{(2)}$, or P_c^*), can be determined from Eq. (6.43) by calculating the nullspace of $\tilde{\mathbf{K}}(P_c(\kappa), \kappa)$. The deformation corresponding to the β degrees of freedom (W_4 and θ_3) are then determined from the Bloch boundary conditions (Eq. (6.40)). Lastly, the deformation of the n$^{\text{th}}$ unit cell can be determined from Bloch's theorem (Eq. (6.3)) according to the relationship

$$\Delta\overset{1}{\mathbf{Q}}_n = \mathrm{e}^{i2\pi n}\Delta\overset{1}{\mathbf{Q}}, \tag{6.49}$$

where $n < 0$ and $n > 0$ correspond to unit cells to the left and right of the reference unit cell, respectively. To then inspect the physical characteristics of the mode shape, either the real or

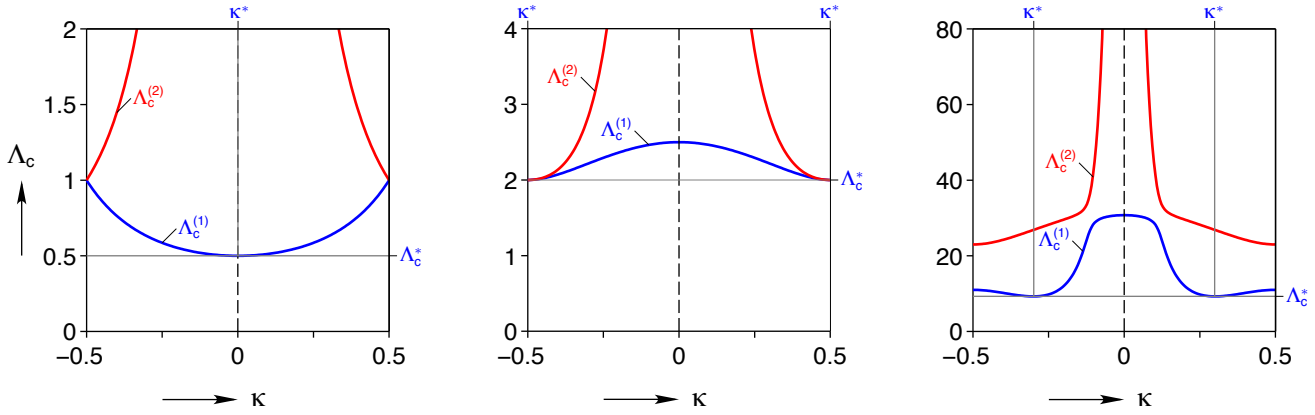

(a) $\eta = \xi = 0$ and $\zeta = 1$ (b) $\eta = \xi = \zeta = 1$ (c) $\eta = 10$, $\xi = 2$, and $\zeta = 3$

Figure 6.3: There are three characteristics behaviors of the rigid link system defined by the material properties of the springs, corresponding to the critical cases: (a) $\kappa^* = 0$ for $\eta = \xi = 0$ and $\zeta \neq 0$, (b) $\kappa^* = 1/2$ for $\eta = \xi \neq 0$ and $\zeta \neq 0$, and (c) $\kappa^* \in (-1/2) \cup (0, 1/2)$ for $\eta \neq \xi \neq 0$ and $\zeta \neq 0$.

imaginary part of $\Delta \overset{1}{\mathbf{Q}}_n$ can be examined.

Results

To gain a better sense of the interpretation of the *Bloch wave* stability analysis, it is useful to examine the $P_c^{(1)}$ and $P_c^{(2)}$ behavior over the First Brillouin Zone (i.e., for $\kappa \in \mathcal{B} = (-1/2, 1/2]$). Three cases are shown in Figure 6.3, demonstrating the possible representative behaviors of the rigid link system. In all cases, the behavior of P_c is symmetric about $\kappa = 0$, which is a result of the translational symmetry of the system; in particular, it can be shown that $\tilde{\mathbf{K}}(\kappa)$ and $\tilde{\mathbf{K}}(-\kappa)$ are similar matrices and, hence, have the same eigenvalues and stability characteristics. It turns out that this is a general property that always arises in Bloch stability analysis and implies that the first loss of stability (P_c^*) need only be searched for over a subset of the First Brillouin Zone ($\kappa \in [0, 1/2]$ for the current system). Additionally, as stated previously, $P_c^{(1)} \leq P_c^{(2)}$ for all $\kappa \in \mathcal{B}$. The first instability P_c^* is therefore defined by the the infimum of $P_c^{(1)}$ as shown in Figure 6.3.

The three characteristic behaviors of the system are dependent on the material properties of the springs in the rigid link system: $\eta = \xi = 0$ and $\zeta \neq 0$; $\eta = \xi \neq 0$ and $\zeta \neq 0$; and $\eta \neq \xi \neq 0$ and $\zeta \neq 0$. In the case that $\eta = \xi = 0$ (Figure 6.3a), there are no rotational springs in the system. This system is highly symmetric, resulting in $\kappa^* = 0$, which corresponds to a mode shape with the same periodicity as the unit cell (Figures 6.3a and 6.4a). When the rotational springs are added into the system such that they have the same properties ($\eta = \xi \neq 0$), the critical behavior shifts to $\kappa^* = 1/2$, which corresponds to a mode shape with a periodicity

of two unit cells (Figures 6.3b and 6.4b). Lastly, when the symmetry of the rotational spring stiffnesses is broken ($\eta \neq \xi \neq 0$), the critical behavior again shifts (Figure 6.3c) and corresponds to $\kappa^* \in (-1/2) \cup (1/2)$. The physical interpretations of these mode shapes are not well defined, as will be discussed further in Section 6.5.2; however, the mode shapes for a few explicit $\kappa \neq \kappa^*$ from $P_c^{(1)}$ for $(\eta, \xi, \zeta) = (10, 2, 3)$ are shown for reference in Figures 6.4c and 6.4d.

6.5.2 Beam with Periodic Bending Stiffness and Stabilizing Spring

The second example looks at the application of Bloch's theorem in context of column buckling of a linear–elastic beam. The solution procedure to this continuous system differs rather significantly from the previously discussed discrete system in Section 6.5.1, although the fundamental concepts remain the same. Due to the increased complexity of the problem, stability is only examined in the context of the loss of uniqueness of the principal equilibrium path (i.e., stability is not explicitly evaluated).

Problem Statement

An infinitely long linear elastic beam is axially compressed by the load p as illustrated in Figure 6.5. The bending stiffness of the beam (EI where E is the elastic modulus and I is the area bending moment of inertia of the beam cross-section) alternates between EI_1 and EI_2 every length L along the beam. Located at the junctures of the differing beam bending stiffnesses are springs with stiffness g, spaced every $2L$ along the beam length. In the context of the *Bloch wave* stability analysis discussed in Section 6.4.2, the lattice vector is $\mathbf{R}_u = 2Lu\mathbf{e}_1$ and the First Brillouin Zone is $\mathcal{B} = \{k \mid 2Lk \in (-\pi, \pi]\}$. At a critical load p_c, the initially straight beam buckles with the displacement field w.

Model

According to classical beam theory, the governing equilibrium equation for out–of–plane displacement of an axially compressed beam is

$$f(x) = EI(x)\frac{\mathrm{d}^4 w(x)}{\mathrm{d}x^4} + p\frac{\mathrm{d}^2 w(x)}{\mathrm{d}x^2} = 0 \quad \forall \quad x \in \mathcal{D} \tag{6.50}$$

where x is the position along the beam length, $\mathcal{D}$ is the domain of the beam, w is the lateral deflection field, EI is the bending stiffness along the beam length, and p is the externally applied

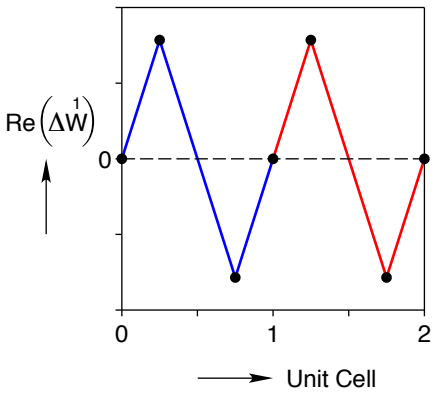

(a) Unit cell periodic ($\kappa^* = 0$)

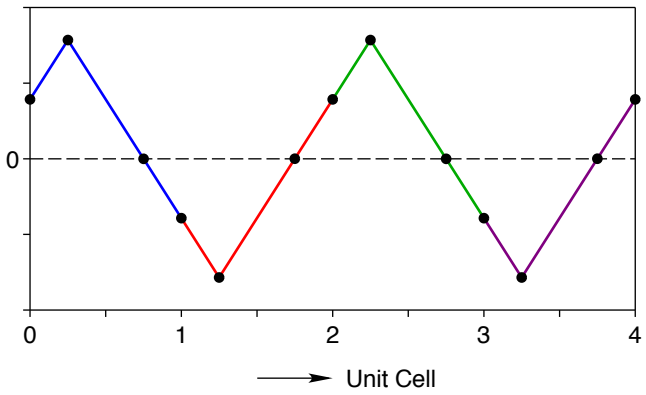

(b) Periodicity of two unit cells ($\kappa^* = 1/2$)

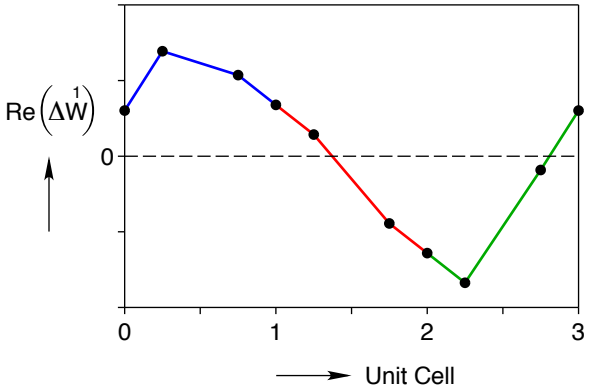

(c) Three unit cell periodic ($\kappa = 1/3 = 2/3$)

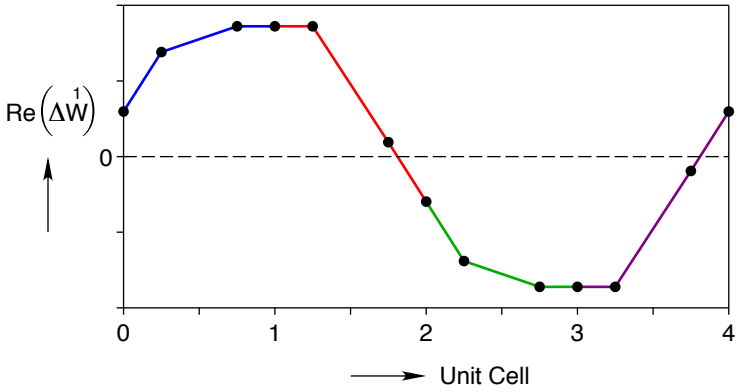

(d) Four unit cell periodic ($\kappa = 1/4 = 3/4$)

Figure 6.4: The periodicity of a mode shape $(\overset{1}{\Delta W})$ is defined by the Bloch wavenumber κ of the instability.

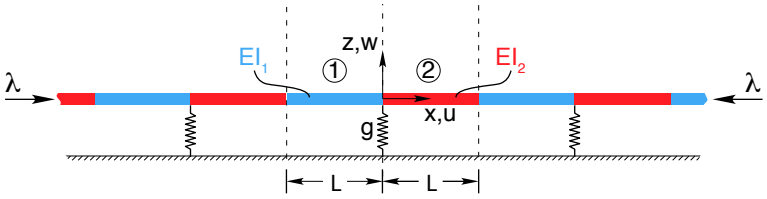

Figure 6.5: An infinite beam with periodic bending stiffness is axially loaded until it first buckles.

axial load; for the unit cell defined in Figure 6.5, $f(x)$ is piecewise defined by

$$f(x) = \begin{cases} EI_1 \frac{\mathrm{d}^4 w_1(x)}{\mathrm{d}x^4} + p\frac{\mathrm{d}^2 w_1(x)}{\mathrm{d}x^2} & \text{for} \quad -L \leq x \leq 0 \\ EI_2 \frac{\mathrm{d}^4 w_2(x)}{\mathrm{d}x^4} + p\frac{\mathrm{d}^2 w_2(x)}{\mathrm{d}x^2} & \text{for} \quad 0 \leq x \leq L \end{cases}. \tag{6.51}$$

Due to the piecewise nature of $f(x)$, continuity of displacements, rotations, moments, and transverse shear between the piecewise sections must be enforced according to the conditions

$$w_1(0) = w_2(0) \tag{6.52a}$$
$$w_1'(0) = w_2'(0) \tag{6.52b}$$
$$EI_1 w_1''(0) = EI_2 w_2''(0) \tag{6.52c}$$
$$EI_1 w_1'''(0) = EI_2 w_2'''(0) + g w_2(0). \tag{6.52d}$$

To properly account for the deformation of the infinite system, Bloch boundary conditions are applied to the boundaries of the unit cell (noting that we can apply Bloch's theorem since Eq. (6.50) is a linear ordinary differential equation). The general form of a Bloch boundary condition for the given system is

$$h(x + 2nL) = h(x)\mathrm{e}^{i2kL}, \tag{6.53}$$

where $h(x)$ is a generic field quantity. Similar to the continuity conditions at the center of the beam (Eq. (6.52)), the displacements, rotations, moments and transverse shear must abide by Eq. (6.53); therefore, the field quantities at the boundary of the unit cell are related by

$$w_1(-L) = w_2(L)\mathrm{e}^{-i2Lk} \tag{6.54a}$$
$$w_1'(-L) = w_2'(L)\mathrm{e}^{-i2Lk} \tag{6.54b}$$
$$EI_1 w_1''(-L) = EI_2 w_2''(L)\mathrm{e}^{-i2Lk} \tag{6.54c}$$
$$EI_1 w_1'''(-L) = EI_2 w_2'''(L)\mathrm{e}^{-i2Lk}. \tag{6.54d}$$

To generlized the analysis, the problem is nondimensionalized according to the relationships

$$P \equiv \frac{pL^2}{EI_1};\;\; X \equiv \frac{x}{L};\;\; W_i \equiv \frac{w_i}{L};\;\; \kappa \equiv \frac{Lk}{\pi};\;\; \zeta \equiv \frac{EI_2}{EI_1};\;\; \eta \equiv \frac{gL^3}{EI_1}, \tag{6.55}$$

noting that the First Brillouin Zone for the normalized wavenumber is $\mathcal{B} = \{\kappa \mid \kappa \in (-1/2, 1/2]\}$. The resulting governing equilibrium equation is

$$0 = f(X) = \begin{cases} \frac{\mathrm{d}^4 W_1(X)}{\mathrm{d}X^4} + P\frac{\mathrm{d}^2 W_1(X)}{\mathrm{d}X^2} & \text{for} \quad -1 \le X \le 0 \\ \zeta\frac{\mathrm{d}^4 W_1(X)}{\mathrm{d}X^4} + P\frac{\mathrm{d}^2 W_1(X)}{\mathrm{d}X^2} & \text{for} \quad 0 \le X \le 1 \end{cases}, \tag{6.56}$$

with the continuity conditions

$$W_1(0) = W_2(0) \tag{6.57a}$$
$$W_1'(0) = W_2'(0) \tag{6.57b}$$
$$W_1''(0) = \zeta W_2''(0) \tag{6.57c}$$
$$W_1'''(0) = \zeta W_2'''(0) + \eta W_2(0) \tag{6.57d}$$

and the Bloch boundary conditions

$$W_1(-1) = W_2(1)\mathrm{e}^{-i2\pi\kappa} \tag{6.58a}$$
$$W_1'(-1) = W_2'(1)\mathrm{e}^{-i2\pi\kappa} \tag{6.58b}$$
$$W_1''(-1) = \zeta W_2''(1)\mathrm{e}^{-i2\pi\kappa} \tag{6.58c}$$
$$W_1'''(-1) = \zeta W_2'''(1)\mathrm{e}^{-i2\pi\kappa}. \tag{6.58d}$$

Solution

The general form of the piecewise solution to the governing equation Eq. (6.56) is

$$W_1(X) = C_1 + D_1 X - \frac{B_1}{P}\sin\left(X\sqrt{P}\right) - \frac{A_1}{P}\cos\left(X\sqrt{P}\right) \tag{6.59a}$$
$$W_2(X) = C_2 + D_2 X - \frac{\zeta B_2}{P}\sin\left(X\sqrt{\frac{P}{\zeta}}\right) - \frac{\zeta A_2}{P}\cos\left(X\sqrt{\frac{P}{\zeta}}\right), \tag{6.59b}$$

where A_j, B_j, C_j and D_j are arbitrary constants. Applying the general solution (Eq. (6.59)) to the continuity conditions (Eq. (6.57)) and the Bloch boundary conditions (Eq. (6.58)) results in the system of equations

$$\mathbf{M}(P;\kappa)\mathbf{u} = \mathbf{0}, \tag{6.60}$$

where

$$\mathbf{u} = [A_1\ B_1\ C_1\ D_1\ A_2\ B_2\ C_2\ D_2]^T \tag{6.61}$$

and

$$\mathbf{M}(P;\kappa) = \begin{bmatrix} \mathbf{M}_{11}(P) & \mathbf{M}_{12}(P) \\ \mathbf{M}_{21}(P) & \mathbf{M}_{22}(P;\kappa) \end{bmatrix} \tag{6.62}$$

such that

$$\mathbf{M}_{11}(P) = \begin{bmatrix} -\frac{1}{P} & 0 & 1 & 0 \\ 0 & -\frac{1}{\sqrt{P}} & 0 & 1 \\ 1 & 0 & 0 & 0 \\ 0 & -\sqrt{P} & 0 & 0 \end{bmatrix}, \tag{6.63a}$$

$$\mathbf{M}_{12}(P) = \begin{bmatrix} \frac{\zeta}{P} & 0 & -1 & 0 \\ 0 & \sqrt{\frac{\zeta}{P}} & 0 & -1 \\ -\zeta & 0 & 0 & 0 \\ -\zeta\frac{\eta}{P} & \sqrt{\zeta P} & \eta & 0 \end{bmatrix}, \tag{6.63b}$$

$$\mathbf{M}_{21}(P) = \begin{bmatrix} -\frac{\cos\sqrt{P}}{P} & \frac{\sin\sqrt{P}}{P} & 1 & -1 \\ -\frac{\sin\sqrt{P}}{P} & -\frac{\cos\sqrt{P}}{P} & 0 & 1 \\ \cos\sqrt{P} & -\sin\sqrt{P} & 0 & 0 \\ \sqrt{P}\sin\sqrt{P} & \sqrt{P}\cos\sqrt{P} & 0 & 0 \end{bmatrix}, \tag{6.63c}$$

$$\mathbf{M}_{22}(P;\kappa) = \mathrm{e}^{-i2\pi\kappa}\begin{bmatrix} \frac{\zeta\cos\sqrt{P/\zeta}}{P} & \frac{\zeta\sin\sqrt{P/\zeta}}{P} & -1 & -1 \\ -\sqrt{\zeta/P}\sin\sqrt{P/\zeta} & \sqrt{\zeta/P}\cos\sqrt{P/\zeta} & 0 & 1 \\ -\zeta\cos\sqrt{P/\zeta} & -\zeta\sin\sqrt{P/\zeta} & 0 & 0 \\ \sqrt{\zeta P}\cos\sqrt{P/\zeta} & -\sqrt{\zeta P}\sin\sqrt{P/\zeta} & 0 & 0 \end{bmatrix}. \tag{6.63d}$$

Since $\kappa = 0$ corresponds to unit cell periodic boundary conditions,

$$\mathbf{M}(P;0)\overset{0}{\mathbf{u}} = \mathbf{0}, \tag{6.64}$$

defines the equilibrium equation for the principal path, which has the trivial solution $\overset{0}{\mathbf{u}} = \mathbf{0}$.

As noted in Section 6.4.1, loss of uniqueness of the principal solution path often corresponds to loss of stability. From the form of Eq. (6.60), we are therefore interested in the eigenvalue problem

$$\mathbf{M}(P_c;\kappa)\Delta\overset{1}{\mathbf{u}} = \mathbf{0} \tag{6.65}$$

such that $\Delta\overset{1}{\mathbf{u}} \neq \mathbf{0}$, which reduces to

$$\det\mathbf{M}(P_c;\kappa) = 0. \tag{6.66}$$

Evaluating the determinant of $\mathbf{M}(P_c;\kappa)$, the resulting characteristic equation is of the form

$$\det\mathbf{M} = z^4 - I_1(P_c)z^3 + I_2(P_c)z^2 - I_1(P_c)z + 1 = 0, \tag{6.67}$$

where $z = \mathrm{e}^{-i2\pi\kappa}$ and

$$I_1(P_c) = \frac{2\sqrt{\zeta}\sqrt{P_c}(P_c-\eta) + \sqrt{\zeta}\cos\left[\frac{\sqrt{P_c}}{\sqrt{\zeta}}\right]\left(2P_c^{3/2}\cos\left[\sqrt{P_c}\right] + \eta\sin\left[\sqrt{P_c}\right]\right)}{\sqrt{\zeta}P_c^{3/2}} + \frac{\left(\zeta\eta\cos\left[\sqrt{P_c}\right] - (1+\zeta)P_c^{3/2}\sin\left[\sqrt{P_c}\right]\right)\sin\left[\frac{\sqrt{P_c}}{\sqrt{\zeta}}\right]}{\sqrt{\zeta}P_c^{3/2}} \tag{6.68a}$$

$$I_2(P_c) = \frac{2\left[\sqrt{\zeta}P_c^{3/2} + \sqrt{\zeta}\cos\left[\frac{\sqrt{P_c}}{\sqrt{\zeta}}\right]\left(2\sqrt{P_c}(P_c-\eta)\cos\left[\sqrt{P_c}\right] + \eta\sin\left[\sqrt{P_c}\right]\right)\right]}{\sqrt{\zeta}P_c^{3/2}} + \frac{2\left[\left(\zeta\eta\cos\left[\sqrt{P_c}\right] + (1+\zeta)(\eta-P_c)\sqrt{P_c}\sin\left[\sqrt{P_c}\right]\right)\sin\left[\frac{\sqrt{P_c}}{\sqrt{\zeta}}\right]\right]}{\sqrt{\zeta}P_c^{3/2}}. \tag{6.68b}$$

Interested in the first loss of stability of the system,

$$P_c^* = \inf_{\kappa\in\mathcal{B}} P_c(\kappa) \tag{6.69}$$

where κ^* is defined such that $P_c^* = P_c(\kappa^*)$.

Due to the nonlinear coefficients I_1 and I_2, the characteristic equation Eq. (6.67) cannot be solved analytically and must therefore be solved numerically. The problem can be somewhat simplified by taking advantage of the specialized polynomial form of Eq. (6.67) where the functional dependence on P and κ are decoupled; however, a numerical solution procedure is required regardless, so this added complexity is overlooked here. There are a number of possible numerical approaches to this problem:

- a **direct root finding** algorithm such as a Newton solver,
- a **hybrid brute force/root finding algorithm** in which one of the parameters is discretized (often κ) and then a root finder is applied to solve for the other parameter at each of these discretized points, after which the case corresponding to the minimum P_c solution is chosen as P_c^*,
- a **hybrid root finder/minimization procedure** in which the solution (P_c,κ) to Eq. (6.67) determined by the root finder is minimized with respect to P_c so as to ensure proper determination of P_c^*.

Of these possibilities, the direct root finder is the least robust as there is no guarantee that the solution corresponds to P_c^*. Of the two remaining solution techniques, the hybrid root finder/minimization procedure is a more efficient implementation of the hybrid brute force/root finding procedure; however, its implementation is more complicated and tends to be less numerically robust due to the periodicity of the characteristic equation with respect to κ. In the results that are presented, the hybrid brute force/root finding algorithm is therefore used for its simplicity and reliability.

For a given solution P_c and κ to the characteristic equation Eq. (6.67) (which need not be P_c^* and κ^*), the corresponding global mode shape can be determined through the use of Bloch's theorem.

From the matrix form of equilibrium (Eq. (6.65)), the coefficient vector $\overset{1}{\Delta\mathbf{u}} \in \mathbb{C}^8$ (Eq. (6.61)) can be determined to within an arbitrary constant by finding the nullspace of $\mathbf{M}(P_c, \kappa)$ (Eq. (6.62)). Substituting the results of $\overset{1}{\Delta\mathbf{u}}$ into the general forms of W_1 and W_2 (Eq. (6.59)), the mode shape within the unit cell can then be piecewise represented. The mode shape of the n$^{\text{th}}$ unit cell is then extrapolated from the mode shape within the unit cell using the nondimensional form of Bloch's theorem (which is derived from Eqs. (6.53) and (6.55)):

$$W(X+2n) = P(X+2n;\kappa)\mathrm{e}^{i2\pi\kappa(X+2n)/2} \tag{6.70a}$$

$$= P(X;\kappa)\mathrm{e}^{i2\pi\kappa(X+2n)/2} \qquad \text{from the periodicity of } P \tag{6.70b}$$

$$= \underbrace{P(X;\kappa)\mathrm{e}^{i2\pi\kappa X/2}}_{W(X)}\mathrm{e}^{i2\pi\kappa n} \qquad \text{splitting the exponential} \tag{6.70c}$$

$$= W(X)\mathrm{e}^{i2\pi\kappa n}, \tag{6.70d}$$

where $n > 0$ correspond to unit cells to the right of $x = 0$ and $n < 0$ correspond to unit cells to the left of $x = 0$. As a final step, either the real or imaginary part of W should be taken to establish a physical interpretation of the results.

Results

In general, the buckling behavior of the beam is highly coupled with the relative spring stiffness $\eta = gL^3/EI_1$ and the ratio of bending stiffnesses $\zeta = EI_2/EI_1$ as shown in Figure 6.6. For both increasing η and ζ, the critical buckling load P_c^* increases (Figure 6.6a). In the case of the critical buckling wavenumber[4], κ^* is predominantly dependent on η, plateauing at a value of $1/2$ (periodicity of 2 unit cells) for large η (Figure 6.6b).

Based on the mapping of κ^* in Figure 6.6b, there are two characteristic behaviors of the defined problem: $\kappa^* = 1/2$ and $\kappa^* \in (0, 1/2)$. In the case of $\kappa^* = 1/2$, the instability corresponds to a fundamental wavelength of exactly two unit cells. Since there are no cases in which $\kappa^* = 0$, the $\kappa^* = 1/2$ case corresponds to the shortest fundamental wavelength of the instability mode shapes for the defined problem. In the case of $\kappa^* \in (0, 1/2)$, the fundamental wavelength is less well defined due to the almost-periodic behavior of *Bloch waves* as discussed in Section 6.3; in particular, the numerical procedure limits solutions to periodic *Bloch waves* and the highly discontinuous mapping between the κ and fundamental wavelength spaces leaves the results up for some interpretation.

To help illustrate some of the issues associated with interpreting the physical meaning of the κ

[4]Only results for $\kappa^* \in [0, 1/2]$ are shown due to the symmetry of the κ^* results with respect to the origin.

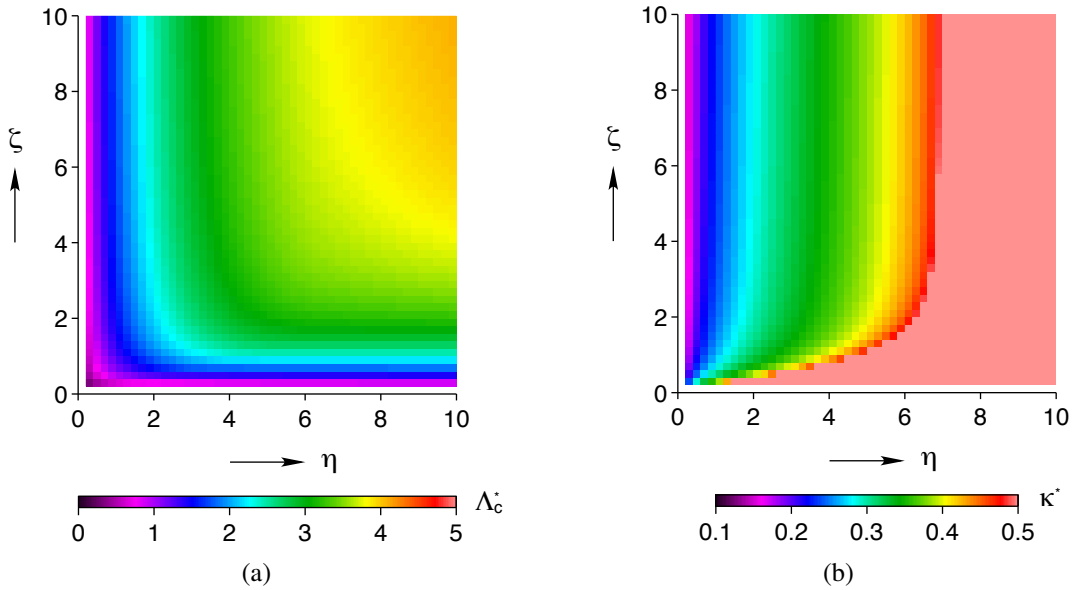

Figure 6.6: Maps of the critical buckling load P_c^* (a), and the corresponding critical buckling Bloch wavenumber κ^* (b), with respect to the spring stiffness η and the bending stiffness ratio ζ, showing increasing buckling load with η and ζ, along with the plateau of the κ^* to $1/2$ for high η.

parameter, the effects of numerical precision on the perceived fundamental wavelength of a particular mode shape are presented in Table 6.1 for the cases $(\eta, \zeta) = \{(50, 20), (1, 1/2), (1/10, 10)\}$. Since the fundamental wavelength of a *Bloch wave* with wavenumber $k = 2\pi\kappa/(2L)$ is defined by the denominator $2Lb$ such that $\kappa \equiv a/b$ (where a and b are integers and a/b is an irreducible rational number), the calculated κ^* must be rationalized to interpret its physical characteristics. Two of the most common ways to rationalize a number are to

- simply truncate the number to a desired number of digits such that

$$\kappa^* \approx \frac{a}{b} \equiv \frac{\text{round}(\kappa^* \cdot 10^n)}{10^n}, \tag{6.71}$$

  where n is an integer defining the desired degree of truncation and the resulting form must be simplified into its irreducible form; or

- find the smallest b such that

$$\left|\kappa^* - a/b\right| < tol, \tag{6.72}$$

  where tol is the desired tolerance of the approximation (which is most often achieved using the method of continued fractions, such as the *rat* function in MATLAB®).

The second method (Eq. (6.72)) is the most applicable to the problem here as it better addresses the issues associated with the discontinuous mapping between the κ and fundamental wavelength spaces. At the boundary of the κ space ($\kappa^* = 1/2$), this procedure results in a consistent result of $b = 2$ as seen in the first row of Table 6.1; however, for the cases in Table 6.1 in which $\kappa^* \in (0, 1/2)$ (i.e., $(\eta, \zeta) = \{(1, 1/2), (1/10, 10)\}$), there is a wide range of interpretations of the normalized wavelength b based on the desired tolerance tol as show in rows two and three of Table 6.1. This ambiguity has little effect on the quantification of P_c^* (which is a continuous function with respect to κ^*), but likely has implications on the prediction of the post-buckling behavior of the structure (such as imperfection sensitivity).

Table 6.1: Comparison of wavelengths predicted by the rationalization of the wavenumber κ^* for three select cases, illustrating some of the issues associated with interpreting the wavelength of the critical instability mode shape.

		Normalized wavelength b based on the rationalization tolerance tol							
(η,ζ)	κ^*	10^{-1}	10^{-2}	10^{-3}	10^{-4}	10^{-5}	10^{-6}	10^{-7}	10^{-8}
(50,20)	$1/2$	2	2	2	2	2	2	2	2
(1,$1/2$)	0.2986068943	1	10	10	67	144	1651	1651	1651
($1/10$,10)	0.1302800588	1	8	8	23	284	284	2249	2249

6.5.3 Honeycomb

Finally, the last example examines the stability analysis of a two-dimensional honeycomb (framed) structure. Unlike the previous two examples, this problem is solved in the context of a nonlinear finite element analysis to discuss some of the aspects associated with a completely numerical procedure. This example also serves as a basis for the analysis discussed in Section 7.2 regarding the behavior of SMA honeycombs.

Problem Statement

A two dimensional infinite hexagonal honeycomb is axially compressed under displacement control along the Y axis, as shown in Figure 6.7. The honeycomb has an orthorhombic unit cell with an internal hexagonal ligament structure defined by the horizontal ligament length $\ell \approx 0.462$ mm, diagonal ligament length $h = 1$ mm, diagonal ligament angle $\theta = 30°$, and ligament thickness $d = 0.025$ mm (noting that the horizontal ligaments have thickness $2d$). The resulting unit cell has

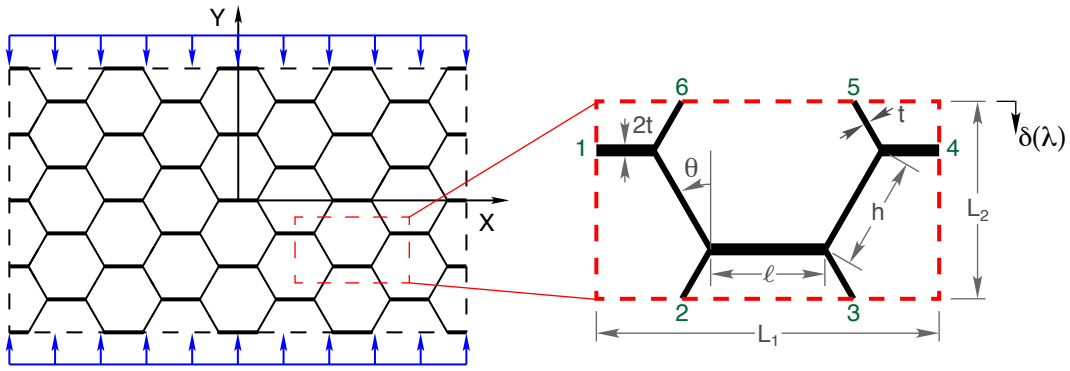

Figure 6.7: An infinite honeycomb with an orthorhombic unit cell is axially compressed until the onset of instability.

width $L_1 = 2(\ell + h\sin\theta) \approx 1.925\,\text{mm}$ and height $L_2 = 2h\cos\theta \approx 1.732\,\text{mm}$. In the context of the general outline of the *Bloch wave* analysis in Section 6.4.2, the honeycomb lattice vector is $\mathbf{R}_{uv} = uL_1\mathbf{e}_I + vL_2\mathbf{e}_J$ and the First Brillouin zone is $\mathcal{B} = \{(k_1, k_2) \mid k_1L_1, k_2L_2 \in (-\pi, \pi]\}$; additionally, to simplify the application of the Bloch boundary conditions, the unit cell was chosen such that only ligament ends (i.e., element nodes) intersect its boundary (see Figure 6.7). Of interest is the critical load p_c in which the infinite honeycomb becomes unstable.

Model

The honeycomb structure is modeled using a framed construction of the beam elements developed in Chapter 5 with the NiTi–like superelastic material properties outlined in Table 6.2. Each beam element therefore consists of two nodes, each of which has M degrees of freedom (where M is three or four depending on the choice of element definition as discussed in Sections 5.2.1 and 5.2.2). For a given loading state p, the behavior of the unconstrained unit cell is defined by the loading tangential stiffness matrix $\mathbf{K}(p)$ and has the solution vector $\mathbf{u}$.

To aide in the discussion, the degrees of freedom are grouped according to their location in the unit cell; in particular, those that lie on the boundary of the unit cell (denoted by a subscript b) and those that lie in the interior of the unit cell (denoted by a subscript i). The boundary degrees of freedom are further grouped according to nodes on opposite faces of the unit cell (subscripts α and

Table 6.2: The ligaments of the honeycomb structure are modeled according to the SMA beam model of Figure 5.2b using NiTi–like superelastic material parameters.

Parameter	Value
$E_A = E_M^+ = E_M^-$	1
$E_l^+ = E_u^+$	0.05
$E_l^- = E_u^-$	0.15
β^+	0.0418
β^-	-0.02125
ϵ_n^+	0.006
ϵ_n^-	0.0012
$\Delta\sigma_A^+ = \Delta\sigma_A^-$	0.002

β). For example, the stiffness matrix is arranged such that

$$\mathbf{K}(\lambda) \equiv \begin{bmatrix} \mathbf{K}_{bb}(\lambda) & \mathbf{K}_{bi}(\lambda) \\ \mathbf{K}_{ib}(\lambda) & \mathbf{K}_{ii}(\lambda) \end{bmatrix} \equiv \begin{bmatrix} \mathbf{K}_{\alpha\alpha}(\lambda) & \mathbf{K}_{\alpha\beta}(\lambda) & \mathbf{K}_{\alpha i}(\lambda) \\ \mathbf{K}_{\beta\alpha}(\lambda) & \mathbf{K}_{\beta\beta}(\lambda) & \mathbf{K}_{\beta i}(\lambda) \\ \mathbf{K}_{i\alpha}(\lambda) & \mathbf{K}_{i\beta}(\lambda) & \mathbf{K}_{ii}(\lambda) \end{bmatrix}. \tag{6.73}$$

For the unit cell defined in Figure 6.7, the boundary nodes (b) correspond to nodes 1 through 6, with the α nodes defined by nodes 1, 2 and 3 and the β nodes defined by nodes 4, 5 and 6.

Solution

The principal solution of the infinite honeycomb is evaluated using an incremental–based loading procedure which is parameterized by the monotonically increasing loading parameter λ. From the global boundary conditions,

$$\begin{aligned} F_X(-\infty, Y) = 0, \quad & F_Y(-\infty, Y) = 0, \quad & M(-\infty, Y) = 0 \\ F_X(\infty, Y) = 0, \quad & F_Y(\infty, Y) = 0, \quad & M(\infty, Y) = 0 \\ F_X(X, -\infty) = 0, \quad & V(X, -\infty) = 0, \quad & M(X, -\infty) = 0 \\ F_X(X, \infty) = 0, \quad & V(X, \infty) = \delta^*(\lambda), \quad & M(X, \infty) = 0, \end{aligned} \tag{6.74}$$

where V is a global displacement in the Y direction, F_X and F_Y are forces in the X and Y directions, respectively, and M is a bending moment. At the start of loading ($\lambda = 0$), the structure loads along the principal solution path which corresponds to unit cell periodic deformation. From Eq. (6.74), the corresponding unit cell periodic deformation corresponds to

$$\begin{aligned}
&F_X^{(1)} = 0, && F_Y^{(1)} = 0, && M^{(1)} = 0 \\
&F_X^{(4)} = 0, && F_Y^{(4)} = 0, && M^{(4)} = 0 \\
&U^{(2)} = F_X^{(3)} = 0, && V^{(2)} = V^{(3)} = 0, && M^{(2)} = M^{(3)} = 0 \\
&U^{(6)} = F_X^{(5)} = 0, && V^{(6)} = V^{(5)} = \delta(\lambda), && M^{(6)} = M^{(5)} = 0,
\end{aligned} \tag{6.75}$$

where U is a global displacement in the X direction and $(\cdot)^{(i)}$ denotes the i^{th} nodal quantity (see Figure 6.7 for node numbering of the unit cell); note that $U^{(2)} = V^{(2)} = V^{(3)} = 0$ to prevent rigid body motion and $U^{(6)} = 0$ from the periodic boundary conditions. At each loading step, the principal path solution is determined using a Newton-Raphson root–finding algorithm.

Stability of the structure is assessed about each equilibrium point in the loading procedure. For the inelastic behavior of the hysteretic trilinear SMA material model, the critical stability equation Eq. (6.23) defined for a conservative system is modified accordingly:

$$\delta\mathbf{u}^H \mathbf{K}(p_c) \overset{1}{\Delta\mathbf{u}} = 0 \quad \forall \quad \delta\mathbf{u} \neq \mathbf{0}, \tag{6.76}$$

noting that this critical state condition is a generalization of the tangent modulus condition for inelastic column buckling (see for example, Shanley [1947]). From the Bloch boundary conditions (Eq. (6.21)), the boundary degrees of freedom are related by

$$\underbrace{\begin{bmatrix} \Delta\mathbf{u}_4 \\ \Delta\mathbf{u}_5 \\ \Delta\mathbf{u}_6 \end{bmatrix}}_{\Delta\mathbf{u}_\beta} = \underbrace{\begin{bmatrix} e^{i2\pi\kappa_1}\mathbf{I} & \mathbf{0} & \mathbf{0} \\ \mathbf{0} & \mathbf{0} & e^{i2\pi\kappa_2}\mathbf{I} \\ \mathbf{0} & e^{i2\pi\kappa_2}\mathbf{I} & \mathbf{0} \end{bmatrix}}_{\mathbf{A}(\boldsymbol{\kappa})} \underbrace{\begin{bmatrix} \Delta\mathbf{u}_1 \\ \Delta\mathbf{u}_2 \\ \Delta\mathbf{u}_3 \end{bmatrix}}_{\Delta\mathbf{u}_\alpha} \tag{6.77a}$$

$$\delta\mathbf{u}_\beta = \mathbf{A}(\boldsymbol{\kappa})\delta\mathbf{u}_\alpha, \tag{6.77b}$$

where $\Delta\mathbf{u}_i$ are a $M \times 1$ vectors corresponding to node numbers $i = 1, ..., 6$ (see Figure 6.7), $\boldsymbol{\kappa} = [\kappa_1, \kappa_2]$, $\kappa_i \equiv k_i L_i/(2\pi) \in (-1/2, 1/2]$ is the dimensionless Bloch wavenumber (for $i = 1, 2$), $\mathbf{I}$ and $\mathbf{0}$ are the $M \times M$ identity and zeros matrices, and the Greek subscripts correspond to labels of groups of degrees of freedom (and are not indices). Applying the Bloch boundary conditions

(Eq. (6.77)) to the critical stability equation (Eq. (6.76)),

$$\delta\tilde{\mathbf{u}}^H(\boldsymbol{\kappa})\tilde{\mathbf{K}}(p_c;\kappa)\overset{1}{\Delta\tilde{\mathbf{u}}}(\boldsymbol{\kappa}) = 0 \quad \forall \quad \delta\tilde{\mathbf{u}}(\boldsymbol{\kappa}) \neq \mathbf{0}, \tag{6.78}$$

where $\overset{1}{\Delta\tilde{\mathbf{u}}} = [\overset{1}{\Delta\mathbf{u}}_\alpha, \overset{1}{\Delta\mathbf{u}}_i]^T$, $\delta\tilde{\mathbf{u}} = [\delta\mathbf{u}_\alpha, \delta\mathbf{u}_i]^T$,

$$\tilde{\mathbf{K}} = \begin{bmatrix} \tilde{\mathbf{K}}_{\alpha\alpha} & \tilde{\mathbf{K}}_{\alpha i} \\ \tilde{\mathbf{K}}_{i\alpha} & \tilde{\mathbf{K}}_{ii} \end{bmatrix}, \tag{6.79}$$

and

$$\tilde{\mathbf{K}}_{\alpha\alpha}(p_c;\boldsymbol{\kappa}) = \mathbf{K}_{\alpha\alpha}(p_c) + \mathbf{K}_{\alpha\beta}(p_c)\mathbf{A}(\boldsymbol{\kappa}) + \mathbf{A}(\boldsymbol{\kappa})^H\mathbf{K}_{\beta\alpha}(p_c) + \mathbf{A}(\boldsymbol{\kappa})^H\mathbf{K}_{\beta\beta}(p_c)\mathbf{A}(\boldsymbol{\kappa}) \tag{6.80a}$$

$$\tilde{\mathbf{K}}_{\alpha i}(p_c;\boldsymbol{\kappa}) = \mathbf{K}_{\alpha i}(p_c) + \mathbf{A}(\boldsymbol{\kappa})^H\mathbf{K}_{\beta i}(p_c) \tag{6.80b}$$

$$\tilde{\mathbf{K}}_{i\alpha}(p_c;\boldsymbol{\kappa}) = \mathbf{K}_{i\alpha}(p_c) + \mathbf{K}_{i\beta}(p_c)\mathbf{A}(\boldsymbol{\kappa}) \tag{6.80c}$$

$$\tilde{\mathbf{K}}_{ii}(p_c) = \mathbf{K}_{ii}(p_c). \tag{6.80d}$$

Since $\delta\tilde{\mathbf{u}} \neq \mathbf{0}$, Eq. (6.78) corresponds to the eigenvalue problem

$$\tilde{\mathbf{K}}(p_c;\boldsymbol{\kappa})\overset{1}{\Delta\tilde{\mathbf{u}}} = \mathbf{0}, \tag{6.81}$$

which implies that the nontrivial solution ($\overset{1}{\Delta\tilde{\mathbf{u}}} \neq 0$) for the loss of stability of the principal path is defined by

$$\det\tilde{\mathbf{K}}(p_c;\boldsymbol{\kappa}) = 0. \tag{6.82}$$

Since $\tilde{\mathbf{K}}(p_c;\boldsymbol{\kappa})$ in Eq. (6.82) is parameterized by $\boldsymbol{\kappa}$, the first loss of stability of the principal path is determined according to

$$p_c^* = \inf_{\boldsymbol{\kappa}\in\mathcal{B}} p_c(\boldsymbol{\kappa}). \tag{6.83}$$

and the corresponding critical wavevector $\boldsymbol{\kappa}^*$ is defined such that $p_c^* = p_c(\boldsymbol{\kappa}^*)$.

The mode shape corresponding to a critical load (be that p_c or p_c^*) corresponds to the eigenvector $\overset{1}{\Delta\tilde{\mathbf{u}}}$ which is determined by calculating the nullspace of $\tilde{\mathbf{K}}(p_c,\boldsymbol{\kappa})$. To define the mode shape for the whole unit cell, $\overset{1}{\Delta\mathbf{u}}_\beta$ are backed out from the Bloch boundary conditions Eq. (6.77). Lastly, the mode shape for the $(n,m)^{\text{th}}$ unit cell of the full infinite structure (where $n < 0$, $n > 0$,

$m < 0$, $m > 0$ correspond to unit cells to the left, right, below, and above the reference unit cell, respectively) is determined from Bloch's theorem (Eq. (6.3)) such that

$$\overset{1}{\Delta\mathbf{u}}_{nm} = \mathrm{e}^{i2\pi(n\kappa_1+m\kappa_2)}\overset{1}{\Delta\mathbf{u}}. \tag{6.84}$$

Practically speaking, there are some issues that need to be addressed to properly implement the *Bloch wave* stability analysis into the finite element framework:

- The positive definiteness of a matrix is efficiently evaluated using an LDU decomposition, with the smallest entry of the diagonal matrix D going to zero (or less than zero) at the loss in positive definiteness of the matrix.
- As the First Brillouin zone defines an infinite set ($\mathcal{B}$), an appropriate numerical procedure must be conducted to evaluate the positive definiteness of $\tilde{\mathbf{K}}$ for all $\boldsymbol{\kappa} \in \mathcal{B}$. One of the more basic approaches is to discretize $\mathcal{B}$ (often onto a uniformly spaced grid) and evaluate the positive definiteness of $\tilde{\mathbf{K}}$ at each of these grid points. This method is rather computationally expensive, but is simple in its numerical implementation (and is the method used here and in Section 7.2). Another possible approach is to use a numerical optimization procedure to minimize the minimum eigenvalue of $\tilde{\mathbf{K}}$ over $\mathcal{B}$. If the minimized minimum eigenvalue is zero or negative, the corresponding wavenumber pair corresponds to an instability in the structure. This method is usually less computationally expensive than the global search method, but at the cost of implementation complexity.
- The evaluation of the positive definiteness of $\tilde{\mathbf{K}}$ is a rather computationally expensive procedure as $\tilde{\mathbf{K}}$ must be computed for each (κ_1, κ_2) pair. For a finite element mesh with N nodes, this results in multiple computations of an $M(N-3) \times M(N-3M)$ matrix (noting that the three dependent Bloch boundary nodes are omitted) defined in Eq. (6.79), along with the evaluation of its positive definiteness. To reduce the computational costs of the problem, the fact that $\tilde{\mathbf{K}}\overset{1}{\tilde{\mathbf{u}}} = \mathbf{0}$ (see Eq. (6.11)) when $\tilde{\mathbf{K}}$ loses positive definiteness can be exploited. From Eq. (6.11),

$$\tilde{\mathbf{K}}(\lambda_c;\boldsymbol{\kappa}) = \begin{bmatrix} \tilde{\mathbf{K}}_{\alpha\alpha}(\lambda_c;\boldsymbol{\kappa}) & \tilde{\mathbf{K}}_{\alpha i}(\lambda_c;\boldsymbol{\kappa}) \\ \tilde{\mathbf{K}}_{i\alpha}(\lambda_c;\boldsymbol{\kappa}) & \tilde{\mathbf{K}}_{ii}(\lambda_c;\boldsymbol{\kappa}) \end{bmatrix} \begin{bmatrix} \overset{1}{\Delta\mathbf{u}}_\alpha \\ \overset{1}{\Delta\mathbf{u}}_i \end{bmatrix} = \begin{bmatrix} \mathbf{0} \\ \mathbf{0} \end{bmatrix}. \tag{6.85}$$

  Solving the second equation in the linear system for $\overset{1}{\Delta\mathbf{u}}_i$ and substituting the result into the

first equation of the linear system, the solution to Eq. (6.11) reduces to solving

$$\left[\tilde{\mathbf{K}}_{\alpha\alpha}(\lambda_c;\boldsymbol{\kappa}) - \tilde{\mathbf{K}}_{\alpha i}(\lambda_c;\boldsymbol{\kappa})\tilde{\mathbf{K}}_{ii}^{-1}(\lambda_c)\tilde{\mathbf{K}}_{i\alpha}(\lambda_c;\boldsymbol{\kappa})\right]\Delta\mathbf{u}_\alpha = \hat{\mathbf{K}}(\lambda_c;\boldsymbol{\kappa})\overset{1}{\Delta}\mathbf{u}_\alpha = \mathbf{0}. \tag{6.86}$$

The solution to Eq. (6.86) corresponds to the loss of positive definiteness of $\hat{\mathbf{K}}$ (which is essentially a statically condensed version of $\tilde{\mathbf{K}}$). In comparison to the $M(N-3)\times M(N-3)$ (where $N >> M$) size of $\tilde{\mathbf{K}}$, the $3M \times 3M$ size of $\hat{\mathbf{K}}$ results in reduced computational cost during the positive definiteness evaluation; furthermore, noting that $\mathbf{A}$ is dependent on $\boldsymbol{\kappa}$, $\mathbf{K}$ is dependent on λ, and

$$\tilde{\mathbf{K}}_{\alpha i}\tilde{\mathbf{K}}_{ii}^{-1}\tilde{\mathbf{K}}_{i\alpha} = \left[\mathbf{K}_{\alpha i} + \mathbf{A}^H\mathbf{K}_{\beta i}\right]\mathbf{K}_{ii}^{-1}\left[\mathbf{K}_{i\alpha} + \mathbf{K}_{i\beta}\mathbf{A}\right] \tag{6.87a}$$

$$= \underbrace{\mathbf{K}_{\alpha i}\mathbf{K}_{ii}^{-1}\mathbf{K}_{i\alpha}}_{I} + \underbrace{\mathbf{K}_{\alpha i}\mathbf{K}_{ii}^{-1}\mathbf{K}_{i\beta}}_{II}\mathbf{A} + \mathbf{A}\underbrace{\mathbf{K}_{\beta i}\mathbf{K}_{ii}^{-1}\mathbf{K}_{i\alpha}}_{III} + \mathbf{A}^H\underbrace{\mathbf{K}_{\beta i}\mathbf{K}_{ii}^{-1}\mathbf{K}_{i\beta}}_{IV}\mathbf{A}, \tag{6.87b}$$

the terms I, II, III and IV only depend on λ and, hence, need only be computed once per loading step.

- It is difficult to determine λ_c such that at least one eigenvalue of $\tilde{\mathbf{K}}$ equals zero exactly; rather, the minimum eigenvalue will straddle zero due to the numerics of the simulation. Typically, a root finding algorithm (commonly a bisection method) is used to converge to the critical loading point to within an desired tolerance (for example, see Triantafyllidis and Schraad [1998]).

- As discussed in Section 6.3, the case of $\boldsymbol{\kappa} = \mathbf{0}$ has a rigid body displacement implicit in its definition. If this rigid body mode is not considered, $\tilde{\mathbf{K}}(\lambda_c;\mathbf{0})$ is always positive semidefinite, yielding false stability information. To overcome this issue, some of the boundary nodes can be pinned to suppress rigid body translations and rotation in the stability analysis for this special case; for example, the two translational degrees of freedom of node 2 and the Y translational degree of freedom of node 3 can be pinned (see Figure 6.7). From the form of the eigenvalue problem (Eq. (6.81)), this pinning procedure corresponds to evaluation of the positive definiteness of a reduced from of $\tilde{\mathbf{K}}$ such that the rows and columns corresponding to the pinned degrees of freedom have been removed.

The principal path mechanical response of the honeycomb during loading has stiff–soft–stiff behavior as shown in Figure 6.8a. According to the Bloch wave stability analysis (Figure 6.8b), the structure loses stability at a macroscopic strain of approximately 16 % with the wavenumber pairs $(2\pi\kappa_1, 2\pi\kappa_2) = (\pm 0.05, \pm 0.04)$ (again noting the symmetry of the solution over the wavenumber

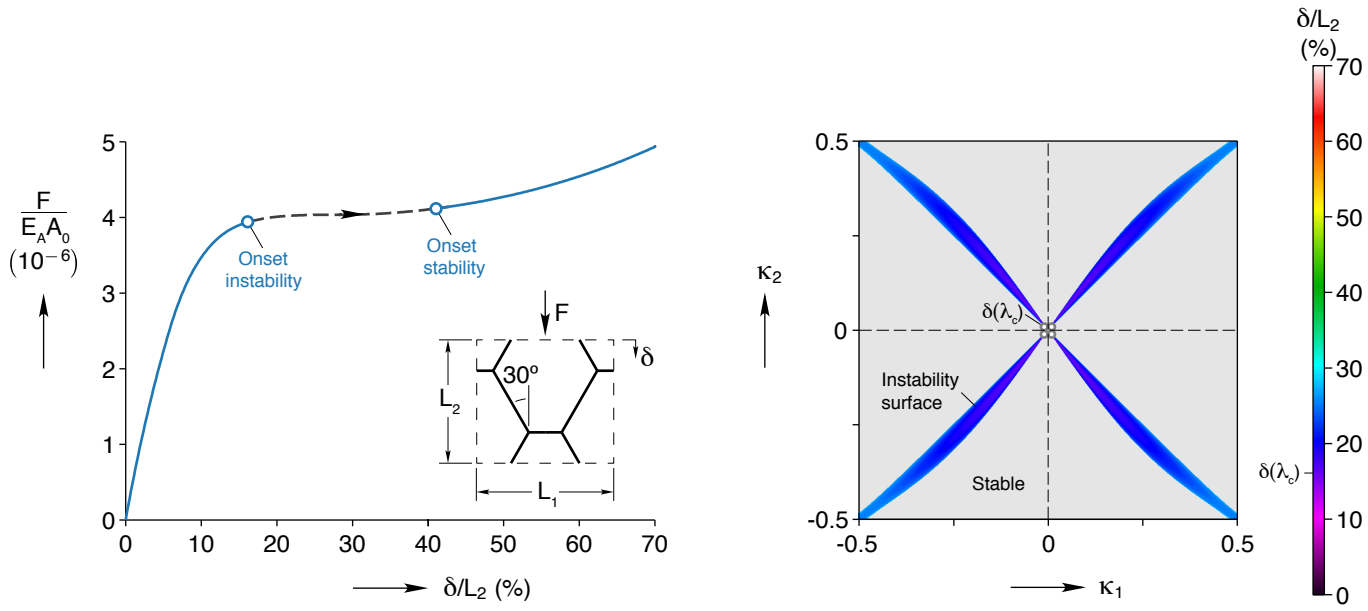

(a) Mechanical response

(b) Instability surface

Figure 6.8: The principal path mechanical response of the honeycomb (where $A_0 = L_1 L_3$ is the projected cross-sectional area of the honeycomb) has stiff–soft–stiff behavior, with the structure losing stability at a macroscopic strain of approximately $16\,\%$.

space as discussed previously in Section 6.5.1). Interestingly, the principal path regains stability at a macroscopic strain of approximately $40\,\%$, suggesting that the honeycomb might unbuckle similar to the superelastic SMA columns examined in Chapter 4.

The critical instability mode shape ($\lambda = \lambda_c$) is derived from Eq. (6.84) with $(2\pi\kappa_1, 2\pi\kappa_2) = (0.05, 0.04)$ and shown in Figure 6.9 (noting that the mode shape results are the same for all of the $(\pm 0.05, \pm 0.04)$ wavenumber pairs). The fundamental wavelength of the instability mode shape is much greater than the unit cell geometry; furthermore, the X and Y periodicity are similar.

6.6 Summary

Bloch's theorem defines the general solution to *linear* differential equations with periodic boundary coefficients, which are typically referred to as *Bloch waves*. In the context of mechanics, Bloch's theorem can be used in linear stability analysis of structures with underlying periodicity (often referred to as *Bloch wave* stability analysis). From general stability analysis, the framework for *Bloch wave* stability analysis was developed and some of its intricacies were discussed. The theory was then applied to a set of example problems, illustrating its implementation in the context of discrete and continuous systems.

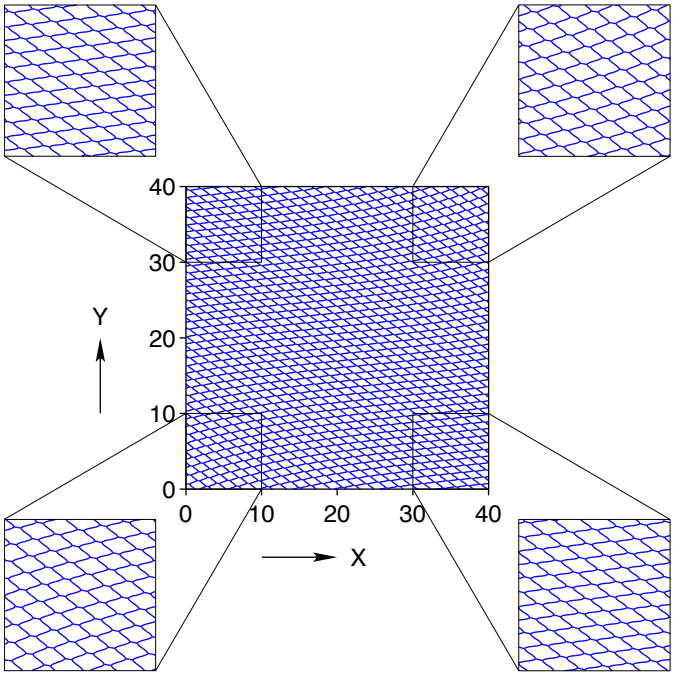

Figure 6.9: The fundamental wavelength of the instability mode shape at $\lambda = \lambda_c$ is much greater than the unit cell geometry.

Chapter 7

Shape Memory Alloy Honeycombs

Micro- and mesoscale cellular lattices make up the structure of many natural systems, such as bee hives, plant stalks, the interior of bones, some woods and cork [Gibson et al., 1982]. As engineering structures, cellular lattices usually take the form of three-dimensional foams or two-dimensional honeycombs. The sparse strut and plate-based configuration of cellular solids results in high specific stiffness (stiffness-to-mass ratio), motivating their usage in lightweight engineered structures (such as aircraft); additionally, the buckling induced collapse which occurs under large deformations can result in ideal energy absorption characteristics, motivating their usage as protective structures (such as in packaging and personal safety equipment).

The construction of a cellular structure from an SMA material is a relatively new approach to realize lightweight, adaptive structures. Operating in the superelastic regime, the SMA enhances the flexibility of the honeycomb, even allowing for recovery of deformations associated with buckling and collapse of the honeycomb. Unlike conventional metal honeycombs, SMA honeycomb energy absorbers could be designed to be reusable. Operating in the shape memory regime, the SMA can be used to actuate shape change of the honeycomb structure. This actuation could function as a large stroke linear actuator, a self healing sandwich panel, or deployable device. With respect to the SMA material performance, the low volume-to-surface area of cellular solids provides ideal thermal conditions for the operation of the SMA material, allowing for improved actuation frequency and reduced superelastic loading rate sensitivity; furthermore, their sparse configuration is ideal for active cooling and quenching during the manufacturing process.

Unfortunately, the extreme sensitivity of SMA material behavior to manufacturing processes has hindered the development of SMA cellular solids. The primary issues associated with the development of complex SMA forms are the dependence of SMA phase transformation temperatures on the material stoichiometry, the necessity of heat treatment and cold work to yield robust SMA properties, and the high temperature reactiveness of SMAs to oxygen in both the solid and molten states [Shaw et al., 2002]. Some open celled SMA foams have been successfully manufac-

tured [Shaw et al., 2002, Grummon et al., 2003]; however, good shape memory and superelastic properties have yet to be achieved due to these manufacturing issues. In the case of honeycombs structures, the problems associated with welding (the manufacturing process traditionally used to manufacture metal honeycombs) can be circumvented through the use of alternative joining methods such as high performance adhesives; unfortunately, these joining techniques often cannot withstand the large deformations experienced by SMAs. Fortunately, the recent advent of a niobium based brazing technique, which robustly joins NiTi while maintaining its unique properties, has opened new possibilities for the design of NiTi honeycombs [Grummon et al., 2006].

Research into the development of SMA honeycombs began in the mid 2000s, building upon the seminal work of Gibson and Ashby [1997] on the behavior of general cellular materials, the experimental work of Papka and Kyriakides on metallic honeycombs [Papka and Kyriakides, 1994, 1998, 1999a,b], and the theoretical work of Triantafyllidis on the properties of honeycombs loaded in in-plane [Triantafyllidis and Schraad, 1998] and out-of-plane [López Jiménez and Triantafyllidis, 2013] compression using Bloch wave stability analysis. Hassan et al. were of the early researchers to examine SMA honeycombs, manufacturing, testing, and modeling cyanoacrilate bonded NiTi honeycombs [Hassan et al., 2004, ASM, 2005, Hassan et al., 2008, 2009]; unfortunately, from a performance standpoint, these honeycombs exhibited less recoverable deformation than expected, largely due to their adhesively bonded joints. To address this concern, Shaw et al. [2007] used the new niobium–based brazing technique developed by Grummon et al. [2006] to manufacture superelastic NiTi honeycombs, observing recoverable in–plane compressive deformations on the order of $50\,\%$ macroscopic strain. With respect to shape memory behavior, Okabe et al. [2008] demonstrated the "self-healing" ability of sandwich beams constructed with adhesively bonded NiTi honeycombs, followed by the construction of bending actuator sandwich beams [Okabe et al., 2011]. From a design prospective, the effects of constitutive parameters on the stability and mechanical characteristics of superelastic SMA honeycombs were recently examined using Bloch wave stability analysis by Michailidis et al. [2009].

This work examines the experimental behavior (Section 7.1) and design (Section 7.2) of SMA honeycombs loaded in in-plane compression. In the examination of the general properties of SMA honeycombs, a comparison is made with monolithic SMAs to examine the tradeoffs between the two forms and the appropriate applications for SMA honeycombs. A parametric study of superelastic SMA honeycombs is then conducted, establishing design criteria for reusable energy absorption applications.

7.1 Experimental Behavior in In-plane Compression

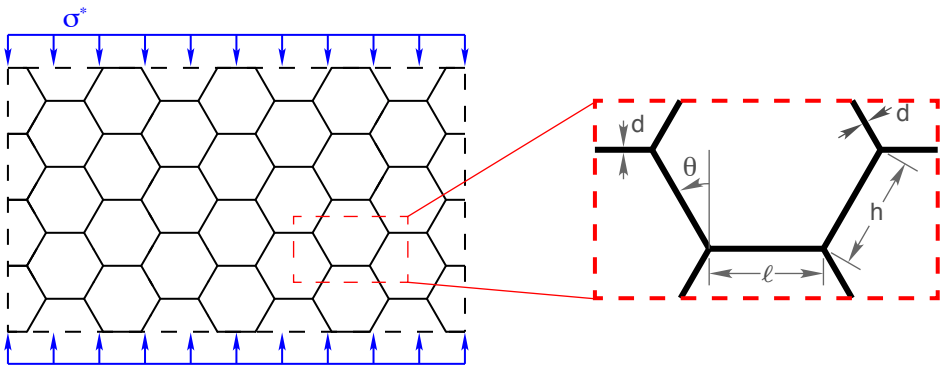

Figure 7.1: Hexagonal honeycomb geometry is defined by the horizontal ligament length ℓ, the diagonal ligament length h, the diagonal ligament orientation θ and the thickness of the ligaments d. In the case of regular hexagonal honeycombs, $\ell = h$ and $\theta = 30°$.

To examine the the trade–offs between monolithic SMAs and SMA honeycombs, their thermomechanical properties can be estimated and compared using basic beam theory. Although the constitutive and kinematic behavior of SMAs are nonlinear, linear elastic beam theory is used here to provide simple scaling laws with the understanding that their validity breaks down for large deformations. For hexagonal honeycombs loaded in in-plane compression as shown in Figure 7.1, Gibson and Ashby [1997] showed that the relative mass density (homogenized/solid SMA) and homogenized/local ratios of maximum strain (ε), transformation stress (σ_0), and elastic modulus (E), respectively scale as

$$\frac{\rho^*}{\rho_s} = \frac{d}{2h}\frac{\ell/h + 2}{\cos\theta(\ell/h + \sin\theta)}, \tag{7.1a}$$

$$\left|\frac{\varepsilon^*}{\varepsilon_{s,\max}}\right| = \frac{1}{3}\left(\frac{d}{h}\right)^{-1}\tan\theta, \tag{7.1b}$$

$$\left|\frac{\sigma_0^*}{\sigma_{0,s}}\right| = \left(\frac{d}{h}\right)^{2}\frac{1}{2(\ell/h + \sin\theta)\sin\theta}, \tag{7.1c}$$

$$\frac{E^*}{E_s} = \left(\frac{d}{h}\right)^{3}\frac{\cos\theta}{(\ell/h + \sin\theta)\sin^2\theta}, \tag{7.1d}$$

where d is the honeycomb ligament thickness, ℓ is the horizontal ligament length, h is the diagonal ligament length (see Figure 7.1), and θ is the angle of the diagonal ligament, $(.)^*$ defines a macroscopic quantity, and $(.)_s$ defines a material property; for a regular honeycomb[1], these relationships

[1] A regular honeycomb is defined such that $\ell = h$ and $\theta = 30°$

reduce to

$$\frac{\rho^*}{\rho_s} = \frac{2}{\sqrt{3}}\frac{d}{h}, \tag{7.2a}$$

$$\left|\frac{\varepsilon^*}{\varepsilon_{s,\max}}\right| = \frac{\sqrt{3}}{9}\left(\frac{d}{h}\right)^{-1}, \tag{7.2b}$$

$$\left|\frac{\sigma_0^*}{\sigma_{0,s}}\right| = \frac{2}{3}\left(\frac{d}{h}\right)^{2}, \tag{7.2c}$$

$$\frac{E^*}{E_s} = \frac{4}{\sqrt{3}}\left(\frac{d}{h}\right)^{3}. \tag{7.2d}$$

Typically, $\rho^*/\rho_s < 30\,\%$ for cellular solids [Gibson and Ashby, 1997] ($10\,\% \leq \rho^*/\rho_s \leq 20\,\%$ for the honeycombs examined here) implying that $d/h < 1/4$. From this observation and Eq. (7.2), SMA honeycombs are therefore expected to have improved recoverable deformation (Eq. (7.2b)) at the cost of decreased transformation stress (Eq. (7.2c)) and stiffness (Eq. (7.2d)). From Eq. (7.1b), it can also be shown that the strain rate ($\dot{\varepsilon} = \mathrm{d}\varepsilon/\mathrm{d}t$) is expected to scale as

$$\left|\frac{\dot{\varepsilon}^*}{\dot{\varepsilon}_{s,\max}}\right| \propto \left(\frac{d}{h}\right)^{-1}, \tag{7.3}$$

indicating lower local strain rates compared to the macroscopic loading strain rate. Due to the loading rate sensitivity of superelastic SMAs (which is due to phase transformation induced latent heating and thermomechanical coupling), superelastic SMA honeycombs are expected to exhibit less loading rate sensitivity than monolithic SMAs. Additionally, the thermal time constant (τ) for convective heat transfer scales with the ratio of volume (V_s) to exposed surface area (S_s) of the solid material [Bergman et al., 2011]:

$$\tau \propto \frac{V_s}{S_s}. \tag{7.4}$$

In the case of a honeycomb, $V_s/S_s \approx d/2$, suggesting that thermal lag scales with the ligament thickness instead of the macroscopic dimensions. Since $d/h = \sqrt{3}\rho^*/(2\rho_s) < 25\,\%$ (Eq. (7.1a)), SMA honeycombs are expected to have good thermal conditions for both superelastic and shape memory operation.

Although some of the above scaling laws were proposed previously by Shaw et al. [2007], they have yet to be fully investigated experimentally. Since the majority of existing SMA experimental data, and much of the community's knowledge of SMAs, corresponds to the tensile behavior of NiTi wire, a set of experiments are presented here to compare the thermo-mechanical responses of NiTi honeycombs under in-plane compression to that of NiTi wires under tension. The purpose

here is to quantify both the advantages and tradeoffs of NiTi honeycombs with respect to the shape memory effect, superelasticity, thermal lag and loading rate sensitivity. The honeycomb and wires specimen details are outlined in Section 7.1.1, followed by a discussion of the experimental setups and results in Section 7.1.2.

7.1.1 Specimens

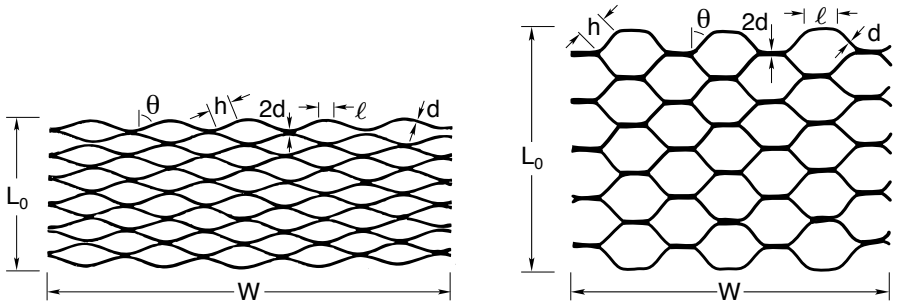

(a) Honeycomb 1 (b) Honeycomb 2

Figure 7.2: Two honeycombs were experimentally characterized: (a) Honeycomb 1 had lens–like bicylindrical cells and (b) Honeycomb 2 had hexagonal cells.

In the comparison of SMA honeycomb and wire performance, multiple honeycomb and wire geometries were examined. With respect to the honeycombs, two geometries were evaluated: Honeycomb 1 had lens–like bicylindrical cells (see Figure 7.2a) and Honeycomb 2 had hexagonal cells (see Figure 7.2b). Each honeycomb specimen was fabricated from $d = 0.2$ mm thick superelastic (at room temperature) NiTi strip. The strips were shape-set into the appropriate corrugations and then joined using a niobium braze (see Grummon et al. [2006] for more details on fabrication). Other geometric parameters for the honeycombs are provided in Table 7.1. The NiTi wires were obtained from Memry Corp and are referred to as Wire 1 and Wire 2. Wire 1 had a diameter of $d_{\mathrm{w}} = 0.76$ mm and is the same as the wire used in Chang et al. [2006], Shaw et al. [2008]; whereas, Wire 2 had a diameter of 1.28 mm. Figure 7.3 shows differential scanning calorimetry (DSC) thermograms of Wire 1 and NiTi material excised from an as-fabricated Honeycomb 1. Based on the measured A_{f} temperatures, Wire 1 was clearly superelastic at room temperature; whereas, Honeycomb 1 was on the borderline of superelastical at room temperature. Although the DSC thermograms are not presented here, Wire 2 and Honeycomb 2 were also superelastic at room temperature. As a final note, due to the differing alloy compositions between the honeycombs and wires, order of magnitude differences are the primary interest in comparing performance.

Table 7.1: Measured SMA honeycomb geometric parameters, approximating both to have hexagonal ligament geometries.

Parameter	Variable	Units	Honeycomb 1	Honeycomb 2
Cell shape	–	–	bicylindrical	hexagonal
Relative density	ρ^*/ρ_s	%	18.5	12.5
Ligament thickness	d	mm	0.2	0.2
Diagonal ligament length	h	mm	2.15	2.6
Horizontal ligament length	ℓ	mm	1.25	2.6
Honeycomb angle	θ	°	70	45
Gage length (height)	L_0	mm	14.45	22.89
Total width	W	mm	38.90	32.04
Total depth	D	mm	5.30	5.34

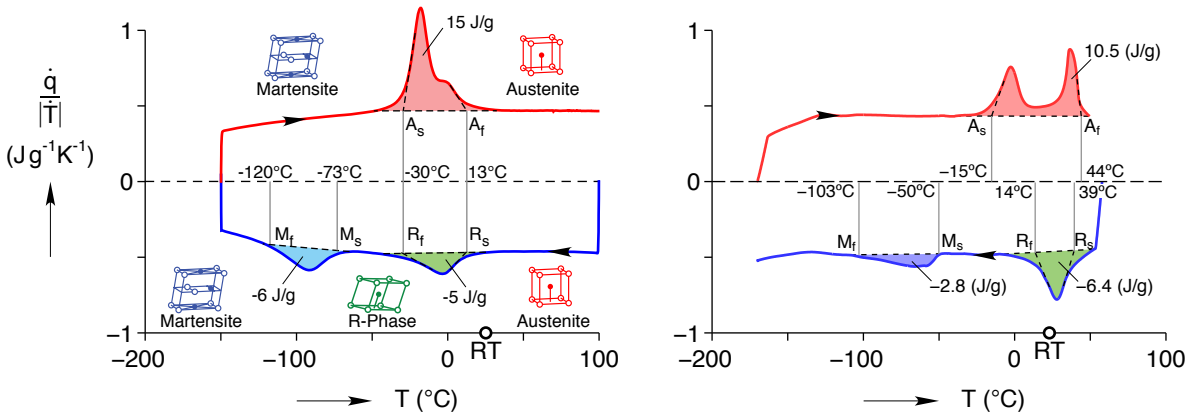

(a) NiTi Wire 1 [Shaw et al., 2008, as found in Figure 3b of]

(b) NiTi material from Honeycomb 1

Figure 7.3: Differential scanning calorimetry (DSC) thermograms of and Wire 1 and Honeycomb 1, both of which were (nearly) superelastic at room temperature.

7.1.2 Experimental Comparison

The thermo-mechanical behaviors of the SMA wires and honeycombs are compared based on three types of experiments: (1) fundamental shape memory and superelasticity cycles, (2) thermal lag, and (3) superelastic rate sensitivity. Although all of the honeycomb experiments are new, due to the prevalence of SMA wire data in the literature, data from experiments in Chang et al. [2006], Shaw

et al. [2008], Churchill et al. [2010] are presented here as representative cases of wire performance; the only exception is the wire thermal lag experiment which is new since the necessary wire data was not found in the literature. In the evaluation of the scaling law predictions of Eq. (7.1), both honeycombs are approximated to have the hexagonal ligament geometry of Figure 7.1 as shown in Figure 7.2. For both honeycombs, this ignores the double thickness of the horizontal ligaments (Figure 7.2); however, for the in-plane loading examined here, the horizontal ligaments carry no load and, hence, this discrepancy does not affect the scaling law predictions.

Shape Memory and Superelasticity

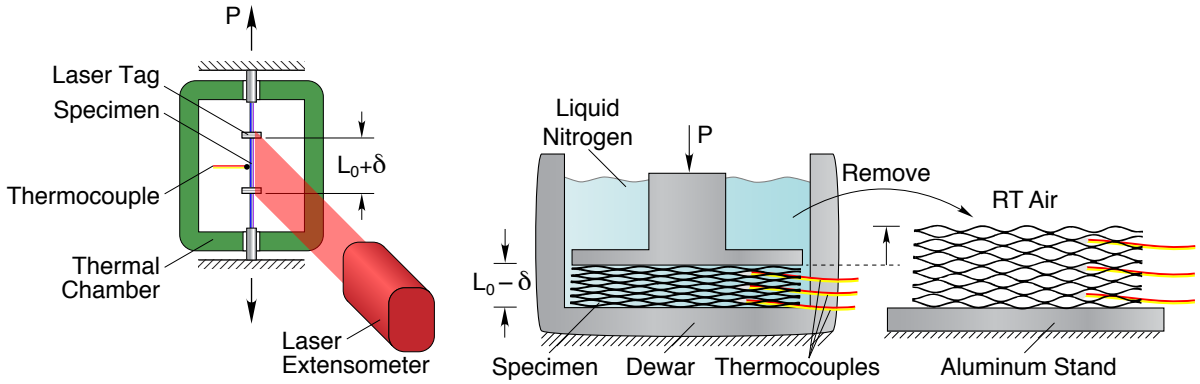

(a) NiTi wire tension

(b) NiTi honeycomb compression & recovery

Figure 7.4: Schematically shown here, the shape memory and superelastic experiments looked to investigate the fundamental thermomechanical properties of Wire 1 and Honeycomb 1, measuring the uniaxial responses under controlled temperature conditions.

The shape memory and superelastic experiments were designed to investigate the fundamental thermomechanical properties of Wire 1 and Honeycomb 1. The experiments were conducted within a uniaxial load frame under controlled environmental conditions as illustrated in Figure 7.4. During each experiment, the axial load P, axial displacement δ, and specimen temperature T were measured. Fine (0.076 mm wire) K-type thermocouples were attached locally to the specimens using OmegaTherm 201 thermal paste to ensure good thermal contact. Although not possible for the wire experiment, the honeycomb experiment was designed such that the room temperature free recovery could be additionally measured, accounting for the differing experimental setups.

The NiTi wire tension setup (Figure 7.4a) tested Wire 1 and included an air temperature-controlled chamber with liquid nitrogen cooling. A laser extensometer was projected onto the specimen through the window of the thermal chamber, measuring the relative displacement (δ) of two retroreflective tags attached to the wire at an initial distance L_0 from each other; additionally, a

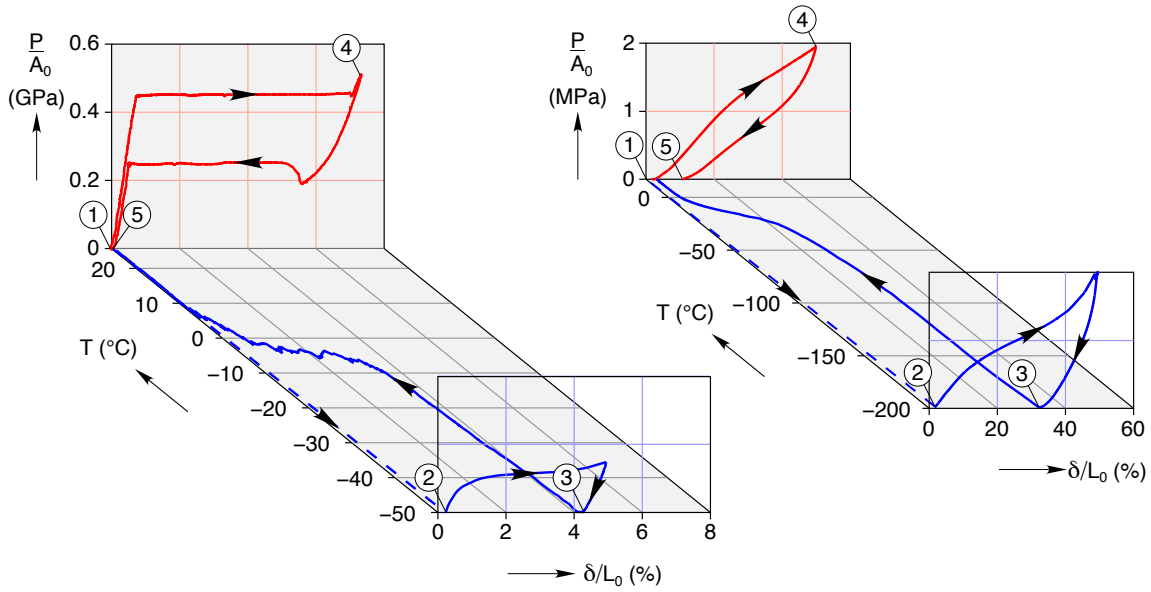

(a) Wire 1 [Shaw et al., 2008, as found in Figure 7 of] (b) Honeycomb 1

Figure 7.5: Shape memory (①–②–③–①) and superelastic (①–④–⑤) responses, showing a $10\times$ increase in recoverable deformation of Honeycomb 1 over Wire 1, in exchange for reduced strength and stiffness. (The dashed lines ①–② denote that only the endpoints of strain were measured, giving an approximate path for this portion of each experiment.)

single thermocouple was attached to the specimen at the middle of the extensometer gauge length. The shape memory and superelastic loading procedure are were as follows:

- **Shape memory cycle**: Starting at room temperature (①), the wire was quenched in liquid nitrogen to ensure that the specimen was fully thermal martensite and then allowed to heat up to $-50\,°\text{C}$ in the thermal chamber (②). At a constant temperature of $-50\,°\text{C}$ (which was less than $A_\text{s} = -30\,°\text{C}$), the wire was then quasistatically loaded to $\delta/L_0 = 5\,\%$ extensometer strain and then unloaded to zero load ($P = 0$), resulting in a residual extensometer strain of approximately $4\,\%$ (③). Under load control at a small load (just enough to keep the wire taut), the temperature was raised back to $25\,°\text{C}$ (①), with the majority of the strain recovery occurring between $-10\,°\text{C}$ and $5\,°\text{C}$.

- **Superelastic cycle**: After the shape memory cycle, the specimen was isothermally loaded slowly under elongation control at $25\,°\text{C}$ to an extensometer strain of approximately $7\,\%$ (④), which was just beyond the termination of the superelastic stress plateau. The elongation was then reversed until the specimen was completely unloaded (⑤). The unloading segment involved another (lower) stress plateau where the reverse transformation occurred. Both stress plateaus were due to localization and propagating of phase transformation fronts, which are a particular manifestation of unstable transformation kinetics well-known to occur during

stress-induced transformations of NiTi in tension (as discussed in detail in Chapter 3).

The results from both experiments are shown in Figure 7.5a with the circled labels referencing the measured thermomechanical response of the wire (tensile engineering stress P/A_0 vs tensile extensometer strain δ/L_0 vs temperature T, where $A_0 = \pi d_w^2/4$ is the reference cross-sectional area of the wire).

The NiTi honeycomb compression setup (Figure 7.4b) tested Honeycomb 1 and consisted of a liquid nitrogen dewar and an open air test stand. To get a sense of the temperature distribution in the honeycomb, three thermocouples were attached along the height of the specimen. The shape memory and superelastic loading procedure were as follows:

- **Shape memory cycle**: A dewar in-line with the load frame was filled with liquid nitrogen. Starting at room temperature (①), the specimen was inserted into the dewar, fully transforming to the martensite phase (②). The honeycomb was then slowly loaded to a peak compressive displacement of $50\,\%$ and then unloaded to a load free state, resulting in a residual strain of $35\,\%$ (③). The shape memory loop was then completed by quickly moving the specimen from the liquid nitrogen to the open air test stand (less than $5\,\mathrm{s}$) where it was allowed to freely recover at room temperature (①).
- **Superelastic cycle**: After the shape memory cycle, the dewar was emptied and allowed to return to room temperature. The specimen was then reinserted into the load frame (①) and isothermally loaded at room temperature to a peak compressive strain of $50\,\%$ (④), followed by unloading to a load free state (⑤).

The results from both experiments are shown in Figure 7.5b with the circled labels referencing the measured thermomechanical response of the honeycomb (compressive engineering stress P/A_0 vs compressive extensometer strain δ/L_0 vs temperature T, where $A_0 = WD$ is the projected reference cross-sectional area of the honeycomb).

In general, the recoverable deformations measured in the honeycomb specimen were approximately $10\times$ greater than the wire. In the case of the shape memory experiment, the magnitudes of the recoverable strains for the wire and honeycomb specimens were respectively 4 % and 35 %, although it should be recognized that both are dependent on the maximum strain imposed (here 5 % and 50 %, respectively). During the superelastic cycles, recoverable strain magnitudes of 7 % and 50 % strain were shown, respectively for the wire and honeycomb specimens (after heating above A_f). Note that since no stress plateau existed in the honeycomb's superelastic response, it was difficult to determine exhaustion of phase transformation during loading, so the measured strain recovery may be a conservative quantification of the honeycomb performance. Nevertheless, this order of magnitude difference is reasonably consistent with the scaling law of a $9.6\times$ increase

in recoverable deformation for the given honeycomb geometry (Eq. (7.1b))[2].

One of the costs of this enhanced recoverable deformation was the decreased load carrying capacity of the honeycomb. While the superelastic behavior of the honeycomb had no stress plateaus, we can start by comparing its stress at the first knee in the response ($\sigma_0^* = 1.25\,\text{MPa}$) to the loading plateau stress of the wire ($\sigma_0 = 450\,\text{MPa}$). This corresponds to a ratio of 2.8×10^{-3}, which agrees reasonably well with the scaling law prediction of 3.1×10^{-3} from Eq. (7.1c) and Table 4.2. Of course this rough comparison ignores the fact that the transformation temperatures of the two NiTi alloys are different by about $30\,°\text{C}$ and superelastic responses were quite temperature sensitive according to the Clausius-Clapeyron law ($6.4\,\text{MPa}\,°\text{C}^{-1}$ for this wire [Chang et al., 2006]). If one shifts the plateau stress of the wire by $-30\,°\text{C}$, the plateau stress would be $\sigma_0 = 260\,\text{MPa}$ and the ratio between honeycomb and wire would be about 4.8×10^{-3}, resulting in a slightly worse correspondence with the scaling law prediction. Comparing instead the two low-temperature martensitic responses (②–③), which are typically not very temperature dependent, the initial knee in the mechanical response was roughly $\sigma_0^* = 0.67\,\text{MPa}$ for the honeycomb and was about $\sigma_0 = 100\,\text{MPa}$ for the NiTi wire. The resulting ratio of stresses is 6.7×10^{-3}, which is larger than predicted by the scaling law (3.1×10^{-3}).

In addition to the loss in load carrying capacity, the stiffness of the honeycomb was also significantly less than the wire. Comparing the initial elastic stiffnesses in the superelastic responses, the steepest portion of the honeycomb's loading response was about $E^* = 5.7\,\text{MPa}$, while the initial (austenite) modulus of the monolithic wire was $E_A = 70\,\text{GPa}$. The corresponding honeycomb-to-wire stiffness ratio was 0.8×10^{-4}, which is reasonably in line with the scaling law prediction of 2.1×10^{-4} (Eq. (7.1d)). Note, however, that the value of E^* measured should be considered as a lower bound, since at room temperature the specimen was not fully austenite.

In this comparison of the honeycomb properties, the $10\times$ improvement in recoverable deformation comes at the severe cost of a reduced effective stress capacity of 10^{-2} and reduced elastic stiffness of 10^{-4}; however, this is not the whole story. Often of interest in the application of active structures is the energy density of the material, which scales as the product of the transformation stress and strain. In comparing the honeycomb energy density to the wire, the ratio of energy densities $\sigma_0^* \varepsilon^* / (\sigma_{0,s} \varepsilon_{s,\max})$ is of order 10^{-1}, which is likely a reasonable trade–off for the improved recoverable deformation; additionally, there are many applications in which low stiffness and stress capacity structures are necessary, such as biological implants.

[2]Note that the scaling law predictions are for hexagonal honeycombs, while Honeycomb 1 had a bicylindrical geometry; however, the geometry was approximated to be hexagonal as shown in Figure 7.2a.

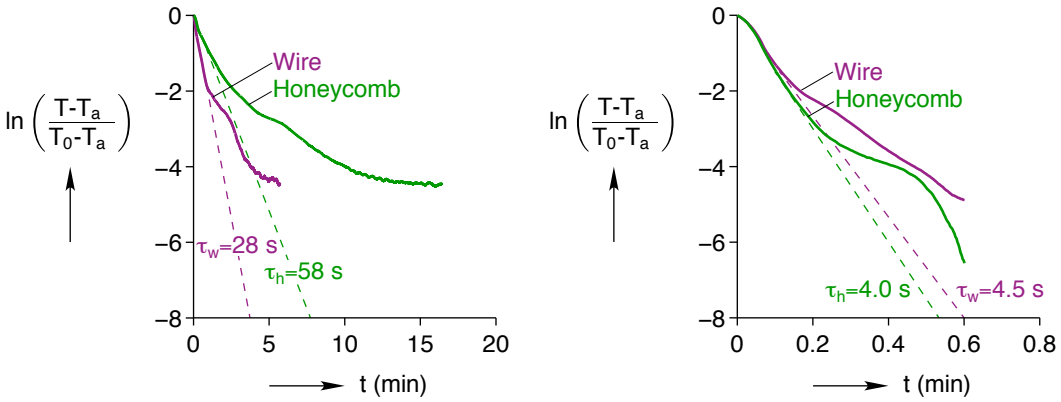

(a) Stagnant air ($U_a = 0\,\mathrm{m\,s^{-1}}$) (b) forced air convection ($U_a = 9\,\mathrm{m\,s^{-1}}$)

Figure 7.6: Starting at a temperature $T_0 = -196\,^{\circ}\mathrm{C}$, the wire heated up to room temperature (T_a) faster than the honeycomb in stagnant air, but slightly slower than the honeycomb under forced convection.

Thermal lag

The thermal lag experiments compared the heat transfer characteristics of Wire 2 and Honeycomb 1. For a fair comparison with the honeycomb, Wire 2 was selected to have a roughly equivalent stroke (7.225 mm) and load capacity (400 N at 300 MPa) to the honeycomb, corresponding to a wire with length $L = 100$ mm and diameter $d_\mathrm{w} = 1.28$ mm. In each experiment, a fine (0.076 mm wire) K-type thermocouple was attached to the middle of the specimen using OmegaTherm 201 thermal paste; additionally, Kevlar thread (which has low thermal conductivity) was tied to the specimen to assist in the maneuvering of the specimen in and out of liquid nitrogen. The specimen then was dipped into a dewar of liquid nitrogen and allowed to thermally equilibrate, followed by removal into room temperature air ($T_\mathrm{a} = 21.3\,^{\circ}\mathrm{C}$) where it was hung horizontally and the temperature response was measured (T). This experimental procedure was conducted in both stagnant ($U_a = 0\,\mathrm{m\,s^{-1}}$) and moving air ($U_a = 9\,\mathrm{m\,s^{-1}}$) to examine both free and forced convection conditions.

The wire was found to have less thermal lag than the honeycomb in stagnant air conditions and comparable thermal lag to the honeycomb in the case of forced convection (Figure 7.6). To quantify the rate of temperature change of each specimen, the thermal lag coefficient (τ) was determined by fitting the initial measured temperature responses to Newton's Law of Cooling:

$$\ln\left(\frac{T(t) - T_\mathrm{a}}{T_0 - T_\mathrm{a}}\right) = -t/\tau \tag{7.5}$$

where $T(t)$ is the transient temperature of the structure as measured by the thermocouple, $T_0 =$

$T(0)$ is the initial temperature of the structure, and T_a is the ambient temperature. Although Newton's law of cooling does not account for latent heat, which is evidently present as seen by the kink in the response, the sensible heating time constant still provides a sense of the recovery rate. In the case of stagnant air (Figure 7.6a), the time constants were $\tau_w = 28\,\mathrm{s}$ and $\tau_h = 58\,\mathrm{s}$ for the wire and honeycomb, respectively, indicating that the wire took less time to heat-up than the honeycomb. This behavior is contrary to the scaling law discussed in Eq. (7.4), where

$$\frac{\tau_\mathrm{w}}{\tau_\mathrm{h}} = \frac{V_\mathrm{s}^{(w)}/S_\mathrm{s}^{(w)}}{V_\mathrm{s}^{(h)}/S_\mathrm{s}^{(h)}} \approx \frac{d_\mathrm{w}/4}{d/2} = 3.2, \tag{7.6}$$

predicts that the thermal lag of the honeycomb (τ_h) should be less than the wire (τ_w). Interestingly, in the case of forced convection (Figure 7.6b), the wire and honeycomb time constants were comparable ($\tau_w = 4.5\,\mathrm{s}$ and $\tau_w = 4.0\,\mathrm{s}$, respectively), resulting in the honeycomb heating slightly faster than the wire. This suggests that the interior surface area of the honeycomb does not function as efficiently as the outer surface area with respect to heat transfer. It is only in the case of forced convection that some benefits of the internal surface area of the honeycomb are realized; although, the performance is still less than that predicted by the scaling law.

In addition to the thermal lag experiments, the load-free shape recovery of Honeycomb 1 during ③–① of Figure 7.5b provides insight into the thermal behavior of SMA honeycombs. To summarize this previously described experiment (see Section 7.1.2), the free recovery process corresponds to the transfer of a deformed honeycomb ($35\,\%$ compressive residual strain) in liquid nitrogen to room temperature air where it was placed on an aluminum stand and allowed to recover deformation load free (Figure 7.4b). During the free recovery, the temperature response was measured at three vertical locations along the height of the honeycomb (see Figure 7.7) to gain a sense of the honeycomb temperature profile. The axial strain was also measured using a video extensometer, which allowed for both global and local measurements. The video extensometer consisted of a Point Grey Research Grasshopper (GRAS-50S5M-C) CCD camera with a Tamron CCTV $75\,\mathrm{mm}$ focal length lens. The Grasshopper camera has a 2448×2048 grayscale CCD which typically allowed about 2200 pixels across the (vertical) gauge length of the honeycomb specimen. The resulting accuracy of the global strain measurement was on the order of $0.05\,\%$ or $1,000^{\mathrm{th}}$ of the total strain at full compression ($-50\,\%$ strain). The camera was run at $5\,\mathrm{fps}$, and a line detection algorithm (similar to Steger [1998]) was used to measure the gauge length in each frame. The video extensometer also allowed homogenized strains (δ_i/L_i) of three individual cells (within the honeycomb (see Figure 7.7) to be measured, although at reduced accuracy ($0.5\,\%$ strain) as there were only about 350 pixels across each cell.

Overall, the strain and temperature of Honeycomb 1 took about five minutes to stabilize during

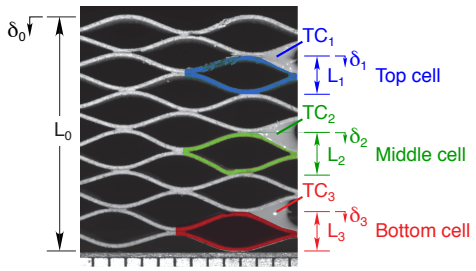

Figure 7.7: Three thermocouples were used to measure the thermal gradient along the height of Honeycomb 1 in the free recovery experiment; additionally, the local homogenized strain (δ_i/L_0 for $i = 1, 2, 3$) of adjacent unit cells were measured using a video extensometer, along with the global honeycomb strain (δ_0/L_0).

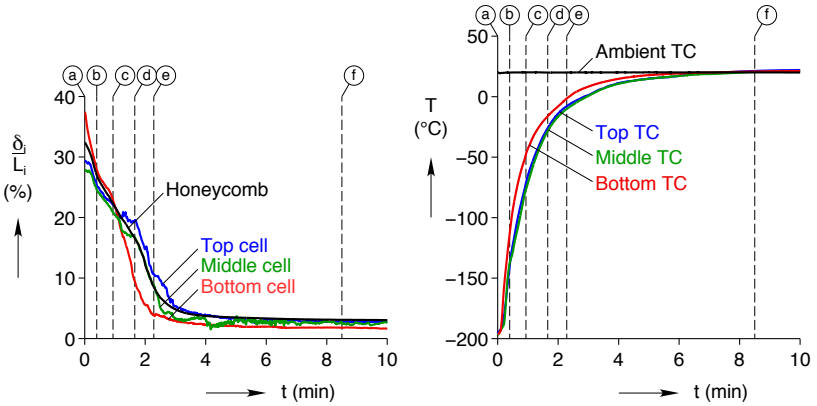

(a) Homogenized strain histories (b) Temperature histories

Figure 7.8: The temperature (T) and homogenized strain (δ_i/L_i for $i = 0, 1, 2, 3$ as marked in Figure 7.7) primarily stabilized within the first five minutes of Honeycomb 1's free recovery experiment, showing kinks in the behaviors around 1.5 min and 2 min.

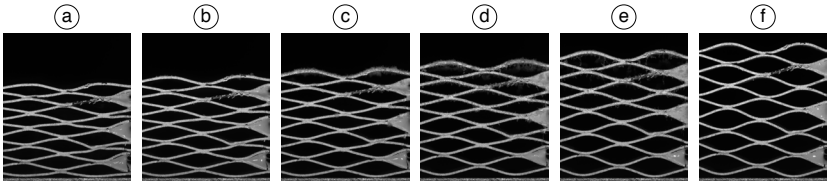

Figure 7.9: The recovery process of Honeycomb 1 was inhomogeneous, progressing from the bottom to the top of the honeycomb.

free recovery, with most of the rapid changes completed in the first three minutes (see the respective homogenized strain (δ_i/L_i) and temperature (T) histories in Figures 7.8a and 7.8b, where $t = 0$ denotes the time at which the honeycomb was removed from the liquid nitrogen and circled labels correspond to the images in Figure 7.9). Globally, the strain history of the entire honeycomb (black line in Figure 7.8a) showed a steep decrease in compressive strain from 35 % to about 20 % in the first 1.5 min, accelerated for about 1 min, then slowed asymptotically thereafter. Locally, the honeycomb unit cells exhibited similar qualitative behavior as the global response; however, the

bottom cell of the honeycomb heated up faster and recovered faster than the middle and top cells (see Figures 7.8a and 7.8b, respectively). This gradient in recovery was likely due to the free recovery setup (see Figure 7.4b), where the aluminum stand acted as a heat sink, allowing the bottom of the specimen to heat faster than the middle and top. In addition to the differing recovery rates, the bottom unit-cell strain started at $38\,\%$ while the middle and top unit-cell strains started at $30\,\%$, indicating that the honeycomb did not deform uniformly during the prior compression in liquid nitrogen (②–③ in Figure 7.5b). This non-uniformity was most likely due to the imperfections in the honeycomb geometry which are evident in Figure 7.7; although, row-by-row collapse of cells can occur during in-plane compression of even nearly perfect honeycombs made of conventional materials [Papka and Kyriakides, 1994, 1998].

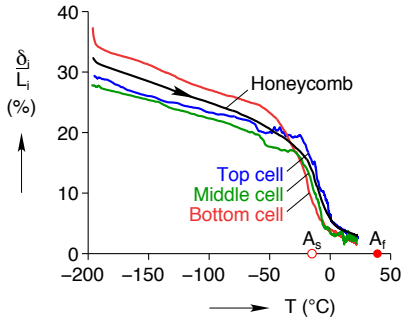

Figure 7.10: The majority of free recovery in Honeycomb 1 occurred over the temperature range $-20\,^{\circ}\mathrm{C}$ to $5\,^{\circ}\mathrm{C}$, comparing well with the first endothermic latent heat peak of the Honeycomb 1 DSC results in Figure 7.3b.

Globally and locally, most of the strain recovery occurred between $-20\,^{\circ}\mathrm{C}$ and $5\,^{\circ}\mathrm{C}$ (see Figure 7.10), comparing well with the first endothermic latent heat peak of the Honeycomb 1 DSC results in Figure 7.3b. Interestingly, about $10\,\%$ strain was recovered before the specimen temperature reached A_s which is perplexing since only minor recovery due to thermal expansion would be expected in this temperature range. In the case of thin structures, in which the Biot number is small, it is common to assume that the temperature was uniform through the thickness; however, in reality, a small thermal gradient exists across ligaments, which is accentuated by the large temperature difference between the environment and the specimen here ($\sim 200\,^{\circ}\mathrm{C}$) . Since the maximum bending strains within the honeycomb occurred in the outer fibers of the ligaments, it is likely that even small amounts of phase transformation that occurred in this 'thermal boundary layer' created a noticeable macroscopic deformation of the honeycomb.

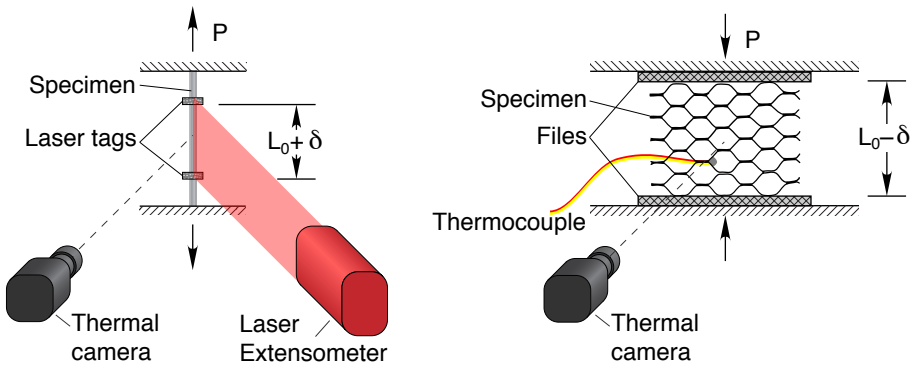

(a) NiTi wire tension

(b) NiTi honeycomb compression

Figure 7.11: Schematically shown here, the superelastic rate sensitivity experiments measured the effects of axial loading rate on the mechanical responses of Wire 1 and Honeycomb 2.

Superelastic rate sensitivity

The loading rate sensitivity experiments were designed to compare the effects of axial loading rate on the mechanical response of Wire 1 and Honeycomb 2. Unlike the loading rate sensitivity found in viscoplastic metals, superelastic loading rate sensitivity is the result of the strong dependence of SMA mechanical behavior on temperature and phase transformation induced latent heating or cooling. The wire and honeycomb experimental setups used in the study were similar (see Figure 7.11), loading the specimen in a uniaxial load frame while measuring the axial load P, axial displacement δ, and the surface temperature field using an infrared thermal camera (ThermaCAM SC1000 digital infrared radiometer). The NiTi wire specimens (Wire 1) were gripped within "V" grooved platens, resulting in a free length of $L = 60\,\text{mm}$ and a laser extensometer gauge length $L_0 = 33.3\,\text{mm}$; whereas, the honeycomb was fixed between two knurled files to simulate clamped boundary conditions, resulting in a gauge length of $L_0 = 22.89\,\text{mm}$. In each experiment, the specimen was loaded in stagnant room temperature air at a constant grip strain rate ($\dot{\delta}/L_0$) to a peak displacement, followed by unloading at a grip strain rate of $-\dot{\delta}/L_0$ to a load free state. To evaluate the rate sensitivity of the honeycomb and wire, a moderately high grip strain rate of $7 \times 10^{-2}\,\text{s}^{-1}$ was conducted on Honeycomb 2, while experiments at grip strain rates of $10^{-4}\,\text{s}^{-1}$, $10^{-3}\,\text{s}^{-1}$ and $10^{-2}\,\text{s}^{-1}$ were conducted on three different Wire 1 specimens (which correspond to the wire experiments found in Churchill et al. [2010]). It should be noted that only one honeycomb experiment was conducted due to large specimen-to-specimen variations associated with the honeycomb manufacturing process, preventing first cycle comparison between honeycomb experiments conducted at different strain rates.

The loading rate sensitivity of Honeycomb 2 was found to be significantly less than Wire 1

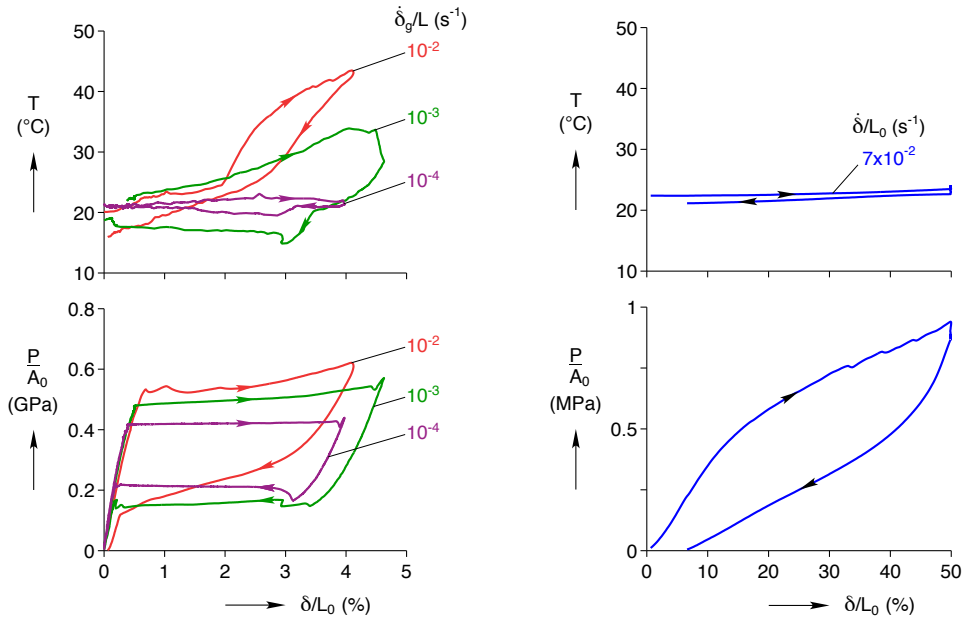

(a) NiTi Wire 1 (b) NiTi Honeycomb 2

Figure 7.12: Comparison of superelastic responses in terms of local specimen temperature (upper plots) and homogenized stress (lower plots), both against gauge strain: (a) NiTi wire at three elongation rates (b) NiTi honeycomb at a moderately fast strain rate.

(see Figure 7.12). In all of the experiments, latent heat was generated faster than it could be transferred to the environment, resulting in temperature increases during loading (and temperature decreases during unloading). In the case of the wire experiments, the ratio of heat generation rate to dissipation rate increased for increased loading rate, resulting in greater temperature variations (see specimen midlength temperature T vs extensometer strain δ/L_0 as shown in upper portion of Figure 7.12a). Since the phase transformation stress increases with increasing temperature (Clausius-Claperyon relationship), the higher strain rate experiments resulted in stiffer mechanical responses (see engineering stress P/A_0 vs extensometer strain δ/L_0 as shown in lower portion of Figure 7.12a). Due to the relatively small temperature change measured in the slowest wire experiment (at most $2\,^{\circ}$C), the mechanical behaviors of Wire 1 as strain rates less than $1 \times 10^{-4}\,\mathrm{s}^{-1}$ are the same and correspond to isothermal behavior. In contrast to the wire experiments, the Honeycomb 1 exhibited very little temperature change: at most a $1.5\,^{\circ}$C change as measured by a thermocouple in the interior of the honeycomb (upper portionFigure 7.12b) and in general across the specimen as measured by thermal imaging. The measured mechanical response of Honeycomb 2 (bottom portion of Figure 7.12b) therefore represents nearly isothermal loading behavior, indicating that Honeycomb 2 is at least three orders of magnitude less sensitive to loading rate than Wire 1.

The SMA honeycomb was expected to exhibit less strain rate sensitivity than the wire due to the bending dominated kinematics of the honeycomb ligaments; however, the degree of rate insensitivity of the honeycomb was at first surprising. From the loading rate sensitivity scaling law (Eq. (7.3)) and the dimensions of the honeycomb ($h/d = 13$), rate sensitivity in Honeycomb 2 was expected to be $\times 10^{-1}$ less than Wire 1, which is two orders of magnitude greater than measured experimentally. A number of factors not included in the scaling law likely contributed to the greater than expected honeycomb rate insensitivity; the greatest factor is likely due to the differing phase transformation morphologies observed between the honeycomb and wire. In the case of tensile SMA wire behavior, phase transformation localizes and propagates as a front with dimension on the order of the wire diameter, resulting in a small surface area to convectively dissipate/provide latent heat; whereas, in the case of a honeycomb, the bending dominated kinematics results in homogenous phase transformation (which was indicated in the Honeycomb 2 experiment by the uniform temperature field in the thermal imaging, not shown here), resulting in a large surface area to convectively dissipate/provide latent heat.

7.1.3 Conclusions

The goal of this work was to illustrate and quantify the improved deformation kinematics and thermal properties of NiTi honeycombs over traditional NiTi wire. Fabricated honeycomb specimens were experimentally tested in in-plane compression, characterizing both the shape memory/thermal lag and superelastic/rate sensitivity properties. It was found that NiTi honeycombs exhibit an order of magnitude increase in recoverable deformation over wire, both in the shape memory effect and superelasticity, in exchange for two orders of magnitude less strength and four orders of magnitude less stiffness; additionally, the thermal lag of the wire and honeycomb were found to be similar, while the honeycomb exhibited three orders of magnitude less rate sensitivity than the wire. With regard to the mechanical behavior, the scaling laws aligned well with the experimental observations; however, the thermal lag prediction slightly overestimated the honeycomb performance, while the rate sensitivity prediction underestimated the honeycomb performance by two orders of magnitude.

There are many possible applications of SMA honeycombs, exploiting different combinations of their improvements over monolithic materials:

- **Compact high stroke actuator or deployable device**: As discussed in Section 7.1.2, a $100\,\text{mm}$ long NiTi wire would be necessary to achieve comparable stroke to the $14.45\,\text{mm}$ long honeycomb tested. This results in a honeycomb actuator approximately $85\,\%$ shorter than the wire; however, to achieve equivalent load carrying capacity between the two actua-

tors, the total volume of the honeycomb actuator is about $20\times$ larger, and the mass would be about $4\times$ larger (for the $18.5\,\%$ dense honeycomb). Thus, compactness comes at the expense of increased volume and mass.

- **Reusable energy absorber**: One of the most common applications of honeycombs (and corrugated materials in general) is energy absorption. The beneficial energy absorption properties are due to the stress plateau found in the structural response when the structure begins to locally collapse; however, the beneficial energy absorption properties of corrugated structures typically lie within the plastic region of the material response. By constructing honeycombs with SMAs, reusable energy absorbers are now possible.
- **Vibration damping**: The hysteresis loop found in the uniaxial behavior of SMAs lends itself to energy dissipation applications; however, the rate sensitivity found in monolithic SMAs limits the potential usage to low frequency dissipation. SMA honeycombs expand the usable frequency range by three orders of magnitude.

Furthermore, the dependency of the structural geometry on the macroscopic response allows the honeycomb to be tuned for different designs by simply changing the unit-cell geometry.

7.2 Design Study for Energy Absorption Applications

Few design tools exist in the field of SMAs due to their complex thermomechanical behavior, much less for SMA honeycombs. The design of an SMA honeycomb with prescribed performance capabilities is therefore a difficult problem that has yet to be addressed. The goal of this study is to better understand the geometric dependencies of SMA honeycomb mechanical properties and their implications on design optimization for reusable energy absorption applications. Under in-plane compression, infinite hexagonal honeycombs are examined (see Figure 7.13), representing structures in which the macroscopic length scale is much greater than the honeycomb unit cell length scale. To represent all feasible geometric designs, a parametric space is defined in Section 7.2.1. Within this space, a discrete number of designs are chosen and evaluated according to the procedures outlined in Section 7.2.2.

7.2.1 Parametric Space of Hexagonal Honeycombs

The geometry of a honeycomb is best defined by the simplest repeating unit within the structure: the unit cell. For the case of a hexagonal honeycomb, the unit cell is defined by the geometry

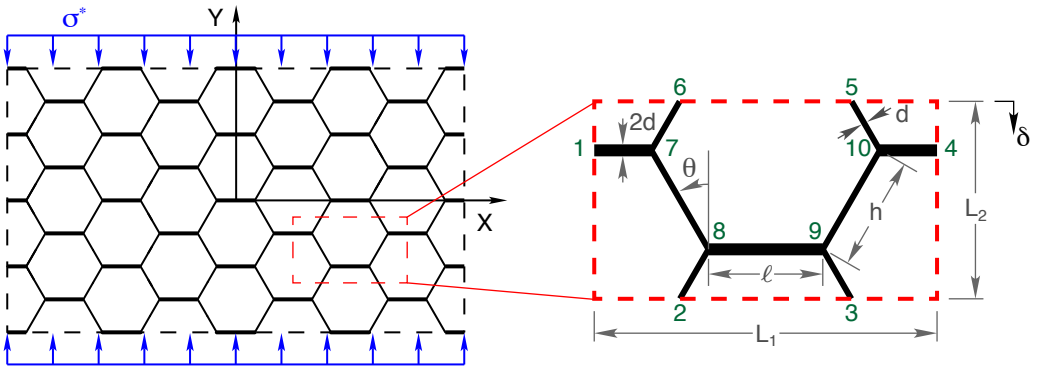

Figure 7.13: Infinite honeycombs with horizontal ligament length ℓ, diagonal ligament length h, horizontal ligament thickness $2d$, diagonal ligament thickness d, and diagonal ligament orientation angle θ are optimized in the context of in-plane compression.

illustrated in Figure 7.13 and is fully defined by the horizontal ligament length ℓ, diagonal ligament length h, hexagonal angle θ and ligament thickness d (noting that horizontal ligaments have a thickness of $2d$ in accordance to traditional manufacturing processes used to construct hexagonal honeycombs). The resulting unit cell has width $L_1 = 2(\ell + h\sin\theta)$ and height $L_2 = 2h\cos\theta$. To more intuitively classify a honeycomb design, the unit cell aspect ratio ($r \equiv L_2/L_1$), diagonal ligament aspect ratio (d/h), and honeycomb angle (θ) are used to define the geometry to within an arbitrary scaling factor.

The unit cell aspect ratio, r, characterizes the unit cell height-to-width ratio as defined by

$$r \equiv L_2/L_1 = \frac{\cos\theta}{\sin\theta + \ell/h} \quad \text{for } |\theta| \leq 90^{\text{o}}. \tag{7.7}$$

Since $0 \leq \ell < L_1$ and $h > 0$ for the class of honeycombs being considered, the maximum aspect ratio (r_{max}) for a given θ is

$$r_{\text{max}} = \cot|\theta|\,, \tag{7.8}$$

which results in a feasible region for r as shown in Figure 7.14a. For increasing r, ℓ/h decreases as illustrated in Figure 7.14b, going to zero at the maximum aspect ratio r_{max} (i.e. $\ell = 0$ at $r = r_{\text{max}}$).

The ligament aspect ratio, d/h, characterizes the slenderness of the diagonal honeycomb ligaments. Since the dominant mode of deformation is bending, which is strongly related to the area moment of inertia of a beam ($I = bd^3/12$ where b is the out-of-plane width), d/h strongly influences the bending stiffness of the ligaments and, thus, the overall stiffness of the honeycomb structure. For increasing d/h, the thickness of the honeycomb ligaments effectively increases as illustrated in Figure 7.15.

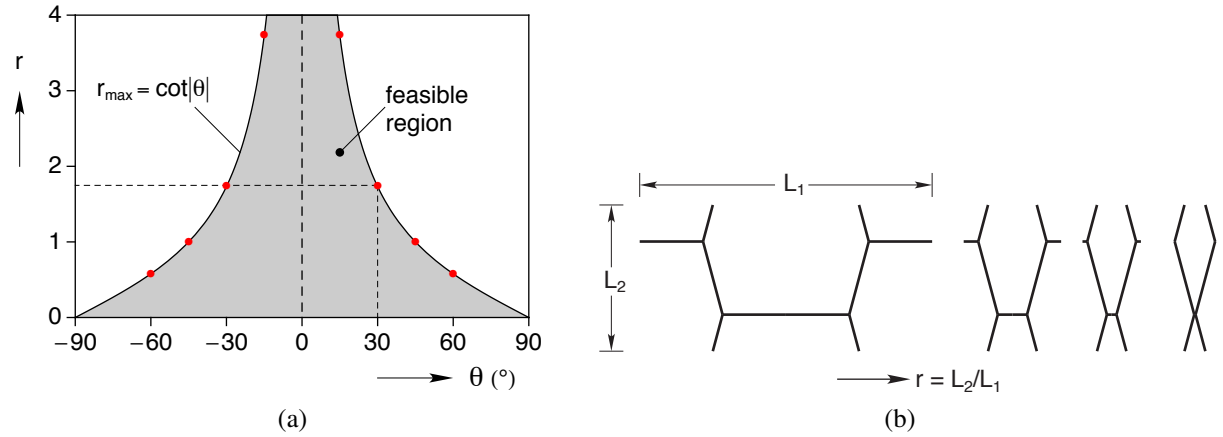

Figure 7.14: The feasible range of r's is dependent on θ, and is limited by $r \leq r_{\max}$ (a). As r increases, the unit cell geometry approaches a diamond shape (b).

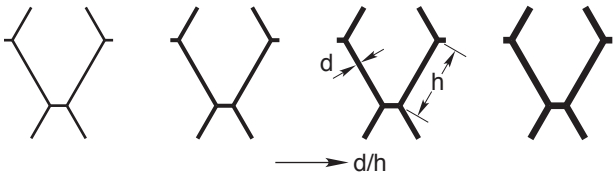

Figure 7.15: As d/h increases, the relative thickness of the honeycomb ligaments increases.

The honeycomb angle, θ, characterizes the alignment of the diagonal elements to the loading orientation. Since buckling is highly dependent on this orientation, θ is expected to strongly influence the stability of the structure. It should be noted that, for cases in which $\theta < 0$, honeycombs exhibit a negative Poisson's ratio (ν) and are usually referred to as *auxetic*. The effects of increasing θ are illustrated in Figure 7.16.

7.2.2 Procedure

To gain a better understanding of the dependencies of SMA honeycomb mechanical properties on geometry, a finite set of geometries were examined within the parametric space with fixed SMA material properties. This discretization was defined according to all combinations of $\theta =$

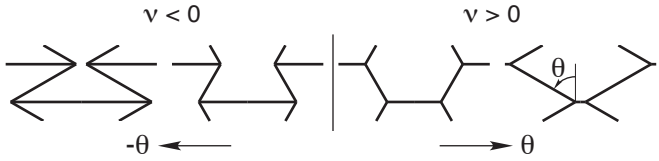

Figure 7.16: As $|\theta| \rightarrow 0$, the diagonal element of the unit cell approaches vertical.

Table 7.2: Constitutive model parameters for the SMA honeycomb parametric study.

Parameter	Value
$E_A = E_M^+ = E_M^-$	1
$E_l^+ = E_u^+$	0.05
$E_l^- = E_u^-$	0.15
β^+	0.0418
β^-	-0.02125
ϵ_n^+	0.006
ϵ_n^-	0.0012
$\Delta\sigma_A^+ = \Delta\sigma_A^-$	0.002

$\{\pm 15^o, \pm 30^o, \pm 45^o, \pm 60^o\}$, $r = \{0.1, 0.2, 0.3, ..., \lfloor r_{max} \rfloor\}$[3], and $d/h = \{0.005, 0.010, 0.015, ..., 0.100\}$, resulting in a total of 2780 cases. For each case, quasi-static finite element simulations were conducted according to a displacement-based loading procedure in the Y direction (see Figure 7.13) along the principal solution path. To model superelastic behavior of NiTi-like SMA honeycombs, the asymmetric, hysteretic, constitutive law outlined in Section 5.1.3 was implemented using the material parameters in Table 7.2.

The principal solution of each honeycomb was evaluated using an increment–based loading procedure which was parameterized by the monotonically increasing loading parameter λ. From the global boundary conditions,

$$\begin{aligned} F_X(-\infty, Y) = 0, \quad F_Y(-\infty, Y) = 0, \quad M(-\infty, Y) = 0 \\ F_X(\infty, Y) = 0, \quad F_Y(\infty, Y) = 0, \quad M(\infty, Y) = 0 \\ F_X(X, -\infty) = 0, \quad V(X, -\infty) = 0, \quad M(X, -\infty) = 0 \\ F_X(X, \infty) = 0, \quad V(X, \infty) = \delta^*(\lambda), \quad M(X, \infty) = 0, \end{aligned} \tag{7.9}$$

where V is a global displacement in the Y direction, F_X and F_Y are forces in the X and Y directions, respectively, and M is am bending moment. At the start of loading ($\lambda = 0$), the structure loads along the principal solution path which corresponds to unit cell periodic deformation. From

[3]The form $\lfloor x \rfloor$ denotes that x is rounded down to the first decimal place.

Eq. (7.9), the corresponding unit cell periodic deformation corresponds to

$$\begin{aligned}
&F_X^{(1)} = 0, && F_Y^{(1)} = 0, && M^{(1)} = 0 \\
&F_X^{(4)} = 0, && F_Y^{(4)} = 0, && M^{(4)} = 0 \\
&U^{(2)} = F_X^{(3)} = 0, && V^{(2)} = V^{(3)} = 0, && M^{(2)} = M^{(3)} = 0 \\
&U^{(6)} = F_X^{(5)} = 0, && V^{(6)} = V^{(5)} = \delta(\lambda), && M^{(6)} = M^{(5)} = 0,
\end{aligned} \tag{7.10}$$

where U is a global displacement in the X direction and $(\cdot)^{(i)}$ denotes the i^{th} nodal quantity (see Figure 6.7 for node numbering of the unit cell); note that $U^{(2)} = V^{(2)} = V^{(3)} = 0$ to prevent rigid body motion and $U^{(6)} = 0$ from the periodic boundary conditions. At each loading step, the principal path solution was determined using a Newton-Raphson solution algorithm.

In evaluating a honeycomb design, two finite element simulations were performed to accurately calculate the mechanical response and critical buckling load of the structure. The first simulation evaluated the mechanical response of the principle branch up to a macroscopic strain (δ/L_2) of 70% using a fine loading step without regard to the loss of structural stability. The second simulation was used to determine the critical buckling load according to the Bloch wave stability analysis outlined in Chapter 6. Starting with a coarse loading step, the loading was incrementally increased until the first indication of instability (if any). A bisection-based loading procedure was then conducted to accurately converge on the critical buckling load to within a tolerance of 7×10^{-5} % macroscopic strain (δ/L_2). For a more detailed discussion on the stability analysis of a honeycomb structure in the context of the finite element analysis, see Section 6.5.3.

7.2.3 Results and Discussion

For each design, the overall energy absorption performance was evaluated. To ensure reusability of the honeycombs and to maintain physically meaningful results, the mechanical response of each design was limited to within operational bounds. For the cases in which the structure became unstable during loading, further investigation was conducted with respect to the corresponding mode of instability. A brief discussion of the relationship between honeycomb design and the macroscopic Poisson's ratio is discussed, followed by the identification of optimum geometric designs with respect to specific energy end energy density measures. Due to the quantity of data collected in this study, the following will first focus on results for $\theta = \pm 30^{\text{o}}$ and then be generalized to the other θ cases.

Performance Constraints

In the first simulation of each honeycomb design, loading was conducted along the principal solution path regardless of the physicality of the response. To maintain physically meaningful behavior in the quantification of energy absorption performance, the mechanical response was truncated according to the following constraints:

- **Local strains within the ligaments must remain within prescribed limits** – The fatigue life of superelastic materials, which dictates the reusability of the structure, is highly dependent on loading conditions. In general, the more extreme the loading condition, the shorter the fatigue life. In this study, local strain limits ($\varepsilon_{\max}$) of 5.0% and 2.5% were imposed on the honeycomb ligament behavior as representative limits for low and high cycle applications for the material definition in Table 7.2, respectively.

- **The macroscopic loading must be less than the critical buckling load of the structure** – Although *Bloch wave* analysis provides information with respect to the onset and nature of instability, the solution at the critical buckling load loses uniqueness. The principal solution followed after the first instability is only one of many possible solution paths. As deformation along the principal path is seldom observed in reality due to imperfections within real systems, it is unlikely that this mechanical behavior accurately represents real SMA honeycomb behavior. Determination of the solution path along secondary branches is a complex problem and beyond the scope of this work (for the reader interested in details on performing these complex path following problems, see for example Sorkin et al. [2014]); however, as the secondary solution paths associated with buckling often result in higher local strains than the principal path, it is expected that local strain limits would be hit near or just after buckling. In general, this is a conservative restriction on performance.

- **Inter-ligament contact is inadmissible** – Inter-ligament contact becomes relevant for negative Poisson's ratio honeycombs (i.e. $\theta < 0$), occurring between nodes 7 and 10 (Figure 7.13). If a contact algorithm was incorporated into the analysis, contact between nodes 7 and 10 would result in a "fused" joint and further loading would result in a significantly stiffer response. In reality, imperfections within the structure would likely result in nodes 7 and 10 sliding along the adjoining ligaments with only mild stiffening of the structural response. Imperfections could be added to the unit-cell geometry to more accurately model this behavior; however, the corresponding stability analysis would likely be highly sensitive to the nature of the imperfection, resulting in a highly complex problem. It is therefore difficult to determine the exact behavior post-contact without significant modeling and computational efforts and is beyond the scope of this study. This is therefore a very conservative

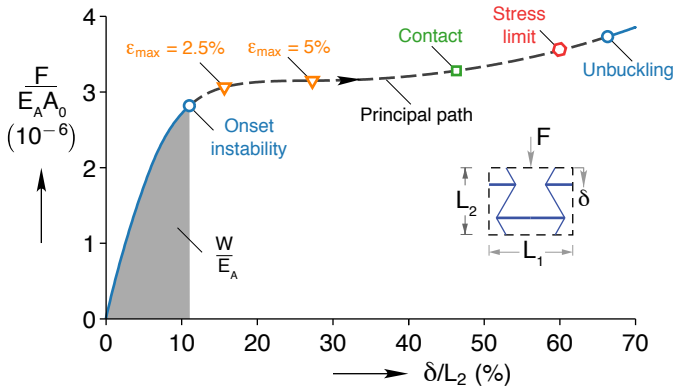

Figure 7.17: Simulation constraints activate at different points along the principal path (where $A_0 = L_1 L_3$ is the projected cross-sectional area of the unit cell), an example of which is shown here for $r = 0.7$, $d/h = 0.025$ and $\theta = -30^{\circ}$, where the normalized absorbed energy (W/E_A) is the integration of the response up to the first active constraint (which is the onset of instability here).

restriction on performance.

- **The macroscopic loading must stay within design requirements** – In application, honeycomb energy absorbers are often designed to absorb a prescribed energy for a given maximum load; for example, energy absorbers used in packaging are designed to absorb energy while exerting a small load on the contents inside. Therefore, this design parameter was incorporated into the analysis through the addition of a limiting macroscopic stress (σ^*).

All design properties were calculated up until the onset of the first active constraint. If no constraints were active, then the properties were calculated up until the end of loading at $70\,\%$ macroscopic strain. Figure 7.17 illustrates the principal solution for one of the honeycomb designs, along with the points in the loading in which each constraint became active and the corresponding measurement of the absorbed energy. Overall, these constraints are expected to be a conservative lower bound of a design's performance while ensuring reusability.

The limiting constraint of a honeycomb design provides insight as to the dominant mechanical behavior. For $\theta = \pm 30^{\circ}$, $\varepsilon_{\max} = 2.5\,\%$, and an arbitrary stress constraint, mappings the first active constraint with respect to r and d/h space are shown in Figure 7.18. These two mappings serve as a representation of the trends found for all θ and result in the following observations:

- Local strain limit based constraints (as depicted by the orange regions), occur for low r, high d/h and high $|\theta|$. These designs correspond to load bearing elements that are short, thick and closer to horizontal than vertical (i.e. stocky cantilever beams). The results for the case of a $5\,\%$ strain limit are similar; however, the strain limited region recedes towards lower r

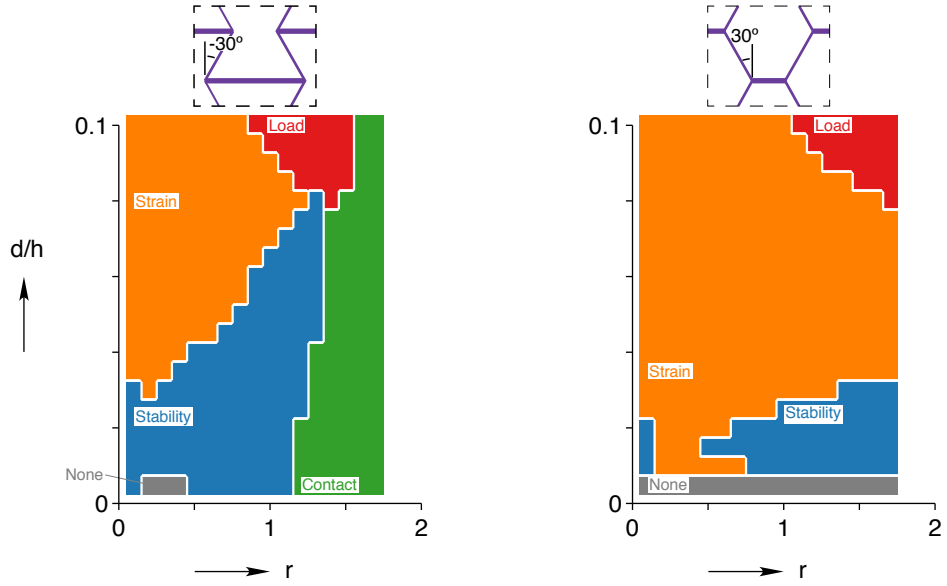

(a) $\theta = -30^{\circ}$ (b) $\theta = 30^{\circ}$

Figure 7.18: Honeycomb performance tends to be limited by the local strain limit ($2.5\,\%$ shown here) for low r and high d/h, the stability limit for high r and low d/h, the macroscopic stress limit for high r and high d/h, and the contact limit for $\theta < 0$ and high r.

and higher d/h.

- Stability based constraints (denoted by the blue regions) stem from high r, low d/h and low $|\theta|$. These designs correspond to loading bearing elements that are long, slender and closer to vertical than horizontal, aligning with classical notions of beam buckling.

- Internal contact (as denoted by the green regions) is only present for designs with $\theta < 0$. For increasing r and decreasing θ the region of internal contact grows. Geometrically, these designs correspond to unit cells in which nodes 7 and 10 (see Figure 7.13 for reference) are close together in the undeformed configuration (see Figures 7.14b and 7.16 for visual trends). As the structure is loaded, these nodes pinch together until contact ultimately occurs.

- Stress limit based constraints (as depicted by the red regions), occur for high r and high d/h, which correspond to long and thick ligaments. The high stiffness of these design cases induce the stress limit earlier in loading.

- Very few cases had no constraints active up to the maximum macroscopic strain of $\delta/L_2 = 70\,\%$ (as denoted by the gray regions). These cases were restricted to low values of d/h and large values of $|\theta|$ and (as shown later) generally exhibited low energy absorption.

Instabilities

The post-buckling behavior of infinite honeycombs is highly complex; however, examination of the *Bloch wave* modes near the critical buckling load provides some insight with respect to the ensuing deformation. The initial macroscopic strain δ/L_2 (λ_c in Section 6.5.3) along the principal path at which different mode shapes become unstable are shown in Figure 7.19 for two honeycomb designs with the same d/h and θ, but different r: $(r, d/h, \theta) = (0.1, 0.03, 30°)$ and $(r, d/h, \theta) = (1.5, 0.03, 30°)$. The critical buckling displacement of the structure (denoted by δ_c) corresponds to the minimum point on the instability surface; although, the exact location of δ_c within the wavenumber space is approximate due to the finite sampling of both the loading increment and the κ space. In the case of the honeycomb with geometric parameters $(r, d/h, \theta) = (0.1, 0.03, 30^o)$ (Figure 7.19a), the instability surface spans a large portion of the Bloch wavenumber space over a relatively shallow variation in δ/L_2. Conversely, for the case of the honeycomb with $(r, d/h, \theta) = (1.5, 0.03, 30°)$ (Figure 7.19b), the instability surface is much narrower, although still relatively shallow with respect to δ/L_2. In both cases, the continuity and shallowness of the surface suggests the post-buckling behavior of the structures will be highly imperfection sensitive; that is, even small imperfections will potentially result in a large change in the corresponding post-buckling behavior. The directionality of the imperfection sensitivity, however, differs between the two geometries. Let

$$\alpha = \arctan \frac{\kappa_2}{\kappa_1} \tag{7.11}$$

be the "direction" of the instability, where κ_1 and κ_2 are the normalized Bloch wavenumbers as defined in Section 6.5.3. With respect to Figure 7.19a, the shallowness of the instability surface is omnidirectional, suggesting the "direction" of the instability is also highly sensitive to imperfection; whereas, with respect to Figure 7.19b, the shallowness of the instability surface is relatively unidirectional, suggesting the "direction" of the instability is likely imperfection insensitive.

Although it is difficult to quantify the exact wavelength of the mode shape corresponding to a particular critical buckling load, it is still illustrative to visualize the calculated mode shapes to get a sense of the general characteristics. As the finite element analysis was only with respect to the honeycomb unit cell, the eigenvector corresponding to the loss in positive definiteness of the structural stiffness matrix only corresponds to the mode shape of the unit cell; however, except for a mode shape with unit cell periodicity, the mode shape has greater dimensionality than the unit cell. To determine the entire mode shape, the *Bloch wave* representation must be used as defined in Eq. (6.84). Note that the calculated mode shapes will involve complex numbers in general; therefore, once the mode shape is calculated (i.e., after applying Eq. (6.84)), either the real or

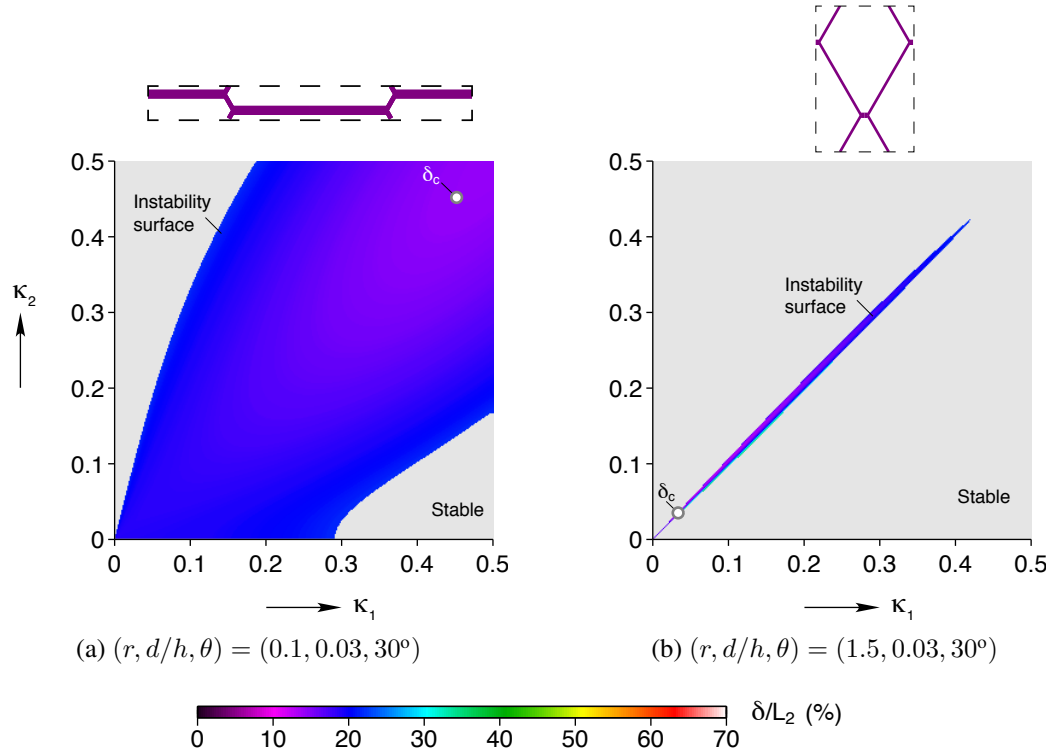

(a) $(r, d/h, \theta) = (0.1, 0.03, 30^o)$ (b) $(r, d/h, \theta) = (1.5, 0.03, 30^o)$

Figure 7.19: The characteristics of the instability surface (initial macroscopic strain δ/L_2 along the principal path at which different instability modes become unstable) vary broadly depending on the honeycomb design; for example, $(r, d/h, \theta) = (0.1, 0.03, 30^o)$ had a broad surface with a minimum (δ_c) in the upper right portion of the wavenumber space, while $(r, d/h, \theta) = (1.5, 0.03, 30^o)$ had a narrow surface with a minimum near the origin of the wavenumber space.

imaginary part can be taken to examine the shape. The mode shapes corresponding to $\delta_c \equiv \delta(\lambda_c)$ in Figure 7.19 are shown in Figure 7.20. Two extremes of mode shapes are shown here, with local deformation shown in Figure 7.20a while there is more global deformation in Figure 7.20b.

Poisson's Ratio

The ligament based construction of honeycombs allows for structures in which the macroscopic Poisson's ratio is not limited to the isotropic elasticity range of $-1 < \nu < 0.5$ and can be tuned according to the honeycomb geometry. As formulated by Gibson et al. [1982] using engineering beam theory, the Poisson's ratio of a linear elastic honeycomb under loading along the Y direction is

$$\nu = \frac{h \cos^2 \theta}{(\ell + h \sin \theta) \sin \theta} = r \cot \theta, \tag{7.12}$$

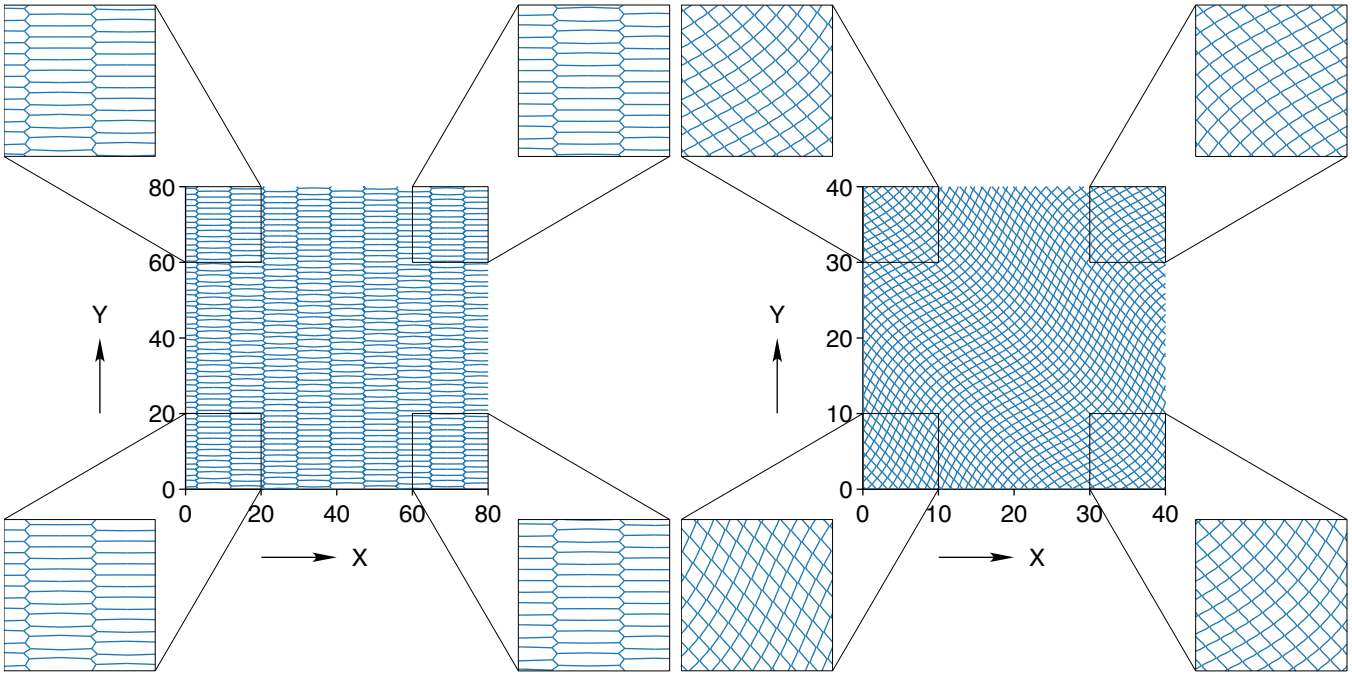

(a) $(r, d/h, \theta) = (0.1, 0.03, 30^{\text{o}})$ (b) $(r, d/h, \theta) = (1.5, 0.03, 30^{\text{o}})$

Figure 7.20: Depending on the normalized wavenumber pair (κ_1, κ_2), the characteristics of the instability mode shape deformation ranged from (a) local to (b) global.

illustrating the auxetic behavior of honeycombs with $\theta < 0$. For a chosen θ, the linear dependence of ν on r results in a simple formulation for the design of a honeycomb's Poisson's ratio. From Eq. (7.8), the Poisson's ratio is limited by

$$0 \leq \nu \leq \nu_{\max} \quad \text{for} \quad 0^\circ \leq \theta \leq 90^\circ \tag{7.13a}$$

and

$$-\nu_{\max} \leq \nu \leq 0 \quad \text{for} \quad -90^\circ \leq \theta \leq 0^\circ \tag{7.13b}$$

where

$$\nu_{\max} = r_{\max} \cot|\theta| = \cot^2|\theta| \,. \tag{7.14}$$

As $\cot^2|\theta|$ monotonically decreases with increasing $|\theta|$ (such that $|\theta| \leq 90^{\text{o}}$, which is the feasible region for physical designs of honeycombs), the greatest Poisson's ratios can be attained for low $|\theta|$; furthermore, as $\cot\theta$ is a point symmetric function about the origin and $r > 0$, honeycombs with $\pm\theta$ have the same $|\nu|$ relationship with respect to r.

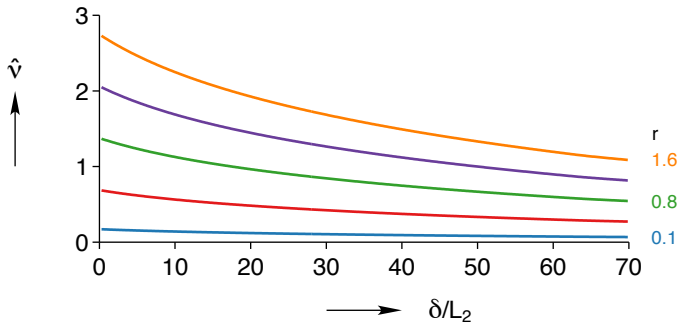

Figure 7.21: As a honeycomb is compressed (shown here for honeycombs with the parameters $d/h = 0.005$ and $\theta = 30°$), the magnitude of the instantaneous Poisson's ratio ($|\hat{\nu}|$) monotonically decreases with greater variations as r increases; furthermore, $|\hat{\nu}|$ increases with increasing r.

Although Eq. (7.12) provides a useful tool for tuning the Poisson's ratio of a honeycomb structure, it is derived from linear elastic engineering beam theory (i.e., small strains, small displacements and small rotations), which is only valid for the initial behavior of the structure. The evolution of the effective Poisson's ratio ($\hat{\nu}$) throughout the loading procedure for honeycombs with $(d/h, \theta) = (0.005, 30^{\text{o}})$ and varying r are shown in Figure 7.21, where

$$\hat{\nu} \equiv -\frac{\varepsilon_X^*}{\varepsilon_Y^*} \tag{7.15}$$

and ε_X^* and $\varepsilon_Y^* = \delta/L_2$ are macroscopic strains. At $\delta/L_2 = 0$, $\hat{\nu}$ abides by Eq. (7.12) and then decreases monotonically with increasing load, with high r designs exhibiting the greatest variations during loading.

Optimum Energy Absorber

The energy absorption performance of the honeycomb designs is evaluated according to two metrics: specific energy absorption and absorbed energy density. Defined as absorbed energy per unit mass (W/m), the specific energy metric optimizes with respect to weight efficiency, resulting in a lightweight energy absorber; whereas, defined as absorbed energy per unit macroscopic volume (W/V^*), the energy density metric optimizes with respect to space efficiency, resulting in a compact energy absorber. Both quantities are normalized with respect to the austenite modulus of elasticity (E_A) and, in the case of specific energy, the mass is normalized with respect to the density of the material, resulting in dimensionless specific energy $W/(E_A V_s)$ and dimensionless energy density $W/(E_A V^*)$, where

$$V_s = 2(2h + \ell)dL_3 \tag{7.16}$$

is the volume of the SMA material and

$$V^* = L_2 L_1 L_3 \tag{7.17}$$

is the macroscopic volume of the unit cell (and L_3 is the depth of the honeycomb which was taken as 1 for this study).

In the case of both energy metrics, optimal designs tended towards designs with high d/h and low $|\theta|$ as shown in Figures 7.23 and 7.24 for $\varepsilon_{\max} = 2.5\,\%$ and no imposed macroscopic stress constraint. In Figures 7.23 and 7.24, optimum designs are defined as those that lie within $5\,\%$ of the maximum energy metric for a given θ, which helps give a sense of the shallowness/steepness of the energy metric over the design space. With respect to the specific energy measure at fixed θ (Figure 7.23), optimal designs tended toward the r boundary between the local strain and stability constraints. When no interface existed between the local strain and stability constraints at high d/h, optimal designs corresponded to high r, bordering the contact limited region in the case of $\theta < 0$ and $r_{\max}$ for $\theta > 0$; furthermore, designs that were limited by local strain constraints showed little to no dependency on d/h. This resulted in a set of optimal designs with nearly identical performance for a given θ. Conversely, only a single optimum design tended to exist for a given θ when using the energy density metric (Figure 7.24). The optimal design always tended towards the contact limited region in the case of $\theta < 0$ and $r_{\max}$ for $\theta > 0$. These general trends were consistent regardless of $\varepsilon_{\max}$.

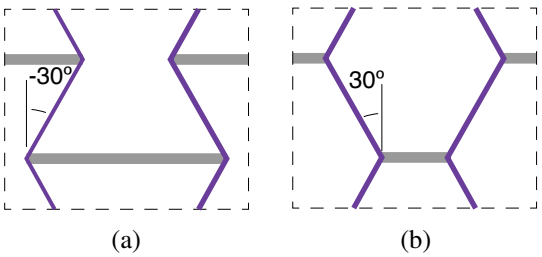

Figure 7.22: Due to the loading orientation, the diagonal ligaments were the only load carrying members, resulting in identical mechanical responses for the $+\theta$ and $-\theta$ designs.

Regardless of energy measure, the designs with $+\theta$ always outperformed (or were equivalent to) the corresponding $-\theta$ designs with the same r and d/h (see Figures 7.23 and 7.24). This improved energy absorption performance for $\theta > 0$ designs was the result of three factors:

- Only $\theta < 0$ designs were susceptible to the very conservative contact constraint (as seen in a comparison of the contact limited regions of Figures 7.23 and 7.24).
- The $-\theta$ configurations were less stable than the $+\theta$ configurations (as seen in a comparison

of the stability limited regions of Figures 7.23 and 7.24).

- Due to the loading orientation, the diagonal ligaments were the only load carrying members of the structure (see Figure 7.22), resulting in identical mechanical responses and total energy absorption for the $+\theta$ and $-\theta$ honeycomb designs. In the case of the energy density metric, the identical unit cell volume for $\pm\theta$ designs resulted in the same energy density performance (as seen in a comparison of the strain limited regions of Figure 7.24); whereas, in the case of the specific energy metric, the greater mass of the $-\theta$ designs resulted in less specific energy absorption (as seen in a comparison of the strain limited regions of Figure 7.23).

In general, SMA honeycombs with $\theta = \{15°, 30°\}$ had the best energy absorption properties (see Figures 7.23 and 7.24 for the case of $\varepsilon_{\max} = 2.5\,\%$). Although the results shown here are only for a single strain limit $\varepsilon_{\max}$, this trend was found for all $\varepsilon_{\max}$. Within these designs, there existed a cutoff $\varepsilon_{\max} = 5\,\%$ where honeycombs with $\theta = 15°$ performed best for $\varepsilon_{\max} < 5\,\%$, while $\theta = 30°$ performed best for $\varepsilon_{\max} > 5\,\%$. So, honeycombs with smaller $|\theta|$ have better applicability for high cycle loading conditions, while honeycombs with higher $|\theta|$ are more suited for low cycle loading conditions.

To gather perspective on the implications of the macroscopic stress constraint, its influence on both energy metrics was examined over a range of values. For a particular θ, the maximum stress ($\sigma^*_{\max}$) was determined for all of the designs within the corresponding r-d/h space. Five macroscopic stress constraints where then chosen, σ^*_i for $i = 1, 2, .., 5$, such that $\sigma^*_i/\sigma^*_{\max} = i/5$, and the corresponding behaviors were compared (noting that σ^*_5 had no macroscopic stress constraint). A representative case is shown in Figure 7.25 for the energy density measure of honeycombs with $\theta = 30°$ and $\varepsilon_{\max} = 5\,\%$. The addition of a macroscopic stress constraint shifted the optimum designs from high r and d/h towards the boundary of the strain-stability-stress constraint boundaries. Although the trends vary somewhat depending on the energy measure and θ, in general, the optimum designs lie along the stress constraint boundary. When the strain, stability and macroscopic stress constraint meet at a juncture, the optimum points tend to cluster around this juncture, forming a ridge of closely performing designs. At higher macroscopic stress constraints, when the macroscopic stress constraint boundary only touches the strain boundary, the optimum designs tend towards higher aspect ratios along the constraint boundary.

7.2.4 Conclusions

Design optimization of infinite, perfectly periodic, superelastic shape memory alloy (SMA) honeycombs was performed with a focus on reusable energy absorption applications. The design space

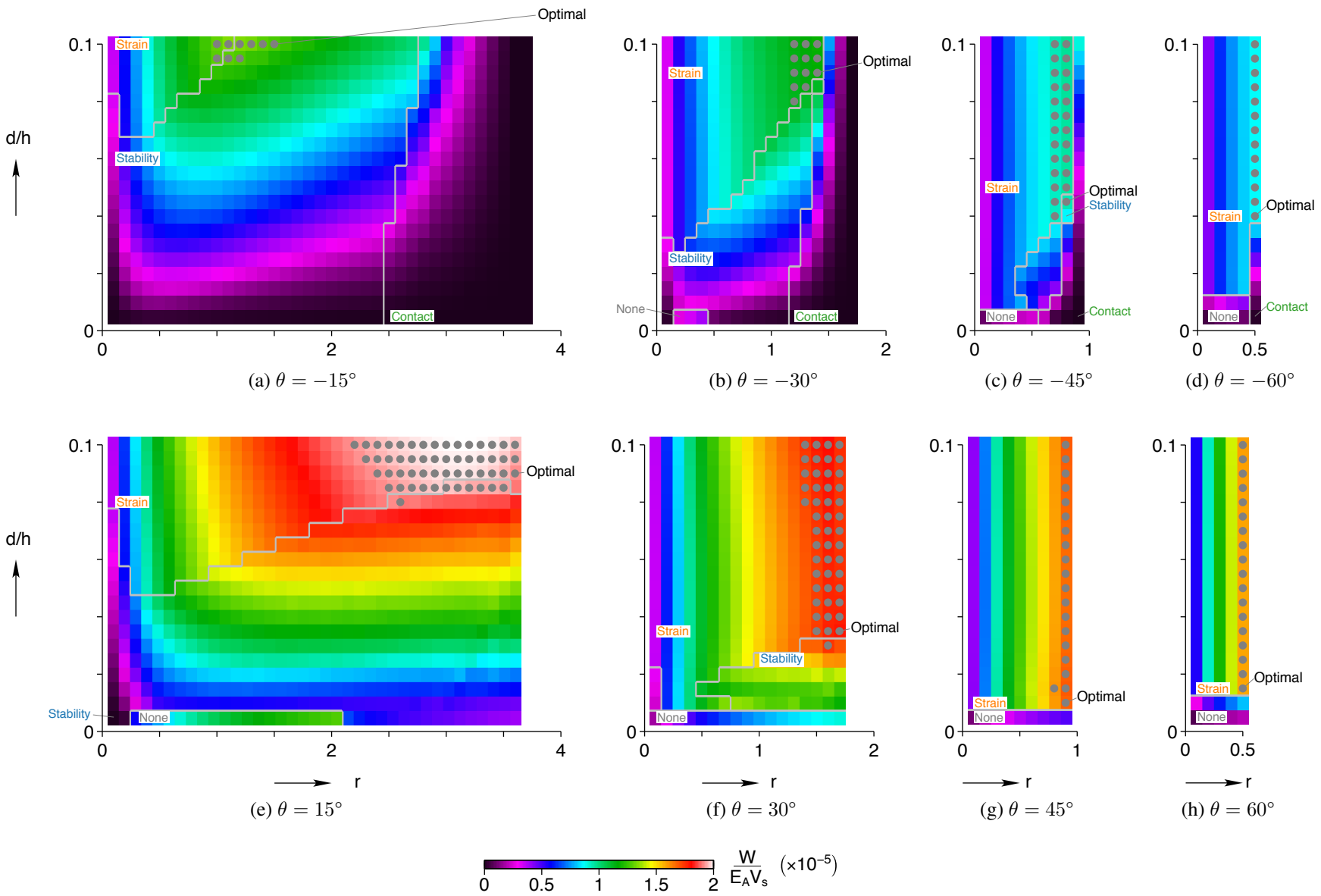

Figure 7.23: In the case of specific energy ($W/(E_A V_s)$) performance with $\varepsilon_{\max} = 2.5\,\%$ and no stress constraint, a large set of designs performed optimally (as marked by the grey dots) which tended to correspond to high r. Overall, designs with $\theta > 0°$ out performed those with $\theta < 0°$ and the $\theta = 15°$ designs performed the best overall.

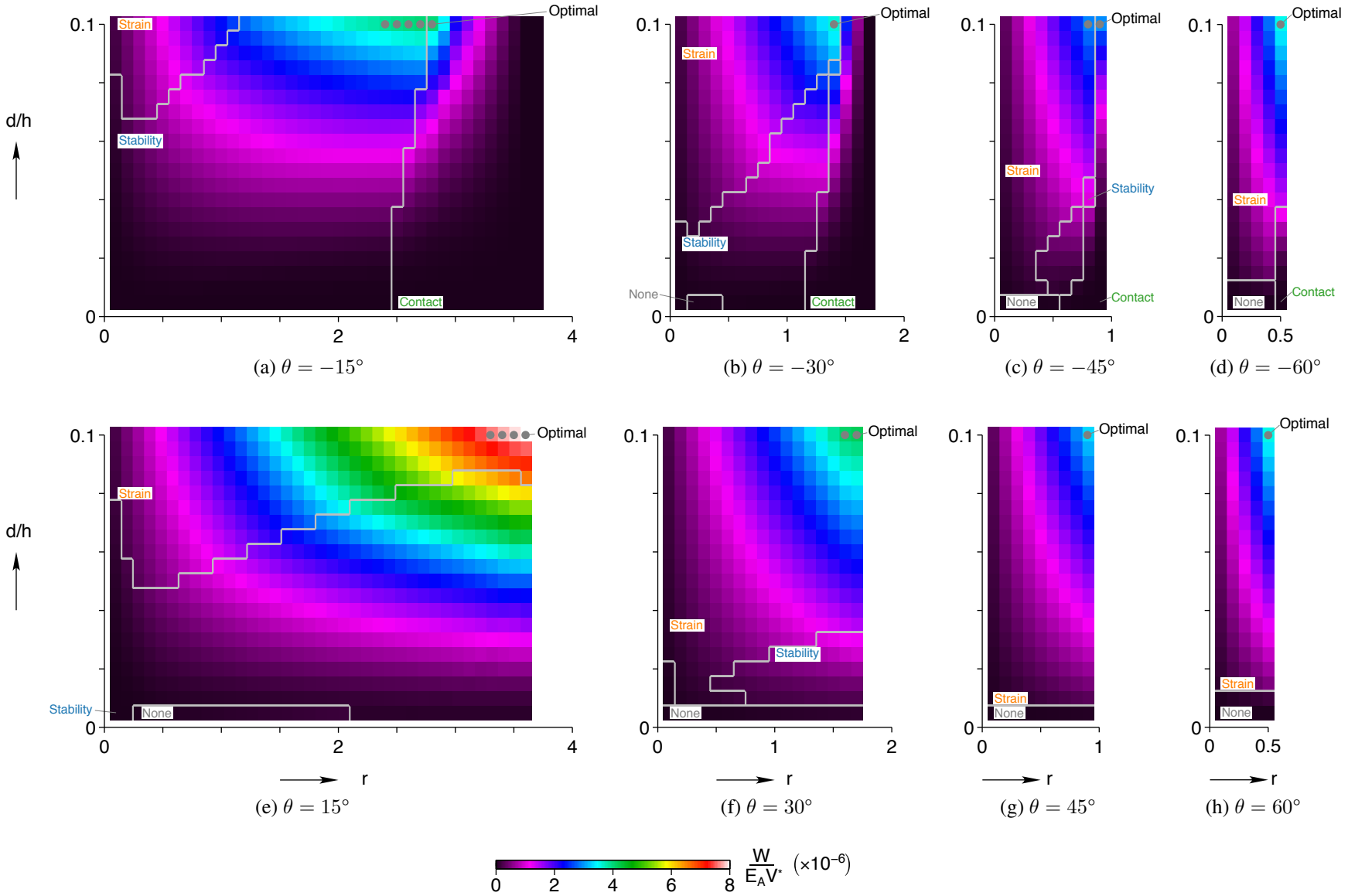

Figure 7.24: In the case of energy density ($W/(E_A V^*)$) performance with $\varepsilon_{\max} = 2.5\,\%$ and no stress constraint, optimal designs (marked by the grey dots) were restricted to a small set of designs which tended to correspond to high r and d/h. Overall, designs with $\theta > 0°$ out performed those with $\theta < 0°$ and the $\theta = 15°$ designs performed the best overall.

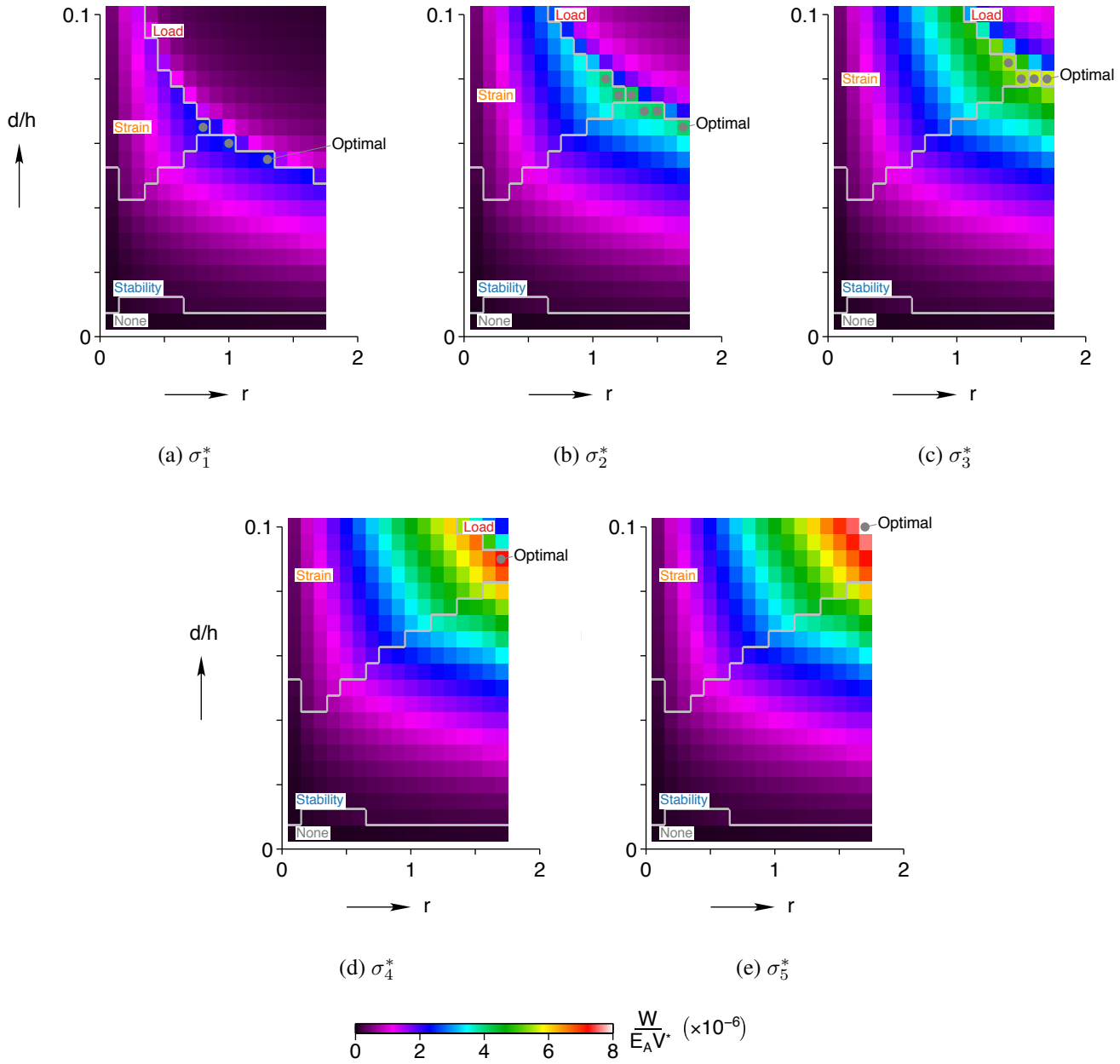

(a) σ_1^* (b) σ_2^* (c) σ_3^*

(d) σ_4^* (e) σ_5^*

Figure 7.25: In the case of energy density performance ($W/(E_A V^*)$) for honeycombs with $\theta = 30°$ and $\varepsilon_{\max} = 5\,\%$, optimal designs (labeled by grey dots) shifted from high to midrange r and d/h as the magnitude of the macroscopic stress constraint ($\sigma_1^* < \sigma_2^* < \sigma_3^* < \sigma_4^* < \sigma_5^* = \sigma_{\max}^*$) was decreased, congregating near the boundary of the strain-stability-stress constraints.

was fully defined by the honeycomb unit cell aspect ratio (r), ligament thickness to length ratio (d/h) and honeycomb angle (θ), which was discretely sampled to probe the behavior of NiTi-like honeycombs. For each design, finite element simulations in conjunction with Bloch wave stability analysis evaluated mechanical behavior and energy absorption performance. To ensure physically relevant results, constraints on the behavior of each design (such as limits on the maximum local strain and macroscopic applied stress, along with structural stability) were imposed. As mass and space efficiency are often desired in energy absorbers, specific energy (energy/mass) and energy density (energy/volume) metrics were used to evaluate energy absorption performance.

Based on the results of the parametric study, the following SMA honeycomb design guidelines were formulated:

- In all cases, designs with $\theta > 0$ outperformed (or were comparable) to those with $\theta < 0$. So, unless an application requires a negative Poisson's ratio, it is reasonable to restrict designs to $\theta > 0$.
- For low strain limits, the set of optimum designs occurs for low $|\theta|$. As the strain limit increases, the set of optimum designs shifts to higher $|\theta|$. In the case of the strain limits used in this study, the best performance occurred for $\theta = 15°$ with a strain limit of $2.5\,\%$ and $\theta = 30°$ with a strain limit of $5.0\,\%$ (regardless of the energy measure).
- When working with honeycombs in which $\theta > 0$, designs with $r = r_{\text{max}}$ usually perform better than other designs with the same θ and d/h and $r < r_{\text{max}}$. Geometrically, these designs correspond to diamond-type unit cells ($\ell = 0$, which might be difficult to fabricate). For the few exceptions where this rule does not hold (such as $\theta = 15°$), these designs still perform within $90\,\%$ of the best performance found for the same θ and d/h. It should be noted that this may not be the case for other in-plane loading directions where the horizontal ligament becomes important. This rule is less absolute for the case in which $\theta < 0$ as interligament contact dominates at high r. As the contact constraint is rather conservative (and likely far from the actual performance of these honeycombs) it is difficult to say whether or not it would be better to use a smaller aspect ratio or maximize the aspect ratio and hope that the contact behavior results in good performance.
- Optimization with respect to energy density is much more sensitive than with respect to specific energy. In general, the optimum energy density design lines up with one of the optimal specific energy designs. So, a honeycomb optimized with respect to volume is likely also optimized with respect to mass, but not necessarily vice versa.

The suggested design process of SMA honeycombs for vertical in-plane compression is to choose a design with $\theta > 0$ and $r = r_{\text{max}}$ (unless an auxetic structure is required); in the case of high

cycle (and low amplitude) loading, $\theta = 15^\circ$ should be chosen, while for the case of low cycle (and potentially high amplitude) loading, $\theta = 30^\circ$ should be chosen. From this point, d/h should be tuned based on the maximum stress constraint, where a higher stress limit allows for higher d/h (and correspondingly higher energy absorption). Due to the many competing factors, this procedure will not necessary result in the true optimum design, but will likely fall within $90\,\%$ of the optimum design performance without the need for an in-depth parametric study.

7.3 Summary & Conclusions

The properties of SMA honeycombs loaded in in–plane compression were experimentally investigated. It was found that SMA honeycombs are $10\times$ more flexible than monolithic SMAs (both in the shape memory effect and superelasticity) and their sparse configuration and bending dominated kinematics results in significantly reduced loading rate sensitivity; however, this comes at the cost of significantly reduced stiffness and strength. From an applications standpoint, SMA honeycombs are therefore most suited as compact high stroke actuators, vibration dampers, and reusable energy absorbers.

To help realize the application of SMA honeycombs as reusable energy absorbers, a parametric study was implemented to develop general rules for their optimal design. In general, it was found that SMA honeycombs with high aspect ratio unit cells and nearly vertical diagonal ligaments (between 15° and 30° from vertical) have the best energy absorption properties. The thickness of the honeycomb ligaments can then be tuned to provide the necessary load carrying requirements for a given application.

Chapter 8

Conclusions & Future Work

The primary objective of this dissertation was to facilitate the development of shape memory alloy (SMA) material models. Due to the prevalence of thin–walled structures in existing SMA applications, the focus within this objective was on beam and framed structures. To better understand the combined uniaxial and bending behavior found in SMA beams, along with the effects of beam cross-sectional geometry, tension, compression, pure bending and column buckling experiments were conducted on superelastic NiTi rods and tubes; furthermore, a novel composite based experimental setup was used to measure the local up–down–up material response of an SMA pulled in tension. Based on this phenomenological understanding, a trilinear material law was implemented into a Shanley column model and within general beam theory to model the deformation of SMA beams. This model was found to capture many of the relevant behaviors found in SMA beams (such as unbuckling behavior in short SMA columns) and was used to model and design superelastic SMA honeycombs.

8.1 Conclusions

The complex material behavior found in SMAs pose many challenges from a modeling perspective. As discussed in this dissertation,

- the up–down–up tensile behavior can cause localization of phase transformation and the deformation field within the material, a phenomenon that is associated with the loss of ellipticity of the governing equilibrium equations and results in a number of computational difficulties (such as non-uniqueness and numerical instability);
- the localization behavior found in SMAs depends not only on the loading conditions, but also the material geometry, which likely has implications on the failure and fatigue behavior of the material; and

- the stiff–soft–stiff uniaxial behavior of SMAs can cause nonintuitive behavior (such as unbuckling), suggesting there may still be behaviors unique to SMAs that have yet to be observed (and understood).

Some assumptions commonly used in the modeling of metals, such as the Euler Bernoulli assumption, appear to hold for SMA beams; however, there are still many that have yet to be confirmed. It is therefore likely that a combined experimental and theoretical effort will be necessary to fully understand the relevant phenomena found in SMAs and accurately/efficiently capture these phenomena within the framework of a constitutive model.

8.2 Future Work

This work provides a foundation for more extensive modeling efforts in the future. The proposed beam model was adopted due to the success of the Shanley column model in capturing unbuckling behavior in superelastic SMAs; however, no other validation was provided to gauge the overall performance of the generalized model. The logical next step would therefore be to examine the performance of the proposed model, using the uniaxial data from Sections 2.3.1 and 2.3.2 and Chapter 3 to calibrate the model and the pure bending and buckling data from Sections 2.3.3 and 2.3.4 to examine the performance capabilities.

In addition to model validation, an appropriate model calibration technique needs to be developed. A likely candidate is a secant modulus based technique that uses the uniaxial response (both in tension and compression) of the material to determine the tangent moduli and trilinear sectioning for the model; however, fitting a sharp cornered trilinear material law to the actual smooth uniaxial data leaves room for interpretation (especially in the case of the compressive response). Ideally, some form of procedure would be developed to address this issue.

Even in the case that a robust calibration procedure can be devised, there are still issues associated with gathering the necessary experimental data to perform the calibration. Both the compression and composite tension experiments require custom and intricate fixturing which are likely beyond the means of most people interested in calibrating an SMA model (especially designers). This begs the question: "what are the effects of neglecting the up–down–up tensile response and compression asymmetry?" In all likelihood, the effects of neglecting the up–down-up tensile response are small, especially in compression dominated loading; however, the large tension-compression asymmetry found in SMAs probably plays a significant role in the overall behavior. It would therefore be desirable to develop a robust calibration technique which only requires basic testing equipment. One such possibility is the use of inverse–based calibration; for example, see

Garbowski et al. [2012].

With the validation and calibration studies completed, the next step would be to generalize the current model to three–dimensional "space rods". This would allow for the modeling of three–dimensional structures such as stents and cables. The transition from two dimensions to three dimensions requires an understanding of the twisting behavior of the material, along with the interaction between twisting, bending and uniaxial loading. Multi–axial experiments will therefore be necessary to better understand the primary phenomena of interest.

These are just a few possible topics that could be pursued in light of the work presented here on quasistatic isothermal loading. Beyond these conditions, topics such as temperature dependence, cyclic behavior, and shape memory behavior are of interest, along with the development of a general three–dimensional model. Therefore, much work still needs to be done to realize robust constitutive laws for the modeling and design of SMA structures.

BIBLIOGRAPHY

Harold Alexander. Tensile instability of initially spherical balloons. International Journal of Engineering Science, 9(1):151–160, 1971.

P.W. Alexander, X. Gao, A.L. Browne, M.A. Voss, D.L. Patterson, L. Hao, C.S. Namuduri, J.H. BROWN, A. Zolno, J.N. Owens, et al. Shape memory alloy active hatch vent, September 2 2014. URL https://www.google.com/patents/US8821224. US Patent 8,821,224.

Melvin S. Anderson. Buckling of periodic lattice structures. AIAA Journal, 19(6):782–788, Jun 1981. ISSN 1533-385X. doi: 10.2514/3.51003. URL http://dx.doi.org/10.2514/3.51003.

Melvin S. Anderson and F. W. WIlliams. Natural vibration and buckling of general periodic lattice structures. AIAA Journal, 24(1):163–169, Jan 1986. ISSN 1533-385X. doi: 10.2514/3.9237. URL http://dx.doi.org/10.2514/3.9237.

Conventional and Auxetic SMA Cellular Structures, 2005. ASME.

Nathan J Bechle and Stelios Kyriakides. Localization in niti tubes under bending. International Journal of Solids and Structures, 2013. doi: 10.1016/j.ijsolstr.2013.11.023. URL http://dx.doi.org/10.1016/j.ijsolstr.2013.11.023.

B. Berg. Twist and stretch: Combined loading of pseudoelastic niti tubing. In Proc. 2nd Int. Conf. on Shape Memory and Superelastic Technologies SMST, volume 97, pages 443–8, 1997.

B.T. Berg. Bending of superelastic wires, part I: Experimental aspects. Journal of Applied Mechanics, 62:459, 1995.

DG Berghaus and JP Cannon. Obtaining derivatives from experimental data using smoothed-spline functions. Experimental Mechanics, 13(1):38–42, 1973.

T.L. Bergman, F.P. Incropera, D.P. DeWitt, and A.S. Lavine. Introduction to Heat Transfer. Wiley, 2011.

K. Bhattacharya. Microstructure of Martensite: Why It Forms and How It Gives Rise to the Shape-memory Effect. Oxford University Press, USA, 2003.

Felix Bloch. Quantum mechanics of electrons in crystal lattices. Z. Phys, 52:555–600, 1928.

B. Bundara, M. Tokuda, B. Kuselj, B. Ule, and J. Tuma. Superelastic tension and bending characteristics of shape memory alloys. Metals and Materials International, 6:293–299, 2000. ISSN 1598-9623. URL http://dx.doi.org/10.1007/BF03028074. 10.1007/BF03028074.

B.C. Chang, J.A. Shaw, and M.A. Iadicola. Thermodynamics of shape memory alloy wire: Modeling, experiments, and application. Continuum Mechanics and Thermodynamics, 18(1):83–118, 2006. ISSN 0935-1175. doi: 10.1007/s00161-006-0022-9. URL http://dx.doi.org/10.1007/s00161-006-0022-9.

Yi-Chao Chen and Timothy J Healey. Bifurcation to pear-shaped equilibria of pressurized spherical membranes. International Journal of Non-Linear Mechanics, 26(3):279–291, 1991.

CB Churchill, JA Shaw, and MA Iadicola. Tips and tricks for characterizing shape memory alloy wire: Part 4–thermo-mechanical coupling. Experimental Techniques, 34(2):63–80, 2010.

Constantin Corduneanu, Nicolae Gheorghiu, Viorel Barbu, Gitta Berstein, and Eugene Tomer. Almost Periodic Functions. Chelsea Publishing Company New York, 1989.

David Dellwo, Herbert B Keller, Bernard J Matkowsky, and Edward L Reiss. On the birth of isolas. SIAM Journal on Applied Mathematics, 42(5):956–963, 1982.

T. Duerig, A. Pelton, and D. Stöckel. An overview of nitinol medical applications. Materials Science and Engineering, 273:149–160, 1999. ISSN 0921-5093.

R.S. Elliott, J.A. Shaw, and N. Triantafyllidis. Stability of pressure-dependent, thermally-induced displacive transformations in bi-atomic crystals. International Journal of Solids and Structures, 39(13-14):3845–3856, 2002a. ISSN 0020-7683.

R.S. Elliott, J.A. Shaw, and N. Triantafyllidis. Stability of crystalline solids–ii: Application to temperature-induced martensitic phase transformations in a bi-atomic crystal. Journal of the Mechanics and Physics of Solids, 54(1):193–232, 2006a.

R.S. Elliott, N. Triantafyllidis, and J.A. Shaw. Stability of crystalline solids–i: Continuum and atomic lattice considerations. Journal of the Mechanics and Physics of Solids, 54(1):161–192, 2006b.

Ryan S Elliott, John A Shaw, and Nicolas Triantafyllidis. Stability of thermally-induced martensitic transformations in bi-atomic crystals. Journal of the Mechanics and Physics of Solids, 50: 2463–2493, 2002b.

JL Ericksen. Equilibrium of bars. Journal of Elasticity, 5(3):191–201, 1975.

Gaston Floquet. Sur les équations différentielles linéaires à coefficients périodiques. Annales de l'École Normale Supérieure, 12:47–88, 1883.

K. Gall and H. Sehitoglu. The role of texture in tension-compression asymmetry in polycrystalline niti. International Journal of Plasticity, 15(1):69–92, 1999.

Tomasz Garbowski, Giulio Maier, Giorgio Novati, T Garbowski, G Maier, a G Novati, and G Novati. On calibration of orthotropic elastic-plastic constitutive models for paper foils by biaxial tests and inverse analyses. Struct Multidisc Optim, 46:111–128, 2012. doi: 10.1007/s00158-011-0747-3. URL http://dx.doi.org/10.1007/s00158-011-0747-3.

G. Geymonat, S. Müller, and N. Triantafyllidis. Homogenization of nonlinearly elastic materials, microscopic bifurcation and macroscopic loss of rank-one convexity. Archive for rational

mechanics and analysis, 122(3):231–290, 1993. URL http://www.springerlink.com/content/w5086q0682238686/.

LJ Gibson, MF Ashby, GS Schajer, and CI Robertson. The mechanics of two-dimensional cellular materials. Proceedings of the Royal Society of London. Series A, Mathematical and Physical Sciences, 382(1782):25–42, 1982. ISSN 0080-4630.

Lorna J. Gibson and Michael F. Ashby. Cellular Solids: Structure and Properties. Cambridge Solid State Science Series. Cambridge Univ Pr, second edition edition, 1997.

C. Grabe and OT Bruhns. Tension/torsion tests of pseudoelastic, polycrystalline NiTi shape memory alloys under temperature control. Materials Science and Engineering: A, 481:109–113, 2008.

David S. Grummon, John A. Shaw, and Antoine Gremillet. Low-density open-cell foams in the niti system. Appl. Phys. Lett., 82(16):2727, 2003. ISSN 0003-6951. doi: 10.1063/1.1569036. URL http://dx.doi.org/10.1063/1.1569036.

D.S. Grummon, J.A. Shaw, and J. Foltz. Fabrication of cellular shape memory alloy materials by reactive eutectic brazing using niobium. Materials Science and Engineering: A, 438:1113–1118, 2006. doi: 10.1016/j.msea.2006.03.113. URL http://dx.doi.org/10.1016/j.msea.2006.03.113.

Julian F Hallai and Stelios Kyriakides. Underlying material response for lüders like instabilities. International Journal of Plasticity, 2013. doi: 10.1016/j.ijplas.2012.12.002. URL http://dx.doi.org/10.1016/j.ijplas.2012.12.002.

M.R. Hassan, F.L. Scarpa, and N.A. Mohamed. Shape memory alloys honeycomb: Design and properties. In Proceedings of SPIE, volume 5387, page 557, 2004.

MR Hassan, F. Scarpa, M. Ruzzene, and NA Mohammed. Smart shape memory alloy chiral honeycomb. Materials Science and Engineering: A, 481:654–657, 2008.

MR Hassan, F. Scarpa, and NA Mohamed. In-plane tensile behavior of shape memory alloy honeycombs with positive and negative poisson's ratio. Journal of Intelligent Material Systems and Structures, 20(8):897–905, 2009. doi: 10.1177/1045389X08099605. URL http://jim.sagepub.com/content/20/8/897.

DM Haughton. Post-bifurcation of perfect and imperfect spherical elastic membranes. International Journal of Solids and Structures, 16(12):1123–1133, 1980.

Timothy J Healey, Qingdu Li, and Ron-Bin Cheng. Wrinkling behavior of highly stretched rectangular elastic films via parametric global bifurcation. Journal of Nonlinear Science, 23(5):777–805, 2013. doi: 10.1007/s00332-013-9168-3. URL http://dx.doi.org/10.1007/s00332-013-9168-3.

Jan Van Humbeeck. Non-medical applications of shape memory alloys. Materials Science and Engineering: A, 273:134–148, 1999.

Alexander Humer. Elliptic integral solution of the extensible elastica with a variable length

under a concentrated force. Acta mechanica, 222(3-4):209–223, 2011. doi: 10.1007/s00707-011-0520-0. URL http://dx.doi.org/10.1007/s00707-011-0520-0.

RG Hutchinson and NA Fleck. The structural performance of the periodic truss. Journal of the Mechanics and Physics of Solids, 54(4):756–782, 2006. doi: 10.1016/j.jmps.2005.10.008. URL http://dx.doi.org/10.1016/j.jmps.2005.10.008.

Gérard Iooss and Daniel D Joseph. Elementary stability and bifurcation theory. Springer-Verlag, New York, NY, 2nd edition, 1990.

Milan Jirsek. Objective modeling of strain localization. Revue française de génie civil, 6(6): 1119–1132, 2002.

A.D. Johnson. Non-explosive separation device, 1992. URL http://www.google.com/patents/US5119555. US Patent 5,119,555.

G.B. Kauffman and I. Mayo. The story of nitinol: The serendipitous discovery of the memory metal and its applications. The Chemical Educator, 2(2):1–21, 1997. doi: 10.1007/s00897970111a. URL http://dx.doi.org/10.1007/s00897970111a.

S. Kyriakides and Y.-C. Chang. The initiation and propagation of a localized instability in an inflated elastic tube. International Journal of Solids and Structures, 27(9):1085–1111, 1991.

Leonardo Lecce and Antonio Concilio. Shape Memory Alloy Engineering: For Aerospace, Structural and Biomedical Applications. Butterworth-Heinemann, 1st edition, October 2014.

F. López Jiménez and N. Triantafyllidis. Buckling of rectangular and hexagonal honeycomb under combined axial compression and transverse shear. International Journal of Solids and Structures, 50(24):3934–3946, Nov 2013. ISSN 0020-7683. doi: 10.1016/j.ijsolstr.2013.08.001. URL http://dx.doi.org/10.1016/j.ijsolstr.2013.08.001.

A. Magnusson, M. Ristinmaa, and C. Ljung. Behaviour of the extensible elastica solution. International journal of solids and structures, 38(46):8441–8457, 2001.

Denys J Mead. Free wave propagation in periodically supported, infinite beams. Journal of Sound and Vibration, 11(2):181–197, 1970.

DJ Mead. A general theory of harmonic wave propagation in linear periodic systems with multiple coupling. Journal of Sound and Vibration, 27(2):235–260, 1973.

DJ Mead. Wave propagation and natural modes in periodic systems: I. mono-coupled systems. Journal of Sound and Vibration, 40(1):1–18, 1975a.

DJ Mead. Wave propagation and natural modes in periodic systems: Ii. multi-coupled systems, with and without damping. Journal of Sound and Vibration, 40(1):19–39, 1975b.

PA Michailidis, N. Triantafyllidis, JA Shaw, and DS Grummon. Superelasticity and stability of a shape memory alloy hexagonal honeycomb under in-plane compression. International Journal of Solids and Structures, 46(13):2724–2738, 2009. ISSN 0020-7683. doi: 10.1016/j.ijsolstr.2009.03.013. URL http://dx.doi.org/10.1016/j.ijsolstr.2009.03.013.

J.C. Michel, O. Lopez-Pamies, P. Ponte Castaneda, and N. Triantafyllidis. Microscopic and macroscopic instabilities in finitely strained fiber-reinforced elastomers. Journal of the Mechanics and Physics of Solids, 58(11):1776–1803, 2010. doi: 10.1016/j.jmps.2010.08.006. URL http://dx.doi.org/10.1016/j.jmps.2010.08.006.

Vishal Nayyar, K Ravi-Chandar, and Rui Huang. Stretch-induced wrinkling of polyethylene thin sheets: Experiments and modeling. International Journal of Solids and Structures, 51(9):1847–1858, 2014. doi: 10.1016/j.ijsolstr.2014.01.028. URL http://dx.doi.org/10.1016/j.ijsolstr.2014.01.028.

Y. Okabe, S. Minakuchi, N. Shiraishi, K. Murakami, and N. Takeda. Smart honeycomb sandwich panels with damage detection and shape recovery functions. Advanced Composite Materials, 17(1):41–56, 2008. ISSN 0924-3046. doi: 10.1163/156855108X295645. URL http://dx.doi.org/10.1163/156855108X295645.

Y. Okabe, H. Sugiyama, and T. Inayoshi. Lightweight actuator structure with sma honeycomb core and cfrp skins. Journal of Mechanical Design, 133:011006, 2011. doi: 10.1115/1.4003139. URL http://dx.doi.org/10.1115/1.4003139.

S.D. Papka and S. Kyriakides. In-plane compressive response and crushing of honeycomb. Journal of the Mechanics and Physics of Solids, 42(10):1499–1532, 1994.

S.D. Papka and S. Kyriakides. Experiments and full-scale numerical simulations of in-plane crushing of a honeycomb. Acta materialia, 46(8):2765–2776, 1998.

SD Papka and S. Kyriakides. Biaxial crushing of honeycombs::–part 1: Experiments. International Journal of Solids and Structures, 36(29):4367–4396, 1999a.

SD Papka and S. Kyriakides. In-plane biaxial crushing of honeycombs–:: Part ii: Analysis. International Journal of Solids and Structures, 36(29):4397–4423, 1999b.

A Srikantha Phani, J Woodhouse, and NA Fleck. Wave propagation in two-dimensional periodic lattices. The Journal of the Acoustical Society of America, 119(4):1995–2005, 2006.

M.A. Rahman, J. Qiu, and J. Tani. Buckling and postbuckling characteristics of the superelastic sma columns. International journal of solids and structures, 38(50):9253–9265, 2001.

Benjamin Reedlunn, Samantha Daly, Louis G. Jr Hector, Pablo Zavattieri, and John A. Shaw. Tips and tricks for characterizing shape memory alloy wire: Part 5 – full-field strain measurement by digital image correlation. Experimental Techniques, 35, 2011. doi: 10.1111/j.1747-1567.2011.00717.x.

Benjamin Reedlunn, Christopher B Churchill, Emily E Nelson, Samantha H Daly, and John A Shaw. Tension, compression, and bending of superelastic shape memory alloy tubes. Journal of the Mechanics and Physics of Solids, 2013. doi: 10.1016/j.jmps.2012.12.012. URL http://dx.doi.org/10.1016/j.jmps.2012.12.012.

E. Reissner. On one-dimensional finite-strain beam theory: The plane problem. Zeitschrift für Angewandte Mathematik und Physik (ZAMP), 23(5):795–804, 1972.

J. Rejzner, C. Lexcellent, and B. Raniecki. Pseudoelastic behaviour of shape memory alloy beams under pure bending: Experiments and modelling. International Journal of Mechanical Sciences, 44(4):665–686, 2002. ISSN 0020-7403.

Frank Richter, Oliver Kastner, and Gunther Eggeler. Finite-element simulation of the anti-buckling-effect of a shape memory alloy bar. Journal of materials engineering and performance, 20(4-5):719–730, 2011. doi: 10.1007/s11665-010-9797-8. URL http://dx.doi.org/10.1007/s11665-010-9797-8.

Gregory S Rohrer. Structure and Bonding in Crystalline Materials. Cambridge University Press, 2001. doi: 10.1017/CBO9780511816116.001. URL http://dx.doi.org/10.1017/CBO9780511816116.001.

F.R. Shanley. Inelastic column theory. Journal of the Aeronautical Sciences (Institute of the Aeronautical Sciences), 14(5), May 1947. doi: 10.2514/8.1346. URL http://dx.doi.org/10.2514/8.1346.

J.A. Shaw and S. Kyriakides. Thermomechanical aspects of niti. Journal of the Mechanics and Physics of Solids, 43(8):1243–1281, 1995. ISSN 0022-5096.

JA Shaw and S. Kyriakides. On the nucleation and propagation of phase transformation fronts in a niti alloy. Acta materialia, 45(2):683–700, 1997.

JA Shaw and S Kyriakides. Initiation and propagation of localized deformation in elasto-plastic strips under uniaxial tension. International journal of plasticity, 13(10):837–871, 1998.

J.A. Shaw, D.S. Grummon, and J. Foltz. Superelastic niti honeycombs: Fabrication and experiments. Smart Materials and Structures, 16:S170, 2007. doi: 10.1088/0964-1726/16/1/S17. URL http://dx.doi.org/10.1088/0964-1726/16/1/S17.

JA Shaw, CB Churchill, and MA Iadicola. Tips and tricks for characterizing shape memory alloy wire: Part 1—differential scanning calorimetry and basic phenomena. Experimental Techniques, 32(5):55–62, 2008. doi: 10.1111/j.1747-1567.2008.00410.x. URL http://dx.doi.org/10.1111/j.1747-1567.2008.00410.x.

John A Shaw, Antoine Gremillet, and David S Grummon. The manufacture of niti foams. In ASME 2002 International Mechanical Engineering Congress and Exposition, pages 3–12. American Society of Mechanical Engineers, 2002.

John A. Shaw, Christopher B. Churchill, Dimitris C. Lagoudas, and P. Kumar. Shape memory alloys. In R. Blockley and W. Shyy, editors, Encyclopedia of Aerospace Engineering, volume 4, chapter 203. John Wiley & Sons, 2010.

Correlated Solutions. Vic-3D 2010 Reference Manual. Correlated Solutions, Inc., Columbia, SC, 2012. URL www.correlatedsolutions.com.

G Song, N Ma, and H-N Li. Applications of shape memory alloys in civil structures. Engineering Structures, 28(9):1266–1274, 2006.

Viacheslav Sorkin, Ryan S Elliott, and Ellad B Tadmor. A local quasicontinuum method for 3d multilattice crystalline materials: Application to shape-memory alloys. Modelling

and Simulation in Materials Science and Engineering, 22(5):055001, 2014. doi: 10.1088/0965-0393/22/5/055001. URL http://dx.doi.org/10.1088/0965-0393/22/5/055001.

C. Steger. An unbiased detector of curvilinear structures. IEEE Transactions on Pattern Analysis and Machine Intelligence, 20(2):113–125, 1998.

Q.P. Sun and Z.Q. Li. Phase transformation in superelastic niti polycrystalline micro-tubes under tension and torsion–from localization to homogeneous deformation. International Journal of Solids and Structures, 39(13-14):3797–3809, 2002.

M.A. Sutton, J.J. Orteu, and H. Schreier. Image Correlation for Shape, Motion and Deformation Measurements: Basic Concepts, Theory and Applications. Springer, 2009. doi: 10.1007/978-0-387-78747-3. URL http://dx.doi.org/10.1007/978-0-387-78747-3.

R. Topliss and R.J. Leedham. Optical image stabilization comprising shape memory alloy actuators, September 30 2014. URL https://www.google.com/patents/US8848064. US Patent 8,848,064.

N. Triantafyllidis and S. Bardenhagen. The influence of scale size on the stability of periodic solids and the role of associated higher order gradient continuum models. Journal of the Mechanics and Physics of Solids, 44(11):1891–1928, 1996.

N. Triantafyllidis and BN Maker. On the comparison between microscopic and macroscopic instability mechanisms in a class of fiber-reinforced composites. Journal of applied mechanics, 52:794, 1985. URL http://scitation.aip.org.proxy.lib.umich.edu/getabs/servlet/GetabsServlet?prog=normal&id=JAMCAV000052000004000794000001&idtype=cvips&gifs=yes&ref=no.

N Triantafyllidis and MW Schraad. Onset of failure in aluminum honeycombs under general in-plane loading. Journal of the Mechanics and Physics of Solids, 46(6):1089–1124, June 1998.

G.R. Tucholski and C.S. Pedicini. Shape memory alloy protective device, December 4 1990. URL https://www.google.com/patents/US4975341. US Patent 4,975,341.

Yuta Urushiyama, David Lewinnek, Jinhao Qiu, and Junji Tani. Buckling of shape memory alloy columns. JSME International Journal Series A, 46(1):60–67, 2003.

Z. Xie, V.A. Neelakantan, R.L. Moses, and J.E. Marano. Temperature dependent variable flow orifice, January 17 2013. URL https://www.google.com/patents/US20130015254. US Patent App. 13/527,922.

Takayuki Yoneyama and Shuichi Miyazaki. Shape Memory Alloys for Biomedical Applications. Woodhead Publishing, November 2008.